

UNIVERSIDADE DE SÃO PAULO

Faculdade de Filosofia, Ciências e Letras de Ribeirão Preto

Departamento de Física

Danilo Maziero

**Localização e estudo de fontes epileptogênicas em
pacientes de epilepsia focal em fase pré-operatória**

Ribeirão Preto – SP

2016

DANILO MAZIERO

Localização e estudo de fontes epileptogênicas em pacientes de epilepsia focal em fase pré-operatória

Tese apresentada à Faculdade de Filosofia, Ciências e Letras de Ribeirão Preto da Universidade de São Paulo. Como parte das exigências para a obtenção do título de Doutor em Ciências.

Área de Concentração:

Física Aplicada à Medicina e Biologia

Orientador:

Prof. Dr. Carlos Ernesto Garrido Salmon

Co-orientador:

Dr. Tonicarlo Rodrigues Velasco

Versão Corrigida

Versão original disponível na FFCLRP

Ribeirão Preto – SP

2016

Autorizo a reprodução e divulgação total ou parcial deste trabalho, por qualquer meio convencional ou eletrônico, para fins de estudo e pesquisa, desde que citada à fonte.

FICHA CATALOGRÁFICA

Maziero, Danilo

Localização e estudo de fontes epileptogênicas em pacientes de epilepsia focal em fase pré-operatória / Danilo Maziero; orientador Prof.

Dr. Carlos Ernesto Garrido Salmon. Ribeirão Preto - SP, 2016.

128 p.:il,

Tese (Doutorado – Programa de Pós-graduação em Física Aplicada à Medicina e Biologia) – Faculdade de Filosofia, Ciências e Letras de Ribeirão Preto da Universidade de São Paulo, 2016.

1. Epilepsia; 2. EEG; 3. EEG-fMRI; 4. Correção de artefatos de Movimento; 5. Imagens de Fontes Elétricas

Nome: Danilo Maziero

Título: Localização e estudo de fontes epileptogênicas em pacientes de epilepsia focal em fase pré-operatória

Tese apresentada à Faculdade de Filosofia, Ciências e Letras de Ribeirão Preto da Universidade de São Paulo, como parte das exigências para a obtenção de Doutor em Ciências.

Aprovado em: ____/____/_____.

Banca Examinadora

Prof. Dr.: _____ Instituição: _____

Julgamento: _____ Assinatura: _____

Prof. Dr.: _____ Instituição: _____

Julgamento: _____ Assinatura: _____

Prof. Dr.: _____ Instituição: _____

Julgamento: _____ Assinatura: _____

Prof. Dr.: _____ Instituição: _____

Julgamento: _____ Assinatura: _____

Prof. Dr.: _____ Instituição: _____

Julgamento: _____ Assinatura: _____

*Dedico este trabalho aos meus pais, Lidia e Antonio,
por todo o apoio e motivação. Sem vocês este passo
não seria possível.*

*To my Family, Lidia and Antonio: Thanks for all the
support and motivation. It would not be possible
without you.*

Agradecimentos / Acknowledgements

To Professor Carlos, for eight years of tutoring, supporting, knowledge and patience offered to me. Thank you for all the valuable advises constantly given to me. You have shown me a different way of looking at Medical Physics and inspired me to pursue this path of questioning and investigating.

To Dr. Tonicarlo, for all the medical knowledge shared and the availability of many mornings (working days or holidays) for reviewing the EEG data of all those patients. I also thank you for being a very good friend and advising me about many personal things. You have been an example of person and professional to me.

To Dr. David Carmichael, a long term co-tutor and a friend of sunny day barbecue and also wet evening's pints. Thanks for being supportive of many of my research ideas and to have contributed to most of them. It has been a pleasure for me to be sharing the happiness of succeeding in publishing articles or getting a project proposal written/approved with your help. Cheers!

To Dr. Victoria Morgan, who patiently taught me a lot about fMRI analysis and also provided good times in Nashville twice. Thank you for always been open mind about my ideas, most of them quite complicated to explain.

Ao meu grande irmão português muito ‘fixe’ Fabio Nery. ‘Pacero’, compartilhamos muitos momentos bons, e são estes que merecem serem lembrados, naquelas terras inglesas. Sou muito grato a você por todo suporte, paciência e amizade, não só entregue a mim enquanto eu estive por ai, mas até hoje todas as vezes que nos falamos. Tenho certeza que tomaremos muitos finos e cafés de boa qualidade em dias muito melhores que os que passaram. Forte abraço e FORÇA!

Ao pessoal da radiologia do Hospital das Clínicas da Faculdade de Medicina de Ribeirão Preto, Luciana, Mario, Adriana, Prof. Antonio Carlos, Léo e ao Cecílio. Muito obrigado pela paciência e ajuda em todas as aquisições que realizei. Em especial, agradeço ao Luciano pelas várias horas extras devotadas às aquisições e transferência de dados.

Agradeço também à Célia da radiologia e a Elídia e Silvia do CIREP pela grande ajuda no agendamento de pacientes.

Muito obrigado à equipe do CIREP, aos médicos, enfermeiros e secretárias, por serem tão amigáveis e prestativos durante meu trabalho com pacientes de epilepsia. Sem dúvida tive muita sorte em ter pessoas como vocês ao meu redor durante este projeto. Especialmente a Ursula, uma grande médica e amiga que me ajudou em todos os momentos desta jornada, além disto, me deu inúmeros conselhos em momentos difíceis. Obrigado também ao professor João Leite, que providenciou todo o suporte para a realização de nossos projetos. Agradeço também ao Cassiano que esteve comigo durante muitas aquisições de EEG-fMRI, muita toquinha e haja gel em rapaz? Obrigado pela amizade e paciência durante estes anos. Aqui também agradeço aos mais de 30 pacientes que se voluntariaram à nossa pesquisa. Cada um de vocês me ensinou muito sobre a vida, superação e com certeza me fizeram refletir e tentar ser mais humano com o próximo.

Também agradeço aos meus amigos e colegas do laboratório InBrain: Team, Gustavinho, Luciana, Prof. Renata Leoni, Maira, Bruno, Ícaro e Milton por todos os momentos de discussão e aprendizado compartilhado e também pelos momentos de descontração. A estes deixo também minhas desculpas pela minha constante bagunça e inquietude. Agradeço também ao Marcio, antigo integrante, que abriu as portas no HC para que as aquisições de EEG-fMRI fossem possíveis, obrigado também por compartilhar muito do seu conhecimento sobre como trabalhar com isto. Em especial agradeço ao Felipe Barreto, pelos anos de amizade e infinitas conversas sobre trabalho e coisas da vida. Obrigado também ao Carlo, que me ajudou em muitas ideias e projetos, além de ser um grande amigo. Globinho, pau na máquina e muito 12 bars blues pra gente!

Aos amigos do Departamento de Física, pessoal do Biomag, Victor, Leonardo e Renan. Obrigado aos meus amigos do Lab GIIMUS. Em especial ao Felipe Grillo, passamos muitas coisas juntos aqui, obrigado por tudo irmão, você me deu muitos conselhos e ótimas visões sobre como se adaptar no ambiente acadêmico/profissional. Ao pessoal da secretaria, Nilza, Ricardo e Sonia. Agradeço também aos professores Oswaldo Baffa Filho e Martin Poletti que contribuíram em muito na minha formação.

Thank you DIBS-ICH-UCL staff, PhD students, PIs and Postdocs who have shared important scientific discussions. Suejen, Ellie, Tim, Maria, Chris, Matt, Kiran, Hannah, Jess, Jon and others, thanks for everything. A special thanks to Prof. Chris Clark who received me there for one year and helped me to feel like home. Cheers!

Agradeço as agências de fomento Capes, CNPQ e FAPESP que financiaram meu doutorado no Brasil, meu projeto no Reino Unido e os equipamentos utilizados em nossos experimentos no Brasil, respectivamente.

Por ultimo, agradeço mais uma vez meus pais, Lidia e Antonio. Obrigado por me apoiarem em cada escolha que fiz na vida até aqui. Por toda a paciência comigo e por entenderem meus inúmeros dias de indisponibilidade e pouco tempo. Agradeço também a todos que compartilharam da minha vida fora da pesquisa nestes últimos anos, em especial a Natalia por todo o companheirismo, discussões e momentos bons que temos passado e finalmente a galerinha do "Mal" pelos momentos de risadas, amizade e divertimento ao longo desta vida.

RESUMO

Maziero, Danilo. **Localização e estudo de fontes epileptogênicas em pacientes de epilepsia focal em fase pré-operatória.** 2016. 128 f. Tese (Doutorado – Programa de Pós-graduação em Física Aplicada à Medicina e Biologia) – Faculdade de Filosofia, Ciências e Letras de Ribeirão Preto, Universidade de São Paulo, Ribeirão Preto – SP, 2016.

As aquisições simultâneas de dados de eletroencefalografia (EEG) e imagens funcionais por ressonância magnética (fMRI) vêm sendo utilizadas com intuito de melhorar o planejamento cirúrgico de pacientes com epilepsia refratária. Entretanto, o processamento classicamente usado nestes dados combinados não é possível em pacientes sem descargas epileptiformes interictais (IEDs) e possui baixa sensibilidade para aqueles em que poucas IEDs são detectadas durante a aquisição simultânea. Além disto, a técnica é sensível ao movimento dos pacientes durante as aquisições, o que reduz a qualidade dos dados, principalmente em pacientes não cooperantes. Neste trabalho é proposto e discutido o uso de dois métodos de processamento, baseados nas técnicas de análise de componentes independentes (ICA) e análise temporal de clusters em duas dimensões (2dtca), para se mapear regiões epileptogênicas. Cada método foi analisado em um conjunto diferente de pacientes e os resultados foram comparados com os obtidos pelo EEG-fMRI clássico. Finalmente, propomos um método que utiliza às medidas de posicionamento da cabeça, obtidas durante a aquisição das fMRI, para aumentar a qualidade dos dados de EEG adquiridos simultaneamente. No estudo usando ICA combinado com imagens de fontes elétricas analisamos os dados de 13 pacientes com diferentes frequências de descargas e observamos que este método encontrou ao menos uma componente independente relacionada à epilepsia em cada paciente. Comparativamente usando o processamento convencional foi possível avaliar 11 dos 13 pacientes, e em apenas sete deles os mapas resultantes foram considerados concordantes com a região epileptogênica (RE). No estudo utilizando 2dTCA avaliamos 20 pacientes e encontramos mapas relacionados com a RE em 14 deles. Neste conjunto de pacientes, 13 apresentaram IEDs durante as aquisições; neles o método clássico de processamento teve resultados concordantes com a RE em seis deles. Finalmente verificamos em três sujeitos saudáveis que o método aqui proposto para corrigir os artefatos induzidos no EEG devido ao movimento é efetivo para altas amplitudes e

velocidades (~1cm e 55mm/s). Concluímos que os métodos ICA e 2dTCA aumentam a sensibilidade do uso de fMRI para mapear RE, principalmente em pacientes com baixa ou nenhuma detecção de IEDs durante às aquisições. Também concluímos que o uso da correção prospectiva de movimento em aquisições de fMRI não reduz a qualidade do dado de EEG adquirido simultaneamente e que às informações de movimento mensuradas podem melhorar a qualidade deste dado em situações de repouso e movimento do sujeito durante o experimento.

Palavras-chave: 1. Epilepsia; 2. EEG; 3. EEG-fMRI; 4. Correção de artefatos de Movimento; 5. Imagens de Fontes Elétricas.

ABSTRACT

Maziero, Danilo. **Localizing and studying epileptogenic sources in patients with focal epilepsy in pre-surgical planning.** 2016. 128 p. Dissertation (PhD – Physics Applied to Medicine and Biology Graduation program) – Faculty of Philosophy, Sciences and Letters of Ribeirão Preto, University of São Paulo, Ribeirão Preto – SP, 2016.

The simultaneous acquisitions of electroencephalography (EEG) and functional magnetic resonance imaging (fMRI) have been applied to improve the surgery planning of patients with drug resistant epilepsy. However, the classical approach of analyzing the EEG-fMRI data is inefficient in patients whom only few or no interictal epileptiforms discharges (IEDs) are detected during the simultaneous acquisition. Another issue of EEG-fMRI acquisition is related to its high sensitivity to motion, which decreases the quality of both data, even worse in non-cooperative patients. In this work we propose and discuss the application of two methods of analyzing fMRI data of patients with focal epilepsy: Independent component analysis (ICA) and two-dimensional temporal clustering (2dTCA). Each method was applied in a distinct group of patients and the results were compared to those obtained by the classic EEG-fMRI analysis. We have also proposed a method to improve the quality of EEG data using the head position measurements obtained, by a prospective motion correction (PMC) system, during the EEG-fMRI acquisitions. In the ICA study, we have used the electrical source images for selecting independent components (ICs) in EEG data of 13 patients with different spiking frequency. The method detected epilepsy-related BOLD activity in all the patients. Comparatively, the classic EEG-fMRI could be applied in 11 patients and epilepsy-related BOLD activities were found in seven of them. In the 2dTCA study, we have evaluated 20 patients and found epilepsy-related maps in 14 of them. Thirteen of the twenty patients have IEDs detected during the simultaneous acquisition; the classic EEG-fMRI provided maps related to the epileptogenic region in six of them. Finally we have verified in three health subjects that the proposed method for correcting motion-induced artefacts in the EEG data is effective for high amplitude and velocities (~1cm and 55mm/s). We concluded that the ICA and 2dTCA methods increase the sensitivity of using fMRI for mapping the epileptogenic region, mainly in patients presenting few or no IEDs in the EEG data simultaneously acquired to the fMRI. The PMC use during the fMRI acquisition does not degrade the quality of the EEG data acquired

simultaneously. In fact, the motion information can be used for improving its quality by correcting motion-induced artefacts.

Key-words: 1. Epilepsy; 2. EEG; 3. EEG-fMRI; 4. Motion-induced Artefacts Correction; 5. Electrical Source Imaging.

LIST OF FIGURES

Fig. 2. 1: 10 20 system.....	15
Fig. 2. 2: EEG trace example from a patient with right temporal lobe epilepsy.	16
Fig. 2. 3: EEG topography of the marker <i>spk</i> -126.87 µV from fig. 2.2.....	17
Fig. 2. 4: Three concentric spheres for one of the simplest head model representation.....	18
Fig. 3. 1: Relative MR signal variations due to the hemodynamic response after a short neuronal stimulus.....	29
Fig. 3. 2: 2D Gradient echo: Pulse sequence diagram for one slice.	31
Fig. 3. 3: K-space diagram for a typical 2D-GE acquisition.	33
Fig. 3. 4: GE-EPI acquisition scheme for one slice.....	35
Fig. 3. 5: EEG-fMRI summarized from acquisition to IED-related BOLD map.	36
Fig. 3. 6: EEG-measured gradient artefact correction flowchart for three channels and ECG.	38
Fig. 3. 7: fMRI data pre-processing flowchart.	39
Fig. 4. 1: EEG-fMRI data analysis.	43
Fig. 4. 2: fMRI-ICA decomposition scheme.	44
Fig. 4. 3: Two-dTCA schematic illustration.....	46
Fig. 5. 1: Workflow illustrating all the steps done from the data acquisition to the results of the methods.....	53
Fig. 5. 2: Workflow of the steps done in the ESI-ICA method.	58
Fig. 5. 3: Independent Components selected by the ESI-ICA method for all the patients... .	63
Fig. 5. 4: Independent Components selected by ICA-fingerprint method for all patients... .	64
Fig. 5. 5: The IC fingerprint of each IC selected by both methods for all patients.	67
Fig. 6. 1. The five categories considered for classifying the t-score maps.....	81
Fig. 6. 2: BOLD maps of patients from the group I (frequent IEDs).	85
Fig. 6. 3: 2dTCA BOLD maps of patients from the group II (infrequent IEDs).	86
Fig. 6. 4: 2dTCA BOLD maps of patients from the group III (No IEDs visually detected).	87
Fig. 7. 1: Schematic overview diagram of the motion corrected and uncorrected EEG-fMRI acquisition.....	97

Fig. 7. 2: Representative EEG data from subject #2 obtained in Experiment 2 (inside the MR scanner, no fMRI acquisition).....	109
Fig. 7. 3: The mean power spectral density at electrode O2 for each subject with eyes closed during keeping still and moving sessions.....	110
Fig. 7. 4: Mean root mean square error calculated before and after REEGMAS for the EEG data from all Experiments.....	111
Fig. 7. 5: The topography of power distribution in the alpha-frequency band (8-12Hz) for each subject in Experiment 2.	113
Fig. 7. 6: EEG-fMRI data after AAS _{GA} based on volume or slice-wise templates and AAS _{BCG} correction before and after REEGMAS.	116
Fig. 7. 7: Improving GA template stability with REEGMAS with and without PMC for fMRI.	119

LIST OF TABLES

Table 5. 1 Summary of electro-clinical and imaging findings	52
Table 5. 2. Results of ESI-ICA criteria of selection.....	65
Table 5. 3. Results of Fingerprint-selected ICs.	66
Table 6. 1. Patient information	76
Table 6. 2. Number of concordant maps for different thresholds.....	83
Table 6. 3. Number of maps classified into the different categories	84
Table 7. 1. GA template (based on slice-wise AAS) variance through fMRI acquisitions.	120

ABBREVIATION

AAS	Average Artefact Subtraction
BCG	Ballistocardiogram
BMA	Bayesian Model Averaging
BOLD	Blood Oxygenation Level Dependency
EEG	Electroencephalograph
EPI	Echo Planar Image
ESI	Electrical Source Imaging
fMRI	Functional Magnetic Resonance Imaging
GE	Gradient Echo
GLM	General Linear Model
IC	Independent Component
ICA	Independent Component Analysis
IEDs	Interictal Epileptiform Discharges
ILAE	International League Against Epilepsy
LTE	Left Temporal Epilepsy
MRI	Magnetic Resonance Imaging
PMC	Prospective Motion Correction
RTE	Right Temporal Epilepsy
2dTCA	Two Dimensional Temporal Clustering Analysis
WHO	World Health Organization

Summary

ABSTRACT	xi
LIST OF FIGURES	xiii
LIST OF TABLES.....	xv
ABBREVIATION	xvi
CHAPTER 1 - THE MOTIVATION FOR STUDYING PATIENTS WITH EPILEPSY	1
1.1 History	1
1.2 Epilepsy	3
1.3 Surgery planning.....	6
1.4 Alternative techniques	7
1.5 Motion effect in EEG-fMRI acquisition.....	10
1.6 Objectives	11
1.7 Thesis structure.....	12
CHAPTER 2 - ELECTROENCEPHALOGRAPHY AND ELECTRICAL SOURCE IMAGING	13
2.1 Neuronal activity origin.....	13
2.2 The EEG recordings	14
2.3 Electrical Source Imaging	17
2.4 Main ESI methods based on distributed sources	20
CHAPTER 3 - FUNCTIONAL MAGNETIC RESONANCE IMAGES AND SIMULTANEOUS ACQUISITIONS OF ELECTROENCEPHALOGRAPHY	23
3.1 Neuronal activity demand and support of energy.....	23
3.2 Magnetic Resonance Imaging background.....	24
3.3 Using magnetic field gradients for generating an image	26
3.4 Different MRI contrast mechanisms.....	27
3.5 Functional Magnetic Resonance Imaging background	28

3.6 The BOLD effect based on the classic hemodynamic function	29
3.7 BOLD contrast detection by GE-EPI acquisition.....	30
3.8 Simultaneous EEG-fMRI acquisitions: preparing EEG and fMRI data for analysis .	35
CHAPTER 4 - SIMULTANEOUS EEG-FMRI AND FMRI DATA ANALYSIS	40
4.1 The General Linear Model in EEG and fMRI data	40
4.2 Classic EEG-fMRI analysis.....	42
4.3 Independent Component Analysis (ICA)	43
4.4 Two-Dimensional Temporal Clustering Analysis (2dTCA)	45
CHAPTER 5 - A COMPARISON OF INDEPENDENT COMPONENT ANALYSIS (ICA) OF FMRI AND ELECTRICAL SOURCE IMAGING (ESI) IN FOCAL EPILEPSY REVEALS MISCLASSIFICATION USING AN AUTOMATIC CLASSIFIER	48
5.1 Background.....	48
5.2 Objective.....	50
5.3 Methods	51
5.3.1 Patient description	51
5.3.2 MRI acquisition	53
5.3.3 EEG data acquisition and processing	54
5.3.4 fMRI analysis by Independent Component Analysis (ICA)	55
5.3.5 Electrical Source Imaging	55
5.3.6 Selection of ICs Based on ESI results (ESI-ICA selection)	57
5.3.7 Classification of independent components (ICA-fingerprint)	59
5.3.8 Classical fMRI analysis by GLM (General Linear Model)	59
5.3.9 Temporal correlation of ICs time course and GLM predictor	59
5.3.10 Fingerprint feature analysis	60
5.4 Results	60
5.4.1 ESI method choice.....	60

5.4.2 Results summary.....	61
5.5 Discussion.....	68
5.6 Conclusion.....	72
CHAPTER 6 - TWO-DIMENSIONAL TEMPORAL CLUSTERING ANALYSIS FOR PATIENTS WITH EPILEPSY: DETECTING EPILEPSY-RELATED INFORMATION IN EEG-FMRI CONCORDANT AND DISCORDANT PATIENTS	74
6.1 Background.....	74
6.2 Objective.....	74
6.3 Methods	75
6.3.1 Patient description	75
6.3.2 MRI acquisition	76
6.3.3 EEG data acquisition and processing	77
6.3.4 Images pre-processing	78
6.3.5 fMRI analysis by two-dimensional Temporal Clustering Analysis (2dTCA).....	78
6.3.6 Classical EEG-fMRI analysis: predictor construction.....	79
6.3.7 Computing t-score maps.....	79
6.3.8 Classifying t-score maps.....	80
6.3.9 Epilepsy concordant maps	82
6.3.10 Temporal analysis of concordant clusters	82
6.4 Results	82
6.4.1 Frequent IEDs (group I)	85
6.4.2 Infrequent IEDs (group II).....	86
6.4.3 No IEDs visually detected (group III)	87
6.4.4 Temporal correlation between each 2dTCA-tc and EEG-based predictor	88
6.5 Discussion.....	88
6.6 Conclusion.....	92

CHAPTER 7 - TOWARDS MOTION INSENSITIVE EEG-FMRI: CORRECTING MOTION-INDUCED VOLTAGES AND GRADIENT ARTEFACT INSTABILITY IN EEG USING AN FMRI PROSPECTIVE MOTION CORRECTION (PMC) SYSTEM....	94
7.1 Background.....	94
7.2 Objective.....	95
7.3 Data and methdos	96
7.3.1 Task	96
7.3.2 EEG data acquisition	96
7.3.3 MRI acquisition	98
7.3.4 EEG recording	98
7.3.5 Motion measurement and fMRI-prospective motion correction	98
7.3.6 Mirror, video camera and screen	99
7.3.7 Moiré Phase Tracking-Retrospective EEG motion artefact suppression (MPT-REEGMAS).....	100
7.3.8 Experiments and processing	102
7.3.8.1 Experiment 1: Baseline EEG acquisition	102
7.3.8.2 Experiment 2: EEG recording inside the scanner without scanning (No fMRI)	102
7.3.8.3 Experiment 3: Simultaneous EEG-fMRI acquisitions.....	102
7.3.9 EEG data quality assessment.....	103
7.4 Results	105
7.4.1 Experiments 1 and 2: EEG quality assessment inside the scanner with REEGMAS without scanning vs baseline EEG	105
7.4.2 Experiment 3: EEG quality assessment inside the scanner with REEGMAS during scanning.....	113
7.4.2.1 Impact of motion on Gradient Artefact stability with and without REEGMAS	114

7.4.2.2 Impact of PMC on Gradient Artefact template stability and resultant EEG data	117
7.5 Discussion.....	121
7.6 Conclusions	126
CHAPTER 8 –GENERAL CONCLUSIONS AND FUTURE PERSPECTIVES	127
REFERENCES	129
Supplementary Material 1	143
Supplementary Material 2	148
Supplementary Material 2 - Simulation.....	164
Appendix - Ethics Committee Approval	170

CHAPTER 1 - THE MOTIVATION FOR STUDYING PATIENTS WITH EPILEPSY

1.1 History

The first report about epilepsy is not accurate; however, there are many reports about seizures and their presence in society predating 3000BC. The earliest detailed report about seizures is from the 5th century BC and it highlights that this condition was once believed to be magical, occult or divine (Hippocrates?). Despite this common belief, the ancient physicians are usually named as the firsts in considering that the seizures were due to natural causes and resided within the brain. Although their knowledge of anatomy and pathophysiology was primitive, relying on the notion of the four temperaments (choleric, melancholic, phlegmatic and sanguine) that were related to the four major body fluids (blood, black bile, yellow bile and phlegm), they were able to report many body alterations related to a seizure, such as changes in pulse, respiration, confusion and loss of consciousness. However, the most important correctly associations done at that time were about the relation between seizures and head traumas, alcohol and pregnancy (eclampsia), which were important points for relating epilepsy to natural causes instead of magic or divine events.

The natural causes of epilepsy began to be better understood in modern age. Its enlightenment was due to the advances in disciplines such as physics, chemistry, anatomy and physiology, allowing the correlation of the processes described by them to the clinical observations of epilepsy patients. Particularly in the 17th century, epilepsy was associated with a brain region that could be somehow irritated causing a seizure, and the predisposition of that region to be irritated was related to chemical and/or mechanical causes. By the 19th century it was stated that epilepsy should be considered as a symptom of a neurological illness that would cause a discharge, a paroxysmal, excessive discharge of neurons from an area within the brain that could affect other healthy areas of the brain [Gross, 1992]. Although this is correctly stated and explained many motor/psychic symptoms observed in seizures, it was also misunderstood by the society that stigmatized those patients considering them dangerous and then limiting their lives to restrict activities.

There were many restrictions imposed to epilepsy patients' lives that were extinguished only in the second half of the 20th century. For example, persons with epilepsy were prohibited from marrying until 1956 (Kale, 1997) in 17 states in the United States of America, they also were not allowed to attend public places like theatre and restaurants until the 1970s. The discrimination of epilepsy patients is yet reported to exist nowadays in both, developed and developing countries. For example, in Germany about 20 years ago, a research showed that about 20% of the people interviewed would object their children in marrying a person with epilepsy (Thorbecke and Rating, 1996). In Turkey, another research from 1997 (Aziz et al., 1997) showed that 70% of the interviewed people believed that epilepsy is resulted from supernatural causes.

Additionally to prohibitions in marrying and to frequent many public places in the past, the stigma over persons with epilepsy also plays an important role in their lives nowadays by decreasing their chances of getting or keeping employed. For example, it was shown that the unemployment risk is almost the double for men and trebled for women with epilepsy in a British community when compared to the healthy population (Jacoby et al., 1998) or about five times greater for a study done in US (Fisher et al., 2000). In Denmark (Jennum et al., 2011), it was found that there is a greater proportion of epilepsy patients (N=65000) in the receipt of social welfare benefits than health controls, indicating also an economical issue. However, in none of these studies the persons with epilepsy were classified in groups such as well-controlled or poor-controlled epilepsy. In fact, when this sort of classification was considered (Jacoby, 1995; Ratsepp et al., 2000; Herodes et al., 2001; Marinas et al., 2011) it was found that the unemployment rate by comparing well-controlled epilepsy patients and the healthy population was similar. Although the employment is only one aspect of a person's life, these studies indicate that well-controlling seizures of persons with epilepsy improve their chance of being employed and also may decrease governmental costs.

The dimension of the issues presented above is highlighted when the numbers of persons with epilepsy is discussed. There are many articles aiming to discuss about the incidence of epilepsy worldwide and also locally (Jacoby et al., 1998; Ratsepp et al., 2000; Noronha et al., 2007; Jennum et al., 2011). It is reported that worldwide, there is an annual incidence of epilepsy in 50/100000 persons in developed countries and

100/100000 in developing countries (Reynolds, 2000). The estimative is that 50 million persons have epilepsy worldwide and that this number increased about 2.4 million every year (WHO, 2016). Specifically in Brazil it is estimated that 1% of the population has active epilepsy, which is about 2 million persons. The annual incidence of epilepsy in Brazil is about 190/100000 persons, resulting in 340000 new cases every year (Gallucci et al., 2005). Another number that is impressive in epilepsy is the number of sudden unexpected deaths in epilepsy. In a recent study, this number was estimated to have an annual incidence rate of 0.81 cases per 100000 for the general population and 1.16 cases per 1000 patients with epilepsy [Thurman et al., 2014]. The risk of patients with epilepsy to commit suicide is about three times higher than that of healthy subjects (Bell et al., 2009). Although this elevated number of deaths related to epilepsy is also related to psychiatric comorbidities, there is a Danish study showing that the number of suicides committed by patients with epilepsy is still doubled in relation to general population after excluding psychiatric comorbidity association (Harris and Barraclough, 1997). It is calculated that up to 70% of these persons could have normal lives if they were properly treated (Shorvon and Farmer., 1988), which does not happen because of explanations such as the patient's concern in being excluded by society after diagnosing or even due to their difficulty in relating their symptoms and seizures to epilepsy. In the following sessions the aspects related to epilepsy's aetiology, diagnosing and treatment (from drugs to surgery) will be presented in order to contextualize the following results and discussions.

1.2 Epilepsy

The condition called Epilepsy can be associated to several different neuronal disorders being due to very different causes. In order to group the different causes of epilepsy the International League Against Epilepsy (ILAE) has proposed an aetiology classification for epilepsy that is described by one of the following three categories: 1- Symptomatic, referring to epilepsy occurring in association with a previous condition. 2- Idiopathic, related to well-characterized disorders with initial onset happening during infancy, childhood and adolescence, such as disorders reflecting a presumed genetic aetiology. 3- Cryptogenic, considered as a neutral category where the cases that the nature of the underlying epilepsy cause is unknown are placed. Examples of the most

common causes of each of the three categories will be provided in the following paragraph.

The symptomatic epilepsies are defined by any epilepsy caused by genetic or acquired causes, which are associated with neuroanatomical or neuropathological abnormalities that are indicatives of an underlying condition or disease. Genetic or congenital causes of epilepsy are for example, West, Lennox-Gastaut and Angelman syndromes, tuberous sclerosis and cortical dysplasia. Acquired symptomatic epilepsies can be related to hippocampal sclerosis, cerebrovascular diseases, brain tumours, they can also follow cerebral infection or head trauma, for example. The Idiopathic epilepsies are those of predominantly genetic causes where no large neuroanatomical or neuropathological abnormalities are present. The idiopathic epilepsies can be caused by single-gene disorders, such as autosomal dominant nocturnal frontal lobe epilepsy and severe myoclonic epilepsy of childhood, or by presumed polygenic disorders, such as idiopathic generalized epilepsy (about 20% of all cases of epilepsy) and benign partial epilepsy (about 15% of all epilepsies)(Guerrini, 2006). Although the Cryptogenic epilepsy is a term used for classifying any epilepsy of unknown origin, it is an important category since about 40% of the epilepsies found in adults are grouped within this category (Shorvon et al., 2011).

The ILAE also have proposed classifying the seizures as presenting focal or generalized onsets. The seizures of focal onset are those characterized by being originated from a well delimited brain region, presenting clinical manifestation concordant with a focal onset of the epileptiform discharge, with or without propagation, presenting during seizure (*ictal*) or between seizures (interictal) focal electroencephalogram (EEG) abnormalities. The generalized epilepsies are then those characterized by generalized seizures, presenting bilateral motor manifestations, and generalized *ictal* and interictal events. The generalized seizures are manifested as a tonic and/or clonic, myoclonic, absence, atonic seizure or epileptic spasms. Each type of seizure presents different duration, electrical waves on the EEG and also clinical responses. Although there are specific characteristics for each type of seizure for both epilepsies (focal or generalized), due to the scope of this thesis, only the focal epilepsy

seizures, particularly those related to lobar epilepsies, will be discussed in the following paragraph.

A focal onset seizure is associated to a brain region (neocortical or Hippocampal and parahippocampal), with or without ipsilateral propagation to neocortical or limbic areas, with or without contralateral spread to neocortical or limbic areas and it may or not be secondarily generalized as tonic/clonic, absence seizures or epileptic spasms. The most common focal epilepsies are the lobar epilepsies.

The conceptual definition of epilepsy for clinicians is defined by the ILAE as ‘a disorder characterized by an enduring predisposition to generate epileptic seizures and by neurobiological, cognitive, psychological and social consequences of this condition’. Epilepsy is then defined by ‘the occurrence of two or more unprovoked seizures at least 24 hours apart’ [Fisher et al., 2005]. Actually, there is a few seizure-related disorders that are not considered epilepsy: 1 - solitary unprovoked epileptic seizures, or seizures occurring within a period of 24 hours or as a single episode of status epilepticus; 2 - febrile seizures or neonatal seizures (occurring in infants less than 28 days of age); 3 - seizures ‘in close temporal association with an acute systemic, metabolic or toxic insult or in association with an acute central nervous system (CNS) insult (infection, stroke, cranial trauma, intracerebral hemorrhage, or acute alcohol intoxication or withdrawal)[ILAE, 2011].

Diagnosing epilepsy is strongly based on the history of the patient, in order to identify in the patient a predisposition to generate the seizures. The electroencephalogram is also a powerful technique applied for diagnosing epilepsy. The diagnose is usually done based on the change of physiological rhythms such as alpha and delta and also by the detection of ictal (during seizures) or interictal (between seizures) events (e.g. spikes, sharp wave, spike-slow-waves complex and multiple spike-slow-wave complex (IFSCN, 1974). About 70% of the patients diagnosed with epilepsy who take anticonvulsivante drugs are able to have their seizures controlled and to live ‘normally’ (Shorvon and Farmer., 1988). However the remaining patients suffer from a condition called drug-resistant epilepsy, which means that even taking one or more anticonvulsivante drugs they still present.

A relatively high percentage of these patients may be favored by a surgery to resecting the cortex region indispensable for generating seizures (Rosenow and Luders, 2001). The epileptogenic zone consists of all tissue needed for generating seizures; therefore a completely resection of it may lead to seizure-freedom. Another common term of the literature related to epilepsy is the seizure onset zone (SOZ), which refers to the region where the seizure actually begins (Rosenow and Luders, 2001). However, both regions are not always size correspondent, then one of the two scenarios will happen: 1 – the epileptogenic zone is smaller than the SOZ, and a partial resection of SOZ may lead to seizure-freedom; 2 – the epileptogenic zone is larger than the SOZ, and then even its total resection will not lead to seizure-freedom [Rosenow and Luders, 2001]. Therefore, the surgery planning is a complex process. Besides that, the surgery must target the epileptogenic zone, but leave eloquent areas the most untouched possible, in order to avoid damages at cognitive regions.

1.3 Surgery planning

The pre-surgical planning of patients with epilepsy is a multimodal process where different diagnosing techniques are evaluated by a multidisciplinary staff. Methods minimally invasive or non-invasive such as magnetic resonance imaging (MRI), video-electroencephalogram (VEEG), single photon emission tomography (SPECT) and positron emission tomography (PET) are preferentially used. Besides that social and psychological evaluations are also realized. However, some patients present even more complexes epileptogenic and seizure onsets zones to be target, such those whom the seizures propagate between different brain regions and patients presenting interictal epileptiform discharges (IEDs) alternating between right and left temporal lobes. There are also epilepsies related to deep structures of the brain such as the mesial temporal lobe, which present discharges hard to be detected by the scalp EEG. Another problem is related to the divergence between the standard methods, where each method targets different regions of the brain. The pre-surgical planning of these patients is therefore more complicated and very often methods such as electrocorticography (ECoG), sphenoidal and/or foramen ovale electrodes might be necessary. These are all invasive methods which are complex to realize and present risks to the patient, therefore they are avoidable as much as possible.

Different noninvasive techniques have arisen as potential solutions to this challenge in patients in whom a divergent diagnosis is obtained with conventional assessments. These techniques aim to improve the accuracy in mapping the SOZ, such as electrical source imaging (ESI) and also to improve our knowledge about the brain response to epilepsy, such as the simultaneous acquisitions of EEG and fMRI (EEG-fMRI).

1.4 Alternative techniques

Electrical source imaging, briefly (for more details see Michel et al., 2004a), is capable to reconstruct a three dimensional source within the brain that generated the electrical potential differences measured by scalp-EEG electrodes. From a physics point of view, the ESI technique is based on an inverse problem. The electromagnetism-inverse problem (e-IP) is an ill-posed problem and needs to be constrained to be solved with a unique solution. Many methods are used to constrain the e-IP in order to obtain the ESI, and they are based on different mathematical and physiological assumptions. Although ESI has been proven as a very accurate method for localizing IED-related activity (Brodbeck et al., 2011; Maziero et al., 2014), it is still underused in the clinical practice of epilepsy.

The underuse of ESI in the clinical practice of epilepsy is partially explained by the following reasons: there are many methods available for solving the inverse problem and no consensus about the accuracy of them (Michel et al., 2004a); the number of electrodes usually applied in clinical routine to acquire the EEG data usually ranges from 16 to 60 electrodes, which is much lower than the number (>128 electrodes) used in the studies related to ESI applicability (Michel et al., 2004b; Brodbeck et al., 2011); ESI accuracy shows different values for studies including epilepsies located in different lobes (Brodbeck et al., 2011; Maziero et al., 2014). These studies generally group the patients as temporal lobe patients and extra temporal patients, and there is no consensus about the group that can have the IED-related activity more accurately mapped. Finally, another important argument is that there is a lower accuracy for mapping the IEDs-related activities in temporal lobe patients, which relates to scalp EEG's inaccuracy of detecting discharges originating in deep brain structures, such as hippocampus.

fMRI is another technique very useful in the neuroscience field. fMRI is based on the blood oxygenation level dependent (BOLD) contrast, which indicates significant hemodynamic changes with respect to the baseline fMRI signal (Ogawa 1990). The relationship between neuronal activity variations and hemodynamic changes makes fMRI a unique indirect mapping tool of the neuronal activity in the brain (Logothetis 2001). Specifically for patients with epilepsy, the fMRI clinic application is mostly related to mapping cognitive areas, which indeed is useful for avoiding damages in brain functions such as speech and hearing, however not informative about the epileptogenic zone.

The classic simultaneous EEG-fMRI analysis has proven to be a useful tool for mapping the IED-related BOLD activity in many instances (Lemieux, 2001; Gotman et al. 2006; Hamandi et al. 2004; Salek-Haddadi et al. 2006; Laufs et al., 2008; Levan et al., 2010; Pittau et al., 2012; Centeno and Carmichael, 2014;). In this classical analysis, a temporal predictor is produced by the convolution of a Hemodynamic Response Function (HRF) (Glover, 1999) with IEDs visually identified in the scalp EEG. Then, a General Linear Model (GLM) is applied to fit the BOLD signal changes in time from each voxel based on the predictor. Finally, statistical comparisons are performed to find the voxels that are significantly correlated to the temporal predictor. The resultant statistical map represents the voxels considered as IED-related BOLD activity. Although this approach has resulted in clinically useful information (Thornton et al. 2011; Grouiller et al. 2011; Pittau et al. 2012), there remain the following limitations:

1. Some patients do not have visually identifiable EEG events.
2. Some patients with IEDs do not have fMRI changes which might be HRF variability due to inter-individual differences, and unmodelled IED variability (Benar et al. 2002 and Menz et al. 2006).
3. The reliance on the EEG subjective visual review done by an expert/neurophysiologist, also termed as EEG visual coding.
4. There is the requirement to have simultaneous EEG-fMRI data, needing MRI scanner compatible EEG and specialist expertise to perform and analyze the study.

As an alternative to the classical EEG-fMRI analysis, other techniques have been proposed in the context of mapping the BOLD responses related to epilepsy

independently of the IED detection by the simultaneous EEG. The Independent Component Analysis (ICA) is a data driven method (for more details, please see chapter 4) that spatially decomposes the fMRI data into spatial maps without *a priori* information or strong assumptions about the fMRI data set (McKeown, 1998). The Independent Components (ICs) were found to map BOLD activities related to normal brain activities during tasks (McKeown, 1998), networks during resting state fMRI acquisitions (Fox, 2005; Damoiseaux et al., 2006; De Luca et al., 2006; Rondinoni et al 2013) and also for mapping the epileptic BOLD-related activity (Rodionov et al., 2007; Moeller et al., 2011; Maziero et al., 2015). Particularly in epilepsy, the ICA had shown sensitivity for mapping BOLD activity related to the IEDs detected during EEG-fMRI acquisitions. However, ICA also presents difficulty of differentiating these BOLD IED-related ICs from other ICs, which can be related to scanner or physiological noise, head motion or BOLD activity not related to epilepsy.

The two-dimensional Temporal Clustering Analysis (2dTCA) (Morgan et al., 2008) is another data-driven method proposed specifically for detecting transient BOLD-related activity independently of *a priori* information (please see chapter 4 for detailed information). The 2dTCA showed promising results mapping BOLD activities related to tasks executed by healthy subjects (Morgan et al., 2009) and also to detect epileptogenic BOLD-related activities in a group of patients with temporal lobe epilepsy without EEG data inside the MR scanner (Morgan et al., 2010). Another study applied in individual fMRI datasets of epileptic patients (Khatamian et al., 2011) of patients whom the classical EEG-fMRI analyses were concordant to the patient's information. The authors compared the maps obtained by 2dTCA to those obtained by classical EEG-fMRI. They reported that the classical EEG-fMRI and 2dTCA found similar results when applied in data of patients whose prolonged interictal events have been recorded by the simultaneous EEG. The authors also concluded that 2dTCA would be interesting only for validating the results found by other methods (Khatamian et al., 2011). However, the data analyzed in their study was restricted to patients showing IEDs during the simultaneous EEG-fMRI acquisition and those in which the classic EEG-fMRI was able to map coherent epileptic BOLD activities. Therefore, the 2dTCA

capability of mapping the epilepsy-related BOLD activity in negative EEG-fMRI and spikeless patients has not been reported.

In summary the non-invasive methods cited above have all provided promissory results in mapping epileptogenic-related activity by electrical (ESI) or haemodynamic (ICA, 2dTCA and EEG-fMRI) brain activity detection. However there are many issues related to them that need to be solved in order to improve their clinical utilization. The classical EEG-fMRI is also proven to be an effective approach for specific groups of patients, however it cannot be applied without specific equipment/training nor in patients whom simultaneous scalp-EEG could not detect IEDs. Therefore there is a considerable amount of data acquired that is not useful for mapping epilepsy-related activity with EEG-fMRI. This method is also highly affected by motion, which decreases its sensitivity in providing useful information in patients with epilepsy during *ictal* and *interictal* events.

1.5 Motion effect in EEG-fMRI acquisition

The impact of motion in EEG data quality degradation is mostly the result of electromagnetic induction for acquisitions realized within the MRI-scanner environment. Faraday's law states that magnetic flux changes through a conductor loop's area induce corresponding voltage fluctuations; in EEG circuits these voltages are superimposed onto the brain-generated signals, making the detection of activities of interest more difficult or almost impossible. This is even more problematic for the application of EEG-fMRI in patients for whom the motion might be unavoidable, such as children or to study patients with epilepsy during *seizures (ictal events)*. Currently, most artefact correction methods are based on post-hoc EEG data processing techniques that rely on the identification of artefact waveforms and their exclusion with the aim of obtaining motion artefact-free signals (Lemieux et al., 2007; Chaudhary et al., 2012b). These processes do not take into account the measured motion, and they only exclude motion-artefact contaminated epochs of EEG data, instead of correcting them.

Subject motion during the simultaneous acquisition of fMRI can also lead to severe image quality degradation. The impact of motion on fMRI is well documented (Hajnal et al., 1994; Satterthwaite et al., 2012) and it causes large amplitude signal changes across consecutive fMRI volumes increasing temporal variance and increasing

type 1 and type 2 errors. A number of techniques ranging from purely data-based (post-processing) (Friston et al., 1996; Lemieux et al., 2007; Power et al., 2014) to methods based on precise and independent measurement motion have been proposed (Eviatar et al., 1997; Eviatar et al., 1999). Recently, a prospective fMRI motion-related signal reduction system based on a camera-tracker system (PMC) and MR sequence acquisition update has been implemented and commercialised. Briefly, an MRI compatible camera is used to image a Moiré-phase tracker (MPT) attached to the head. The tracking information is converted into the head's position (three translations and three rotations). This information is then used to update the radio frequency pulses and the gradients, applied in the imaging process in real time with promising results (Maclare et al., 2013, Todd et al., 2015).

The possibility of using the motion parameters provided by the PMC system for improving the quality of the EEG data acquired simultaneously to fMRI is a potential solution towards EEG-fMRI data insensitive to motion. In that direction, Levan et al. (2013) have proposed to use the motion information in order to correct the so-called ballistocardiogram (BCG) artefact, present in EEG-fMRI acquisitions (for more details see chapters 3 and 7). Although the authors have presented promising results in correcting the BCG artefact, they did not correct the EEG data for head motion-related artefacts nor discussed the effects on EEG data due to use PMC for improving fMRI data.

1.6 Objectives

Our global objective is to contributing with mapping and understanding epileptogenic sources using EEG and fMRI data, acquired/analysed separately and/or simultaneously. Therefore, we aim at providing methods of acquiring higher quality data and also alternatives for analysing data that would be discarded by conventional analyses such as the classic EEG-fMRI. In order to achieve our objective we have subdivided it in specific goals as follows:

- To apply ESI for facilitating the selection of independent components resulting from decomposing fMRI data of patients with epilepsy by using independent component analysis.

- To understand the reasons of failure of classic EEG-fMRI and ICA, when the results of these methods are obtained directly or indirectly by comparison to the classical hemodynamic response
- Provide alternative methodologies for mapping epilepsy-related BOLD activity in patients whom classical EEG-fMRI fails or is not possible to be obtained (spikeless patients).
- Improve data quality of EEG-fMRI acquired during high amplitude and fast head motion.
- Provide insights about the penalties of using PMC for correcting fMRI data on the EEG data acquired simultaneously

1.7 Thesis structure

This thesis is organized based on the background of the imaging techniques used, in the experiments, results and discussion related to each of the objectives cited above. In chapter 2 the reader will be presented to the origin of neuronal activity measured by scalp EEG and also to the Electrical Source Imaging. Further in chapter 3, the neuronal coupling that allows the BOLD signal to be measured by the fMRI is presented. In that chapter the reader will also be presented to the gradient echo and echo planar imaging, two MRI acquisition schemes largely used in our studies. The results from the first and the second objectives were published as a manuscript in the Brain Topography Journal (Maziero et al., 2015), and are presented in chapter five. In chapter five another publication resultant from this thesis is mentioned (Maziero et al., 2014), this publication is related to the study realized for understanding which ESI method would be more accurate for being used in the methodology referent to objective 1. The results related to the third objective were also written as a manuscript that is under review. These results are presented in chapter six. Finally, the results related to the fourth and fifth objectives were also published as a manuscript in the NeuroImage journal (Maziero et al., 2016), and are presented in chapter seven.

CHAPTER 2 - ELECTROENCEPHALOGRAPHY AND ELECTRICAL SOURCE IMAGING

2.1 Neuronal activity origin

The neuronal activations produce ionic time varying currents at the cellular membrane level. These neuronal activations can be differentiated in two main forms (Nunez, 1995; Lopes da Silva, 2002). The first one is the fast depolarization of the neuronal membranes, where the result is the action potential. The action potential is related to the variable sodium and potassium conductance through the cellular membrane. Those conductions are reflections of rapid changes in membrane permeability for sodium and potassium ions and therefore to its electrical potential changes. These changes are abrupt (1 to 2 ms) jumps of intracellular potential from negative to positive, followed by a quick return to the resting negative intracellular negative potential. The second kind of activation is related to inhibitory and excitatory post synaptic potentials, IPSP and EPSP, respectively. These are relatively slower potentials (often slower than 250Hz) and are related to the neurotransmitters and corresponding receptors associated with the synapses. The concentration of the ions involved with IPSPs and EPSPs are responsible for the signal of the post synaptic potential measurement. Basically, the trans-membrane current is carried by positive ions inwards (e.g. Na^+) during a EPSPs and it is carried by negative ions (Cl^-) inwards or positive ions outwards (K^+) in the case of the IPSPs. Therefore, the current flux is directed to the extracellular medium during IPSPs and to the intracellular medium in the case of the EPSPs.

The currents flowing in or outwards the cellular membrane generate a sink or a source in the extracellular medium due to EPSPs and IPSPs, respectively. Because there is no charge accumulation anywhere in the medium, the currents flowing in or out of the neuron at the synaptic active area (sources and sinks) are compensated by currents flowing in the opposite direction elsewhere along the neuronal membrane [Mulert and Lemieux, 2010]. Therefore, it is straight forward to associate the synaptic activity at a given soma-dendritic neuron membrane to the cause of a source-sink configuration at the extracellular medium surrounding the neurons. Such a combination of source and

sink of equal magnitude is called a *current dipole* (a pair of equal and opposite electric charges is called an electric dipole). The current dipole is oriented along the axon.

2.2 The EEG recordings

The distribution and shape of the neurons producing sink-source configuration are also important aspects for the electrical activity detection by the electroencephalography (EEG). A random disposition of neurons implies in a random direction for their current dipoles, which may lead to a locally null electrical field and then to a null or very small voltages. The EEG is based on the detection of the electrical potential differences or voltages (ΔV) caused by neuronal activity. This detection is done by electrodes positioned inside or outside the skull. The outside skull acquisition is also called scalp-EEG and it is the most used in neurology clinic practice. Henceforward the scalp-EEG will be called as EEG. The voltage measured in an electrode (Fig. 2.4, $V(\vec{r}_j)$) and generated by a current dipole (Fig. 2.4, $\vec{J}(\vec{r}_g)$) is proportional to the scalar product between the current dipole vector and distance vector between the dipole localization (Fig. 2.4, \vec{r}_j) and the position of the electrode. Hence, current dipoles

parallel to the scalp does not generate voltage variation in the scalp. The synchronous electrical activity of pyramidal neurons placed perpendicularly to the cortical surface can be detected by electrodes positioned in the scalp. In summary, the electrical activities detected by the voltages measured on the scalp-EEG are due to synchronic electrical activities of a relatively large group of pyramidal neurons modeled as electrical dipoles (Nunez and Srinivasan, 2006). These voltages have the same temporal behavior of the electrical activities. They are often slower than 250Hz (Ullsperger e Debener, 2010) with amplitudes of μV , when detected on the scalp (centimeters away from their origin).

In the clinical practice the EEG electrodes are often positioned based on the international systems 10|10 or 10|20 (Fig. 2.1). These systems are based on anatomic markers that are used in order to standardize the electrode positions.

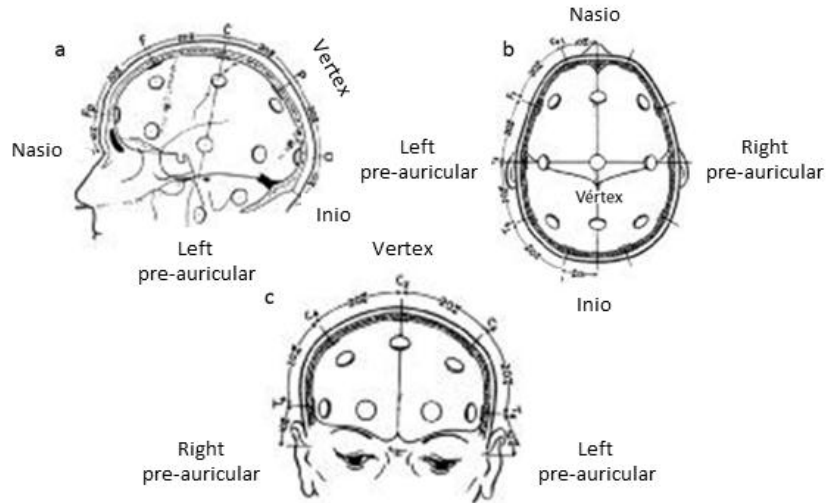


Fig. 2. 1: 10|20 system. a) lateral, b) superior and c) frontal views. This figure was Modified from Webster (1997).

The most common anatomical markers used in the 10|20 system are the fiducials: Nasion, inion, vertex and right and left pre-auricular. The electrodes placement begins by measuring the distance from the nasion to inion by three different paths: passing through the vertex and through each of the pre-auricular (left and right) (Fig. 2.1a and 2.1b). Additionally the curve that connects both pre-auricular passing through the vertex (Fig. 2.1C) has also its distance measured. Those distances are divided in intervals of 10 (10|10 system) or 20% (10|20 system) of their total lengths in order to find where each electrode will be placed. The electrodes are also named in order to facilitate their localization on the scalp. The nomenclature is basically based on the lobe that is underneath the electrode, such as frontal (F), parietal (P), temporal (T) and occipital (O). For the electrodes above inter-lobe junctions the notation uses both lobes names, such as fronto-temporal (FT), temporo-parietal (TP) and parieto-occipital (PO). The notation also includes a numbers for identifying the lines where each electrode is placed, which increases from the top of the head to the bottom and is odd for electrodes placed at the left-hand hemisphere and even for those on the right-hand hemisphere. Finally, there are the electrodes tagged with z, such as FPz and Cz, which are placed on the medium line that divides the brain in two hemispheres.

In the clinical practice, the EEG information is often displayed and analyzed with montages in order to facilitate the comprehension of the electrical signal measured according to the pathology to be diagnosed. A standard EEG data view is called

referential montage, where all the channels are visualized in reference to one electrode (potential difference). In epilepsy, the reference electrode is also chosen in order to highlight the brain region where the epileptogenic discharges are generated. For example, an electrode called FCz (fronto-temporal at the central line) can be used as reference for differentiating whether a frontal IED (often named as spike, spk) is originated in the right or left frontal lobe (Fig. 2.2).



Fig. 2. 2: EEG trace example from a patient with right temporal lobe epilepsy. The data displayed is referenced to the electrode FCz and the *spk* markers represent the IEDs detected.

Figure 2.2 illustrates the time course of the electrical potential difference between each electrode and the reference at FCz. This also exemplifies the information obtained from the EEG data, where the horizontal axis is the time and the vertical axis the ΔV (μ Volts) measured at different spatial location (each electrode).

Another useful view of the EEG data is the topographic maps, or topographies. These maps represent the ΔV distribution observed at the scalp (Fig. 2.3), considering all the electrodes used for measuring the EEG data, for a time point.

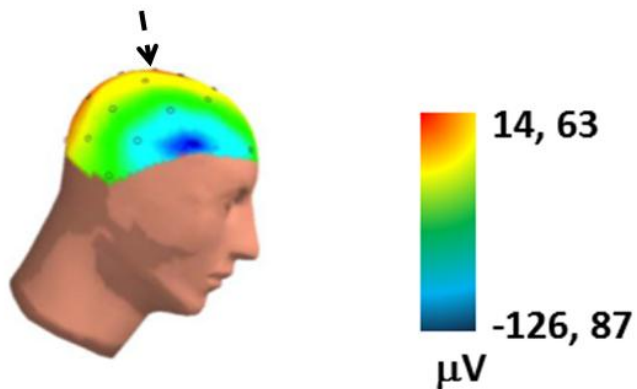


Fig. 2. 3: EEG topography of the marker spk -126.87 μ V from fig. 2. The color scale represents the electrical potential differences between each electrode and the reference at Pz (black arrow).

The EEG topographic map is important information for the neurophysiologist. It is often helpful in pre-surgical planning or to implant depth electrodes. However, it is a preliminary analysis without accuracy about the source localization of the measured ΔV . Therefore, more advanced methods such as the electrical source imaging (ESI) may provide significant support for using the EEG data for directly delimitating the epileptogenic zone.

2.3 Electrical Source Imaging

Electrical Source Imaging (ESI) is the application of the electromagnetic inverse problem on the ΔV values measured by the EEG. The aim is to determine the current distribution (position and intensity) in the brain responsible for generating that ΔV distribution. There are several mathematical and physiological complications for solving this inverse problem, and then it is more intuitive to understand first the forward problem.

In one of the simplest model, the head can be modeled as a system composed by the brain tissue, cerebral spinal fluid (CSF), pia matter, skull and scalp. In a more complete head model, the electrical properties can change in each spatial point of the grid. The forward problem here is applied considering these components as three concentric spheres with different electrical properties (conductivity and permittivity). It is also assumed that the electrical sources are contained only in the inner sphere. The electrodes are placed at the surface of the outer sphere (Fig. 2.4).

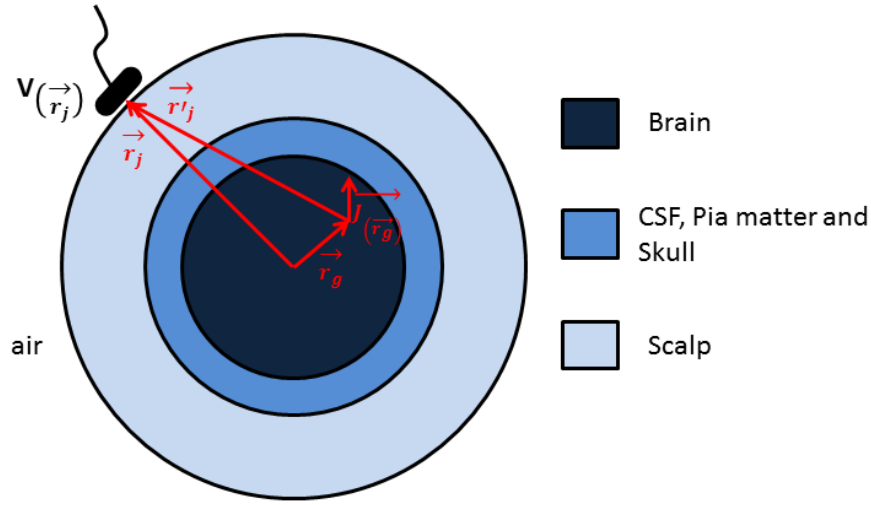


Fig. 2. 4: Three concentric spheres for one of the simplest head model representation.

The representative model for relating the electric potential measured V at the electrode placed in the \vec{r}_j position on the scalp due to the existence of electrical sources characterized by the current dipole density ($\vec{j}_{(\vec{r}_{dp})}$) contained in one or more volumes of the grid ($d^3\vec{r}_g$) within the brain is illustrated in Figure 2.4 and described as follows (Trujillo et al., 2004):

$$V(\vec{r}_j) = \int G_{(\vec{r}_j, \vec{r}_g)} \vec{j}_{(\vec{r}_g)} d^3\vec{r}_g \quad \text{Eq. 2.1}$$

Where $G_{(\vec{r}_j, \vec{r}_g)}$ is the Lead Field, a variable that incorporates the geometrical and physical properties of the problem (diameter and electrical conductivity of the spheres in one of the simplest head model). The equation 2.1 is the mathematical form of the electromagnetism forward problem. It can also be discretized by considering that $\vec{j}_{(\vec{r}_{dp})}$ are distributed within a 3D grid of finite and discrete points. Then, equation 2.1 can be re-written as a linear system of equations:

$$V_{U_N}(r) = G_{U_N \times 3U_g} \cdot J_{3U_g} + \mathcal{E}_{U_N} \quad \text{Eq. 2.2}$$

Here, U_N and U_g are the total number of electrodes and the number of points composing the grid, respectively. The $3U_g$ indicates that the vector \vec{J} has three components (J_x , J_y e J_z). \mathcal{E}_{U_N} parameter is introduced for taken into account the noise related to the EEG acquisition. Then, considering this problem as stationary and that the electrical sources are dipoles, the equation 2.2 can be written as follows:

$$V = \begin{bmatrix} v(r_1,1) & \dots & v(r_1,T) \\ \vdots & \ddots & \vdots \\ \vdots & \ddots & \vdots \\ v(r_N) & \dots & v(r_N,T) \end{bmatrix} = G(\{r_j, r_{dip_i}\}) \begin{bmatrix} d_{1,1}e_{1,1} & \dots & d_{1,T}e_{1,T} \\ \vdots & \ddots & \vdots \\ \vdots & \ddots & \vdots \\ d_{p,1}e_{p,1} & \dots & d_{p,T}e_{p,T} \end{bmatrix} \quad \begin{array}{l} \text{Eq} \\ . \\ . \\ 2.3 \end{array}$$

Where $v(\mathbf{r}_N, T)$ is the voltage detected by the N different electrodes at the T distinct time instants. The voltages detected by the N electrodes are related to the electrical fields generated by the p dipoles located at the distance \mathbf{r}_{dip} , with magnitude $d_{p,T}$ and orientation \mathbf{e}_p , which all can change through the time.

In summary, the matrices in equation 2.3 illustrate that it is possible to associate electrical dipoles within the brain, knowing their positions, with the voltages measured by multiple electrodes. This association is possible if the matrix $G(\{r_j, r_{dip_i}\})$, where r_j relates the j electrode position and r_{dip_i} with the dipole i position, is known. However, we are interested in the matrix that contains the $d_{p,T}$ and \mathbf{e}_p . This is the \mathbf{J} matrix, where V is measured by the electrodes and G can be estimated. This characterizes the electromagnetism inverse problem based on EEG data.

\hat{J} values are estimated as the electrical sources that generate the voltages measured at the scalp with the smallest error possible. J is often obtained by the minimum squares method, where the coefficients of J_{3U_g} that minimizes the residual of the quadratic sum, as follows

$$\hat{J} = \arg \min_J \|V_{U_N} - G_{U_N \times 3U_g} J\|^2 \quad \text{Eq. 2.4}$$

The solution for this equation is written as

$$\hat{J} = (G_{U_N \times 3U_g}^T G_{U_N \times 3U_g})^{-1} G_{U_N \times 3U_g}^T V_{U_N} \quad \text{Eq. 2.5}$$

which is not unique. The most complicated aspect about the inverse problem is its ill-posed problem characteristic. The solution plurality is due to the infinite possibilities of dipole combinations within the brain that are capable of generating the V_{U_N} detected on the scalp.

Equation 2.4 and its solution (Eq. 2.5) characterize the ESI as an ill-posed problem, which needs regularization in order to be solved. Tikhonov and Arsenin (1977) have suggested using penalties factors on matrix J in order to regularize the problem.

The penalty factor (R) is included in Equation 2.4 as follows:

$$\hat{J} = \arg \min_J \left\{ \|V_{U_N} - G_{U_N \times 3U_g} J\|^2 + \lambda^2 \|RJ\|^2 \right\} \quad \text{Eq. 2.6}$$

Where λ is often calculated by the L-curve method, and represents the relative weight between the adjusted data error with the penalty factor (matrix R).

There are many methods for regularizing the inverse problem in order to provide solution under determined penalties. These methods are classified mainly as two groups: 1- distributed sources, where the inverse problem solution is considered as a three dimensional region within the brain; 2- equivalent dipoles, which represent the source distribution as one or more electrical dipoles. Both types of sources are applied for studying patients with epilepsy, and there is no consensual about their advantages and tradeoffs. In the following section a brief introduction for the main ESI methods is presented. For a detailed review about the different methods, please see Michel (2004a).

2.4 Main ESI methods based on distributed sources

- Minimum Norm Estimative (MNE) (Hämäläinen and Ilmoniemi, 1984): This is the simplest method for calculating the ESI. The MN provides an ESI solution by finding the electrical source distribution of lowest intensity. This is possible

by assuming the R in Eq. 2.6 as an identity matrix. The results obtained by MNE usually favor superficial sources in order to provide an individual configuration for the electrical source. This is a limitation, particularly for deep electrical sources, such as from mesial temporal lobe, where the method may fail in mapping.

- LORETA (*Low resolution electromagnetic tomography*) (Pascual et al., 1994): The method is based on the physiological information that an electrical activity detected by EEG is due to the synchrony of the neurons and their neighbors. Mathematically this is obtained by assuming the matrix R as a Laplacian operator. Therefore, LORETA provides solutions with smooth current density values, which are often spread and can result in the so-called ghost solutions.
- LAURA (*Local Autorregressive Average*) (Menendez et al., 2001): It is applied as a restriction on MN method where the electrical sources are assumed to decay with the distance squared. The method results in an auto-regression with coefficients that depend on the distance between the solution points. A tradeoff of LAURA is that the auto-regression cannot be estimated exclusively based on the data acquired.
- BMA (Bayesian Model Averaging) (Trujillo et al., 2004): All previous methods provide a map of \hat{J} by assuming different mathematical and anatomical constraints (R) in equation 2.6. The ESI map, or source configuration, for that assumption is found by minimizing the error, as shown in equation 2.2. The BMA also uses equation 2.6 and mathematical or anatomical constraints, in fact BMA can be applied after any method of source estimation is used for providing the map of \hat{J} . In a first step, Bayesian statistics is applied in order to calculate the *a posteriori* probability of a source configuration due to the measured voltages (V) for a specific head model. The head model is obtained by considering that the points of the grid are composed by different combinations of the brain compartments. The brain compartments are inserted by the user as a priori information about anatomical regions and or functional activations. A set of solutions is obtained for each head model available and the solution with the highest probability of being provided by the data is selected. The final solution is

obtained by a weighted average that takes into account the probability of a \hat{J} distribution given the measured voltages and the probability of a head model given those voltages. BMA represents a potential improvement for ESI, because it was implemented in order to improve ESI accuracy, mainly for situations where the sources are in deep structures of the brain, which usually are poor mapped by the other methods. The method was evaluated in simulated data and in a few dataset of healthy subjects realizing simple cognitive tasks (Trujillo et al., 2004), however its application for studying patients with epilepsy was never consistently done.

CHAPTER 3 - FUNCTIONAL MAGNETIC RESONANCE IMAGES AND SIMULTANEOUS ACQUISITIONS OF ELECTROENCEPHALOGRAPHY

The neuronal activities, such as the post synaptic inhibitory and excitatory potentials measured by EEG, demand a considerable amount of energy. The mechanisms related to providing energy to those neurons are associated to consuming glucose and oxygen, which modify the brain hemodynamics. These changes on brain hemodynamics are the basis for the so-called neurovascular coupling. Hemoglobin is an important molecule to the oxygen-transport in the blood directly; therefore it is related to the neurovascular coupling. Besides that, this molecule's magnetic properties are dependent on the binding of oxygen to its core, which provides a relation between energy consumption and magnetic properties variations. The combination of all these facts results in the Blood Level Oxygenation Dependent (BOLD) contrast, which can be detected by a proper magnetic resonance experiment generally denominated as fMRI experiment.

3.1 Neuronal activity demand and support of energy

The association among neuronal activity and the BOLD contrast is related to the neuronal consumption of energy during its activation. This energy is provided in form of Adenosine-tri-phosphate molecule (ATP). ATP is a product of the oxidative phosphorylation of the Adenosine-di-phosphate (ADP), which is possible due to the electrons resulting from the glucose being metabolized by the Kreb's cycle. The ATP is then hydrolyzed to ADP providing energy to the system (Magistretti and Pellerin, 1999). The ADP resulting from this process can be transformed again into ATP and then re-inserted to the same process of providing energy to the system. This on demand process depends on ADP, glucose and oxygen (O_2) levels, then the rate of oxygen consumption by the oxidative phosphorylation indicates how much energy is being required in that region. Therefore, it is clear that the O_2 supply to the neuronal site in activity plays an important role to the process.

The hemoglobin is a specific molecule that transports the O_2 in the blood. The most important part of the hemoglobin is its iron core called *heme* group. When O_2 is

bind to the *heme* group the molecule is called oxyhemoglobin (O_{Hb}), a hemoglobin lacking O_2 in its *heme* group is called deoxyhemoglobin (De_{Hb}). The amount of O_{Hb} and De_{Hb} depends on how much blood arrives and departs to/from a specific brain region. Although the neurovascular coupling mechanisms are yet objectives of research, it is well known that an additional neuronal activity increases ATP consumption and consequently the glucose and O_2 (Magistretti and Pellerin, 1999) demand on the neuronal site on activity is increased.

The oxygen extraction fraction (OEF) from the hemoglobin in the vessels increases and consequently increases the amount of De_{Hb} . In order to guarantee the O_2 level in the tissue, cerebral blood volume (CBV) and cerebral blood flow (CBF) also increase comparatively to the baseline values in rest. The variations in those hemodynamic and metabolic variables (CBV, CBF and OEF) result in a significant variation of the O_{Hb}/De_{Hb} ratio and consequently in the magnetic properties in the activated region.

3.2 Magnetic Resonance Imaging background

The magnetic resonance phenomenon is related to an intrinsic property of the atomic nucleus, the spin angular momentum. The spin angular momentum is characterized by a property called spin quantum number. Any nucleus with spin quantum number different than zero also has a magnetic moment and it can experience the Zeeman effect. For medical applications the proton (1H , spin quantum number = $\frac{1}{2}$) is the nucleus of most interest due to its abundance within the human body.

A sample of nuclei with non-zero spin quantum number, such as the protons present in water, will experience the Zeeman effect when exposed to a magnetic field. In MRI scanners this magnetic field is called static magnetic field and henceforward it will be called \vec{B}_0 . This magnetic field is applied during all the experiment. In a classical view of the Zeeman effect, the magnetic moment of the nucleus precesses around \vec{B}_0 with a frequency ($\vec{\omega}$) with a frequency ($\vec{\omega}$) in an equilibrium state described by the Larmor equation:

$$\vec{\omega} = \gamma \vec{B}_0 \quad \text{Eq. 3.1}$$

Where γ is the gyromagnetic ratio ($=2\pi \cdot 42.578$ MHz/T for the proton). The direction of the nuclear magnetic moment can be changed if a second magnetic field is also applied. This second magnetic field is not static; its frequency must be equal or very close to $\vec{\omega}$ to promote a change in the equilibrium of the nuclei, the resonance condition. In modern nuclear magnetic resonance experiments, this field is pulsed and called radiofrequency (RF) pulse (\vec{B}_1). After turn off the pulse, the nucleus returns to the equilibrium state.

In a sample, an enormous number of microscopic magnetic moments (μ_i) are present. In this way, the phenomenon is described using the macroscopic magnetization (\vec{M}) represented as the summation of all magnetic

moments $\left(\vec{M} = \frac{1}{V} \sum_{\substack{\text{protons} \\ \text{in } V}} \vec{\mu}_i, V \text{ is the volume where the moments are} \right)$. Basically,

when the spins are experiencing the static magnetic field they may align parallel or antiparallel to the magnetic field lines. The summation of all parallel and antiparallel aligned spins result in the net magnetization, which is the representative vector of all spins contributing to the signal to be detected by the nuclear magnetic resonance technique. This net magnetization at the equilibrium state is represented by the magnetization vector oriented in the \vec{B}_0 or longitudinal direction ($\vec{B}_0 = M_0 \hat{B}_0$). The application of the resonant RF pulse changes the orientation of the magnetization vector, returning again to the equilibrium orientation when the pulse is turn off. The magnetization vector evolution is described by its two components referred to the static magnetic field direction: longitudinal and transverse. When several interacting spins are present, the return of the magnetization to the equilibrium, after the RF pulse, involves the relaxation process. In Magnetic Resonance (MR) equipment, the temporal variation of the transverse component of the magnetization is detected through the Faraday induction law in the receiver coil. The temporal variation of the magnetic flux due to the transverse magnetization generates the MR signal, thus the NMR phenomenon is detected. For imaging, the transverse magnetization is explored in order to provide spatial information about the sample. In the most of human brain MRI experiments, this information is related to the water content of the different brain tissues.

3.3 Using magnetic field gradients for generating an image

After the transverse magnetization is detected, it is necessary to differentiate in the ^1H signal the magnetization contribution from different spatial positions. The space coding is done by applying extra magnetic fields with a linear spatial behavior in order to change linearly the magnetization precession frequency in the region of interest. These spatial coding fields are called gradients and they are applied as pulses in different physical directions (X, Y and Z), even more than one at the same time and during different events:

1 – Magnetization excitation, the so-called slice selective gradient (\vec{G}_{ss}), which is applied simultaneously to a RF pulse. The frequency spectrum of the RF pulse and the gradient strength define the thickness of one slice in the sample. The central plane of this slice is perpendicular to the direction of the applied gradient (\vec{G}_{ss}). This gradient can be a linear combination of the physical gradient directions (X, Y and Z). The position of the slice in the gradient direction is defined by the gradient strength and the central frequency of the RF pulse. During the excitation, the magnetization vector flips in the plane perpendicular to the \vec{B}_1 direction. The flip angle is defined by the magnetic field strength and duration of the RF pulse.

2 – Magnetization preparation: The so-called phase or preparation gradient (\vec{G}_p) is applied without any RF pulse and before the reading process. During the application of this gradient, the transverse magnetization in each point of the sample accumulates a phase due to the spatial frequency variation created by the preparation gradient. The accumulated phase is proportional to the point position and the strength and duration of the applied gradient. Therefore at the end of this gradient, planes in the sample containing transverse magnetization with equal phase are obtained. The direction of these planes with prepared magnetization is perpendicular to the applied gradient \vec{G}_p , it also can be a linear combination of the physical gradient directions. The phases change continuously throughout these planes.

3 – The readout gradient: it is also called frequency gradient (\vec{G}_r) and it is applied without any RF pulse and during the reading process (acquisition window). The readout gradient is always perpendicular to the phase

gradient and makes the frequency-encoding of the signal detected in the probe. Planes with equal frequency are encoded and they can be decoded after a 1D Fourier Transform. The direction of these parallel planes is perpendicular to the applied gradient \vec{G}_r and can be also a linear combination of the physical gradient directions.

A pulse sequence is defined as a sequence of events involving gradients, RF pulses and acquisition windows with a specific temporization. Several sequences are available in the MR scanners; a general classification of the sequences is considering the acquisition form. In 2D acquisitions, each mentioned gradient is applied in perpendicular directions between them and the raw data is stored slice by slice excited by the RF pulses. After that, a 2D Fourier Transform is applied to the raw data in order to obtain the image of each slice. In 3D acquisitions, two phase gradients are applied; one of them is parallel to the slice selection gradient, if any. 3D Fourier Transform is applied to the 3D acquired raw data in order to obtain the image. Even when the MR signal comes from the transverse magnetization of the whole excited region in the sample, the intensity of each pixel in the image is related to the transverse magnetization in the correspondent point in the sample.

3.4 Different MRI contrast mechanisms

A basic parameter of any image is the difference between two neighbor points: the contrast. Different medical imaging techniques have different contrast mechanisms based on the physical phenomenon involved. In MRI, the pixel intensity is related to the transverse magnetization during the reading process. The main factors involved in this magnetization value are physical properties of the sample related to MR phenomenon: proton density and relaxation times. The weighting level of the each property in the pixel intensity of the resultant image is dependent on the pulse sequence used and its timing parameters.

The density proton is always present in the pixel intensity and indicates directly the water content in the most of MR images. Relaxation times characterize the times needed for the magnetization to return to the equilibrium state ($\vec{B}_0 = M_0 \hat{B}_0$). The longitudinal relaxation time (T1), also known as spin-lattice relaxation time, is related to the time needed for the longitudinal magnetization to return to the equilibrium value (M_0). The transversal relaxation time (T2) or spin-spin relaxation is related to the time

needed for the transverse magnetization to return to the equilibrium value (0). Another interpretation of this property is related to the phase coherence. Transverse magnetization exists due to the phase coherence of the spins in a specific voxel, thus T2 is related to the time needed by the spins to lose their phase coherence on the transversal plane due to the intrinsic magnetic interactions between spins.

For this thesis, the most important contrast mechanism is a combination of T2 relaxation and local magnetic field inhomogeneity, the T2*. This contrast appears in pulse sequences where the phase coherence lost is not only due to the unavoidable intrinsic spin-spin interactions, for example Gradient Echo (GE) sequence. In our specific case, the magnetic susceptibility variations in a tissue region affect.

3.5 Functional Magnetic Resonance Imaging background

Functional Magnetic Resonance Imaging is a MR modality based on the detection of the Blood Oxygenation Level Dependence contrast. The BOLD contrast has been widely applied in brain studies and has provided innumerable important insights about brain functions (Ogawa et al., 1990; Glover 1990; Fox et al., 2005), which is strongly associated to its non-invasive data acquisition and its relatively high spatial resolution. However, the BOLD contrast is an indirect measurement of the neuronal activity and it is associated to the variation of hemodynamic and metabolic parameters.

The BOLD contrast measures relative variations of the transversal relaxation time also affected by the local magnetic field inhomogeneity (T2*). It is well known that neuronal activities require energy (Pellerin et al., 1998), which is achieved by consuming glucose and oxygen (O_2). The mechanisms involved in transporting O_2 from the blood to the tissue originate the BOLD signal, therefore the magnetic properties of the hemoglobin is a key factor. The oxyhemoglobin is a diamagnetic (Pauling and Coryell, 1936) molecule with no net unpaired electrons in the *heme* group, thus its magnetic interaction with neighbor water molecules is weak. On the other hand, deoxyhemoglobin has paramagnetic properties (Pauling and Coryell, 1936) due to the unpaired electron; therefore it presents stronger influence in the neighbor water molecules, modifying the local magnetic fields. The change in the concentration ratio of both molecules in the blood vessels ($[O_{Hb}]/[De_{Hb}]$) that is surrounding a tissue region where neurons present increased activity is what explains the BOLD contrast detected

by fMRI. The increase of O_2 consumption causes a local increase of $[De_{Hb}]$ and consequently a $T2^*$ reduction due to the increases in the magnetic field inhomogeneity, thus a MR signal reduction will be expected. However, a signal increase is observed due to the hemodynamic response of the brain, where the local $[O_{Hb}]$ is increased due to the greater increment in the cerebral blood flow (CBF) (Ogawa et al., 1990). The BOLD signal variations were proved to be detectable by a gradient echo sequence (Ogawa et al., 1990). The GE sequence combined with echo-planar-imaging (EPI) technique is the most used acquisition sequence in fMRI, more details will be presented further.

3.6 The BOLD effect based on the classic hemodynamic function

Cerebral blood volume (CBV), CBF and O_2 consumption variations due to over-basal neural activity are the parameters applied by the balloon model for modeling the hemodynamic response in the MR signal, the so-called hemodynamic response function (HRF) (Buxton, 2001). The balloon model is one of the most referenced in literature for explaining the BOLD signal variation during a fMRI experiment (Buxton, 2012). This model is summarized by assuming that the vascular system behaves as a balloon, which has elastic characteristics that influence its capability of inflating and deflating. The following figure is an example of relative MR signal variations due to the hemodynamic response after a short neuronal stimulus, where the temporal evolution of the BOLD contrast can be explained by the balloon model.

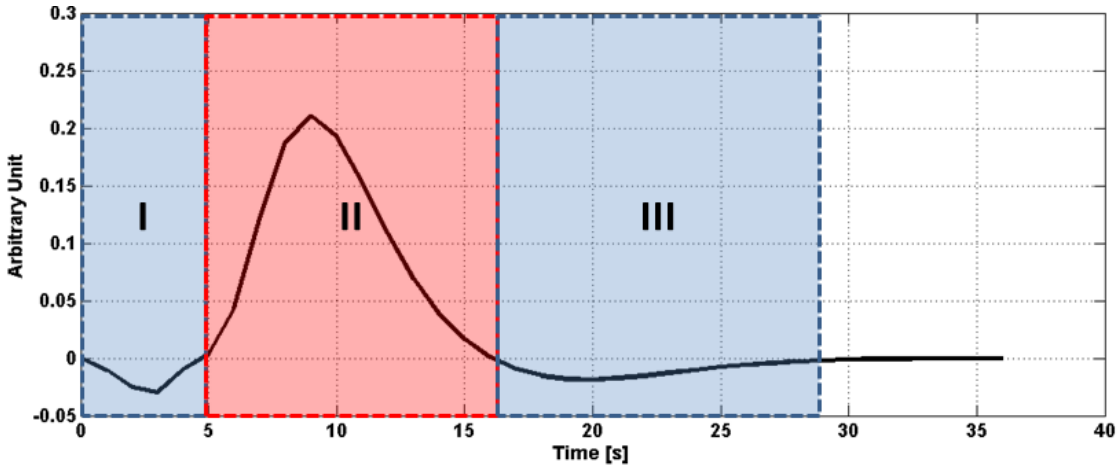


Fig. 3. 1: Relative MR signal variations due to the hemodynamic response after a short neuronal stimulus. The numbers I, II and III are related to the initial dip, positive response and undershoot, respectively.

Figure 3.1 shows the hemodynamic response effect in the MR signal, a typical signal course following neuronal activity associated with external stimulus or spontaneous brain activity. By the balloon model the signal evolution can be divided in three blocks: I- initial dip, right after the neuronal activation, the consumption/extraction of O₂ increases the concentration of De_{Hb}, reducing the relative signal. II – BOLD positive response, the CBF and CBV increase, with opposing effects: increase of CBF leads the O₂ to be transported to the region activated, decreasing the concentration of De_{Hb} and increasing the signal. The CBV increase happens in relation to the higher concentration De_{Hb}, decreasing the signal. However, the CBF increase is larger than the signal reduction caused by the extraction of O₂ and CBV increase, which results in a positive BOLD response. III – Undershoot, due to the slower CBV relaxation in relation to CBF and O₂ extraction there is an increased concentration of De_{Hb} while the CBF and O₂ extraction decreases, which leads the BOLD signal to be negative for a certain time, until the baseline is reestablished.

The curve presented in Fig. 3.1 is an example of a standard or canonical HRF. This curve is often composed by two gamma functions, where the maximum signal (block II) is delayed in about 5-6s in relation to the undershoot minimum value (block I), as described by Glover et al. (1999) and implemented in the *spm_hrf.m* function.

3.7 BOLD contrast detection by GE-EPI acquisition

Even in high field scanners, the BOLD signal variations are very small and require a T2* sensitive sequence to be detected. The gradient echo sequence is sensitive to small T2* fluctuations, therefore it is widely applied in BOLD detection studies (Jochimsen et al., 2004; Parks et al., 2005).

The GE is a sequence that applies magnetic field gradients for dephasing and rephasing the transversal magnetization in order to provide an echo. A simple 2D GE scheme for one slice is illustrated in Figure 3.2, different channels are showed: RF, gradients and acquisition (indicated as Echo). The sequence is basically composed by a RF pulse (located at the vertical line on the left hand side of the Figure 3.2) and three gradients (G_{ss}, G_p and G_r, as explained in the section 3.3). As mentioned, the gradients are applied for the spatial-frequency codification.

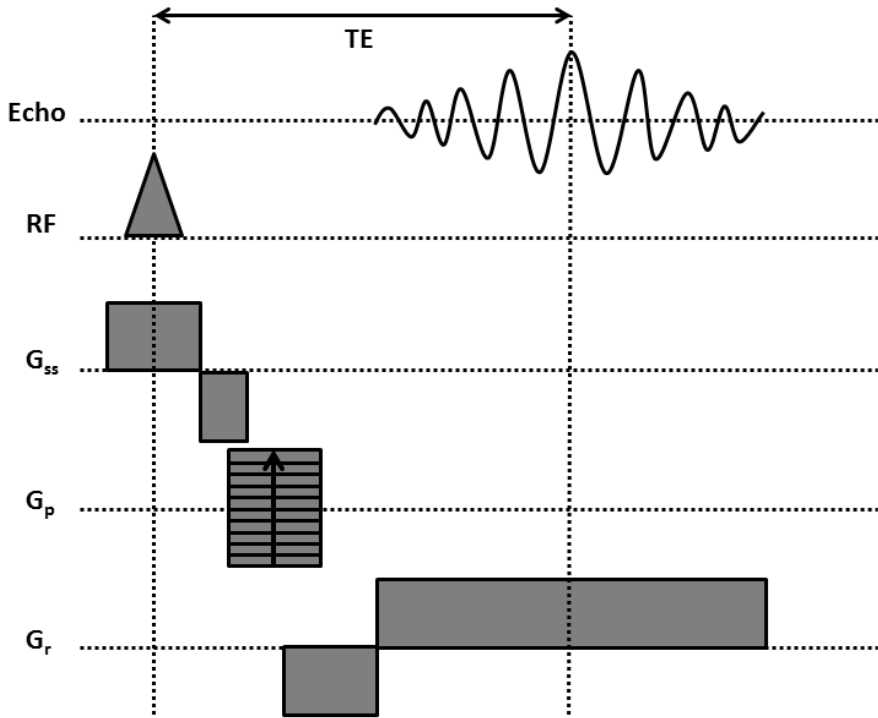


Fig. 3. 2: 2D Gradient echo: Pulse sequence diagram for one slice.

The combination of the G_{ss} gradient strength and central frequency of the RF pulse determines the position of the selected slice for imaging. In order to acquire data for another slice in the sample, the central frequency is changed. Ordinarily in this sequence, the slice selection gradient has a negative lobe after the end of the RF pulse, which is used for refocusing the magnetization of the spins affected by the simultaneously application of RF and gradient fields. The several lines in the phase gradient (G_p) channel indicated that the sequence is repeated in certain interval with different G_p values in order to differentiate the phase of the signal in the direction of this gradient. This interval repetition introduces an important timing parameter in the sequence: the repetition time (TR) defined as the interval between two successive RF excitation pulses. The frequency gradient (G_r) is also applied concomitant with G_p during the preparation stage; this fact is part of the main idea of GE sequence to create an echo during the signal acquisition. Another important timing parameter in the sequence is indicated by the central position of the echo related to the central position of the RF pulse; this time interval is the echo time or time-to-echo (TE).

A common way to describe the acquisition sequences in MRI is using the k-space diagrams as presented in figure 3.3. In these diagrams are represented the inverse space of the images related to the pulse sequences showed in Figures 3.2 (Fig. 3.3a) and 3.4 (Fig. 3.3b). Each axis contains the spatial frequency related to the gradient applied: horizontal axis related to Gr gradient and vertical axis to Gp gradient. After the slice selective RF and Gss pulse and the latter rephasing lobe, a phase encoding (Gx) gradient is applied in order to set the point of acquisition at the lowest edge, in phase encoding direction, of the k-space. After that, there is a pre-readout gradient that sets the acquisition to the lowest edge of frequency encoding direction (preparation stage as previously mentioned), which results that the acquisition will start in the left hand side lowest corner of the k-space. Then, the readout gradient is applied in order to acquire the information throughout that line of phase encoding from the left to the right hand side in the first acquisition line (Fig 3.3, more inferior blue arrows). In this specific example, the blue arrows represent three lines of the k-space corresponding to three repetitions in figure 3.2 with different values of Gp (kx-direction in figure 3.3-a) and three RF pulses also. The center positions of each gradient echo due to the block RF pulse/Dephasing/Rephasing gradient are in the vertical axis ($ky=0$). The black circles indicate the k-values to be filled during the 2D acquisition of the selected slice. It is important to note that each point in the k-space contains encoded information of the whole sample, because the probes receive the integrated signal. The sampling density and the dimension of the acquired k-space represent more details in the image, but also more time consumption. Therefore, the k-space is not totally filled in some acquisitions. When the raw data related to one slice (2D acquisition) is totally acquired, even with a partial k-space, a 2D Fourier transform is applied to obtain the slice imaging. Although the k-space can be acquired by multiple repetitions of the GE sequence, this is a time consuming process and not ideal for studying the dynamic of the brain activity, where multiple slices are necessary for full brain coverage.

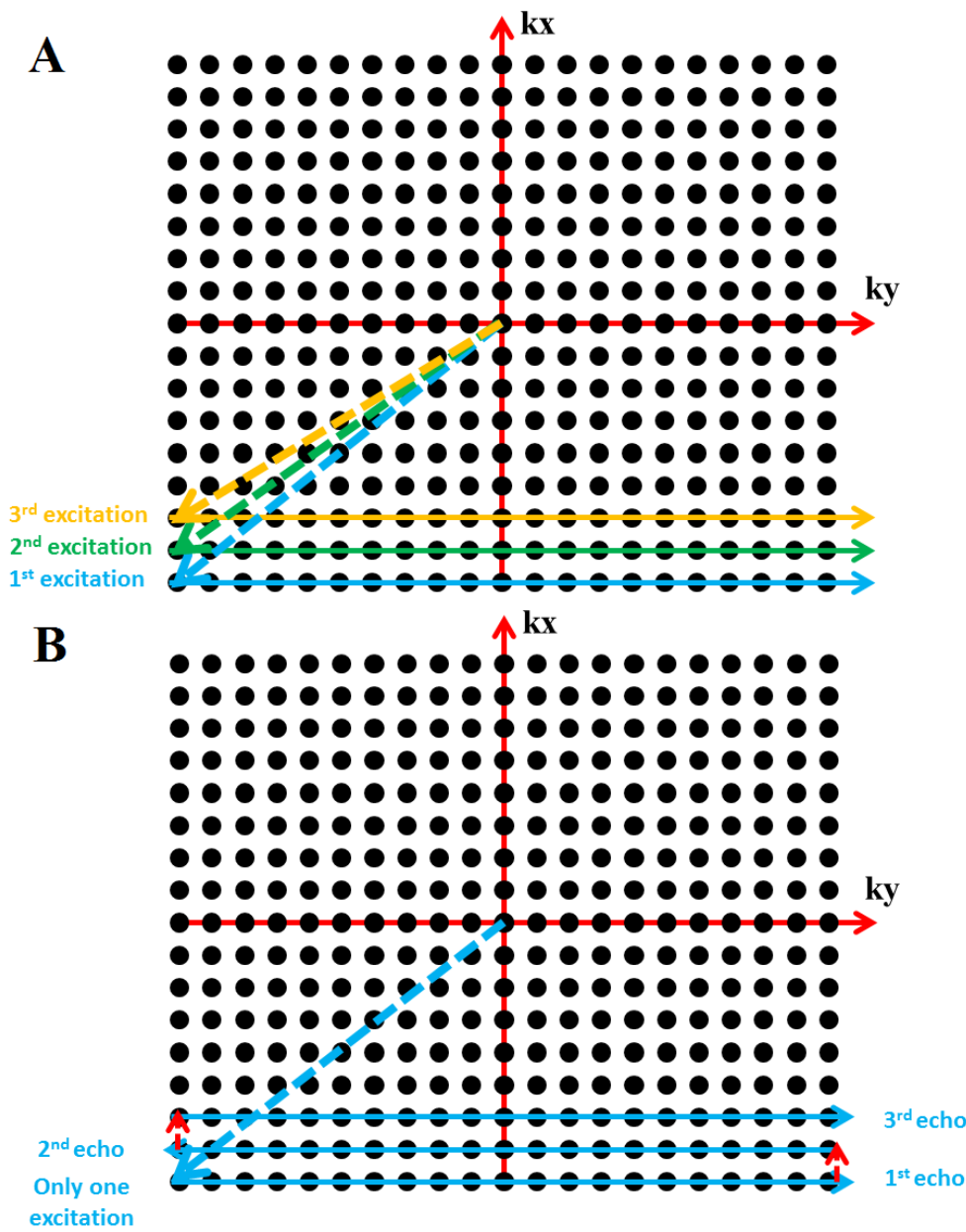


Fig. 3. 3: K-space diagram for a typical 2D-GE acquisition. A) Diagram related to the pulse sequence illustrated in 3. 2. Lines with different colors are related to the 1st (blue), 2nd (green) and 3rd (yellow) successive excitations. B) Diagram for the GE-EPI sequence illustrated in 3.4. The blue arrows represent the frequency encoding reading direction for the lines 1-3 of an ascendant reading. The small red arrows connecting successive blue arrows represent the first phase encoding gradients (Gx in Fig. 3.3), also known as bleeps.

One alternative for a fast full brain acquisition is to acquire more than one k-space line with a single excitation. In this procedure, the slice could be acquired with

few or just one excitation. T2* weighting effect reduces the signal duration in gray matter to 45-50ms for a magnetic field strength of 3T (Mulert and Lemieux, 2010), therefore a fast acquisition scheme is also important in order to provide a reasonable signal to noise ratio for the raw data of each slice. Echo planar imaging (EPI) is an alternative for acquiring all k-space information by one or multiple echoes for each slice (Mansfield, 1977). Here, we will be focused on the single-shot EPI (Fig. 3.4), which is the acquisition of all the phase encoding lines from k-space with only one echo. EPI combines the acquisition of several k-space lines within one RF pulse, resulting in one fMRI slice after one TR. This is possible due to the multiple echoes obtained by varying Gr (Gy in figure 3.4) and Gp (Gx in figure 3.4) gradients in a fast way. Each echo contains different phase information created by the small Gx variations. At the end of the readout gradient line a small amplitude and very fast Gx is applied in order to position the acquisition in the phase encoding line immediately above the one acquired previously. However, the acquisition of this phase encoding line will be done from the right hand to the left hand side, therefore a negative readout gradient is applied. This process is repeated (Fig. 3.3-b) until all the k-space lines are acquired within one single RF excitation, therefore using an EPI sequence is possible to acquire several slices, a volume, during the repetition time interval. In EPI sequences the echo of maximum signal also matches with the acquisition of the k-space central line.

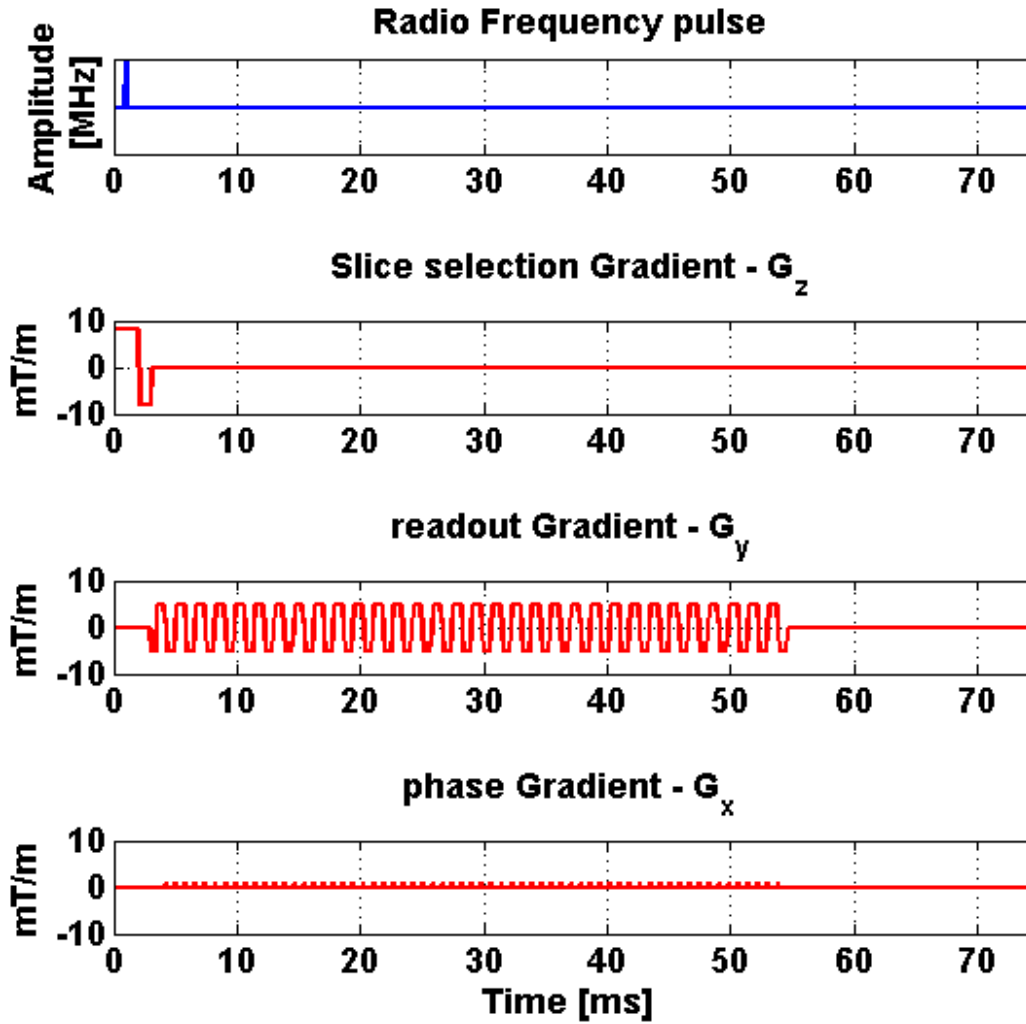


Fig. 3.4: GE-EPI acquisition scheme for one slice. From top to bottom: Radiofrequency pulse, slice selection (G_z), readout (G_y) and phase (G_x) gradient pulses.

3.8 Simultaneous EEG-fMRI acquisitions: preparing EEG and fMRI data for analysis

Simultaneous electroencephalography and functional magnetic resonance imaging (EEG-fMRI) is a multimodal technique for the brain activity study that aims to benefit from the temporal resolution of the EEG and the spatial resolution of the fMRI. The studies involving EEG-fMRI are focused on recording the timing *when* the electrical activity happen with the EEG data and mapping the spatial region *where* BOLD activation is related to that activity using the fMRI data (Fig. 3.5).

EEG-fMRI has been widely applied to study healthy (Mulert et al., 2004; Laufs et al., 2003) and pathologic brain activity, such as for studying patients with epilepsy (Lemieux, 2001, Laufs et al., 2008, Centeno and Carmichael, 2014; Pittau et al., 2012, Levan et al., 2010). More recently EEG-fMRI has been proven to be capable of mapping BOLD signal changes associated with epileptic seizures (Chaudhary et al., 2012a) using events detected in EEG. In this thesis, we focus on EEG-fMRI for mapping and understanding interictal epileptiform discharges, therefore the method explanation will be developed based on this topic.

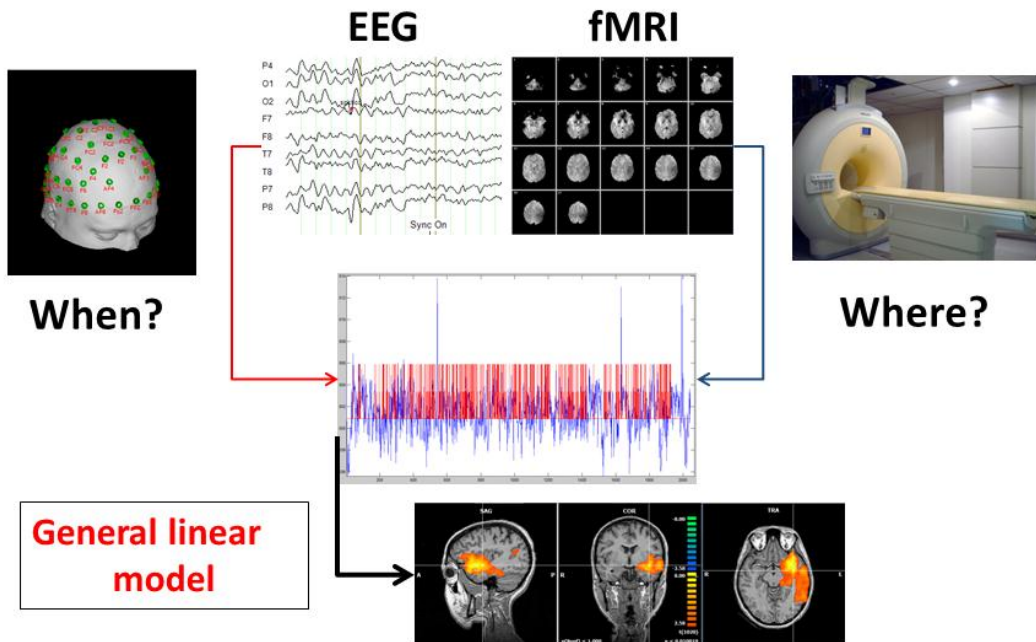


Fig. 3. 5: EEG-fMRI summarized from acquisition to IED-related BOLD map.

The acquisition of EEG data simultaneously to fMRI is technological challenging. In the experiment, an EEG system (electrodes, amplifier, batteries and cables) is positioned close/inside a MR-magnet, therefore it must be compatible with the MR-scanner environment (i.e. ferromagnetic components must be avoided). There are many issues related to the interaction of acquiring images and EEG simultaneously. One of them is related to the RF pulses, which deposit electromagnetic energy in conductors (e.g. electrodes, cables and amplifiers), increasing their temperature. This could damage the EEG amplifiers and in the worst scenario harm the patient by scalp burning. The switching gradients applied for imaging are also dangerous for the EEG equipment,

because they can induce high current levels into the system. Many of these issues were tangled in the past and safety practises for acquiring EEG-fMRI had been proposed (Lemieux et al., 2001).

There are also issues related to the EEG data quality, which is affected by many factors, such as voluntary (head motion) and involuntary motion (heartbeat-related), by the activity of the helium pump and by the voltages induced by switching the gradients. The easiest one to be dealt is the helium pump artefact, which disappear by turning the helium pump off. The real challenge is related to the voltages induced by the switching gradients, the so-called gradient artefact (GA) and also by voluntary motion. The GA is a consequence of the imaging process, where the gradients applied for induce currents that are overlapped to the brain activity of interest. However, these voltages are periodic, because the gradients are switched very similarly for every slice acquisition. Allen et al. (1998) have taken advantage of this EPI characteristic and proposed the Artefact Average Subtraction (AAS). The method samples successive GA as epochs related to the EEG acquired during the specific slice/volume, then the epochs of EEG data are averaged and each epoch is subtracted from that averaged epoch. As the artefact is periodic and the brain activity is expected to change through the time, the AAS results in EEG data free of GA. This is the first step for providing useful EEG data from an EEG-fMRI acquisition. The second step is to correct the BCG. Allen et al. (1999) also have verified that the AAS approach could be applied for correcting the BCG data, improving EEG data quality and facilitating its interpretation. An illustrative scheme of EEG data GA and BCG-artefact correction is illustrated in Figure 3.6.

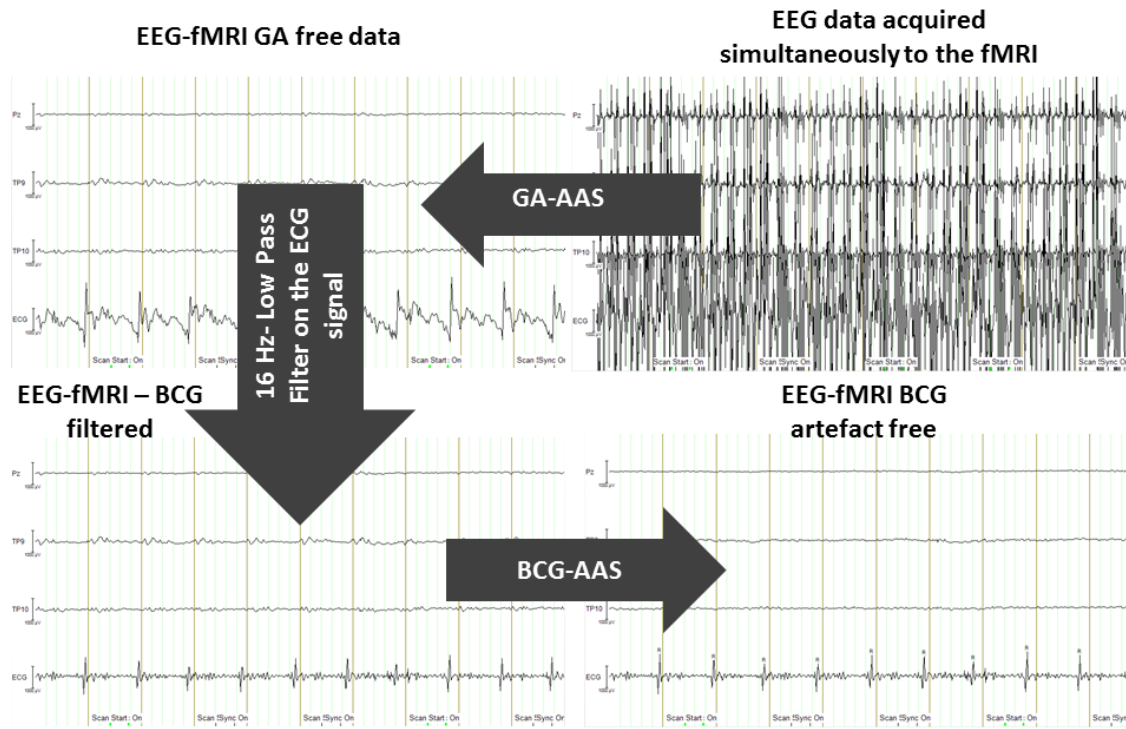


Fig. 3. 6: EEG-measured gradient artefact correction flowchart for three channels and ECG.

The AAS is a robust method for correcting periodic artefacts when they are stable through the time. Therefore, the method may not provide good quality EEG data in acquisitions realized under motion conditions or for subjects that present variations in their pulse-related artefact. In these cases other approaches are necessary and they will be discussed in details in chapter 7.

As discussed previously, there is a time interval (TR) between two successive fMRI volumes to be acquired. Therefore the BOLD response is not continuously acquired, which leads to its limited temporal resolution. This is also a problem for comparing the hemodynamic response that occurs during one single volume. For example, the acquisition timing for the slice at the top of the head will be delayed in relation to the slice at the bottom of the head, considering an ascending acquisition. There is also the head motion from the time when the first volume is acquired and the time when the last volume is acquired. These can play an important role in the results if not dealt properly. Most software for analysing fMRI data follow a sequence of pre-processing steps, illustrated in Figure 3.7. The pre-processing usually starts with slice time correction, which is related to the first problem described, where the T2* signal

measured in the different slices (and times) within a volume are interpolated in order to be possible to consider the whole fMRI volume as it was acquired at the same time point.. The same is applied for the volume realignment, which deals with the head motion during the volume-volume acquisition. This problem is usually overcome by doing the co-registratrion of every volume with the first volume acquired. This approach is interesting for slow and low amplitude motion.

Other pre-processing steps can be applied, such as spatially and temporally filter in order to improve the signal to noise ratio and also for suppressing the contribution of T2* signal related to low and/or high frequencies, which are often associated to physiological and acquisition artefacts, respectively (De Martino et al., 2007). The images can also be normalized to a template, which is might be done for allowing that the brain images from different subjects can be overlaid onto a standard space, such as a brain atlas.

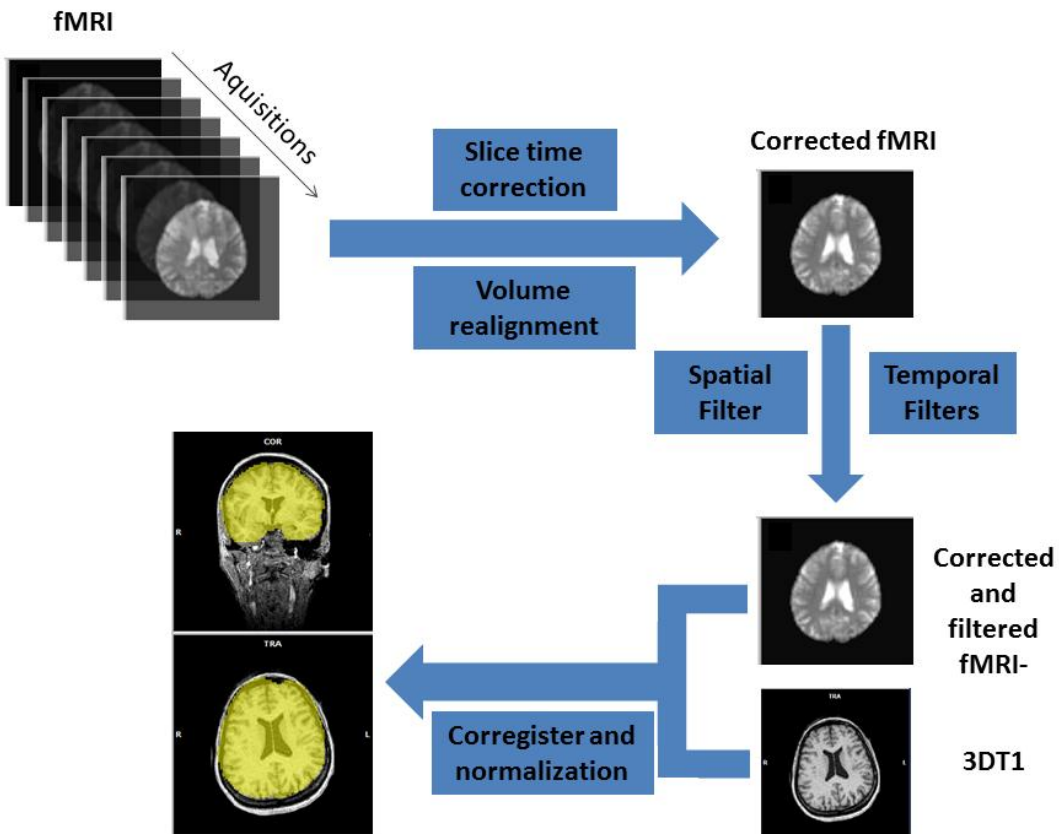


Fig. 3. 7: fMRI data pre-processing flowchart.

CHAPTER 4 - SIMULTANEOUS EEG-FMRI AND FMRI DATA ANALYSIS

In the previous chapter it was discussed how the EEG-fMRI data is acquired and also the standard procedure for providing useful data for further analysis. In this chapter the different methods for analyzing fMRI data, particularly of patients with epilepsy, will be presented. The scope of this thesis is on classic EEG-fMRI (Lemieux et al., 2001), 2dTCA (Morgan et al., 2008) and ICA (McKeown et al., 1998), which can be classified as dependent or independent (data-driven) of a priori information about the experiment realized in order to provide a brain map. The classic EEG-fMRI is a method that depends on a priori information, specifically in epilepsy it depends on information about the IEDs detected during the simultaneous acquisitions. On the other hand, 2dTCA and ICA are data-driven methods, which are independent of a priori information about the experiment.

In EEG-fMRI and 2dTCA methods, the temporal evolution of the MR signal of each voxel in the acquired volume is modeled following a statistical linear model, known as General Linear Model (GLM). In the method proposed for correcting motion-induced artefacts on the EEG data simultaneously acquired to the fMRI, a GLM was also applied. Therefore, in order to facilitate the understanding of the methods, the concept of GLM is firstly introduced and then contextualized for each of the methods.

4.1 The General Linear Model in EEG and fMRI data

The variable Y is measured in an arbitrary experiment. The measurements are represented by the values Y_j , where $j=1, \dots, J$, are the samples. Each sample can be composed by a set L ($L < J$) of explanatory variables (disregarding the error) x_{jl} , where $l = 1, \dots, L$ is the index of these variables.

The GLM is then applied for explaining the Y_j due to the linear combination of all explanatory variables summed to an error:

$$Y_j = x_{j,1}\beta_1 + \dots + x_{j,l}\beta_l + \dots + x_{j,L}\beta_L + \varepsilon_j \quad \text{Eq. 4.1}$$

Where β_l is a factor related to the unknown explanatory variables $x_{j,l}$. Here, we are considering that the errors ε_j are independent between observations (uncorrelated)

and follow a normal random distribution, with mean equal to zero and constant (homogeneity) variance σ^2 , $N(0, \sigma^2)$.

There are many statistical models derived from the GLM, one current used in this thesis (for ESI, classic EEG-fMRI, 2dTCA and REEGMAS) is the multiple linear regression as described by the equation 4.1.

The application of GLM to analyze EEG or fMRI data is easier understood by described its math by matrices. This is due to the possibility of organizing the measures from each time instant in lines, and each voxel as a different column. The J observations described by equation xx1 can be reorganized as the following system of equations:

$$\begin{aligned} Y_1 &= x_{11}\beta_1 + \dots + x_{1l}\beta_l + \dots + x_{1L}\beta_L + \varepsilon_1 \\ &\vdots = \vdots \\ Y_j &= x_{j1}\beta_1 + \dots + x_{jl}\beta_l + \dots + x_{jL}\beta_L + \varepsilon_j \\ &\vdots = \vdots \\ Y_J &= x_{J1}\beta_1 + \dots + x_{Jl}\beta_l + \dots + x_{JL}\beta_L + \varepsilon_J \end{aligned} \quad \text{Eq. 4.2}$$

Or even as matrixes:

$$\begin{pmatrix} Y_1 \\ \vdots \\ Y_j \\ \vdots \\ Y_J \end{pmatrix} = \begin{pmatrix} x_{11} & \cdots & x_{1l} & \cdots & x_{1L} \\ \vdots & \ddots & \vdots & \ddots & \vdots \\ x_{j1} & \cdots & x_{jl} & \cdots & x_{jL} \\ \vdots & \ddots & \vdots & \ddots & \vdots \\ x_{J1} & \cdots & x_{Jl} & \cdots & x_{JL} \end{pmatrix} \begin{pmatrix} \beta_1 \\ \vdots \\ \beta_l \\ \vdots \\ \beta_L \end{pmatrix} + \begin{pmatrix} \varepsilon_1 \\ \vdots \\ \varepsilon_j \\ \vdots \\ \varepsilon_J \end{pmatrix} \quad \text{Eq. 4.3}$$

These matrixes can be summarized by the following equation:

$$Y = X\beta + \varepsilon \quad \text{Eq. 4.4}$$

Where Y is the column for the observations, ε is the error associated to each measurement and β is the vector containing the β parameters, also called as regressors or temporal predictors: $\beta = [\beta_1, \dots, \beta_l, \dots, \beta_L]^T$. The matrix X , $J \times L$, is named the design matrix, which contains one line for each observation and n column for each parameter modeled (explanatory variable). The number of regressors in the design matrix is specific for each problem. In our case, for the classic EEG-fMRI and 2dTCA we have

used at least seven regressors (the IEDs, three translational and three rotational parameters). For the REEGMAS implementation we have used 18 parameters (three translational and three rotational position, their velocities and the velocities squared).

The goal of this approach, is to find the vector β that relates Y and X in a linear form in order to provide the minimum ε . It is a matrix inversion problem and the generalized least square method can be used. If we assume the homoscedasticity condition for the matrix containing conditional variance of the error, i.e. uncorrelated and homogenous noise between observations as commented, ordinary least square can be applied. In this specific case, the solution is described as:

$$\hat{\beta} = (X^T X)^{-1} X^T Y \quad \text{Eq. 4.5}$$

In fMRI experiments, this linear model is applied on each individual voxel in the fMRI volume; therefore different $\hat{\beta}$ vectors are estimated for each voxel composing that volume. In the context of this thesis, this model is also applied on each channel in the EEG data, therefore different $\hat{\beta}$ are estimated for each channel. A second part of the fMRI analysis involves a statistical test over hypothesizing that one or more elements from $\hat{\beta}$ explain the signal measured with a small error. This can be done by using a contrast vector.

4.2 Classic EEG-fMRI analysis

The classical EEG-fMRI data analysis is a procedure that may provide an epilepsy-related BOLD map (Lemieux et al., 2001). Figure 4.1 describes the main steps involved in this procedure. First, the IEDs need to be visual identified by a specialist (e.g. neurophysiologist), and then EEG data timing and the fMRI volumes are synchronized. The volumes where the IEDs were identified by the specialist are then used as a priori information for building the temporal predictor. For doing so, often delta functions are convoluted with a hemodynamic response function such as that described by Glover et al (1999), the standard HRF as described in the previous chapter. Although there are other possibilities involving different basis functions, for example

sine and cosine functions (Moeller et al., 2011), most of the papers only explore the standard HRF parameters (e.g. time to peak and peak duration).

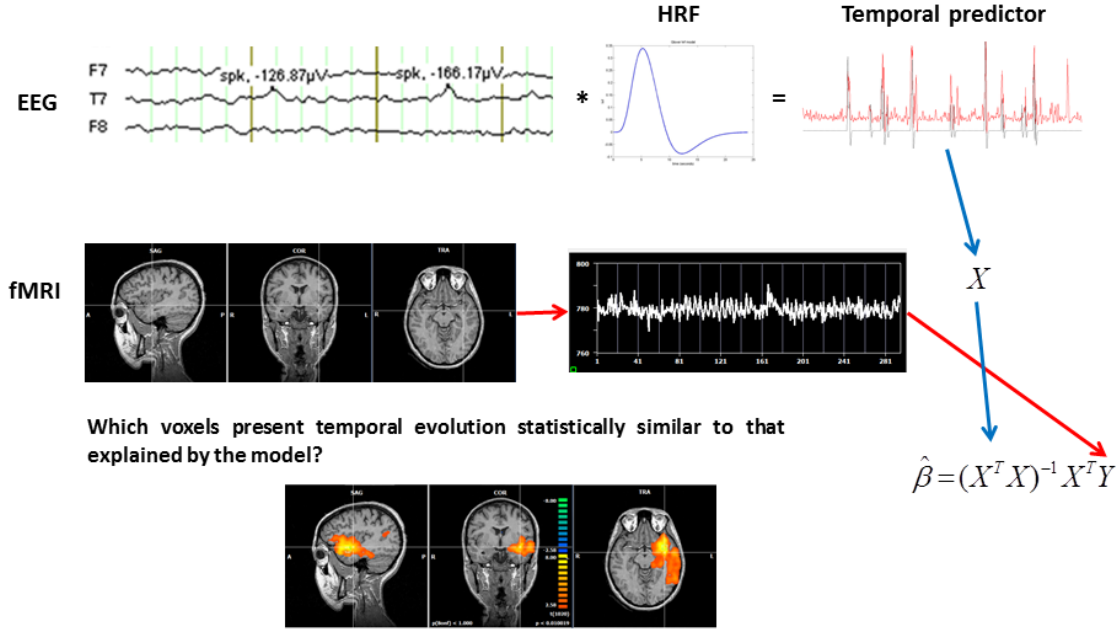


Fig. 4. 1: EEG-fMRI data analysis. The EEG detected IEDs are convoluted with an HRF function to produce a temporal predictor. The GLM is applied on each fMRI voxel (Y) using the temporal predictor (X), for estimating a $\hat{\beta}$ for each voxel. Finally, a statistic map exhibiting voxels whom time courses are similar to the regressors is obtained.

The GLM is applied in order to build a temporal model for the expected BOLD response for a voxel where the IEDs is changing the T2* response. Finally, statistical maps are generated in order to evidence voxel whom time course evolution is statistically explained by the model. The t-value for each voxel is calculated as follows:

$$t = \frac{c^T \hat{\beta}}{\sqrt{Var(\varepsilon)c^T(X^T X)^{-1}c}} \quad \text{Eq. 4.6}$$

Where c is the contrast vector and $Var(\varepsilon)$ is the variance of the associated error.

4.3 Independent Component Analysis (ICA)

Based on complementary principles of localization and connectivity (Phipps et al., 1984), McKeown et al. (1999) suggested that fMRI signal of brain areas activated due to the execution of psychomotor tasks should not be affected by physiologic,

acquisition or head motion artefacts. Therefore it would be possible to separate each of the process in components spatially independent, each of them associated to an exclusive time course and one map (Fig. 4.2).

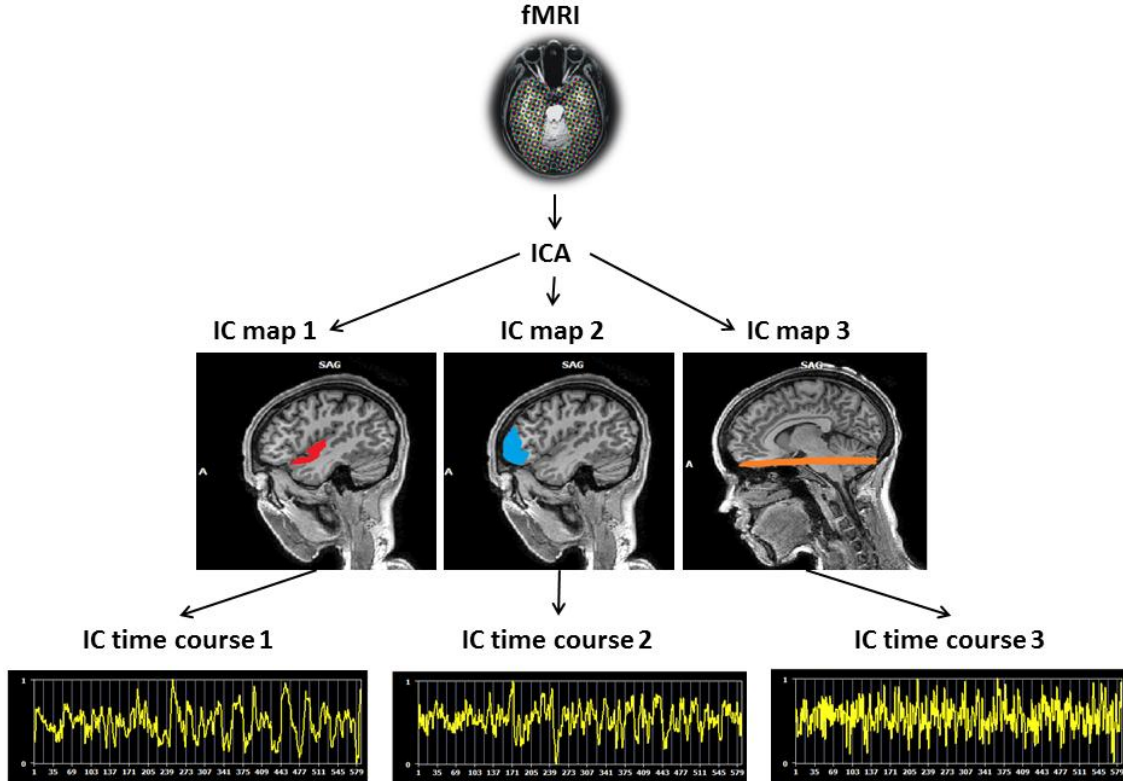


Fig. 4. 2: fMRI-ICA decomposition scheme. In this example, the fMRI decomposed by the ICA results in three independent components, and each of them shows a different time course

The authors assumed that different brain process would be represented by one or more spatially-independent components (ICs); each one associated to a time course and a spatial map. The authors also assumed that each IC-map is specified by a spatial distribution of fixed values for each voxel. This represents the possibility of overlapping of multifocal brain regions of statistically dependent fMRI signal influence [McKeown et al., 1998]. Therefore the authors assumed that the IC-maps are spatially independent between each other and are unique for each brain process.

The ICA decomposition of fMRI data can be written as the product of two matrices:

$$X = AS \quad \text{Eq. 4.7}$$

Where X is a matrix of $T \times M$ dimensions (T is the number of volumes acquired and M is the number of time courses) that represents the fMRI data. S is a $N \times M$ matrix where each row S_i ($i=1,\dots,N$) contain a spatial map ($N \leq T$). These maps must be pairwise independent in a statistical sense. A , $T \times N$ matrix, represents the mixing matrix with the columns A_j ($j=1,\dots,N$) containing the time course of the N spatial-independently maps.

There are no a priori assumptions for the matrix A , but the fixed numbers of components to decompose the fMRI. Besides that the noise signals, such as acquisition and motion artefacts are also considered as one or multiple independent components. The ICA is based on finding the matrix A which minimizes the estimation of the statistical dependence between the rows of S . The mutual information is commonly used as a measure of the statistical dependence. Therefore, the decomposition of X can be defined as a linear transformation:

$$S = A^{-1}X \quad \text{Eq. 4.8}$$

Where A^{-1} is the pseudo-inverse of A and is determined in order to provide the minimum mutual information between the components within S_i .

4.4 Two-Dimensional Temporal Clustering Analysis (2dTCA)

The two-dimensional Temporal Clustering Analysis (2dTCA) (Morgan et al., 2008) is a data-driven method proposed specifically for detecting transient BOLD-related activity independently of *a priori* information. The 2dTCA extracts BOLD-related activities from the fMRI data series based on the assumption that $T2^*$ fluctuations must be inside a reasonable range to be considered as BOLD-related (Handwerker et al., 2004); otherwise they will be related to artifacts such as motion and susceptibility. The method groups voxels presenting time courses that exhibit transient fluctuations, the assumed response to an IED, at the same time in histograms composed by the number of voxels exhibiting these fluctuations at each fMRI volume. Theoretically, different sources of activity are represented by different histograms that exhibit temporal and spatial similarity among their signal fluctuations.

The first step in applying 2dTCA is related to exclude most of the voxels present on the fMRI dataset that are not related to BOLD activity. In other words, in the first stage of 2dTCA the algorithm is focused on excluding voxels alike to have their signal evolution explained by artefacts. The exclusion of voxels is done based on two criteria: 1-voxels with T2* variations outside a predetermined threshold and 2- voxels where the signal change do not exceed two standard deviation in relation to that voxel time average. The second criterion is applied for disregarding voxels where the signal variations are not related to spiking. All the voxels excluded by these criteria are considered non BOLD-related voxels, and they are averaged in order to produce the so-called global time course.

The second step is related to removing signal drifts from the voxels considered as BOLD-related. For these voxels there is also an individual subtraction between them and the global time course. The 2dTCA algorithm creates 2d mapping based on all voxels considered as BOLD-related.

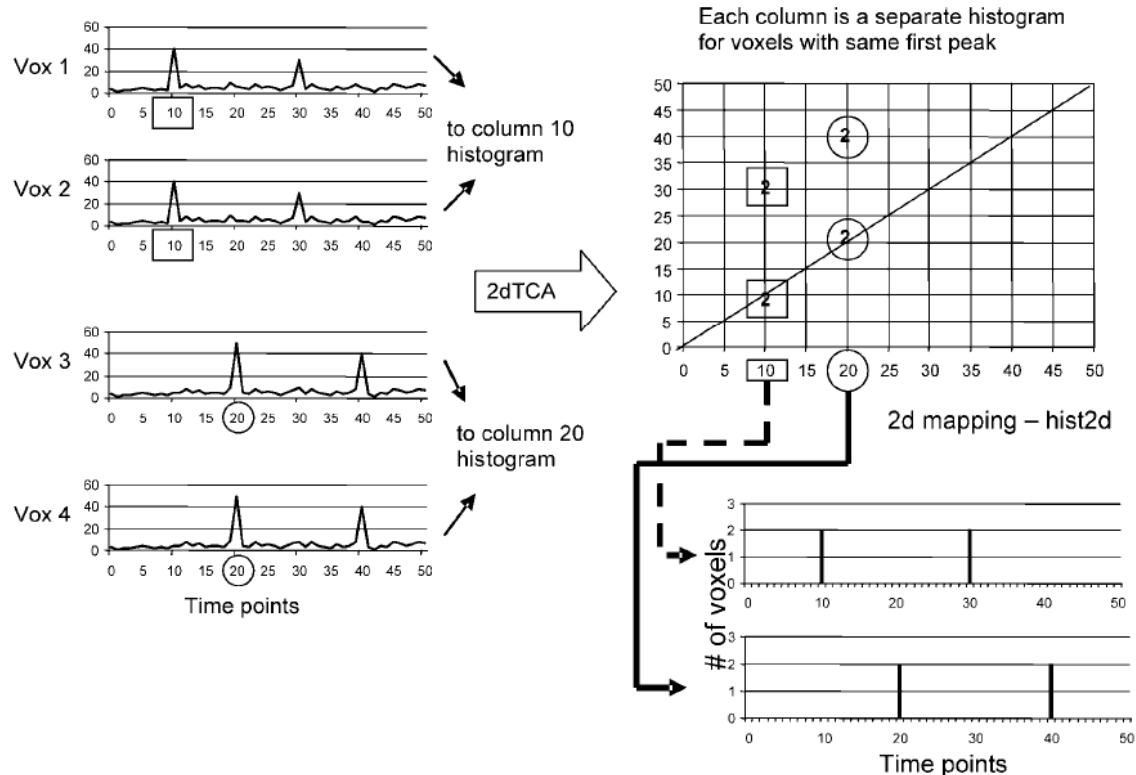


Fig. 4. 3: Two-dTCA schematic illustration. Modified from Morgan et al. (2008)

In order to better understand how the 2dTCA groups the fMRI information in clusters related to similar brain process one example considering four voxels of 50 volumes acquisition as BOLD related is showed in Figure 4.3. The 2dTCA algorithm creates a 2d mapping of each of the 4 voxels into an N by N matrix (hist2d),, where N is related to the number of volumes acquired (50), by incrementing the values as the following equations for all voxels (Morgan et al., 2008):

$$\begin{aligned}
 & \text{For } Z(y)_{y=1 \text{ to } N}, \\
 & \text{hist2d}(x, y) \\
 & = \begin{cases} \text{hist2d}(x, y) + 1, & \text{if } Z(y) \geq \text{threshold} \\ \text{hist2d}(x, y) + 0, & \text{if } Z(y) < \text{threshold} \end{cases} \quad \text{Eq. 4.9}
 \end{aligned}$$

Where $\text{threshold} = \text{mean}(Z) + 1.5 * \text{STD}(Z)$ and $x = \min(y)$ at which $Z(y) \geq \text{threshold}$. Therefore, the x-axis of hist2d is related to the number of voxels which the signal increase was detected for the first time, for example (Fig. 4.3), two (voxels one and two) for volume ten and other two (three and four) for volume 20. The y-axis accounts for the time at each significant signal increase was detected, for example two (voxels one and two) at volumes ten and 30 and two (voxels three and four) at volumes 20 and 40. In theory a reference time course, or a temporal predictor, can be created from each column of the 2d-histogram generated by the 2dTCA. To determine the most significant histograms, the diagonal of $\text{hist2d}(1:N, 1:N)$ is considered. Any points on the diagonal that exceed a given threshold are selected as indicators of times at which many voxels first experienced a significant signal increase. The corresponding columns of hist2d are the resulting signal components or reference time courses [Morgan et al., 2008].

Similarly to the process of EEG-fMRI, each reference time course is considered a temporal predictor and they are used into a GLM analysis in order to find voxels where the $\hat{\beta}$ are alike to be explained by these predictors, allowing that t-tests can be done and a statistical parametric map obtained.

CHAPTER 5 - A COMPARISON OF INDEPENDENT COMPONENT ANALYSIS (ICA) OF FMRI AND ELECTRICAL SOURCE IMAGING (ESI) IN FOCAL EPILEPSY REVEALS MISCLASSIFICATION USING AN AUTOMATIC CLASSIFIER

This chapter is related to our objectives of providing alternatives of using EEG-fMRI data for mapping BOLD signals related to epilepsy in cases whose EEG-fMRI was impossible or inconclusive. Besides that we have proposed a method for decreasing the dimensional problem associate with applying ICA for decomposing fMRI data of patients with epilepsy. These results were published as an original article at the Brain Topography Journal, with the following doi: <http://dx.doi.org/10.1007/s10548-015-0436-4>

5.1 Background

Some studies have applied ICA with some success to analyze fMRI data of epilepsy patients, reporting interesting results in mapping regions related to known or presumed epileptogenic zones (Rodionov et al. 2007; Moeller et al. 2011; Hunyadi et al. 2013). The motivation for the application of ICA to EEG-fMRI data in epilepsy is the lack of strong assumptions regarding haemodynamic responses to epileptic events where there is much greater uncertainty in the possible haemodynamic responses, or a strong assumption about the events themselves (potentially overcoming limitations of scalp EEG sensitivity and interpretation). ICA could therefore provide useful localizing information for patients with epilepsy with infrequent IEDs and also with more variable and poorly characterized haemodynamic responses found in pathology of mixed etiology, as reported by Hunyadi et al. (2013). In that study, the authors could relate the IC maps to the ictal onset zone (IOZ) in many cases. The authors applied a retrospective approach for selecting the ICs, which was based on *a priori* knowledge of the IOZ (interictal onset zone) from surgery outcome data. This study further suggested the existence of epilepsy related ICs, the remaining challenge being to select the ICs prior to the surgery to aid the planning process.

The major limitation of ICA-fMRI for epilepsy localization to be a useful clinical tool is that ICA typically generates a large number of ICs (normally 10s to 100s), which need to be interpreted. Different strategies have been proposed to facilitate the selection of relevant ICs related to physiological processes and to exclude those related to artifacts. Two examples are the IC-fingerprint method (De Martino et al. 2007) and the linear correlation between IC's time course and a model of the expected response (Schmithorst and Brown, 2004; Moritz et al. 2005). The IC-fingerprint method is based on a set of temporal and spatial features derived from visual assessment of a range of ICs from fMRI studies of normal subjects in normal conditions (Fox et al. 2005) (i.e. training data) that are used to subsequently classify each new IC. The IC-fingerprint is defined as the representation of an IC in a multidimensional space of 11 features. Each feature considers a particular information about the IC, five of them are related to the temporal frequencies of the component time course, one to the IC time course temporal entropy, one to the temporal one lag auto-correlation and the other four are related to the IC spatial characteristics (degree of clustering, skewness, kurtosis and spatial entropy). In its original format (De Martino et al., 2007), the method uses the features presented in each fMRI IC for classifying it in six classes: (1) BOLD-related ICs (task-related, transiently task-related and brain state-related), (2) residual motion artifacts, (3) typical EPI susceptibility artifact, (4) physiological noise with highly localized peaks (e.g., large vessels), (5) and (6) noise at high spatial (SDN, spatially distributed noise) or temporal (tHFN, temporal high-frequency noise) frequency.

In the context of epilepsy it was reported that the same classifier was capable of selecting ICs that were representative of BOLD responses associated with IEDs that were also mapped by classical EEG-fMRI analysis (Rodionov et al. 2007). Although the authors had shown that the classifier is capable of reducing the total number of ICs to those BOLD-related and also that some of these ICs were spatio-temporal related to the GLM-derived results, they also concluded that there were remaining BOLD-related ICs that could include epileptic activity not evident on the scalp EEG [Rodionov et al., 2007]. A straight forward hypothesis resulting from their conclusions is that there were remaining ICs IED-related in the group of ICs classified as non-BOLD-related. The classifier, for example, could misclassify ICs related to epileptic activities that present

their BOLD signal in a wider time frequency than the commonly verified in task-related BOLD ICs. Therefore we can hypothesize that the IED-related ICs found by IC-fingerprint may not be all the ICs related to epileptic activity present into the set of ICs decomposed by ICA.

Usually the use of the electrical information is restricted to the building of a very simple binary predictor (i.e. IED event onset and duration) utilized in the GLM applied to each fMRI voxel time course. The predictor is based on IED information of one or few electrodes (e.g. the electrode presenting the maximum discharge electronegativity), although more channels are utilized in the EEG recordings. A method that may improve the utilization of the electrical information in fMRI analysis of patients with epilepsy is Electrical Source Imaging (ESI). This method is based on the electromagnetic inverse problem (Helmholtz, 1853) applied in the scalp EEG data (for more details see Michel et al. 2004). ESI is a method that allows the representation of the sources within the brain of electrical activity detected on the scalp. In the context of epilepsy, ESI applies inverse source estimation methods to scalp EEG in order to localize the region responsible for the epileptic seizures. ESI has reported encouraging results in studies that evaluate the correlation between the sources represented by the method and areas of the brain that have significant hemodynamic activity in GLM applied to EEG-fMRI data of patients with focal epilepsy (Bagshaw et al. 2006; Benar et al. 2006; Boor et al. 2007; Grova et al. 2008; Lemieux et al. 2001; S. Vulliemoz et al. 2009; Seeck et al. 1998).

5.2 Objective

The aim of this study was to apply the ICA to decompose fMRI data of epilepsy patients known to present IED-related BOLD responses in simultaneous EEG-fMRI acquisitions. Our main goal was to evaluate the ability of the IC-fingerprint tool to classify ICs known to be related to epileptic activity. To do this requires strong knowledge of the location and time course of the activity. Therefore here we suggest comparing ICs based on their spatial correlation to ESI maps and evaluating their temporal correlation with the IEDs. Unlike comparison to the GLM results alone (Rodionov et al., 2007), this avoids the requirement of strong assumptions regarding the IED selection and haemodynamic response to IEDs, potentially removing the added

value of ICA. The results were validated by comparison of each IC to the available clinical information of each patient and also with the results obtained by classical GLM analyses of the EEG-fMRI data. Due to the poor performance of the classifier it was not widely applied to EEG-fMRI data without IED. Instead we evaluated main factors contributing to the misclassification of epileptic components by comparing the features of ICs selected by IC-fingerprint to those selected by spatial correlation to the IEDs based on ESI. Finally we applied the same comparison to patients who did not have IEDs during the simultaneous EEG-fMRI acquisition, but had sufficient IED outside the scanner to allow the ESI calculation.

5.3 Methods

5.3.1 Patient description

The study was approved by the local Medical Ethics Committee of the Clinical Hospital of Ribeirão Preto and written informed consent was obtained from all patients. We acquired EEG-fMRI data from 18 patients from the Ribeirão Preto Epilepsy Surgery Center (CIREP). Patients were recruited during pre-surgical evaluation following previously described protocols (Velasco et al. 2011). The patients' data were included in our analysis based on two selection criteria: (1) no technical problems (e.g. problems with EEG equipment or the scanner), (2) no large head movement (fMRI data with movements higher than 2mm based on realignment parameters were excluded). From the initial 18 patients, two were excluded by the criteria number 1 (the battery discharged in the middle of one acquisition and the scanner crashed in another), and three by the number 2. The remaining 13 patients were classified in two categories: I- patients presenting at least two IEDs (spikes, slow spike-wave and sharp wave) in the simultaneous EEG-fMRI acquisition and II- no IED detected during the EEG-fMRI acquisition and at least one IED detected in the EEG recorded outside the scanner just before the EEG-fMRI acquisition. Finally the category I was subdivided in Ia- GLM result concordant with the clinical information obtained by the pre-surgical evaluation (Table 5.1) providing a population with a reasonable knowledge of the IZ and a related BOLD response, and Ib- EEG-fMRI map discordant with the clinical information obtained by the pre-surgical evaluation/surgery region and outcome (Table 5.1) or there

was no sensitivity by the classical analysis. In summary there were 7 patients in the category Ia, 4 in Ib and 2 in the category II. The category Ib and the category II provide a population where ICA would be most beneficial.

Table 5. 1 Summary of electro-clinical and imaging findings

Table 1 Summary of electro-clinical and imaging findings

Cases	VEEG localization	MRI finding	Surgery outcome	ESI location	EEG-fMRI results
1	Temporal L	L-MTS	I	L-Inferior T G; L-middle T G; L-hippocampus; L supramarginal G; L inferior PL;	L-Superior T G; L-fusiform G; L-parahippocampal G; L-insula; L-inferior F G
2-L	Temporal L	Normal	n/a	L-Inferior T G; L-superior T G; L-hippocampus	L-Superior T G; L-inferior F G; L-insula; L-middle T G; L-parahippocampal G; L-fusiform G
2-R				R-Insula; R-temporal pole	R-Superior T G; R-inferior F G; R-middle T G; R-parahippocampal G; R-inferior T G; L-inferior T G
3	Temporal L	Bilateral-MTS	III	L-Insula; L middle T G; L-superior F G	L-Middle T G
4	Temporal R	R-MTS	I	R-Insula; R superior T G	R-Middle and superior T G
5	Temporo-parietal R	R-MTS	n/a	R-Insula; R superior T G; R-middle T G; R-inferior F G	R-Lentiform nucleus
6	Temporal R	R-MTS	I	L and R insula; R-hippocampus	R-Insula; R fusiform; R-superior T G; R and L parahippocampal G
7	Temporal L	R-MTS	n/a	L and R insula; L-middle T G	L-Inferior T G; L-middle T G
8	Temporal R	R-MTS	I	R Insula; R-mesial T Lobe	No sensitivity
9	Temporal R	R-MTS	I	R-Inferior T G; R-middle T G; R-hippocampus; R-superior F G; L-insula	Not concordant
10	Temporal R	R-TCA	I	R and L-hippocampus; R-inferior and middle T G; R-superior F G	No sensitivity
11	Temporal L	L-MTS	I	L-Insula; L-hippocampus	No sensitivity
12	Frontal R	R-IFGGN	I	R-Middle F G; R-inferior F G; L-hippocampus	No IEDs during EEG-fMRI
13	Temporal R	R-MTS	I	R-Insula; R-mesial T lobe	No IEDs during EEG-fMRI

Surgery outcome is expressed as the Engel score: I - Free of disabling seizures; II - Rare disabling seizures ("almost seizure-free"); III - Worthwhile improvement IV: No worthwhile improvement; n/a no information available. ESI and EEG-fMRI location of clusters presenting values higher than the threshold are presented. The MRI finding location is also presented. Abbreviations: MTS = Mesial Temporal Sclerosis; IFGGN= Inferior Frontal Gyrus Glial Neoplasm; TCA=Temporal Cavernous Angioma L=Left; R=Right; n/a: not available; G:Gyrus, T=Temporal, F=Frontal.

The patients 1, 3, 6 and 8-13 had surgery outcome information, but only cases 1, 3, 6 and 8 had already a post-surgery 3dT1. In these four cases we could compare the resection cavity location with each IC selected, in the 6 remaining we compared the ICs selected with the surgery indication and outcome

The next section details the steps illustrated in the flow diagram presented in Figure 5.1.

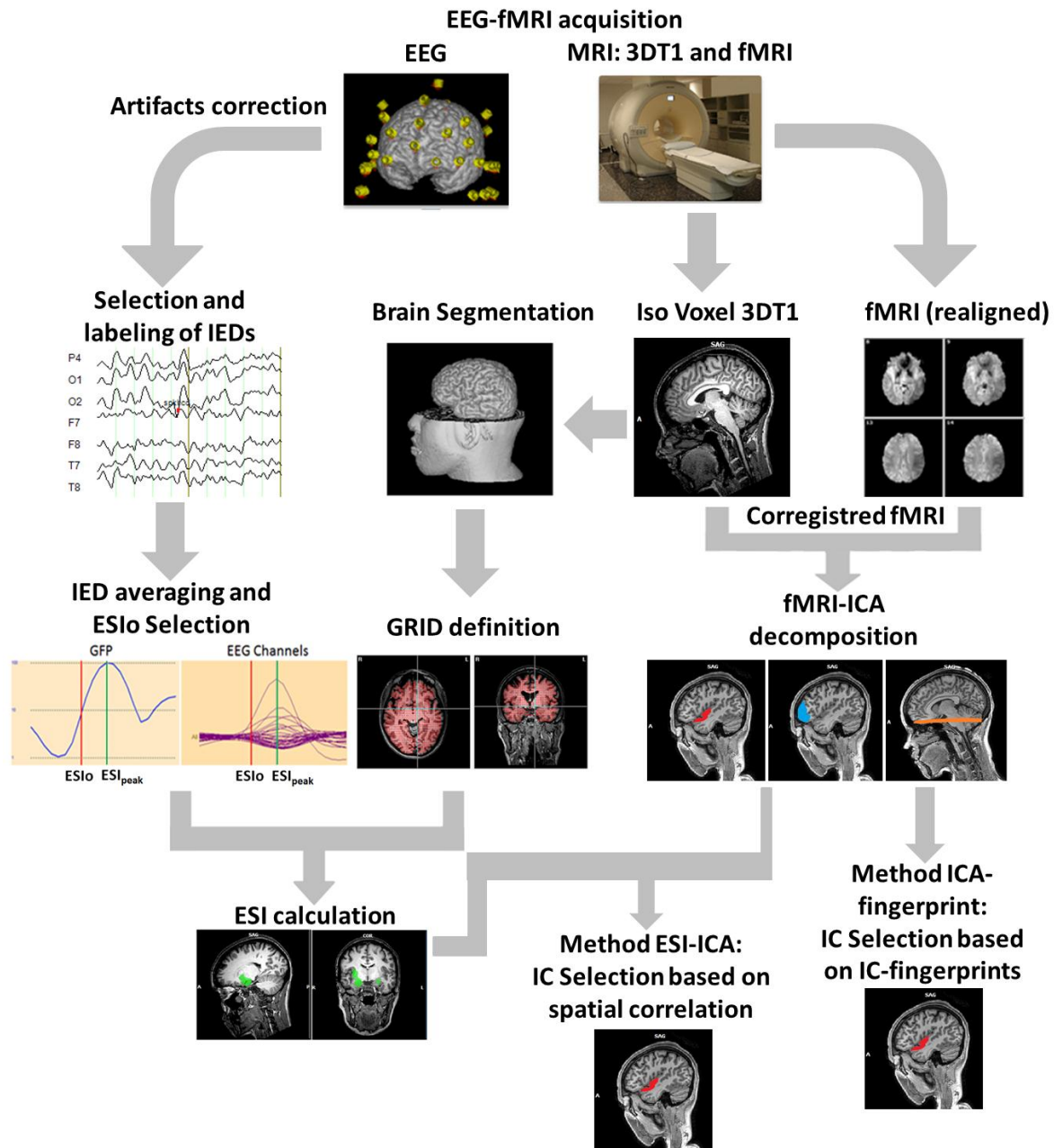


Fig. 5. 1: Workflow illustrating all the steps done from the data acquisition to the results of the methods.

5.3.2 MRI acquisition

Images of patients 1, 2 and 3 (Table 5.1) were acquired using a Magnetom Vision 1.5T scanner (Siemens, Erlangen, Germany) with a head coil. The image parameters were: TR/TE = 1890/50 ms, FA=90°, slice thickness=5mm, 16 slices, FOV=220 mm and

acquisition matrix 64x64. The number of volumes in each acquisition was 600 or 1024. A MPRAGE 3DT1 was acquired with TR/TE =9.7/4 ms, FA = 12°, slice thickness=1mm, FOV=256 mm and acquisition matrix=256x256. Images of patients 4-13 (Table 5.1) were acquired using an Achieva 3T scanner (Philips, Best, Netherland) with a SENSE head coil of eight channels. For the patients 4-7 one or two 10 minutes (300 volumes) echo-planar imaging (EPI) sessions were performed, for patients 8-13 one or two EPI of 20 minutes (600 volumes) was acquired. The EPI parameters were the same in both cases as follows: TR/TE = 2000/20 milliseconds (ms), flip angle (FA)=90°, slice thickness=5mm, 30 slices, field of view (FOV)=230 mm, acquisition matrix=64x64 and SENSE=2. High resolution anatomical images were acquired with a 3D-TFE sequence, TR/TE =6.75/3.1 ms, FA = 8°, inversion delay=900 ms, shot interval=2000ms isotropic voxel of 1mm, FOV=256 mm, acquisition matrix=256x256 and SENSE=1.

In this study we had data from two different field strengths; therefore the subcategory Ia with knowledge of the significant BOLD responses from standard GLM analysis also avoids the possibility of differing BOLD sensitivity being responsible for any failures of ICA to detect epileptic related BOLD changes.

5.3.3 EEG data acquisition and processing

EEG was recorded using MR-compatible systems EEG cap (Brain Products, Gilching, Germany). For the patients 1-7 a 32-electrodes (Ag/AgCl, internal resistance of 5kΩ and reference between Cz and Fz) EEG cap was used according to the 10-20 international system and two channels, ECG and EOG, were recorded in order to remove physiological artifacts. For patients 8-13 the EEG data was acquired in the same system, but using a 64 electrodes cap (63+ECG) according to the 10-10 system.

Gradient and pulse artifacts were removed offline using average artifact subtraction methods (Allen et al. 1998, 2000). The artifact-corrected EEG was downsampled from 5000Hz to 250Hz and filtered (high-pass 1Hz and low-pass 35Hz). Interictal epileptiform discharges time instants were identified and marked (EEG-visual coding process) consensually by two experienced neurophysiologists, with selection based on the location and morphology of each IED.

From these temporal markers the IED-based temporal predictor and the average IED for each channel to be used in GLM and ESI analysis were obtained.

5.3.4 fMRI analysis by Independent Component Analysis (ICA)

Using Brain Voyager Qx 2.4 (BrainInnovation, Maastricht, Netherlands), fMRI voxel time-series were realigned and spatially smoothed with a Gaussian Kernel of 6mm full width at half maximum. The data was also temporally high pass filtered based on a periodic function containing three cycles over the whole time series, Finally a Gaussian temporal low pass filter with FWHM of 0.35 Hz was applied.. The pre-processed fMRI data was then analyzed using principal component analysis (PCA) implemented in FSL 4.1 (FMRIB, Oxford, England) to estimate the most appropriated number of ICs to be found for each patient independently. Although other studies (Rodionov et al., 2007; Moeller et all., 2011) apply a common number of ICs (usually between 80-100) for decomposing the fMRI data set of all patients, we believe that using the PCA for estimating this number would eliminate the possible dependence of the number of ICs with the datasets acquired in different scanners (1.5 and 3.0T) and different number of volumes.

Finally the fast-ICA algorithm present in the software Brain Voyager QX 2.4 was applied to decompose the fMRI data in the number of estimated ICs. The z-scores in IC maps are used for descriptive purposes and as discussed in literature they have no definite statistical interpretation (McKeown et al., 1998). Therefore in this study we considered negative and positive z-scores.

5.3.5 Electrical Source Imaging

The global field power (GFP) on the average IED was estimated and two different instants were marked in order to calculate the ESI of spike onset (ESIo) and propagation (ESIpeak). ESIo was defined as the 50% rising phase of the averaged IED (ESIo) and the ESIpeak as the maximum peak of electronegativity presented in the GFP (Lantz et al. 2003).

We have chosen the method for solving inverse electromagnetic problem based on two studies previously realized by our group:

1 – We applied six different methods of solving the e-IP based on IEDs of 20 focal epilepsy patients that presented abnormalities in their MRI. We compared the ESI maps obtained by each method with the location of the abnormality by applying a score system in order to allow us to evaluate the sensitivity of each method for temporal and extra temporal patients. More details about the methodology applied in this analysis are available in Maziero et al. (2014).

2 – The method presenting highest sensitivity in ‘study 1’ was applied in other 19 patients with focal epilepsy who have undergone to surgery and were seizure free after one year (ENGEL I). Fifteen of these patients had the EEG data acquired by a 64 electrodes cap (Easycap, Herrsching, Germany) and the remaining five by a 128 electrodes cap of the same company. These data were acquired using two or four amplifiers (Brain Products, Gilching, Germany).

In both studies the ESI was estimated using a three spheres volume conductor model of the head and a grid that covered the gray matter, excluding the cerebellum, in native MRI. Although in literature the authors usually do not describe and/or justify the threshold values applied over ESI solutions (Lantz et al., 2003; Michel et al., 2004; Vulliemoz et al., 2009; Brodbeck et al., 2011) there is one study that applied a threshold value justified by a Receiver Operating Characteristic (ROC) analysis (Grova et al. 2008). In their manuscript, the authors choose a threshold value of 60% of the maximum based on the higher Area under the Curve obtained by testing the relation between the ESI map and the epileptogenic source considering different thresholds. Here, we were interested in avoiding the background activity but allowing a solution wider than that concentrated at the maximum primary current density (PCD) peak. Therefore both ESI solutions were thresholded in 50% of the PCD maximum value and then grouped together using a Matlab R2011b (Mathworks, USA) routine, resulting in an individual volume of interest (VOI). We considered that both ESI_o- and ESI_{peak}-related BOLD responses are involved in a single IC, because there are large differences between the scales of IEDs (measured in milliseconds) and ICs representing hemodynamic response (measured in seconds).

5.3.6 Selection of ICs Based on ESI results (ESI-ICA selection)

Figure 5.2 presents a schematic diagram illustrating the IC selection based on ESI map spatial correlation. The first step was to calculate the spatial correlation between each IC and ESI map (VOI composed by ESIO and ESIpeak). For a single patient all IC unthresholded maps were spatially compared to the ESI maps-resultant VOI by spatial correlation. We calculated the R (Pearson's coefficient) and an associated p-value resultant for each comparison. The ICs were chosen as being spatially concordant with the ESI if they were at least 50% of the maximum R obtained for that subject, we also considered the p-value $<10^{-5}$ for selecting the IC. Both criteria were chosen to guarantee a high degree of spatial correspondence between the IC-map and the ESI map. Finally we visually reviewed the ICs selected based on the spatial correspondence to ESI to exclude artefact ICs such as radio frequency and susceptibility artifacts or those corresponding to typical resting state networks (Fox et al. 2005), mainly those related to auditory brain areas.

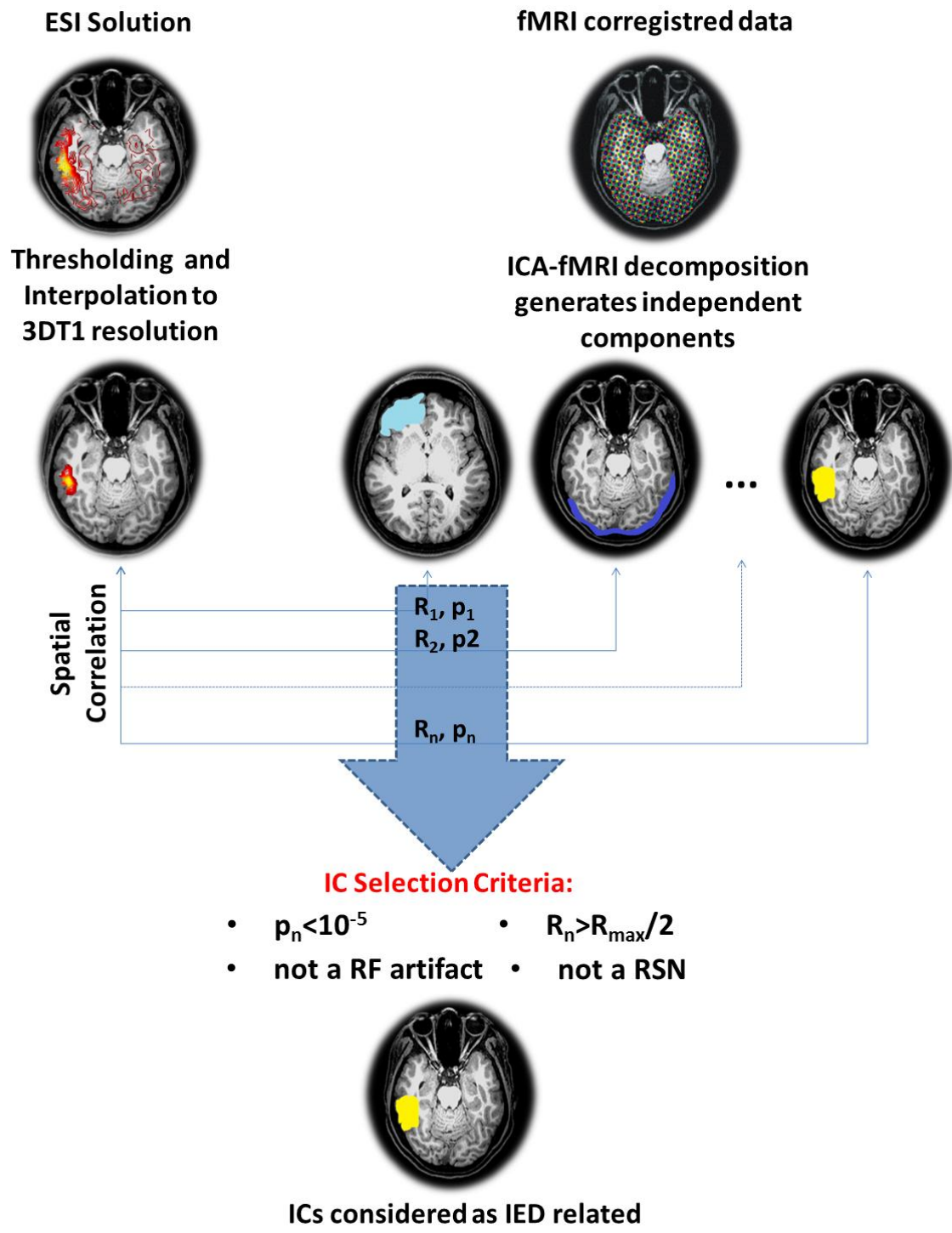


Fig. 5. 2: Workflow of the steps done in the ESI-ICA method.

As described above, for the spatial correlation between IC and ESI maps we considered negative and positive Z-scores, but for convenience of illustration all maps were thresholded with a $Z>4.0$ and were overlaid onto 3DT1 images of native space after co-registration to the EPI images.

5.3.7 Classification of independent components (ICA-fingerprint)

The individual independent components were first classified in two groups of ICs: (1) BOLD activity, grouping responses related to IED and to normal brain activity; (2) non BOLD activity such as motion (MOT), spatially distributed and high frequency noise and blood vessels (Vessels). This classification was based on IC-fingerprint tool available in Brain Voyager QX 2.4, with visual inspection undertaken following the definition of Martino et al. (2007). In a second step the group 1 was reclassified into two subgroups: (1a) normal brain activity found in resting state comprising of the following networks; the sensory motor, auditory, visual areas and the default mode network (DMN) (Greicius and Menon, 2003; Fox et al. 2005); (1b) regional IED-related changes of the BOLD signal. The ICs in this subgroup that had relation to the patient's clinical information were considered as ICs of interest for this study.

5.3.8 Classical fMRI analysis by GLM (General Linear Model)

The pre-processed fMRI data were analyzed using a GLM to identify BOLD signal related to IED. For each patient and type of IED a predictor was modeled as stick functions convolved with the canonical HRF and the motion effects (using the 6 scan realignment parameters). The spatial maps were obtained with $t> 2.0$, $p<0.05$ (uncorrected). For anatomical localization, GLM maps were overlaid onto 3DT1 images of native space after co-registration to the EPI images.

5.3.9 Temporal correlation of ICs time course and GLM predictor

Using Matlab R2007b (Mathworks, USA) we calculated the temporal correlation between the temporal predictor used in the GLM and the time courses of the selected ICs for each patient and section method.

5.3.10 Fingerprint feature analysis

In order to compare the features of the ICs selected by the two selection methods we plotted them in polar graphs. For illustration, we also plotted the fingerprint of a classical resting state network, such as auditory, visual or the default mode network as defined in (Fox et al., 2005). Finally, we statistically compared the features of the ICs selected by the IC-fingerprint tool to those selected by ESI using an unpaired T-test.

5.4 Results

5.4.1 ESI method choice

In the first study (Maziero et al., 2014) we have verified that the Bayesian model averaging method had a sensitivity of 86% (for temporal lobe patients) in EEG datasets acquired with few electrodes (e.g. from 16 to 44). This method also presented more restricted solutions that were more representative of epileptogenic activities than those obtained by the other methods. The equivalent dipoles method also presented 86% of sensitivity for temporal lobe patients; however we have chosen the BMA due to its distributed source characteristics, which allow us to calculate spatial correlation with each IC map. In the same study, we have verified a poor concordance of BMA for extra temporal patients (50%).

In the second study, where the ESI solutions were compared to the area resected in well succeeded surgeries (ENGEL I), we have verified an ESI sensitivity comparable to the first study for the 64 electrodes configuration EEG dataset. We have verified for temporal and extra temporal lobe patients a sensitivity of 89% and 40%, respectively. Although the sensitivity for temporal lobe patients is high and concordant with the first study and also to others in literature (Brodbeck et al., 2011), the sensitivity of the method for extra temporal patients was also low in this study. We believe that this is related to the gray matter segmentation realized by the toolbox IBASPM (www.thomaskoenig.ch/Lester/ibaspm.htm). Two of the 3 patients whom the ESI fails in provide an accurate map presented the epileptogenic region in very superficial regions of frontal and parietal lobes. We have noticed that even when we included this regions manually to the segmentation, they were not all considered in the process of generating the Lead Field matrix, and then they were not included as possible solution points composing the anatomical a priori information. The last is crucial for the BMA,

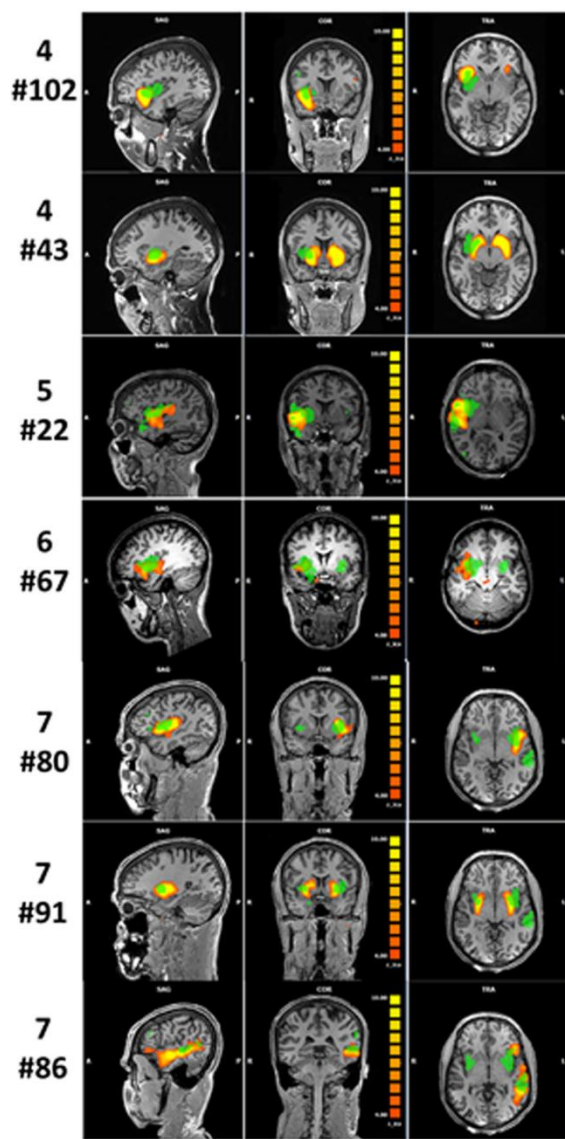
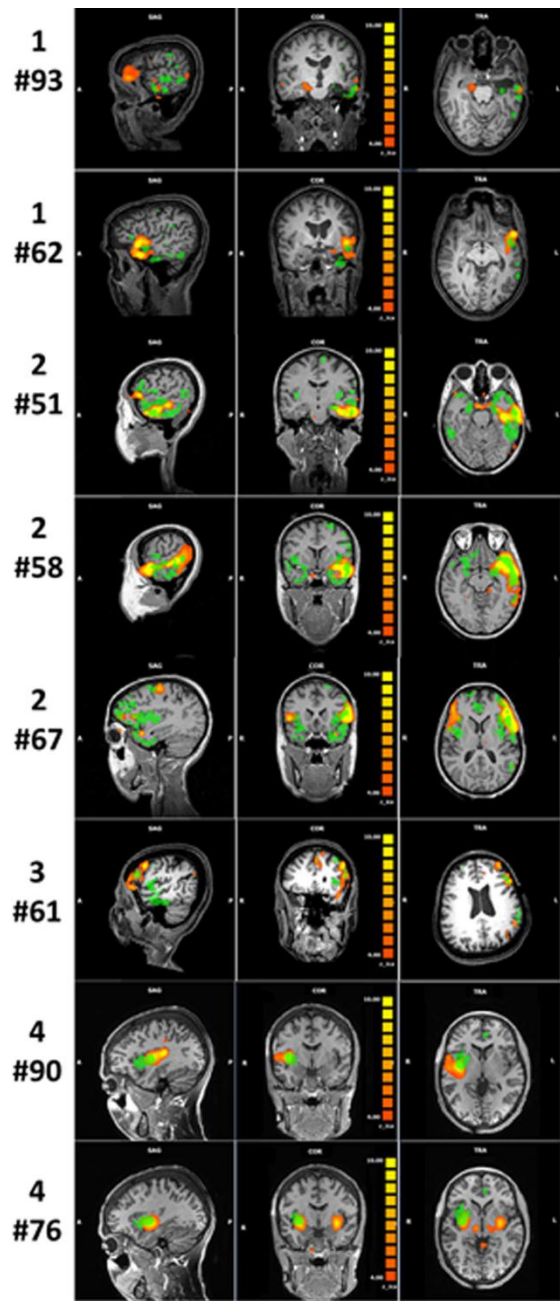
which we believe to play a key role for the low sensitivity. However, we have verified that the method successfully mapped the epileptogenic region in all the patients whom data of 128 electrodes were available, all these patients presented temporal lobe epilepsy.

Based on both results and that most of the patients to be studied were patients with temporal lobe epilepsy we have chosen BMA as the method for providing the ESI to be applied in selecting ICAs.

5.4.2 Results summary

The regions found by ESI and EEG-fMRI maps are summarized in Table 5.1, where it is possible to compare them to the electro-clinical information, MRI findings, surgery location/indication and outcome of each patient. The scope of this work was not in discussing the classic EEG-fMRI maps, therefore they are presented at the Supplementary Material 1.

The ESI-selected ICs (using spatial correlation with the ESI map) are presented in Figure 5.3. The ESI-ICA selected at least one IC in all patients (four ICs in one patient, three ICs in two patients, two ICs in five patients and one in five patients). For the patients in the category Ia (EEG-fMRI concordant to clinical information) at least one IC was shown to be IED-related by having a significant temporal correlation to the temporal predictor based on the spikes. For patients in the category Ib (IEDs recorded but EEG-fMRI not concordant or no result) no IC had a temporal correlation to the IED-based temporal predictor. In this latter category it is possible the ICs therefore contained information beyond that available from a GLM analysis. The remaining patients (category II) did not have IED-based temporal predictor because no IEDs were detected during the EEG-fMRI acquisition; however there were two ICs ESI-selected for each of them.



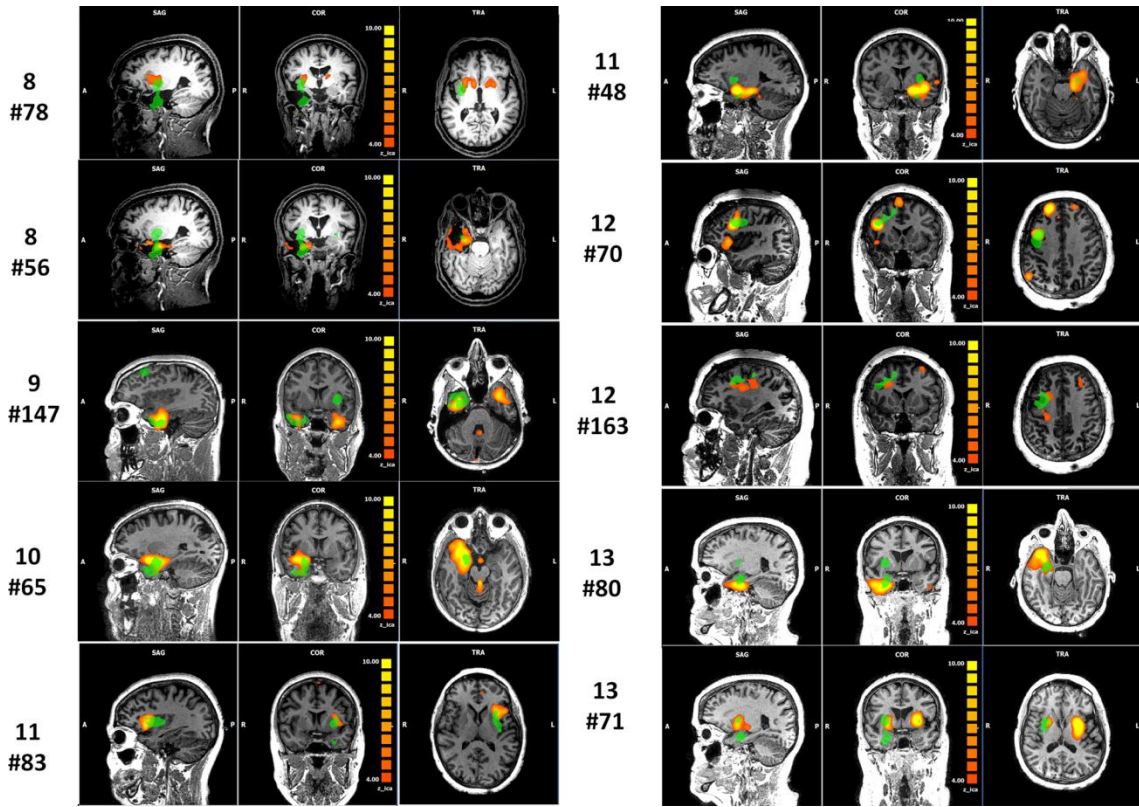


Fig. 5. 3: Independent Components selected by the ESI-ICA method for all the patients. The warm color scale with $Z>4.0$ represents the IC map, and the ESI solution is presented in green. The different ICs selected for each patient is labeled with its number.

The fingerprint-selected ICs (using the automatic classifier) are presented in Figure 5.4, and some of them (those were also selected by ESI-ICA) are presented in Figure 5.3. The classifier selected three ICs in three patients, two in five patients, one in five patients and no ICs in one patient, summing to 24 ICs. Three ICs from those found for the patients in category Ia and other three for the patients in the category Ib were significant temporal correlated to the spikes. Only one IC was found for the patients in the category II. Another relevant information is that the patient #2 had bi-temporal discharges and each type of IED was evaluated individually by the ICA-fingerprint approach (#2-right and #2-left). Five in thirteen patients had at least one IC that was selected by both methods.

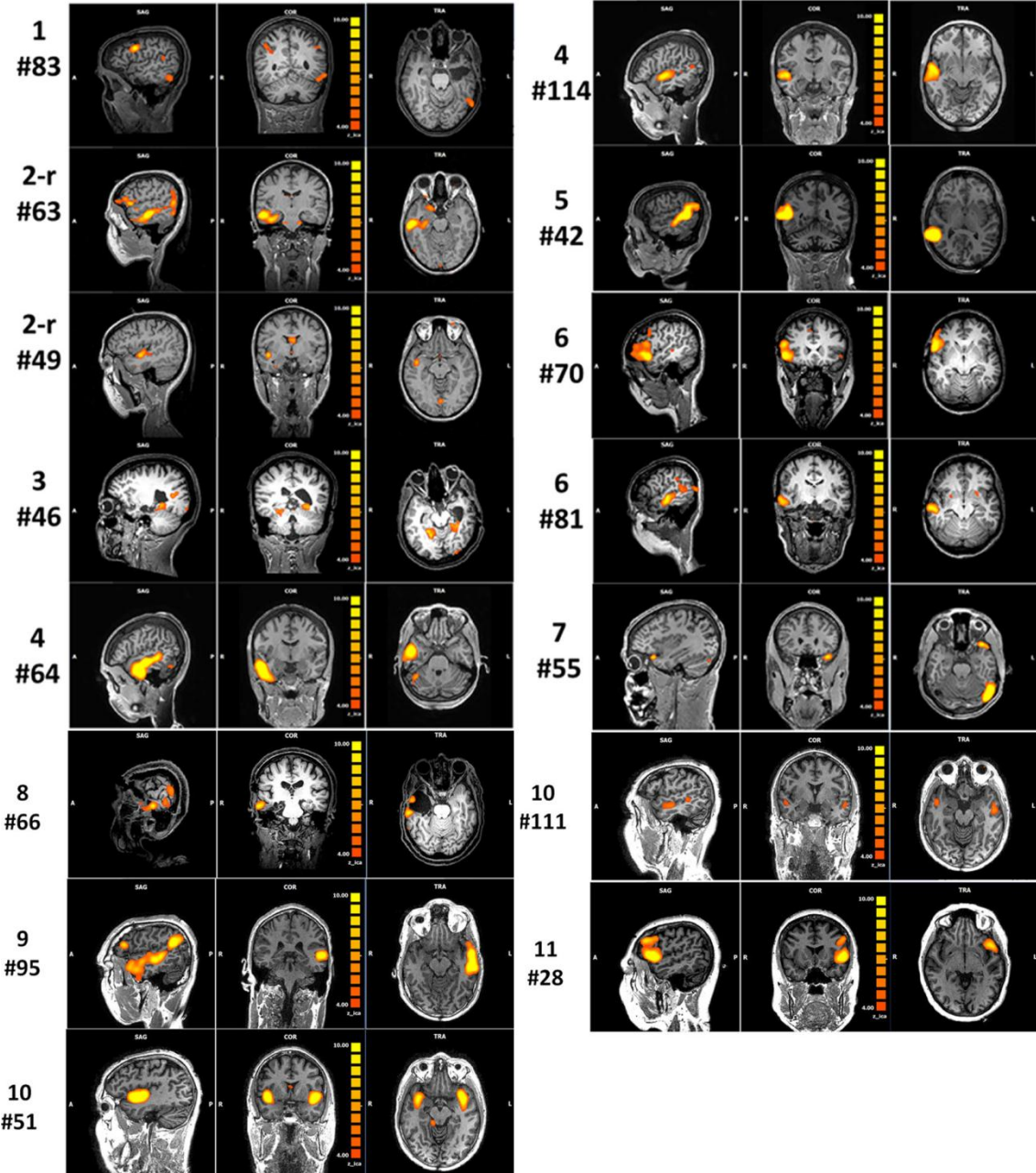


Fig. 5.4: Independent Components selected by ICA-fingerprint method for all patients. The warm color scale with $Z>4.0$ represents the IC map. The ICs #51 and 58 for the patient number 2, #90 for the number 4, #22 for the five and #82 and 85 for the patient number 7 are presented in figure 5.3. The different ICs selected for each patient is labeled with its number.

Table 5.2 summarizes the spatial location, spatial correlation with ESI and temporal correlation with the IED predictor (based on visual EEG coding) of each ESI-selected IC.

Table 5. 2. Results of ESI-ICA criteria of selection

Case	# of high ESI-IC correlated	IC number	Spatial correlation with ESI	Temporal corelation R (p) with temporal predictor	Location	IC-fingerprint classification
1	2	93	0.10	0.02 (0.42)	L Middle TG; L inferior FG; R hippocampus	tHFN
		62	0.08	-0.26 (6×10^{-17})	L Middle TG; L superior TG; L inferior FG	Vessel
2	3	58	0.211	-0.05 (0.09)	L Superior TG; L middle TG	tHFN
		67	0.138	-0.07 (0.02)	RL Inferior FG; L pre central G	BOLD
		51	0.122	-0.002 (0.95)	L Middle TG; L inferior FL	BOLD
3	1	61	0.089	-0.36 (9.6×10^{-20})	L Middle FG; L middle TG; L superior TG; R inferior FG	Vessel
4	4	90	0.241	0.04 (0.31)	R Inferior FG; R superior TG	BOLD
		76	0.182	-0.09 (0.02)	RL Insula	Vessel
		102	0.175	0.12 (0.004)	RL Inferior FG;	EPI
		43	0.159	0.03 (0.39)	RL Thalamus	EPI
5	1	22	0.405	-0.13 (0.001)	R Inferior FG; R superior TG; R middle TG	BOLD
6	1	67	0.254	-0.13 (0.01)	RL Insula; R inferior FG; L inferior TG	tHFN
7	3	80	0.28	0.027 (0.52)	L Insula; R inferior FG	BOLD
		86	0.16	-0.13 (0.001)	RL Thalamus	BOLD
		91	0.17	0.005 (0.9)	L Inferior FG; R superior TG; R middle TG	Vessel
8	2	78	0.11	0.02 (0.62)	RL Thalamus	Vessel
		56	0.09	-0.03 (0.51)	R hippocampus; R middle TG; R superior TG	EPI
9	1	147	0.18	-0.006 (0.88)	RL Hippocampus; RL middle and inferior TG	EPI
10	1	65	0.26	0.015 (0.72)	R Hippocampus; R insula; R superior TG	BOLD
11	2	83	0.12	0.009 (0.83)	LR Insula; L superior TG	BOLD
		48	0.18	0.06 (0.15)	L Hippocampus; L insula; L superior TG	tHFN
12	2	70	0.10	-	RL Superior FG; R middle FG; R inferior FG; R inferior PL	BOLD
		163	0.16	-	R Middle FG; R superior FG; L middle FG	tHFN
13	2	80	0.14	-	R Middle TG; R inferior TG	EPI
		71	0.11	-	RL Insula	MOT

of high ESI-IC correlated shows the number of ICs with spatial correlation coefficient $R > R_{max}/2$ and $p < 10^{-5}$; Spatial Correlation with ESI presents the Pearson's Coefficients resultant from the spatial correlation between the IC and the ESI map; Temporal correlation R (p) with temporal predictor shows the R and p values of the temporal correlation between IC time course and the EEG-fMRI temporal predictor. The Location of each statistical significant cluster found by the ICs is presented in Location.

Abbreviations: R-Right; L-Left; FG-Frontal Gyrus; TG- Temporal Gyrus; RL- Right and Left (Both Sides); tHFN - temporal high frequency noise; EPI - artefact related to imaging acquisition; MOT - Motion related artefact.

Table 5.3 summarizes the spatial location and the temporal correlation with the IED predictor (based on visual EEG coding) of each fingerprint-selected IC.

Table 5. 3. Results of Fingerprint-selected ICs.

Case	Clinical info-concordant BOLD IC [#]	IC number	Temporal correlation R (p) with temporal predictor	Location
1	1	83	-0.05 (0.11)	L Inferior TG; L superior TG; RL middle FG
2 Right	2	49	0.02 (0.45)	R Superior TG
		63	0.02 (0.46)	R Mesial TL; R middle TG; L inferior FG
2 Left	2	51	-0.002 (0.95)	L Middle TG; L inferior FL
		58	-0.05 (0.09)	L Superior TG; L middle TG
3	1	46	0.06 (0.11)	RL Hippocampus; R cuneus G
4	3	64	0.06 (0.15)	R Inferior TG; R middle TG
		90	0.04 (0.31)	R Inferior FG; R superior TG
		114	0.02 (0.64)	R Superior TG
5	2	22	-0.13 (0.001)	R Inferior FG; R superior TG; R middle TG
		42	0.04 (0.32)	R Middle TG; R superior TG; L cuneus G
6	2	70	0.05 (0.33)	R Middle FG; R inferior FG; R superior TG
		81	-0.09 (0.06)	R Middle TG; RL thalamus
7	3	55	0.12 (0.005)	L Superior TG; L cerebellum portion
		80	0.03 (0.52)	L Insula; R inferior FG
		86	-0.13 (0.001)	RL Thalamus
8	1	66	-0.16 (5×10^{-5})	R Middle TG; R angular G
9	1	95	-0.11 (0.009)	L Middle TG; L angular G; L middle FG
10	3	51	0.06 (0.17)	RL Insula
		111	0.005 (0.89)	RL middle TG
		65	0.015 (0.72)	R Hippocampus; R insula; R superior TG
11	2	28	0.10 (0.01)	L Middle and inferior FG; L superior TG
		83	0.009 (0.83)	LR Insula; L superior TG
12	1	70	-	RL Superior FG; R middle FG; R inferior FG; R inferior PL
13	-	-	-	-

#Clinical-concordant BOLD IC is the number of ICs selected by fingerprint tool; IC number is the number of each IC that matched the criteria; Temporal correlation R (p) with temporal predictor shows the R and p values of the temporal correlation between the IC time course and the EEG-fMRI temporal predictor; The Location of each statistical significant cluster found by the ICs is presented in Location.

Abbreviations: R-Right; L-Left; FG-Frontal Gyrus; TG- Temporal Gyrus; RL- Right and Left (Both Sides).

Both methods selected a similar number of components (25 and 24 respectively), but only 9/49 were commonly selected. The small number of shared ICs, taken together with the relatively few components selected by the fingerprint method that were significantly correlated with the GLM temporal predictor, shows that it did not classify all IED-related activity correctly. However, all but IC55 in case #7 and in cases 8, 9 and 11 (EEG-fMRI discordant), selected by the ESI-ICA method were significant temporally correlated with the GLM-predictor suggesting an epilepsy-related IC was separable and selectable. In cases #5 (IC22) and #7 (IC86) they were selected by both methods.

The IC-fingerprints of all ICs selected by both methods are plotted in Figure 5.5 for all patients.

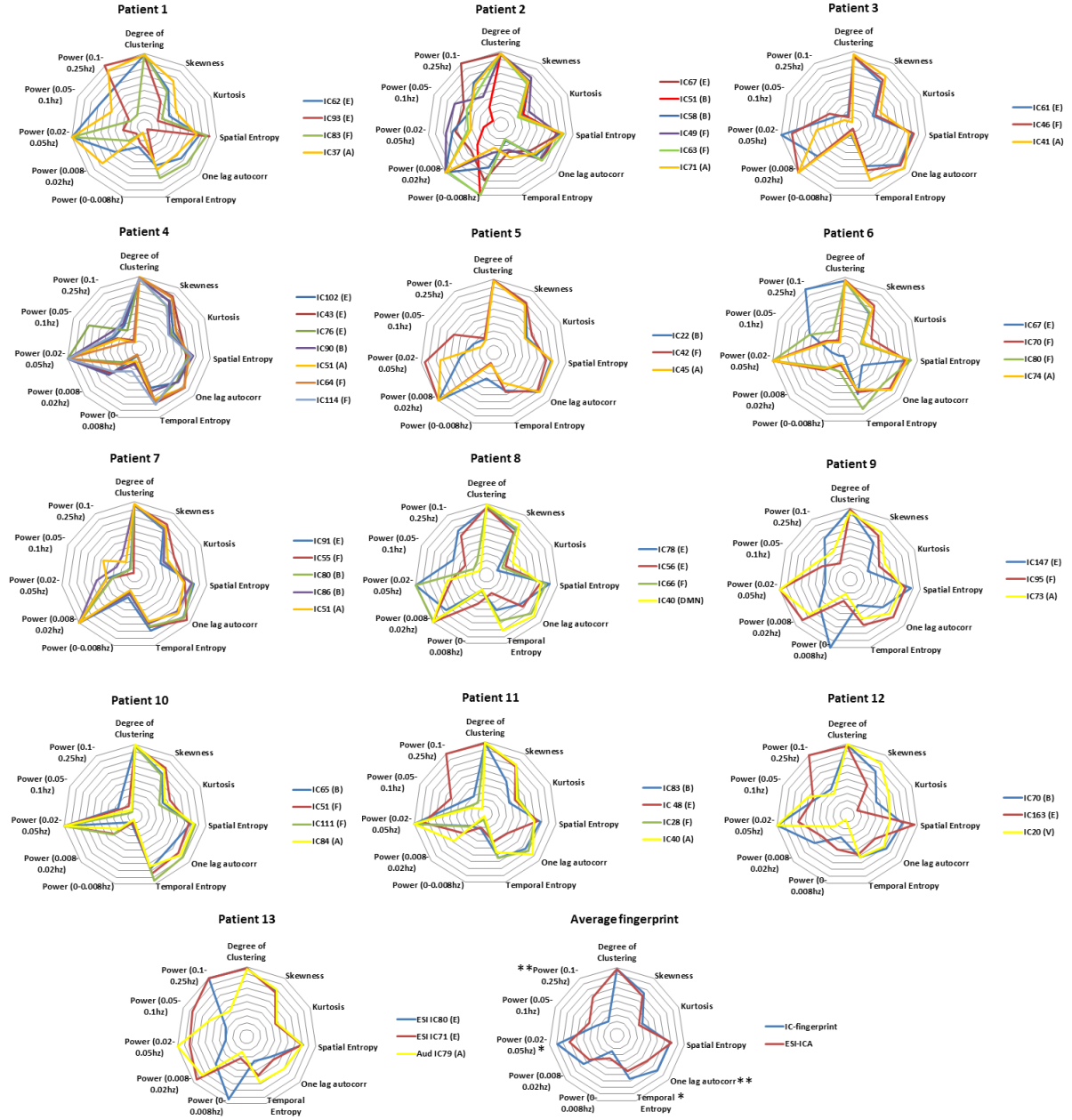


Fig. 5. 5: The IC fingerprint of each IC selected by both methods for all patients are exhibited. The ICs selected by the spatial correlation to ESI map is labeled as E, ICs selected by IC-fingerprint tool labeled as F, those ICs selected by both methods are labeled B, and ICs representing the auditory component are labeled A. The mean fingerprint obtained for the ICs selected by each method is also illustrated. The * highlights the parameters found to be statistically different ($p<0.05$) in the comparison between both methods.

All ICs selected by the IC-fingerprint contained the maximum power in the temporal frequency band from 0.008 to 0.02Hz in patients 2, 3, 5 and 7. For patients 1, 4, 6, 9, 10, 11 and 12 the IC-fingerprint selected ICs presented the highest power in the frequency band from 0.02 to 0.05Hz, and the IC selected for the IC-fingerprint in patient 8 has the highest power in the frequency band from 0.02 to 0.05Hz and also in the band from 0.008 to 0.02Hz. The ICs selected by ESI have the highest power in the band frequency 0.008 to 0.02Hz for patients 2, 5, 7, 8 and 13, in the band frequency 0.02-0.05Hz for patients 1, 3, 4, 6, 8, 10, 11 and 12. In cases #1 (IC93), #2 (IC67), #6 (IC67), #11 (IC48), #12 (IC163) and #13 (IC71) there were ICs selected by ESI-ICA presenting high power values in the highest frequency band (0.1-0.25Hz). Finally, for patients 2 (IC 51, also selected by IC-fingerprint), patient 9 (IC 147) and patient 13(IC 80) there were ICs with the highest power in the frequency band from 0 to 0.008Hz. The polar graphs of both average fingerprints are shown in Figure 5.5. Unpaired t-tests were done to detect the statistically significant differences ($p<0.05$) between each of parameters obtained by the compared methods. The one lag autocorrelation, temporal entropy and the power at the band frequency for 0.02 to 0.05Hz were lower and the power band of 0.1-0.25 was found to be higher for the ESI-ICA components compared to those classified as BOLD components by the classifier.

5.5 Discussion

In this study we analyzed the results of ICA decomposition of fMRI data in 7 patients with focal epilepsy in whom EEG-fMRI analysis provided concordant maps (patients from the category Ia). We also analyzed the ICA decomposition of fMRI data in 4 patients who presented discordant EEG-fMRI maps or no significant results (category Ib). Finally we applied the ICA in fMRI data of two patients with focal epilepsy who did not have IEDs during the EEG-fMRI acquisition, but had at least one IED in data acquired outside the scanner prior to the scanning (category II). Using the spatial correlation between ESI maps and each IC obtained in the fMRI decomposition we selected 25 ICs judged to be spatially related to the epileptic focus. We also selected ICs using an automated component classification (IC-fingerprint tool), which selected 24 ICs. We validated these ICs with the patient's clinical information, MRI findings and surgery outcome (in those subjects where it was available). However, only 9 ICs were

selected by both methods, by comparing the features of the ICs selected by each method demonstrated differences in four of the eleven descriptive features used by the IC-fingerprint tool to classify components as BOLD related. This suggests that IED-related ICs require a different classifier and that they show greater variability particularly in their temporal frequency characteristics. This might be explained by the unconstrained nature of IEDs and corresponding event-related model.

The IC-fingerprint found ICs strongly hypothesized to be related to epilepsy in patients 4 (IC64) and 7 (IC86), and clearly related to the surgery cavity of seizure free patients, such in patients 10 (IC65) and 12 (IC70). However it misclassified other very strong epilepsy-related (related to the surgery cavity of Engel I outcome) ICs, such as in patients 1 (IC62), 8 (IC56), 11 (IC48) and 13 (IC80). Regions such as the insula and thalamus were also found, both are frequently considered to be related to the epileptic network in TLE and so should not be considered artefactual despite being potentially unhelpful for surgical targeting (Aghakhani et al., 2006 and Isnard et al. 2000). The IC-fingerprint found two maps related to these regions, in patient 11 (IC83) and in patient 10 (IC51), however it misclassified ICs related to these regions in patients 4 (IC43 and 76), 7 (IC91), 8 (IC78) and 13 (IC71). We also found instances where the classifier sometimes missed ICs potentially related to the IZ even in patients who presented a worthwhile improvement (Engel III) as surgery outcome. For example in the patient 3, the IC #46 was selected by IC-fingerprint tool and was related to the surgical cavity. However the IC-fingerprint misclassified the IC61 (Fig. 5.3), which was spatial discordant to the surgical cavity and could represent the difference between SOz and IOZ given that the patient still has seizures. Finally we also found evidence for the detection of epileptic-related activity mixed with physiological noise as reported by a previous study (Rodionov et al., 2007). This was noticed in patient 7 (IC 55), where the IC-map (Fig. 5.4) consists of a large cluster of activated voxels close to the transverse sinus and to the vein of Labbé and a small cluster in left the temporal pole suggesting that this IC is more closely related to BOLD response of brain's vascular system (Kim and Ogawa, 2012) than to a temporal lobe epileptic activity.

Most of the differences between the ICs selected or not selected by the classifier were found to be related to the power over the different signal band frequencies

considered by it. The IC-fingerprint tool is a classifier derived from training a Support Vector Machine algorithm by an expert user with datasets from healthy volunteers (De Martino et al. 2007). It considers that a task-related BOLD IC may exhibit the highest power in the frequency bands from 0.008 to 0.02Hz and from 0.02 to 0.05Hz, a high degree of clustering, high one lag autocorrelation, high temporal and spatial entropies (De Martino et al. 2007). The power band of 0.1-0.25Hz is often found to have a strong element of physiological noise. However the ICs selected by ESI in patients 1 (IC93), 2 (IC67), 6 (IC67), 11 (IC48), 12 (IC163) and 13 (IC80 and IC71) are concordant with the clinical information and the surgery area. For all the patients in the category Ia, the ICs selected by ESI had the highest temporal correlation with the GLM-predictor. Particularly for the patient 1 (IC62) and patient 6 (IC67), the ICs are spatially consistent with the surgical cavity that rendered the patients seizure free outcome, indicating that these components are epilepsy-related. Despite this they did not show the pattern of a task-related BOLD IC used by the IC-fingerprint classifier (Fig. 5.5). Based on the ICs ESI-selected spatial maps and their relation to the surgery area we can hypothesize that the BOLD frequency of epilepsy patient may be different in some cases and that the IC-fingerprint tool may misclassifies these epilepsy-related ICs. This hypothesis is supported by the ICs found to be related to the patient clinical information and surgery area/outcome, such as in cases (ICs 51 and 58 of patient 2, IC147 of patient 9 and all ICs in patients 5 and 7) where the frequency band with the highest, or the second highest (IC80 of patient 13) power was in different bands (0-0.008hz or 0.1-0.25hz), instead of the classifier defined BOLD frequency bands. There were ESI-selected ICs presenting lower power in the 0.02-0.05Hz frequency band, also supporting our hypotheses. It is of note that given this frequency range of plausible IED related components the standard application of high pass filters designed for cognitive task-based fMRI could remove significant signal in addition to noise components. The reduced one lag autocorrelation for the ESI-selected ICs could be explained by the unconstrained nature of IEDs producing a BOLD time course with less predictability than a BOLD response related to normal brain activities driven by controlled task paradigms (used for training by IC-fingerprint tool). The temporal entropy was found to be smaller for the ICs spatial correlated to the ESI map. This might be explained by

considering that although the predictability of an IED-related BOLD response is smaller than a task-related BOLD response (generally block design experiments), the distribution of IEDs tends to be clustered in runs of IEDs in our (predominantly) TLE patients group. Therefore it is plausible to find BOLD responses with a smaller temporal entropy due to IEDs than that expected for the BOLD response related to task-driven brain activity.

The ESI maps were primarily used here for finding ICs hypothesized to be epilepsy related by a source independent of assumptions about the haemodynamic response. However we had noticed that ESI can be an alternative for reducing the dimensionality of the resultant number of ICs produced by the ICA decomposition in epilepsy patients' fMRI data. This is illustrated by the fact that in our analysis we had ICA decompositions resulting in a range of ICs varying between 80 and 225, which were restricted to between 1 and 4 potential epilepsy-related. We also verified that combining ESI and ICA might provide complementary information about epilepsy that would be dubious or even neglected if the methods were used separately. This is supported by the ICs found for patients 1 (IC62), 8 (IC56), 9 (IC147) and 13 (IC80), where the ESI had mapped more regions than a single focal activity and the ICs selected by the classifier were not as well related to the surgery cavity/patient outcome as those obtained by the ESI-ICA combination. One possibility for further investigation is to include the spatial correlation between ESI-IC maps as a feature in a classifier.

Finally we compared the number of patients with epilepsy related maps found by each method (EEG-fMRI, ICA-IC-fingerprint, ESI-ICA) summarized in supplementary material 1 (Table S1.1). The criteria for this comparison followed that applied by Groullier et al (2011) and it is further explained in the supplementary material 1. The classical GLM analysis of EEG-fMRI mapped epileptic related BOLD activities in 7/13 patients, applying the ICA IC-fingerprint we found epileptic-related BOLD activities in 12/13 patients and we found at least one epileptic-related IC for all the patients by the ESI-IC spatial correlation.

It is difficult to define an appropriate measure of specificity for the epilepsy related maps given by the different methods (given the lack of ground truth in many epilepsy cases). However, the specificity of the ICA-based results is lower than for the

EEG-fMRI results. This is because although the ESI or fingerprint reduces the number of ICs there are still typically both multiple maps and maps that could contain results driven by non-epileptic processes. Therefore ICA is capable of mapping epileptic-related activities in cases where the traditional EEG-fMRI cannot. However, one of the current methods applied for selecting the ICs containing these activities currently lacks the required specificity for this task. We had shown that the inclusion of ESI maps as a priori information might be interesting for improving the selection of ICs.

Clinical Significance

The clinical significance of applying ICA on fMRI data of patients with epilepsy is mainly focused on the possibility of mapping the epilepsy related BOLD activities without the needing of strong assumptions for analyzing the data. It would also open the possibility of mapping epileptic BOLD activity without the requirement for simultaneous acquisitions of EEG data, which would widen its application to be available at most centers or to help increase the yield of EEG-fMRI studies with a low number of IEDs during the recording period (Salek-Haddadi et al. 2006). However, validation of methods that can reliably select the ICs related to epilepsy from the ICA decomposition into typically 30-100 components are needed. Among other strategies, the automatic classifier is one of the tools available to select ICs but it was not found here to be reliable for selecting epileptic related BOLD activity. We also used ESI for selecting epileptic related ICs in a few patients, obtaining results that were significantly related to the clinical information and to the resection cavity and outcome where available. However, this method is subject to many of the same limitations as GLM based EEG-fMRI. Therefore our results show that ESI could be used to retrain the automatic classifier to find specific the fingerprint of epilepsy-ICs or even included into the classifier as epilepsy-related information.

5.6 Conclusion

The IC-fingerprint tool was found to not be a reliable approach for selecting IED-BOLD related ICs in EEG-fMRI data of epilepsy patients with or without IEDs during the data acquisition. The features that were different in the epilepsy ICs selected based on comparison to ESI were the one lag autocorrelation, temporal entropy and the

power in two frequencies bands (of 0.02-0.05 Hz and 0.1-0.25). The IC-fingerprint tool used in this work is that it relies on features related to frequency bands that are appropriate for canonical BOLD responses to typical cognitive paradigms in a normal brain, but not appropriate for the unconstrained nature of epileptic discharges. This is because the IC-fingerprint tool is a classifier trained with cognitive fMRI from health volunteers, led us to conclude that this classifier need to be changed to better select epilepsy-related ICs. ESI can help to selected ICs related to epilepsy and it therefore could be helpful to retrain the automatic classifier.

CHAPTER 6 - TWO-DIMENSIONAL TEMPORAL CLUSTERING ANALYSIS FOR PATIENTS WITH EPILEPSY: DETECTING EPILEPSY-RELATED INFORMATION IN EEG-FMRI CONCORDANT AND DISCORDANT PATIENTS

This chapter is related to our objective of providing alternatives of using EEG-fMRI data for mapping BOLD signals related to epilepsy in cases whose EEG-fMRI was impossible or inconclusive.

6.1 Background

The 2dTCA showed promising results mapping BOLD activities related to tasks executed by healthy subjects (Morgan et al., 2009) and also to detect epileptogenic BOLD-related activities in groups of patients with temporal lobe epilepsy without EEG data inside the MR scanner (Morgan et al., 2010). However, the applicability and sensitivity of the method have been questioned when it is applied in individual fMRI datasets of epileptic patients (Khatamian et al., 2011). The authors compared the maps obtained by 2dTCA to those obtained by classical EEG-fMRI. They reported that the classical EEG-fMRI and 2dTCA found similar results when applied in data of patients whose prolonged interictal events have been recorded by the simultaneous EEG. The authors also concluded that 2dTCA would be interesting only for validating the results found by other methods (Khatamian et al., 2011). However, the data analyzed in their study was restricted to patients showing IEDs during the simultaneous EEG-fMRI acquisition and those in which the classic EEG-fMRI was able to map coherent epileptic BOLD activities. Furthermore, none of these studies have considered the negative histograms resulting from decreased BOLD signals in the 2dTCA analysis and their potential to map epilepsy related activity.

6.2 Objective

To our knowledge the 2dTCA has never been evaluated for mapping epileptic-related activity in patients whose fMRI is expected to improve the epilepsy diagnosis, such as in patients with inconclusive (not sensitive/discordant) EEG-fMRI results, or those where the EEG-fMRI analysis is not possible (patients with no IEDs during fMRI acquisition). Besides that, 2dTCA is often based on the detection of positive variations,

in relation to the baseline of T2* signals. Here, we propose to evaluate and compare the sensitivity of classic EEG-fMRI and 2dTCA methods to localize epileptic activity in a group of focal epilepsy patients with and without IEDs presented during simultaneous EEG-fMRI acquisition as a more objective measure of their general usefulness in individual presurgical evaluations. To do this we will discuss the differences and similarities between EEG-fMRI and 2dTCA resulting maps. In addition, the evaluation will include 2dTCA maps resulting from both negative and positive histograms in order to discuss whether negative histograms provide useful information about epilepsy. Finally, as a secondary aim we hope to provide some guidelines or suggestions on the implementation of these approaches.

6.3 Methods

6.3.1 Patient description

We acquired EEG-fMRI data of patients with focal epilepsy from the Ribeirão Preto Epilepsy Surgery Center. Patients were enrolled during pre-surgical evaluation following previously described protocols (Velasco et al. 2011), which is based on video-EEG, MRI, *foramen ovale* electrodes, SPECT and PET. A total of 20 patients (13 M, mean = 39 yrs \pm 13 yrs) (Table 6.1) were considered eligible by the following selection criteria: (1) the surgery follow up six months after surgery was Engel score I and (2) no large head movement (fMRI data with movements greater than 2 mm volume-to-volume, based on realignment parameters, were excluded). The study was approved by the local Medical Ethics Committee of the Clinical Hospital of Ribeirão Preto and written informed consent was obtained from all patients.

Table 6. 1. Patient information

Patient	MRI findings	VEEG localization	Surgery Location	#of IEDs on EEG-fMRI	
Frequent IEDs (Group I)					
1	RFGN	R Frontal	RFL	66R	15R
2	LHA	L Parietal	LCH	60L	82L
3	RMTS	R Temporal	RTL	19L	10L
4	LDW_LFG	L Frontal	LFL	22L	-
5	RMTS	R Temporal	RTL	104R	84R
6	LMTS	L Temporal	LTL	42L	54L
7	RMTS	R Temporal	RTL	23R	30R
8	RMTS	R Temporal	RTL	-	16R
Infrequent IEDs (Group II)					
9	LMTS	L Temporal	LTL	7L	5L
10	RMTS	R Temporal	RTL	1L 1R	1L 2R
11	CA	R Temporal	RTL	1R	7R
12	LMTS	L Temporal	LTL	1L	3L
13	RMTS	R Temporal	RTL	7R	-
No IEDs visually detected (Group III)					
14	LMTS	L Temporal	LTL	0	
15	RFGN	R Frontal	RFL	0	
16	LMTS	L Temporal	LTL	0	
17	RMTS	R Temporal	RTL	0	
18	RMTS	R Temporal	RTL	0	
19	RMTS	R Temporal	RTL	0	
20	RMTS	R Temporal	RTL	0	

IEDs – interictal epileptic discharges during EEG-fMRI (2 runs per patient), R - Right, L - Left, B - Bilateral, FL - Frontal Lesionectomy, LCH-Left Central Hemisphere, TL - Temporal Lesionectomy, MTS - Mesial Temporal Sclerosis, CA - Cavernous Angioma, LDWG_LFG - Low differentiation between white and gray matter in left frontal gyrus, RFGN - Right frontal glial neoplasia. HA - Hemispheric Atrophy. The “-” indicates fMRI run excluded due to excessive head movement. Grouping characteristics described in the text.

6.3.2 MRI acquisition

All images were acquired at Hospital das Clínicas, Ribeirão Preto, São Paulo, Brazil using a 3.0T Achieva MRI scanner (Philips Healthcare, Best, Netherlands). The T2* weighted gradient-echo echo-planar imaging (EPI) sequence was acquired using an eight channel SENSE head coil with the following parameters: 32 ascending slices (2.8x2.8x4 mm³) covering the whole brain without slice gap, slice/volume TR =

62.5/2000 ms, TE = 30 ms, flip angle = 90°. Each fMRI run was composed of 600 volumes, obtained in 20 minutes. All patients were instructed to keep their eyes closed during the fMRI acquisitions. High resolution T1-weighted anatomical images were acquired with a 3D-TFE sequence: TR/TE = 6.75/3.1 ms, FA = 8°, inversion delay = 900 ms, shot interval=2000 ms, isotropic voxels of 1 mm and SENSE = 1.

6.3.3 EEG data acquisition and processing

EEG was recorded using an MR-compatible EEG system (Brain Products, Gilching, Germany). A 63-electrode (Ag/AgCl, internal resistance of 5kΩ and reference at FCz) EEG cap (Easycap, Herrsching, Germany) was used according to the 10-10 international system. An additional channel for ECG was recorded in order to remove physiological artifacts. Gradient and pulse artifacts were removed offline using the average artifact subtraction method (Allen et al. 1998; Allen et al. 2000). The gradient artifact-corrected EEG data were down sampled from 5000Hz to 250Hz. The IED times were identified and marked by an experienced neurophysiologist. The IEDs were grouped based on their laterality.

We classified the patients into three different groups according to the number of IEDs identified by the neurophysiologist. This classification was based on a previous study (Saleki-Haddadi et al., 2006) where the authors reported EEG-fMRI to detect epilepsy-related BOLD changes in a patient who had 12 IEDs detected during simultaneous EEG-fMRI acquisition of 35 minutes. Our runs were composed of 20 minutes of EEG-fMRI acquisition, therefore a comparable number of IEDs to our study would be 7. Here, we considered any patient presenting more than 7 IEDs in a single hemisphere in one run of EEG-fMRI acquisition as a frequent IED patient in order to group the patients as follows:

I - Frequent IEDs: Eight patients presenting more than 7 IEDs in a single hemisphere in a single run of the simultaneous EEG-fMRI acquisition were included in this group.

II - Infrequent IEDs: Five patients presenting between 1 and 7 IEDs in a single hemisphere during a single run of the simultaneous EEG-fMRI were included in this group.

III - No IEDs visually detected: Seven patients did not have any IED detected during the simultaneous EEG-fMRI acquisitions and were included in this group.

6.3.4 Images pre-processing

All image pre-processing was done in SPM 12 (<http://www.fil.ion.ucl.ac.uk/spm/software/spm12>) using Matlab 2013a (The MathWorks, Natick, USA). The fMRI data were corrected for slice timing artifact, motion corrected, co-registered to the anatomical images and spatially normalized to the MNI atlas. The anatomical images were also normalized to the MNI atlas and segmented into white and grey matter. The latter was used for generating a mask for including only voxels within the grey matter, which were further analyzed by 2dTCA and EEG-fMRI. The fMRI images were interpolated to iso-voxels (3x3x3 mm³), spatially smoothed by a Gaussian filter of FWHM = 6 mm and temporal high-pass filtered at 0.008 Hz.

6.3.5 fMRI analysis by two-dimensional Temporal Clustering Analysis (2dTCA)

As described by previous studies (Morgan et al., 2008; Khatamian et al., 2011) the 2dTCA method applies two steps for excluding background and non-interesting voxels before clustering them temporally (see Morgan et al., 2008 for more details). The first step is to exclude voxels showing T2* fluctuations outside an expected BOLD-response range, which is established by the user. Here, we assumed this range to be between 0.5-8 percent of BOLD signal mean through time. Previous studies (Morgan et al., 2010; Khatamian et al., 2011; Lopes et al., 2012) considered thresholds similar to ours, however they were interested only in positive changes. Here, we applied 2dTCA algorithm for both positive and negative fluctuations. The second step is to exclude all voxels that do not have transient changes larger than 1.5 standard deviations of their temporal average when all volumes acquired are considered. Both thresholds were chosen based on the BOLD-related fluctuations expected to be detected by fMRI studies (Handwerker et al., 2004) and also due to the interest in detecting transient (spike) BOLD activities using 2dTCA. The 2dTCA is a data-driven method which does not require the simultaneous EEG data; therefore, all the 20 patients were analyzed with this method.

The output of the 2dTCA algorithm is a set of histograms indicating number of voxels meeting the above two criteria (0.5 to 8% signal change and greater than 1.5 standard deviations above the temporal mean) at each TR. The length of the histogram is the number of TRs in one run. Different timing profiles are represented by different histogram outputs; therefore, multiple histograms are created per run. The resulting histograms were then used individually as temporal predictors for applying the general linear model (GLM) in SPM 12. We included the motion effects (using the 6 scan realignment parameters) as confounds for the GLM analysis.

6.3.6 Classical EEG-fMRI analysis: predictor construction

Thirteen patients from groups I and II had IEDs recorded during EEG-fMRI; therefore, they were included in the classical EEG-fMRI analysis. For each patient and type of IED, a predictor was modeled as stick functions convolved with the canonical hemodynamic response function (Glover et al., 1999). For patients #1, #2, #4, #5, #7, #9, #11, #12 and #13 we obtained only one predictor per run of fMRI, due to the unilateral discharges presented during the EEG-fMRI acquisition (Table 6.1). However, for patients #3, #6 and #10 we derived between one and three predictors, depending on the presence of bilateral discharges in each run acquired (Table 6.1). For example, patient #3 had only left discharges in the first run and so only one predictor was obtained for that run; however had bilateral discharges during the second run resulting in one predictor considering right discharges, one considering left and one considering right and left together. We also included the motion effects (using the 6 scan realignment parameters) as confounds for the GLM analysis. The GLM was applied to each predictor individually.

6.3.7 Computing t-score maps

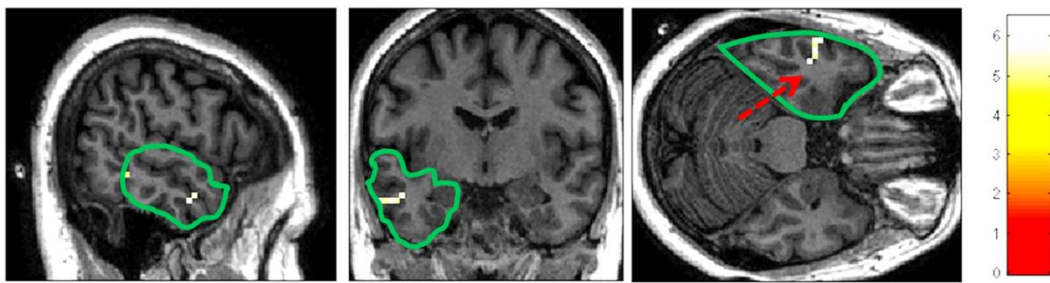
For both methods (IED-based or 2dTCA histograms), we only evaluated maps with $t > 0$. This was done based on the assumption that the positive BOLD response related to epileptic sources is more likely to correspond to electro-clinical findings than the negative BOLD changes, as reported by others studies (Salek-Haddadi et al., 2006; Rodionov et al., 2007). This means that for the negative 2dTCA histograms the GLM analysis identified any positive BOLD changes concurrent with transient focal negative

BOLD spikes. The t -maps produced by each approach were initially thresholded at t -values with equivalent $p(\text{FWE corrected}) < 0.05$ and cluster size $k > 5$. However, this threshold was observed to be very restrictive for the IED-derived EEG-fMRI maps, resulting in few maps with supra-threshold voxels (only one concordant to patient's epilepsy information). Therefore, we assumed a threshold of $t > 3.1$ (equivalent to $p < 0.001$, uncorrected) for the maps produced by classical EEG-fMRI. Then, we evaluated the number of resultant maps for the two different significance thresholds and for various cluster size thresholds of 5, 10, 15 and 30 voxels.

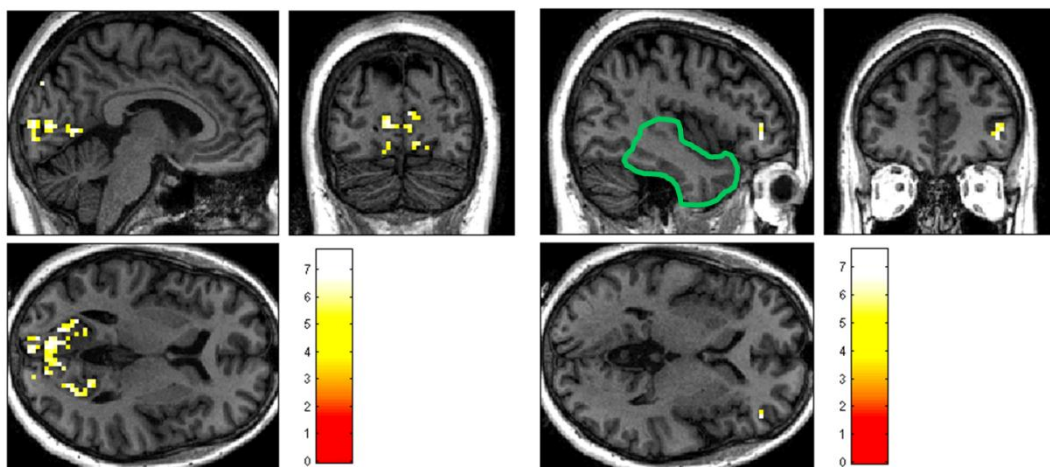
6.3.8 Classifying t -score maps

All t -maps obtained for each run/patient were visually classified into five categories as follows: (1) Epilepsy concordant maps, as described below in section 2.9; (2) Resting state networks (RSN) related maps according to literature (Damoiseaux et al., 2006; De Luca et al., 2006); (3) Discordant maps presenting consistent activation of clusters mapping gray matter regions different than RSN related regions or the surgery cavity; (4) Artefact related maps were selected based on previous descriptions (De Martino et al., 2007), where maps related to motion residual artefacts, EPI susceptibility artefacts, vessel artefacts (e.g. physiological related, presenting peaks at large vessels) and also maps showing high levels of spatially distributed noise were considered as artefact-related; (5) Not sensitive or informative maps which were maps not presenting supra-threshold voxels or presenting supra-threshold voxels spread all over the brain (e.g. in white matter, ventricles and cerebellum). An example of each category is illustrated (Figure 6.1) for patient #10, a left temporal lobe epilepsy patient.

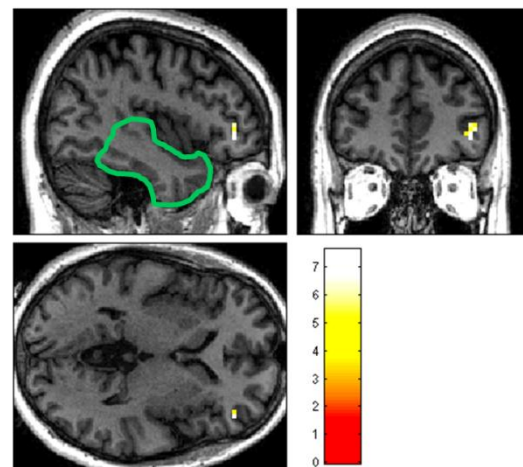
Epilepsy-related



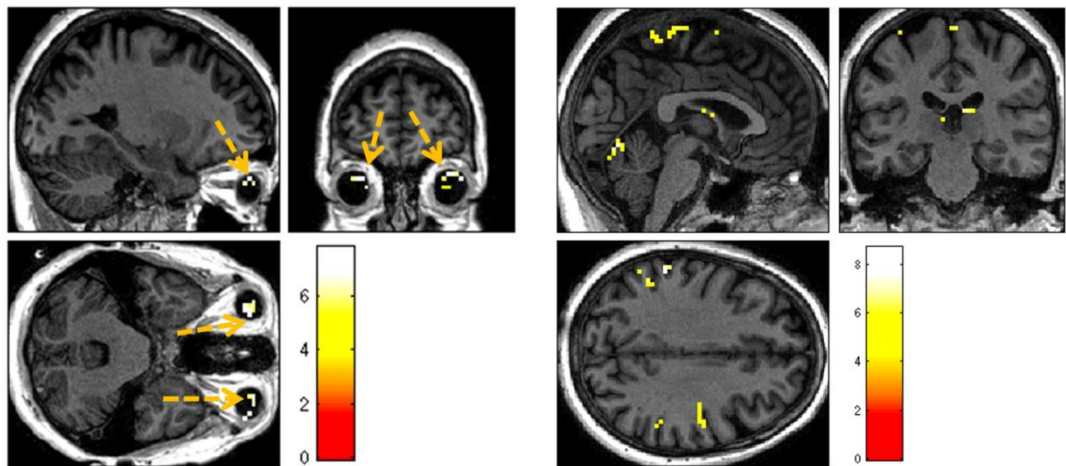
RSN-related



Discordant



Artefact-related



Not informative

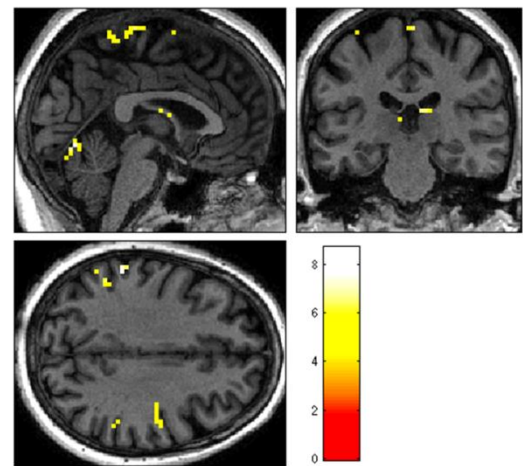


Fig. 6. 1. The five categories considered for classifying the t-score maps. The images are presented in neurological convention (right on right). The t-score maps are threshold at $p(\text{FWE}) > 0.05$ and with a minimum cluster size $k > 5$. The borders of the surgical resection are shown in green, and the cluster matching the

concordant criteria is indicated by the red arrow. The RSN-related map illustrates a visual activation. Artefactual activations are indicated by orange arrows.

6.3.9 Epilepsy concordant maps

Each t-map was evaluated based on its concordance to the surgery location and the surgery outcome (Engel score I for all patients) of each patient. The concordance was evaluated by adapting a procedure previously applied by others (Grouiller et al., 2011, Maziero et al., 2015). We compared the first, second and third global maxima of each t-map produced by both approaches and its relation to the surgery cavity/indication and surgery outcome. We considered the epilepsy-related area as the resection area and its immediate proximity, which was assumed to be 15 mm from resection margins/indication and within the same sublobar cortical region. Therefore, any map presenting from the first to the third t-maximum cluster inside this region was considered as epilepsy-related, the cluster matching the criteria was called epilepsy-concordant cluster.

6.3.10 Temporal analysis of concordant clusters

The fMRI time courses from each voxel within the epilepsy-concordant cluster resulting from 2dTCA were extracted from the fMRI data of each patient. This process resulted in the so-called 2dTCA-concordant time courses (2dTCA-tcs). The time courses were used for calculating the temporal correlation between 2dTCA-tcs and the EEG-based temporal predictor determined by convolving the IEDs with the hemodynamic response function were computed. This was done in order to determine whether the maps resulting from 2dTCA were BOLD responses related to the IEDs detected by the scalp EEG. This was only computed for the patients from Groups I and II (IEDs detected while scanning). The analyses were done in Matlab 2013a (The MathWorks, Natick, USA).

6.4 Results

We analyzed data of twenty patients with focal epilepsy whose surgery outcome was Engel I (Table 6.1). The 2dTCA analysis was performed on all 20 patients. Thirteen of these patients showed IEDs during the simultaneous EEG-fMRI acquisition and had classic EEG-fMRI analysis performed. The classic EEG-fMRI analysis best

performance (Table 6.2) was for the smallest threshold ($p(\text{unc})<0.001$ and $k>5$ voxels). Of the six patients with epilepsy concordant maps, five patients were from group I (frequent IEDs) and one patient from group II (infrequent IEDs). The 2dTCA had its best performance at the threshold level of $p(\text{FWE})<0.05$ and $k>5$ voxels (Table 6.2), The 2dTCA analysis resulted in epilepsy-concordant maps for fourteen patients in its best performance (Table 6.2). The 2dTCA epilepsy concordant maps were resultant from six patients from group I, four patients from group II, and four patients from group III. The 2dTCA method mapped epilepsy-related activity in four of the five patients in whom the classic EEG-fMRI analysis produced concordant maps.

Table 6. 2. Number of concordant maps for different thresholds

	2dTCA (N=20)									
	$p(\text{unc})<0.001$					$p(\text{FWE})<0.05$				
k-threshold	5	10	15	30	60	5	10	15	30	60
#patients	13	13	13	14	10	14	11	10	8	6
1 st max	9	9	9	8	6	9	8	6	5	4
2 nd max	1	1	1	1	2	1	1	2	2	1
3 rd max	3	3	3	6	2	4	2	2	1	1
EEG-fMRI (N=13)										
#patients	6	3	3	2	1	1	2	2	1	1
1 st max	3	2	2	1	1	1	1	1	0	0
2 nd max	1	1	1	1	0	0	1	1	1	1
3 rd max	2	0	0	0	0	0	0	0	0	0

N is the number of patients in which each analysis method was applied. Bold indicates threshold with best performance used for method comparison.

The number of activation maps resultant from 2dTCA considering all patients and runs was 194 ranging from 3 and 16 per patient (Table 6.3). Considering our classification categories, the method generated 18/194 epilepsy concordant maps, 37/194 discordant, 26/194 related to RSN, 43/194 related to artefacts and 70/194 not informative or not sensitive maps. From the 18 epilepsy concordant maps 11 were obtained from negative histograms. For the EEG-fMRI analysis there were 31 maps distributed between 1 and 6 per patient (Table 6.3), considering 13 patients. Considering our classification categories the method produced 6/31 epilepsy concordant maps, 15/31 discordant, 3/31 artefact related maps and 7/31 were not informative or not sensitive maps.

Table 6. 3. Number of maps classified into the different categories

<i>2dTCA (maps thresholded at p(FWE)<0.05 and k>5)</i>						
Patient	# of maps	# of concordant maps	# of discordant maps	# of RSN-related maps	# of artefact-related maps	# not informative/sensitive map
Frequent IEDs (Group I)						
#1	8 (4N)	0	2 (1N)	0	5 (3N)	1
#2	8 (3N)	1	2	0	3 (2N)	2 (1N)
#3	16 (10N)	3 (1N)	7 (1*)(4N)	0	0	6 (3N)
#4	3 (1N)	1 (1N)	1	0	1	0
#5	15 (8N)	1	2 (2N)	4 (2N)	3 (3N)	5 (1N)
#6	9 (4N)	1 (1N)	0	0	1 (1N)	7 (3N)
#7	13 (6N)	2 (1N)	2 (1N)	0	0	9 (4N)
#8	3 (2N)	0	2 (2N)	0	0	1
Infrequent IEDs (Group II)						
#9	12 (6N)	1 (1N)	1*	1	4 (3N)	5 (2N)
#10	11 (6N)	0	3 (2N)	0	2 (1N)	6 (3N)
#11	13 (8N)	2 (1N)	2 (1N)	5 (2N)	4 (4N)	0
#12	13 (6N)	1 (1N)	3 (1*)	3 (1N)	3 (2N)	3 (2N)
#13	11 (6N)	1 (1N)	0	4 (1N)	1	5 (4N)
No IEDs visually detected (Group III)						
#14	5 (3N)	1 (1N)	0	0	0	4 (2N)
#15	8 (3N)	0	1	3 (2N)	2 (1N)	2
#16	12 (5N)	0	2 (1N)	3 (2N)	5 (2N)	2
#17	4 (2N)	1 (1N)	1 (1N)	0	0	2
#18	11 (5N)	1 (1N)	2	3 (1N)	3 (3N)	2
#19	10 (4N)	0	1**	0	4 (3N)	5 (1N)
#20	9 (2N)	1	3 (1*)(1N)	0	2	3 (1N)
<i>EEG-fMRI (maps thresholded at p(unc)<0.001 and k>5)</i>						
Frequent IEDs (Group I)						
#1	2	1	1	0	0	0
#2	2	0	0	0	0	2
#3	4	1	2	0	0	1
#4	1	0	1	0	0	0
#5	2	1	1	0	0	0
#6	4	0	1	0	3	0
#7	2	1	1	0	0	0
#8	1	1	0	0	0	0

Infrequent IEDs (Group I)						
#9	2	0	2	0	0	0
#10	6	0	4	0	0	2
#11	2	0	2	0	0	0
#12	2	0	0	0	0	2
#13	1	1	0	0	0	0

N indicates the number of maps resultant from negative histograms; * indicates maps showing from 1st to 3rd maxima on temporal lobe network structures (e.g. insula and thalamus); ** indicates maps showing from 1st to 3rd maxima on contralateral temporal lobe, for TLE patients.

6.4.1 Frequent IEDs (group I)

The number of IEDs detected in the run where each method provided epilepsy-related maps varied from 16-84 for 2dTCA and from 16-104 for the classic EEG-fMRI results (Table 6.1). Some examples are shown in Figure 6.2. Both methods provided epilepsy-related maps for patients #3, #5 and #7. For both methods we also verified significant t-score clusters not related to the surgery cavity in some cases.

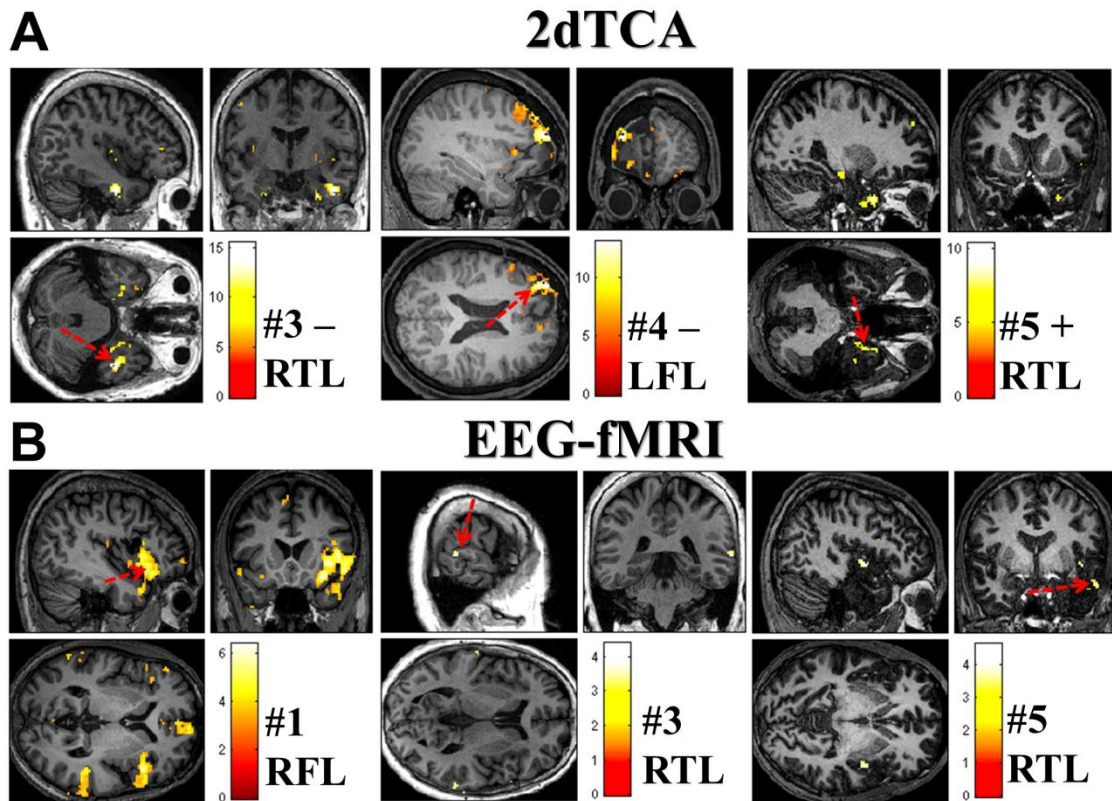


Fig. 6. 2: BOLD maps of patients from the group I (frequent IEDs). A) The epilepsy-related maps found by 2dTCA ($p(\text{FWE}) < 0.05$ and cluster threshold of 5 voxels), and B) the epilepsy-related maps found by classic EEG-fMRI

($p(\text{uncorrected}) < 0.001$ and cluster threshold of 5 voxels). The cluster matching the concordance criteria is indicated by the red arrow. For each patient, the signals + or - indicate whether the map was resultant from a positive or a negative histogram, respectively. The surgery location is described for each patient. For patients #1, #4 and #5 the maps are overlaid on their postsurgical anatomical image.

6.4.2 Infrequent IEDs (group II)

The number of IEDs detected in the run where the 2dTCA provided the epilepsy-related maps varied from 3-7 and from 1-7 for the classic EEG-fMRI results (Table 6.1). Some examples are shown in Figure 6.3. Both methods provided epilepsy-related maps only for patient #13. For both methods we also verified significant t-score clusters not related to the surgery cavity in some cases.

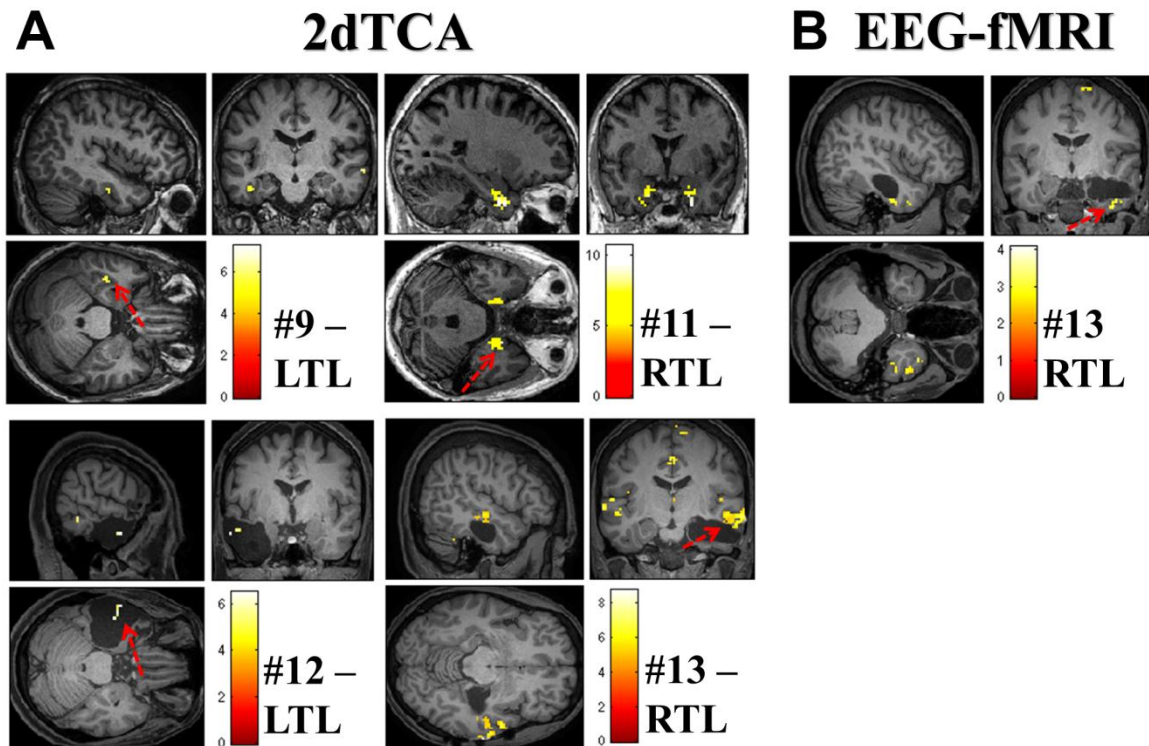


Fig. 6. 3: 2dTCA BOLD maps of patients from the group II (infrequent IEDs) ($p(\text{FWE}) < 0.05$ and cluster threshold of 5 voxels). The cluster matching the concordance criteria is indicated by the red arrow. For each patient, the signals + or - indicate whether the map was resultant from a positive or a negative histogram, respectively. The surgery location is described for each patient. For patients #12 and #13 the maps are overlaid on their postsurgical anatomical image.

6.4.3 No IEDs visually detected (group III)

The 2dTCA provided epileptic-related maps for 4 out of 7 patients without IEDs on the EEG-fMRI acquisition (Fig. 6.4). The classic EEG-fMRI could not be performed due to the absence of IEDs in the EEG data acquired simultaneously to the fMRI. Three out of four epilepsy related maps in this group came from negative 2dTCA histograms.

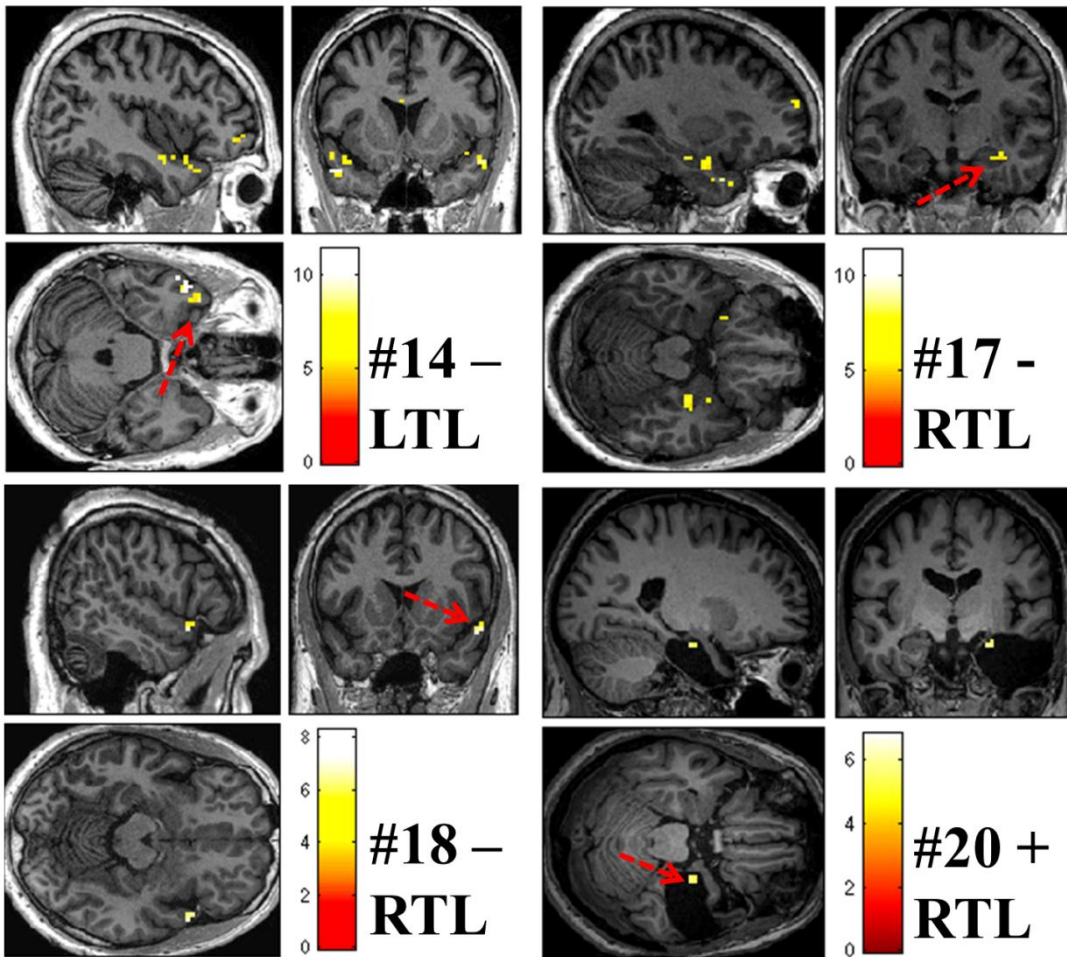


Fig. 6. 4: 2dTCA BOLD maps of patients from the group III (No IEDs visually detected) ($p(\text{FWE})<0.05$ and cluster threshold of 5 voxels). The cluster matching the criteria is indicated by the red arrow (1st global maximum in all patients). For each patient, the signals + or - indicate whether the map was resultant from a positive or a negative histogram, respectively. The surgery location is described for each patient. For patient #20 the maps is overlaid on patients' postsurgical anatomical image

6.4.4 Temporal correlation between each 2dTCA-tc and EEG-based predictor

From ten patients (Groups I and II) there were 14 epilepsy-related maps resulting from 2dTCA, only two had significant temporal correlation ($p < 0.05$) between the 2dTCA-tcs and the EEG-based temporal predictor. These patients were the #2 (run 1, $R=0.14$ and $p=0.001$) and #3 (run 1, $R=0.13$ and $p=0.002$) which both had frequent IEDs.

6.5 Discussion

In this work we systematically compared EEG-fMRI and 2dTCA (based on positive and negative histograms) for localizing interictal epileptic activity non-invasively with MRI. Accuracy was based on spatial concordance with surgical resection area in these patients with Engel I seizure free outcome. The classical EEG-fMRI analysis produced 6/13 concordant maps considering the patients from groups I (frequent IEDs) and II (infrequent IEDs), this percentage is consistent with a previous study (Thornton et al., 2010), where the authors reported a concordance between EEG-fMRI maps and the seizure onset region in 33% of their patients in whom IEDs were detected during the simultaneous EEG-fMRI acquisitions. The classic EEG-fMRI analysis was not applied to 7 of our patients, due to the absence of IEDs recorded during the simultaneous acquisition. On the other hand, the 2dTCA analysis provided concordant maps in 14/20 patients, 10 from the groups I (frequent IEDs) and II (infrequent IEDs) and 4 from the group III (no IEDs). In four patients (#3, #5, #7 and #13) both methods did provide epilepsy concordant maps, while in two patients (#1 and #8) was EEG-fMRI alone successful. A previous study (Khatamian et al., 2011) reported that 2dTCA has a poor performance in mapping the regions mapped by the classical EEG-fMRI analysis for patients with few IEDs recorded by the simultaneous EEG. In our results, we verified that 2dTCA provided concordant maps in 4/5 patients from group II, which is inconsistent with the previous report. We believe that the primary reason for this difference is based on the patient inclusion criteria applied in their study, where only patients with concordant EEG-fMRI maps were included in the analysis.

Another difference between this study and previous ones implementing 2dTCA and EEG-fMRI is the use of negative histograms. This refers to the search for fMRI signals that have specific negative percent signal change and decrease in signal below the mean through time (negative transient signal changes). In this work, the 2dTCA was used to calculate the negative histograms, and then concurrent positive BOLD changes were identified with the $t>0$ contrast in the GLM. In doing such, smaller regions of increased signal were identified that corresponded in time with larger regions of decreased signal detected by the 2dTCA algorithm (which is biased towards spatially large signal changes). The idea that positive and negative BOLD responses to epileptic activity are sometimes concurrent was described by Kobayashi et al. (2006). Their work and others' (Salek-Haddadi et al., 2006; Rodionov et al., 2007) suggested that widespread deactivations (negative signal changes) concurrent in time with activations (positive signal changes) may illustrate the effect of the epileptic discharge on the rest of the brain, and are remote to the epileptic activity. Our results show that in 8 patients only the negative histograms yielded positive activation concordant with the resection region which further supports this theory. Three patients had both a positive and negative histogram that were concordant (patients #3, #7 and #11), while 3 patients had positive histograms alone which were concordant with the resection. More work is needed to characterize the differences between the negative and positive histograms and BOLD signal changes.

Our results have consistently shown evidences that the epilepsy-related information detected by each method may be different. Firstly, we have noticed that only 4/13 patients presenting IEDs were mapped by both methods, even in such cases the spatial overlap among the areas mapped by each of them are small or even nonexistent. Secondly, there were temporal correlation between 2dTCA-tcs and EEG-based temporal predictor in only two patients (patients #2 and #3). However none of these temporal correlation were strong (highest $R=0.14$).

The fMRI data analysis is strongly dependent on thresholding the statistical maps. Although some statistical conventions are often applied, such as for p -value <0.05 , it is often complicated to set a threshold capable of correcting the multiple comparisons without being too restrictive of the data; and even more complicated when

different analysis methods are compared. In our study we set the thresholds individually for each method based on the performance of each at different thresholds ($p(\text{uncorrected}) < 0.001$ and $p(\text{FWE}) < 0.05$) and the minimum number of voxels composing a cluster (5, 10, 15, 30 and 60) above that threshold. In our results, the 2dTCA presented a better performance at a threshold of $p(\text{FWE}) < 0.05$ (Table 6.2) and the classic EEG-fMRI at $p(\text{unc}) < 0.001$. We believe that this difference is due to 2dTCA data driven assumption that only considers the T2* variations and looks for times at which large numbers of voxels are spiking in signal intensity together. On the other hand the EEG-fMRI analysis is based on the fusion between IEDs-detected by EEG and the assumption of a related HRF detected by the T2* variations, which might reduce its statistical power due to the many assumptions related to the neuro-vascular coupling for its application. It is important to note that even if only the 1st global maximum of the map is considered, there are concordant maps in 9/20 patients for the 2dTCA analysis. It is also important to note that independently of the threshold applied (Table 6.2), the 2dTCA analysis provided a higher number of epilepsy-related maps than the EEG-fMRI, and also that usually the patients/regions mapped were not the same.

One of the most challenging issues in EEG-fMRI analysis of patients with epilepsy is dealing with patients with no concurrent IEDs during the fMRI (Group III). There are a few approaches for dealing with this issue, such as the method proposed by Gruiller et al (2011). In their approach, the authors proposed using the averaged IED topography from out of scanner EEG acquisitions for producing a correlation-based predictor based on the spatial correlation between that topography and the topography of each EEG time point acquired simultaneously to the EEG. However, this approach has the tradeoff of needing the detection of a considerable number of IEDs outside the scanner to provide adequate signal to noise ratio for the averaged topography. This may be rare in patients such those from group III, who are often submitted to up 72-100 hours of video-EEG and often have just a few IEDs detected by the EEG and visually coded by the neurophysiologists. Besides that, IEDs generated by deep structures of the brain (such as mesial temporal lobe) can be neglected by scalp-EEG (Velasco et al., 2006; Tao and Baldwin 2007), which might also decrease the approach's sensitivity. On the other hand, the 2dTCA is a data driven method capable of mapping epileptic-related

BOLD activity independent of the detection of IEDs. This is illustrated by the results obtained for patients from group III (Fig. 6.4), where concordant maps were found.

Data driven methods often result in multiple maps when they are applied to fMRI data of epilepsy patients. The number of maps increases the difficulty of choosing which map is derived from the BOLD signal related to the electrical activity of interest. Methods such as ICA might result in over 200 maps per fMRI run (Rodionov et al., 2007, LeVan and Gotman, 2009; LeVan et al., 2010; Maziero et al., 2015). In our study the 2dTCA algorithm produced between 3 and 16 maps per subject. The number of maps produced for 2dTCA is considerable (194 considering all the patients and runs), but they were dramatically reduced by a visual verification where RSN-related, artefactual, not informative and not sensitive maps were excluded. The most difficult discriminations were required to separate the 55 remaining maps into epilepsy concordant and discordant. However, as any other pre-surgical evaluation method applied to epilepsy, the convergence of 2dTCA with other information such as EEG and MRI (when a lesion is detected) was verified to be helpful and interesting. We believe that the use ESI might help in such task. However ESI accuracy lies on many parameters, such as the number of electrodes used for acquiring the data and also the method chosen for calculating the electromagnetism inverse problem (Maziero et al., 2014), which is a topic for further investigation.

Even EEG-fMRI, which is not a data driven approach, often results in multiple maps. For example, in patients showing bilateral discharges during the acquisition such as #3, #6 and #8 (Table 6.1) we analyzed three resultant EEG-fMRI maps (one considering only right temporal IEDs, one considering left and one considering both). However this number could be higher if we had considered HRFs with different times to peak (Bagshaw et al., 2004). If we had considered four different HRFs times-to-peak, as in a previous study (Bagshaw et al., 2004), we would have 12 maps to be analyzed for one run where bilateral discharges were recorded and 24 for patients showing bilateral discharges in both runs acquired (patient #9, Table 6.1). In our results, the classical EEG-fMRI analysis produced 31 maps for 13 patients and 26 of those maps were either epilepsy concordant or discordant maps. Therefore, the large number of maps to be

analyzed is not exclusively associated to data driven methods, but is often neglected by those applying EEG-fMRI.

Finally, our results have consistently shown evidence that the epilepsy-related information detected by each method may be different. Firstly, we have noticed that only 4/13 patients presenting IEDs were mapped by both methods, even in such cases the spatial overlap among the areas mapped by each of them are small or even nonexistent. Secondly, there were temporal correlation between 2dTCA-tcs and EEG-based temporal predictor in only two patients (patients #2 and #3). However none of these temporal correlation were strong (highest $R=0.14$). This is a strong indicator that a wider use of fMRI for mapping epilepsy-related activity can be achieved by combining different modalities such as ICA, EEG-fMRI and 2dTCA. In fact, in this study 16/20 patients are concordantly mapped when both methods are considered. This is an important result towards improving fMRI application in clinical practice of epilepsy, which often has its use mostly restricted to cognitive mapping. Besides that, it is clear that the data driven methods can provide insights about mapping the epilepsy-related BOLD activity will be obtained whether more groups, mainly where EEG-fMRI equipment/expertise is not available.

6.6 Conclusion

In this work we compared the 2dTCA algorithm to the classic EEG-fMRI approach to localize epileptic activity in 20 focal epilepsy patients with Engel I surgical outcomes. Accuracy was quantified as concordance with resection area. While we believe that both of these methods are most useful when used in conjunction with other presurgical evaluations, our results provide a few suggestions. First, a conservative t-map threshold provides more accurate results for the 2dTCA algorithm, while a less stringent threshold should be used for the EEG-fMRI method. Second, negative 2dTCA histograms with positive t-maps are useful in many cases. Third, expertise in classifying maps of no-interest such as resting state networks is valuable in reducing the number of maps to consider, and then only localizing the global maximum t-score cluster is accurate in many cases. Finally, while EEG-fMRI is most accurate in patients with high numbers of IEDs detected on concurrent EEG, 2dTCA can be useful in evaluating

patients even when no concurrent EEG spikes are detected or EEG-fMRI is not effective.

CHAPTER 7 - TOWARDS MOTION INSENSITIVE EEG-FMRI: CORRECTING MOTION-INDUCED VOLTAGES AND GRADIENT ARTEFACT INSTABILITY IN EEG USING AN FMRI PROSPECTIVE MOTION CORRECTION (PMC) SYSTEM

This chapter is related to our objective of improving the quality of EEG data acquired simultaneously to fMRI under motion influence. These results were published as an original article at the NeuroImage Journal, with the following doi: 10.1016/j.neuroimage.2016.05.003

7.1 Background

Subject motion during the acquisition of fMRI can lead to severe data quality degradation. The impact of motion on fMRI is well documented (Hajnal et al., 1994; Satterthwaite et al., 2012) and it causes large amplitude signal changes across consecutive fMRI volumes increasing temporal variance and increasing type 1 and type 2 errors. A number of techniques ranging from purely data-based (post-processing) (Friston et al., 1996; Lemieux et al., 2007; Power et al., 2014; Tierney et al., 2015) to methods based on precise and independent measurement motion have been proposed (Eviatar et al., 1997; Eviatar et al., 1999). Recently, a prospective fMRI motion-related signal reduction system based on a camera-tracker system (PMC) and MR sequence acquisition update has been implemented and commercialised. Briefly, an MRI compatible camera is used to image a Moiré-phase tracker (MPT) attached to the head. The tracking information is converted into the head's position (three translations and three rotations). This information is then used to update the radio frequency pulses and the gradients, applied in the imaging process in real time with promising results (Maclarens et al., 2013, Todd et al., 2015).

EEG quality degradation due to motion is mostly the result of electromagnetic induction. Faraday's law states that magnetic flux changes through a conductor loop's area induce corresponding voltage fluctuations; in EEG circuits these voltages are superimposed onto the brain-generated signals, making the detection of activities of interest more difficult or even impossible. This is even more problematic for the application of EEG-fMRI in patients for whom the motion might be unavoidable, such

as children or to study patients with epilepsy during *seizures*. Currently, most artefact correction methods are based on post-hoc EEG data processing techniques that rely on the identification of artefact waveforms and their subtraction with the aim of obtaining motion artefact-free signals. These processes do not take into account the measured motion (Lemieux et al., 2007; Chaudhary et al., 2012b).

Systems to detect motion induced voltages based on dedicated sensors, such as piezoelectric devices (Bonmassar et al., 2002) and carbon loop wires (Masterton et al., 2007), have shown promise. While these are able to deal with small amplitude movements ($\sim 1\text{mm}$ and 1°), neither performed well in removing voltages induced by large motion events (Masterton et al., 2007). Furthermore, in the case of the wire loops, there is the requirement for additional technology related to the data acquisition and this can pose safety risks in some circumstances (Abbott et al., 2014). Finally, the additional requirement for fMRI data correction during subject motion is not addressed by these systems thereby limiting their impact. A PMC camera system has only previously been used for correcting the ballistocardiogram (BCG) artefact (Levan et al., 2013) found in EEG data acquired inside MRI scanners. While promising this previous work did not address large scale movements or the effects of applying PMC itself on EEG quality during fMRI data acquisition which may suggest that correction of EEG and fMRI is problematic using this approach.

7.2 Objective

In this study, we aimed to focus on improving EEG data quality while suppressing fMRI motion artefacts using a commercially available PMC-camera system. We derived a model of voltage changes induced in the EEG from motion using the accurate measurement of head's motion recorded by the PMC system and used it to attenuate these artefactual signals. We tested this approach with and without large amplitude movements by modelling and removing motion induced voltages and assessed the EEG quality. Additionally, we determine the impact of PMC on the gradient artefact template temporal stability (i.e. the variance between EEG epochs for each fMRI volume or slice) which contains both motion and gradient artefact instability. We also verify our experimental findings by determining the effect of PMC updating the magnetic field gradients on the EEG gradient artefact (GA) in the presence of

motion (i.e. the variability of the voltages induced exclusively by the magnetic field gradient switching with or without PMC).

7.3 Data and methods

We acquired simultaneous EEG-fMRI data in three healthy subjects (two male, both 25 years old, and a female, 23 years old).

7.3.1 Task

During all recordings subjects were instructed to open and close their eyes every 60 (for sessions outside the scanner) or 30s (for sessions inside the scanner). Two different movement tasks were performed: In the ‘keeping still’ sessions subjects were instructed to keep as still as possible. In ‘motion’ sessions subjects were instructed to move performing repeated repetitions of the following movements (see Figure 7.1): shaking their head side to side (right-left), nodding their head (back and forth) and rotating their head followed by a short period (~5s) without movement. The subjects were instructed to start the first block with their eyes open allowing them to calibrate the motion’s amplitude (via visual feedback of the marker position). In the second block the movements were repeated with eyes closed. Three repetitions of each block were made in each session.

7.3.2 EEG data acquisition

During all recordings subjects were instructed to alternate between eyes opened and eyes closed via a verbal queue. This was done in order to evaluate the practical contribution of EEG-motion artefact correction to measure physiological signal changes from the brain (the alpha rhythm in this case).

Figure 1 presents a schematic diagram summarizing the acquisition set-up.

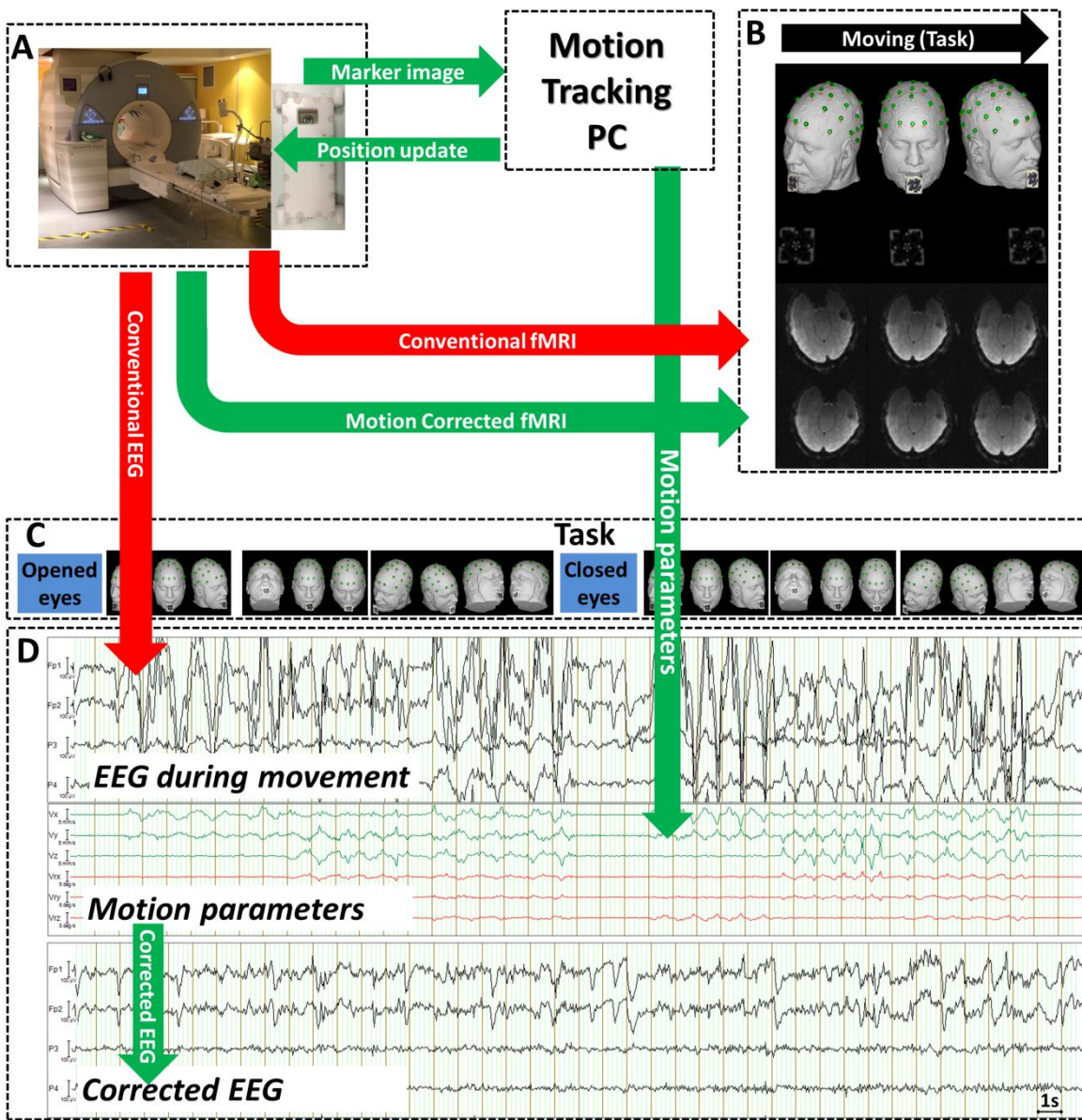


Fig. 7. 1: Schematic overview diagram of the motion corrected (green arrows) and uncorrected (red arrows) EEG-fMRI acquisition. The camera is mounted in the scanner above the subjects head (A) and is used to record head position (illustrated by a head model, B top row) via a MPT marker (B, second row). As the subject moves (as per the task in C) the marker movement is recorded by a camera (B, second row). fMRI will normally be affected by this motion (B, third row) however the marker movement is converted into the subjects head position which can be fed back to the scanner (A) in real time to update the RF and gradients pulses, stabilising the fMRI images (B, bottom row). The EEG data are also affected by the motion (D, top row). However, it is possible to remove the spurious voltages induced by this motion using a model derived from the same position information

(3 translational and 3 rotational velocities are illustrated in the middle row of figure D), resulting in the corrected EEG (D, bottom row).

7.3.3 MRI acquisition

All images were acquired at Great Ormond Street Hospital, London, United Kingdom, using a 1.5T Avanto (Siemens, Erlangen, Germany). The functional images were acquired using a gradient-echo echo-planar imaging (GE-EPI) sequence with the following parameters: 30 ascending slices (3x3x3 mm³) covering the whole brain with a slice gap of 0.5 mm, slice/volume TR= 74/2220ms, TE=30ms, flip angle= 75°. Each fMRI run was composed of 100 volumes, obtained in 222 seconds. The posterior half of a 32 channel head coil was used for signal reception to allow for video recording of the subject motion and visual feedback of the motion to be provided to the subject (see section 2.6).

7.3.4 EEG recording

The EEG data were recorded using a MR-compatible Amplifier (Brain Products, Gilching, Germany). An MRI compatible cap (Easycap, Herrsching, Germany) with 31 EEG-electrodes placed as the 10-20 international system, and an ECG channel, all made of Ag/AgCl with internal safety resistors and referenced to FCz was used. The EEG data were acquired with a sampling rate of 5 kHz and band-pass filtered from 0.1 to 250Hz. The EEG acquisition was synchronized with the MR-scanner by the SyncBox device (Brain Products, Gilching, Germany), allowing the EEG acquisition to be time-locked with the fMRI acquisition gradient switching-related artefact, facilitating its correction (Mandelkow et al., 2006). Before analysing, all the EEG data were down sampled to 500Hz.

7.3.5 Motion measurement and fMRI-prospective motion correction

A MR-compatible camera (Metria Innovation Inc., Milwaukee, USA) was used for tracking a MPT marker (Maclarens et al., 2013) attached to a ‘bite bar’ specifically developed for each subject based on a dental retainer.

To make the bite bar a dental stone cast was produced from a dental alginate impression taken of each subject’s maxillary dentition. A ‘dual-laminate’ (DB Orthodontics, West Yorkshire, England), thermoplastic, 3mm thick bite guard was then

thermoformed to the maxillary dentition using a Biostar machine (Scheu-Dental, Iserlohn, Germany). The ‘soft’ side of the ‘dual-laminate’ ensured a snug fit around the teeth whilst facilitating easy insertion and withdrawal of the guard, whilst the ‘hard’ side ensured that the bite bar didn’t move when the subject bit down. A 6cm x 2cm x 3mm strip of ‘dual-laminate’ was then formed into a bar with a 90 degree angle using localized heat. The bar also incorporated housing for the MPT marker. Finally, the bar was joined to the incisor region of the bite guard using medical grade cyanoacrylate glue.

The MPT camera was used for recording the marker motion with six degrees of freedom, three translations (x, y and z axis, defined as right-left, posterior-anterior and feet-head, respectively) and three rotations (about x, y and z axis, respectively) with a sampling rate of 85 Hz and recorded on a computer located outside the scanner room. The same computer was connected to the scanner to update the Radio Frequency and Gradients pulses used for MRI signal acquisition before every fMRI slice is acquired (Maclare et al., 2013, Todd et al., 2015). Motion tracking was used in the scanner to record the motion parameters throughout the experiments. Real-time updating of the MRI gradients was switched either on or off in the scanner’s software in different sessions to test its effect (see section 2.8).

We analyzed the motion characteristics for each subject by calculating the root-mean-square (RMS) for each of the six velocities derived from motion measurements (three translations and three rotations) and detecting the minimum and maximum amplitude on the axis with the largest RMS. We also calculated the fast Fourier transform on the motion data from the same axis, to allow us to check the motion’s spectral characteristics. For simplicity we reported the frequency of the highest motion-related peak (e.g. the highest peak in the spectra at a non-zero frequency).

7.3.6 Mirror, video camera and screen

We were interested in large amplitude movements in the maximum range that can be reliably tracked with our motion tracking system within the range from -10 to 10mm and -6 to 6°. Subjects were provided with a visual display of the marker position in real time via a screen mounted outside the bore and a mirror to allow them to monitor their movements during the task. We also recorded video of the subject with the EEG in

BrainVision Recorder (Brain Products, Gilching, Germany) via a second MRI compatible camera (NNL eye-tracker camera NordicNeuroLab, Bergen, Norway) in order to visually monitor movement and aid the identification of events in the EEG.

7.3.7 Moiré Phase Tracking-Retrospective EEG motion artefact suppression (MPT-REEGMAS)

The EEG time series data at any given electrode acquired inside the scanner in the presence of motion can be described as follows:

$$EEG_{raw} = EEG_{physiological} + EEG_{motion} \quad \text{Eq. 7.1}$$

Where the voltage acquired by each electrode (EEG_{raw}) is the linear sum of the voltage generated by the neurons and physiological artefacts, such as eye-blanks and muscular activities ($EEG_{physiological}$) and a motion-related voltage(EEG_{motion}). The latter can be related to changes in magnetic flux by the Faraday's Law of induction:

$$EEG(t)_{motion} = - \frac{d\phi_B}{dt} \quad \text{Eq. 7.2}$$

Where $\frac{d\phi_B}{dt}$ is the temporal derivative of the magnetic flux through the electrode
+ wire + head circuit area.

Here we assumed that $\frac{d\phi_B}{dt}$ is purely a function of head motion relative to the laboratory (here scanner) coordinates. Motion can be due to the movement of the electrodes-head system and/or second order effects, such as those related to head acceleration and cap inertia. In both cases, we have a voltage induction in the electrodes proportional to the head motion in a fixed frame.

The following steps were all implemented in Matlab 2013a (The MathWorks, Natick, USA). The MPT-camera recorded motion data were low-pass filtered at 11Hz using a zero-phase Butterworth filter of order eight resulting in smoother data in order to limit the variance of the derivatives. The 11Hz cut-off was chosen after checking the motion parameters spectrogram and verifying that the main signal related to subject motion was below this frequency. We note that this rate is also the typical rate of 2D-EPI data acquisition, where there is rarely motion fast enough to corrupt within slice

acquisition (i.e. <100ms timescale). The 6 velocities were calculated as the temporal derivatives of the MPT-derived motion parameters. We also calculated the squared velocities to account for second order effects that might be present due to differences in movement between the skull and the EEG cap or non-linear movement of wires. The resulting 18 parameters (6 positions, 6 velocities, 6 velocities squared) were interpolated to 500Hz to match the EEG sampling rate (after down sampling). We used a general linear model to estimate $EEG(t)_{motion}$, for time points from t_1 to t_T , where T is the final time point based on the 18 motion parameters described above:

$$(EEG(t)_{raw}) = (EEG(t)_{physiological}) + \begin{pmatrix} M(t_1)_{p1} & M(t_1)_{p2} & \cdots & M(t_1)_{p18} \\ M(t_2)_{p1} & M(t_2)_{p2} & \cdots & M(t_2)_{p18} \\ \vdots & \vdots & \ddots & \vdots \\ M(t_T)_{p1} & M(t_T)_{p2} & \cdots & M(t_T)_{p18} \end{pmatrix} \begin{pmatrix} \beta_{p1} \\ \beta_{p2} \\ \vdots \\ \beta_{p18} \end{pmatrix} \quad \text{Eq. 7.3}$$

Where $M(t)_p$ is the matrix of motion parameters at time t and β_{pi} are the factors to be estimated. The equation 3 can be written as:

$$EEG(t)_{raw} = M(t)\beta + \varepsilon(t) \quad \text{Eq. 7.4}$$

Here, $\varepsilon(t)$ represents the residual of the EEG temporal series with variance related to our motion model removed (i.e. $EEG(t)_{physiological}$). β can be estimated in order to minimize the residual $\varepsilon(t)$

$$\beta = M(t) (M(t)^T M(t))^{-1} EEG(t)_{raw} \quad \text{Eq. 7.5}$$

Finally, the motion artefact corrected $EEG(t)_{physiological}$ can be recovered for each electrode at each time point by the following:

$$EEG(t)_{physiological} = EEG(t)_{raw} - M(t)\beta \quad \text{Eq. 7.6}$$

We refer to the process of calculating the $EEG(t)_{physiological}$ using Eq. 7.6 and the tracking information as Retrospective EEG Motion Artefact Suppression (REEGMAS).

7.3.8 Experiments and processing

7.3.8.1 Experiment 1: Baseline EEG acquisition

We acquired baseline sessions of EEG data outside the scanner with subjects asked to keep still and to open and close their eyes every 60s.

7.3.8.2 Experiment 2: EEG recording inside the scanner without scanning (No fMRI)

Two sessions of EEG data were recorded inside the scanner without MRI scanning: the first while keeping still (EEG_{2S}) and the second while moving voluntarily (EEG_{2M}).

The EEG data was down-sampled to 500 Hz and imported into Matlab. Two processed versions of each EEG dataset were obtained for further analysis: EEG_{2S} and EEG_{2M} without REEGMAS correction but with BCG artefact correction by Average Artefact Subtraction (AAS_{BCG}) (Allen et al., 1998) and EEG_{2S-C} and EEG_{2M-C} with REEGMAS correction followed by BCG artefact correction by AAS_{BCG} as implemented in BrainVision Analyzer 2.0 (Brain Products, Gilching, Germany).

7.3.8.3 Experiment 3: Simultaneous EEG-fMRI acquisitions

Experiment 3a: EEG and fMRI data were acquired with the PMC system recording motion data but *not* updating the imaging gradients ('fMRI/PMC-off'). We have acquired two successive sessions; with the subjects keeping still (EEG_{3aS}) and while moving voluntarily (EEG_{3aM}), respectively.

Experiment 3b: EEG and fMRI data were acquired with the PMC system recording motion and updating the scanning gradients ('fMRI/PMC-on'). We have acquired two successive sessions; with the subjects keeping still (EEG_{3bS}) and while moving voluntarily (EEG_{3bM}), respectively.

The EEG data from both experiments 3a and 3b were down-sampled to 500 Hz, imported into Matlab and REEGMAS was applied as described in section 2.7, resulting in motion-corrected EEG (EEG_{3aS-C} , EEG_{3aM-C} , EEG_{3bS-C} and EEG_{3bM-C}). In order to correct the GA we have applied the Average Artefact Subtraction (AAS_{GA}) (Allen et al., 2000). Henceforward we refer to GA correction as AAS_{GA} and to ballistocardiogram (BCG) artefact correction as AAS_{BCG} . In this study we built the templates in two

different formats, volume-volume (volume-wise) (Allen et al., 2000) and slice-slice (slice-wise) (Niazy et al., 2005). Firstly, a volume-wise GA template was formed by averaging volumes ($n=15$, each 2220ms, using 33.3s of data in total) we chose a low number of volumes to reduce motion sensitivity. Secondly, a slice-wise GA template was formed by averaging slice epochs ($n=15$, each 74ms, using 1.1s of data in total). This is possible because the gradients applied are identical for each slice with the only difference being the RF pulse frequency offset. Following this, AAS_{BCG} was applied to both the REEGMAS corrected EEG (EEG_{3aS-C}, EEG_{3aM-C}, EEG_{3bS-C}, EEG_{3bM-C}) and the original EEG without REEGMAS correction (EEG_{3aS}, EEG_{3aM}, EEG_{3bS}, EEG_{3bM}). We define the GA template variability as the slice-wise or volume-wise epoch-epoch that maybe caused by any factor (e.g. motion, scanner instability, GA). The GA is only the voltages resulting from the magnetic field gradients switching themselves.

After the processing described above, the EEG data from all experiments were then down-sampled to 100Hz and a pass-band filtered from 0.5-40Hz in BrainVision Analyzer 2.0. This is a common filter width for clinical EEG visualisation. All further analysis was performed in Matlab 2013a.

7.3.9 EEG data quality assessment

For the data acquired during the moving sessions of Experiment 2, we evaluated the importance of each parameter to the motion regression model by calculating an F-test score using the function *ftest.m*.

The quality of the REEGMAS artefact correction was assessed by comparing the EEG obtained in the scanner (Experiments 2 and 3) to the EEG acquired outside the scanner room (Experiment 1) in the following ways:

1. We visually assessed the EEG data comparing the presence of physiologic signals/markers, such as eye-blink artefacts and presence of signal in the alpha-rhythm frequency band (8-12Hz). To assess the impact of the motion correction across channels, the power topography over the scalp in the alpha rhythm frequency band (8-12 Hz in our study) was visualised. The alpha topography was the power in the frequency band 8-12Hz averaged over an epoch of 5 seconds following the first period

of eyes closed. We compared EEG data acquired during both ‘keeping still’ (EEG_{2S}), ‘motion’ uncorrected (EEG_{2M}) and corrected (EEG_{2M-C}) sessions.

2. The EEG power spectral density (PSD) was calculated by applying the Welch method (*pwelch.m* function) using Hamming windows of 3 s with 1.5-second overlap during keeping still/motion sessions in eyes closed periods. The PSD was normalised at each frequency by the sampling rate and the number of samples inside each window (dB/Hz). The mean PSD was calculated for the baseline EEG (Experiment 1 during eyes closed periods). Additionally we calculated two standard deviations of this baseline EEG-PSD across time and assumed that points lying outside this range were likely to be due to artefacts.

3. The Root Mean Square Error (RMSE) defined as the difference between the uncorrected (or corrected) EEG-PSD and the baseline EEG mean PSD was calculated for each frequency from 0.5 to 40 Hz with a frequency resolution of 0.33Hz. Then we calculated the average RMSE over the entire frequency range obtaining the Mean Root Mean Square Error (MRMSE). Finally, we applied a one-sample t-test in order to compare the MRMSE obtained for EEG data before and after REEGMAS correction.

For Experiment 3 data, we assessed GA template (slice-wise) stability for each EEG session by calculating the variance of Root Mean Square EEG amplitude (EEG-RMS) across slices based on the rationale that inter-slice variance is increased by noise and therefore summarises the stability of the GA template (slice-wise). The combined impact of motion and GA induced voltages and then can be compared under the different conditions and corrections tested. The EEG-RMS was calculated from the raw/REEGMAS corrected down-sampled EEG, given by the following equation:

$$RMS_{EEG} = \sqrt{\frac{(\sum_{i=1}^N E_i^2)}{N}} \quad \text{Eq. 7.7}$$

Where E_i is the voltage measured by the electrode i and N is the number of electrodes.

In this study each fMRI slice was acquired in 74ms. The EEG was down-sampled to a rate of 500Hz, resulting in 37 (k) points at which the GA template stability could be estimated (i.e. 37 samples were obtained in the 500Hz EEG during the 74ms slice acquisition period). The GA template (slice-wise) variance was calculated at each of

these 37 points across 3000 repetitions of the GA (j corresponding to the number of slices obtained in each session) by the following equation.

$$\rho GA_{template}(k) = \frac{1}{3000} \sum_{j=1}^{3000} (RMS_{EEG}(j, k) - \mu(k)_{EEG})^2 \quad \text{Eq. 7.8}$$

Where,

$$\mu(k)_{EEG} = \frac{1}{3000} \sum_{j=1}^{3000} RMS_{EEG}(j, k) \quad \text{Eq. 7.9}$$

We then compared the GA template stability (slice-wise) $\rho GA_{template}$ for each session (motion versus keeping still) of Exp. 3a and 3b (fMRI/PMC-on and fMRI/PMC-off) to the fMRI/PMC-off, keeping still session using a one-sampled paired t-test. This required 37 tests, one for each time point in the template (k), therefore we applied a Bonferroni correction and considered significant differences at a p-value of <0.05 corrected.

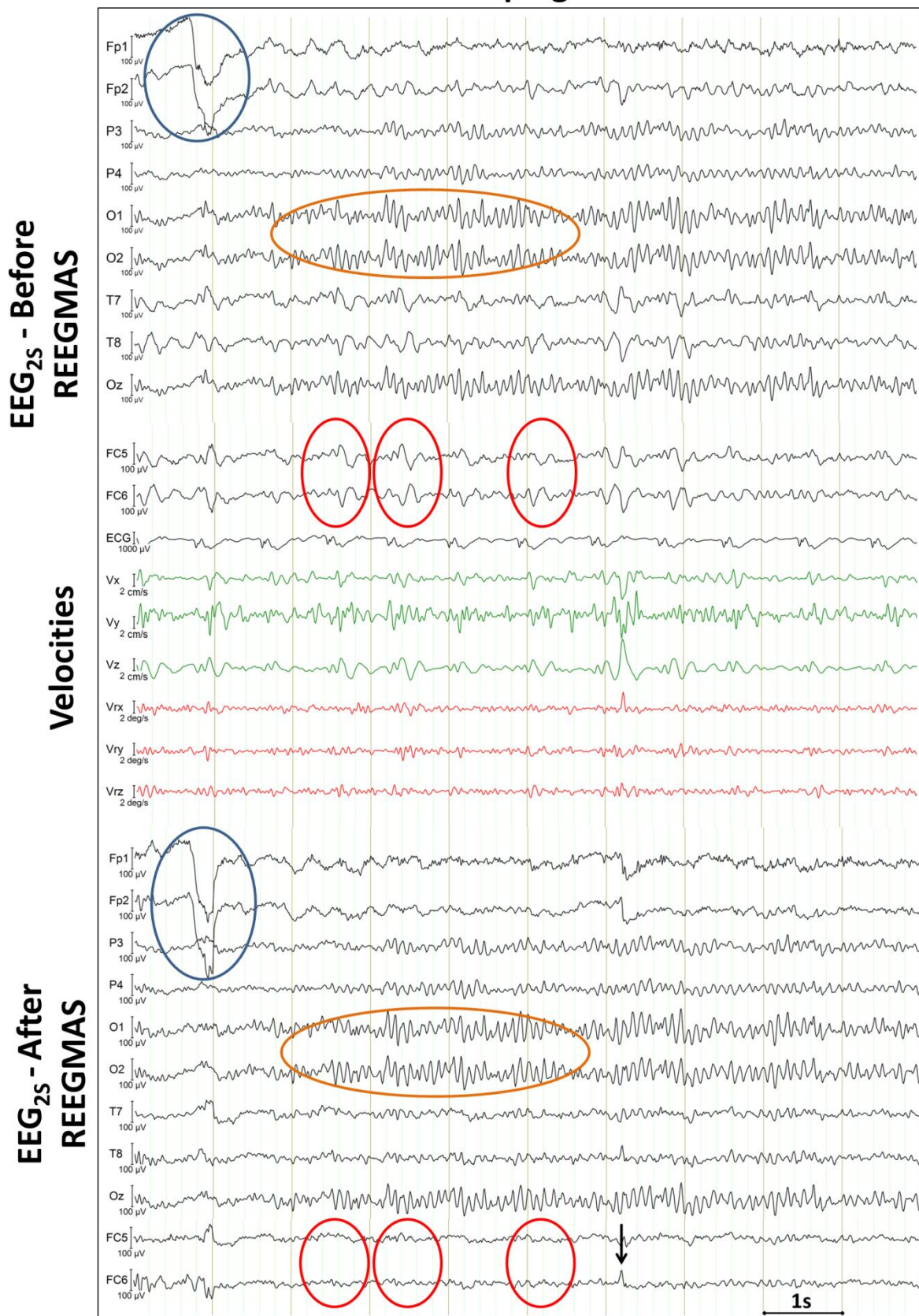
7.4 Results

7.4.1 Experiments 1 and 2: EEG quality assessment inside the scanner with REEGMAS without scanning vs baseline EEG

In all subjects, in the moving session (EEG_{2M}), the maximum RMS velocity was for translations along the X axis: V_{X RMS}= 22.5, 23 and 20 mm/s for subjects #1, #2 and #3, respectively (Range: [-42.9 to 28.6mm/s], [-32.2 to 38.6mm/s] and [-41.2 to 19.4mm/s]). The peak frequency of motion was 0.43, 0.71 and 0.55Hz, for subjects #1, #2 and #3, respectively. All motion-related model regressors explained a significant amount of variance. The motion-related quantity that explained the most variance in the EEG was the velocity of motion as expected followed by position and squared velocity (see Supplementary Material 2 Table S2.1).

EEG_{2S} data (recorded during the keeping still sessions of Experiment 2, in scanner without fMRI acquisition) were of high quality with a clearly visible alpha rhythm during epochs of eyes closed (orange regions, Fig. 7.2A) and the presence of eye-blink artefacts (blue region, Fig. 7.2A). The REEGMAS correction improved the visual appearance EEG_{2S} attenuating BCG artefacts (red region, Fig. 7.2A), even prior

to applying AAS_{BCG} on EEG_{2S-C}. REEGMAS correction did not change the visual appearance of alpha rhythm nor the eye-blink artefacts. In the moving session (EEG_{2M}), large amplitude voltages were clearly visible during subject movement that can be seen in the MPT tracking derived velocity measurements (Fig 2B, middle panel). Following REEGMAS correction a substantial qualitative improvement in EEG_{2M} was observed in EEG_{2M-C} with strong attenuation of the large amplitude motion-related voltages (Fig. 7.2B). Application of REEGMAS improved the visual appearance of physiological signals such as the alpha rhythm (orange region in Fig. 7.2B) in the keeping still (Fig. 7.2A) and moving (Fig. 7.2B) sessions. Similar results were obtained for the other two subjects (see supplementary material 2 Fig. S2.1 and S2.2).

A**Keeping Still**

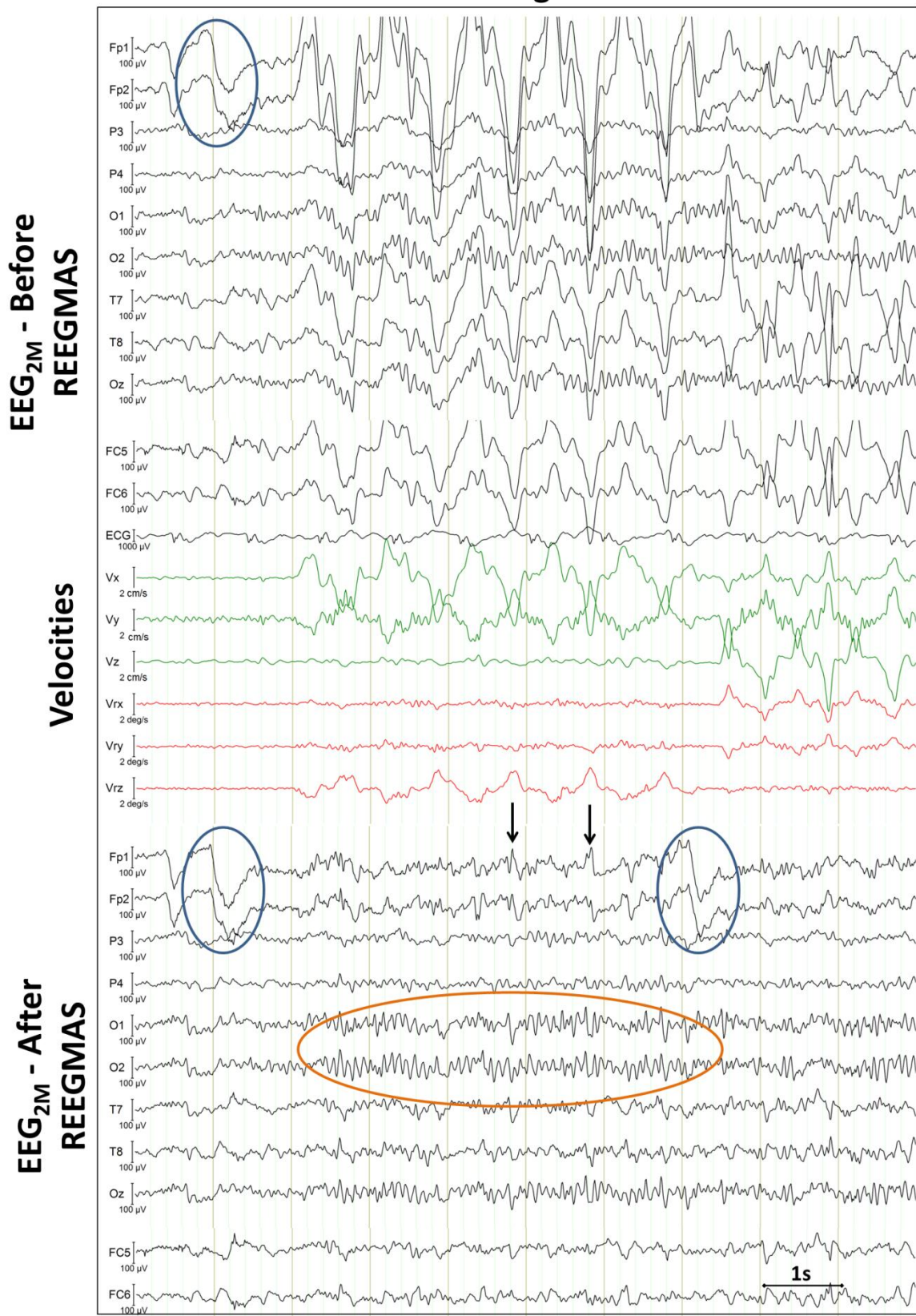
B**Moving**

Fig. 7. 2: Representative EEG data from subject #2 obtained in Experiment 2 (inside the MRI scanner, no fMRI acquisition). A ten second epoch following the first eyes closed period is shown for the subject keeping still (A) and subject moving (B) sessions. In both A and B the EEG is displayed before (EEG_{2S} and EEG_{2M}) (top) and after (EEG_{2S-C} and EEG_{2M-C}) (bottom) REEGMAS correction. The middle section shows the translational (green cm/s) and rotational (red degrees/s) velocities measured by the MPT motion tracking system. The blue ellipses highlight the eye-blink artefacts; red ellipses highlight the cardiac pulsation-related artefacts and the orange highlight the alpha-rhythm detection. The black arrows point to residuals remaining after motion correction. To visualise the effect of REEGMAS the EEG data presented in A-B were not AAS_{BCG} corrected.

In the keeping still session of experiment 2, the PSDs were similar for the EEG_{2S} (dashed black curve) and EEG_{2S-C} (dashed red curve) for all the subjects (Fig. 7.3A, top row). In general the quantitative analysis (MRMSE) did not show statistic differences ($p > 0.05$) between EEG_{2S} and EEG_{2S-C} (Fig. 7.4A, see also Supplementary Material 2 Table S2.2a).

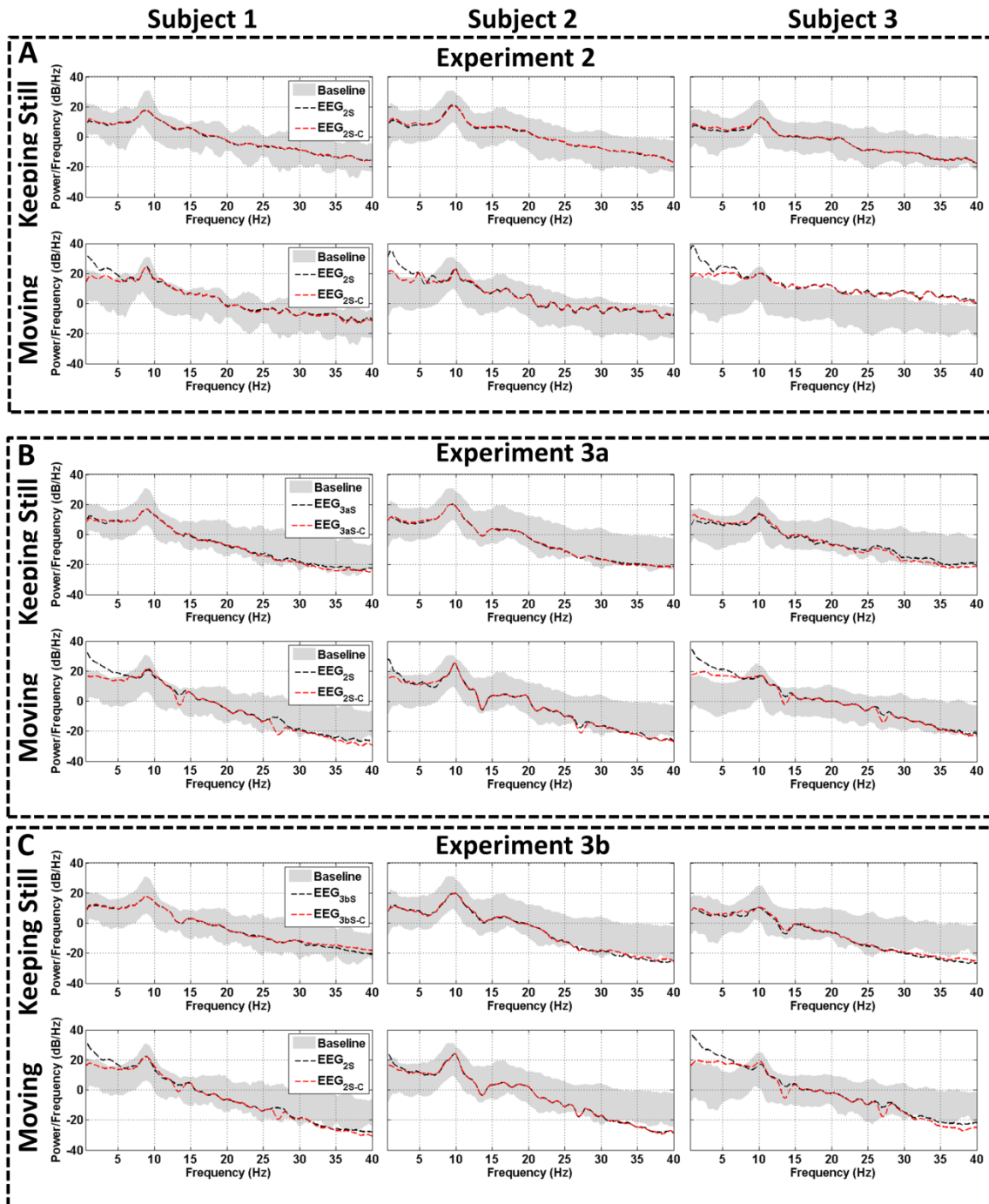


Fig. 7.3: The mean power spectral density (PSD) at electrode O2 for each subject with eyes closed during keeping still (top row of each figure) and moving (bottom row in each figure) sessions. The mean PSD for each subject is presented for Experiment 2 (in-scanner, no fMRI) (A), Experiment 3a (fMRI/PMC-off) (B) and 3b (fMRI/PMC-on) (C). The shaded grey area represents two standard deviations from the mean baseline (Exp. 1) spectra obtained outside the MRI scanner. The

black dashed line refers to the mean power spectra of the EEG acquired in-scanner (Experiments 2 and 3) but not corrected by REEGMAS and the red dashed line to the same data corrected by REEGMAS. Electrode O2 is shown due to its sensitivity to detect the alpha-rhythm.

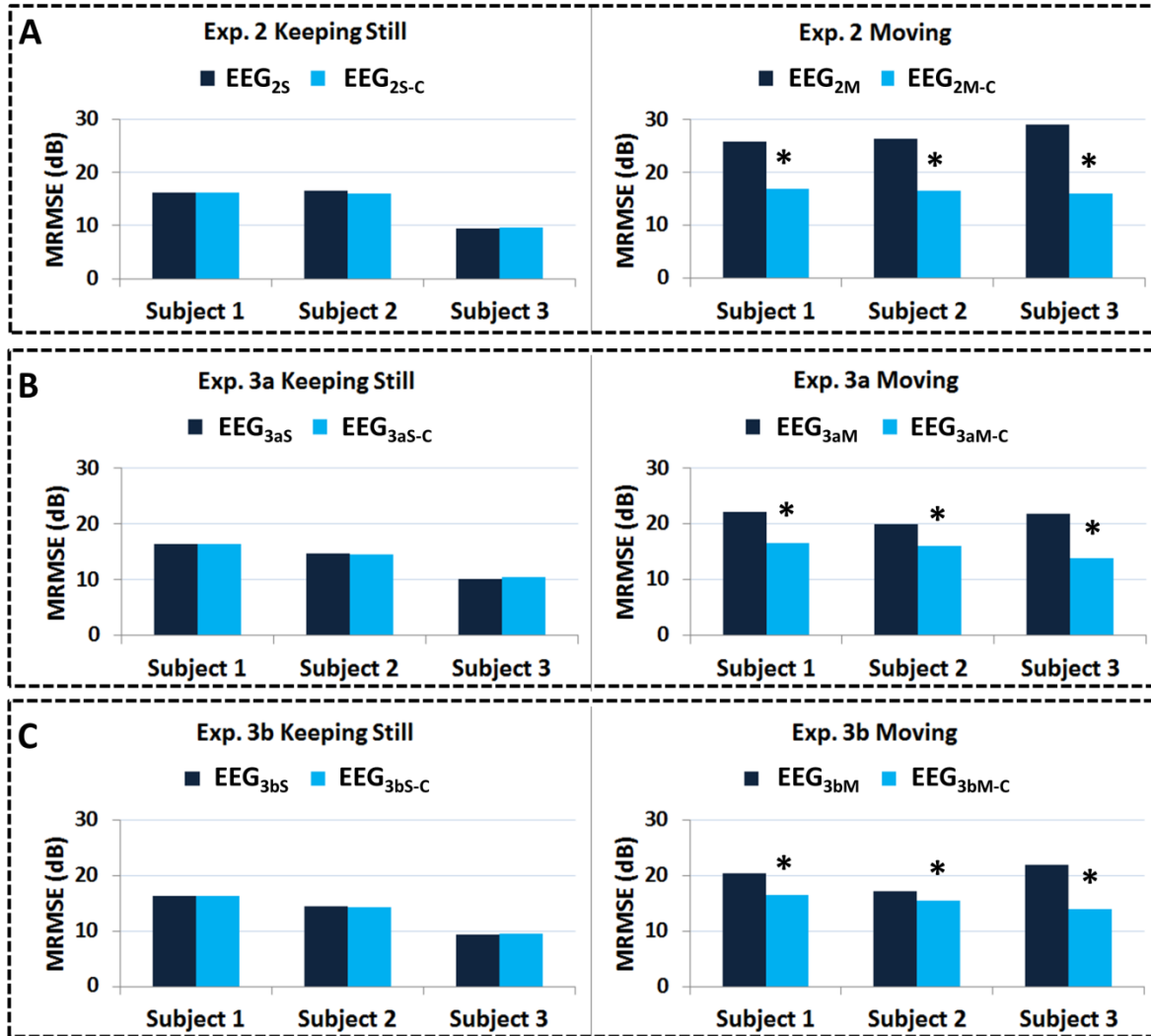


Fig. 7.4: Mean root mean square error (MRMSE) calculated before (dark blue) and after (light blue) REEGMAS for the EEG data from Experiments 2 (A), 3a (B) and 3b (C). Figures on the left hand side are related to keeping still sessions and those on the right hand side are related to moving sessions. The '*' symbol means significant ($p < 0.05$) reduction on the MRMSE after applying the REEGMAS.

We observed an increase in EEG power, predominantly in the frequency range of 0.5-7Hz during moving sessions (EEG_{2M}) for all subjects (Fig. 7.3A, bottom row). REEGMAS decreased the power in this frequency range to baseline levels for all

subjects. Similar results were obtained in other electrode locations (data from one temporal, parietal, central and frontal electrode are provided in Supplementary material 2 Figures S2.3-S2.6). The motion correction decreased the MRMSE significantly ($p<0.05$, Supplementary material 2 Table S2.2), for all subjects (Fig. 7.4A, right hand side), when compared to the uncorrected EEG data. We also note that residual gradient artefact can be observed in some subjects at the frequency of the slice acquisition and harmonics (13.5 & 27 Hz). In some subjects/conditions the power at these frequencies decreased towards to the levels found before without scanning suggesting AAS_{GA} has provided a better correction of the GA following REEGMAS.

As expected, the electrodes with the largest voltage values in the alpha band (8-12 Hz in our study) are the parietal/occipital electrodes when subjects were still (Fig. 7.5, top row). The alpha rhythm (Fig. 7.5, middle row) was contaminated by motion induced voltages, mainly in frontal electrodes (subjects 1 and 2) and in temporo-occipital electrodes (subject 3). After REEGMAS, the alpha power was distributed over the occipital channels and more closely corresponded to the topography seen in the still session for all three subjects (Fig. 7.5, bottom row)

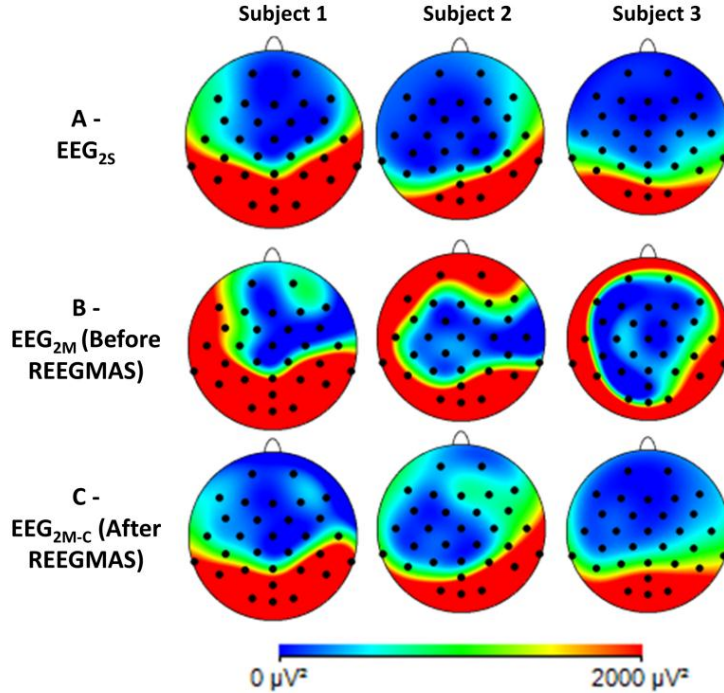


Fig. 7.5: The topography of power distribution in the alpha-frequency band (8-12Hz) for each subject in Experiment 2 (in-scanner, no fMRI acquisition, eyes closed). (A) EEG_{2S} (Keeping still session); (B) EEG_{2M} (Moving session before REEGMAS correction) and (C) EEG_{2M-C} (after motion corrected by REEGMAS). The BCG artefacts were corrected based on the subject's ECG by the AAS methods for both sessions (still and moving).

7.4.2 Experiment 3: EEG quality assessment inside the scanner with REEGMAS during scanning

For moving sessions of Experiment 3a (EEG_{3aM}), the maximum RMS for the velocities was for translations along the X axis: V_X _{RMS} = 16.5 and 18.7mm/s for subjects #2 and #3, respectively (Range: [-29.6 to 23.1mm/s] and [-34.5 to 26.3mm/s]), and along the Z axis for subject #1: V_Z _{RMS} = 30.2mm/s (Range [-54.4 to 39.8mm/s]). The peak frequency of motion was 0.45, 0.51 and 0.52Hz, for subjects #1, #2 and #3, respectively.

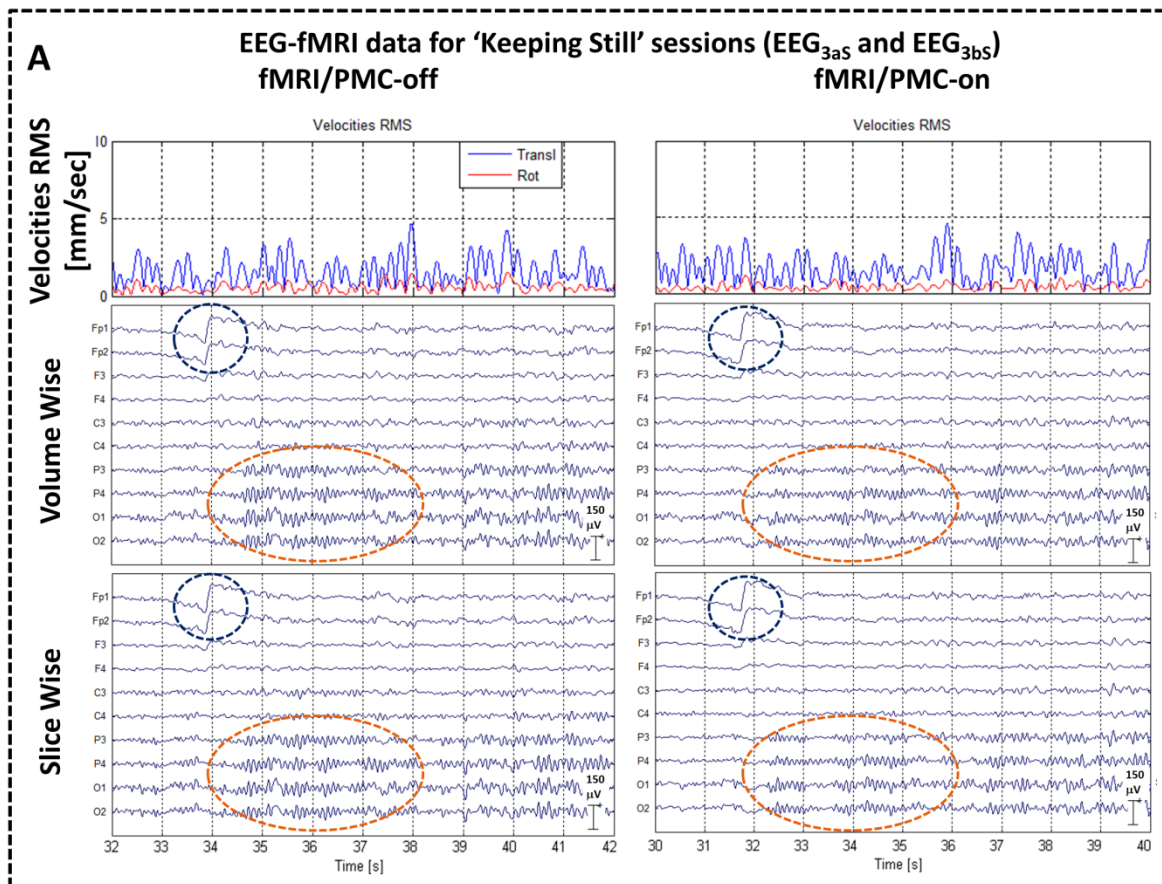
For experiment 3b (EEG_{3bM}), the maximum RMS for the velocities was for the translations along the X axis: V_X _{RMS} 15, 15.2 and 20.80mm/s for subjects #1, #2 and #3, respectively (Range: [-22.9 to 27.1mm/s], [-13.6 to 32.7mm/s] and [-33 to 36.3mm/s]). The peak frequency of motion was 0.36, 0.38 and 0.49Hz, for subjects #1, #2 and #3, respectively.

7.4.2.1 Impact of motion on Gradient Artefact stability with and without REEGMAS

The AAS_{GA} correction of EEG data (EEG_{3aS} and EEG_{3bS}) acquired in the keeping still sessions (Fig. 7.6A, top row) resulted in EEG data of good quality for both volume (Fig. 7.6A, middle row) and slice wise (Fig. 7.6A, bottom row) templates independent of the fMRI/PMC being off (Fig. 7.6, left hand side) or on (Fig. 7.6, right hand side); the alpha-rhythm was clearly visible (Fig. 7.6A orange regions) and its frequency's power distribution was comparable to that recorded in Exp. 1 (Fig. 7.2B and C, top rows) for all three subjects. We verified that during the keeping still sessions (EEG_{3aS} and EEG_{3bS}) the GA template (slice-wise) had small variability ($\rho_{GA_{template}}$), meaning that it was temporally stable in fMRI/PMC-off (Fig. 7.7a, bottom, left hand side) and fMRI/PMC-on (Fig. 7.7a, bottom row, right hand side) acquisitions. As expected, the AAS_{GA} correction of EEG data (EEG_{3aM} and EEG_{3bM}) acquired during the moving sessions (Fig. 7.6B, top row) resulted in decreased EEG data quality compared to the still sessions when No REEGMAS was applied and standard volume-wise AAS_{GA} correction was used (Fig. 7.6B second row). However, the strong residuals in the EEG data (3aM and 3bM) corrected by volume-wise based AAS_{GA} (Fig. 7.6b, second row) were attenuated (EEG_{3aM} and EEG_{3bM}) when corrected by slice-wise AAS_{GA} (Fig. 7.6b, third row). Following REEGMAS, AAS_{GA} and AAS_{BCG}, the EEG data (EEG_{3aM-C} and EEG_{3bM-C}) quality was sufficiently improved to show physiological electrical activity, such as the alpha rhythm, in both volume (Fig. 7.6B, third row) and slice-wise (Fig. 7.6B, fourth row) based AAS_{GA}, the latter was less contaminated by GA. Furthermore eye-blink artefacts (blue circles in Fig. 7.6B, second row) were clearly distinguishable from motion events following motion correction (blue circles in Fig. 7.6B, fourth and fifth rows). The visual and quantitative improvement was observed for all subjects.

The GA templates (volume-wise and slice-wise) variability was dramatically increased during motion (Fig. 7.7A, first and second rows). The GA template variability was substantially reduced by slice-wise AAS_{GA} compared to volume-wise AAS_{GA} (Fig. 7.7A, third and second rows respectively). The GA template stability (slice-wise) was then further improved by REEGMAS where visually the stability approaches that seen when the subject was still (c.f. Fig. 7.7A third row and fourth row respectively). The

PSD analyses of the data from Experiment 3 with fMRI acquisition (Fig. 7.3B and C and Supplementary Material 2 Fig. S2.3-S2.6), have shown results comparable to the EEG acquired in Experiment 2 without fMRI acquisition. For all Subjects there was a significant reduction ($p<0.05$) of the MRMSE after applying REEGMAS prior to GA correction of the EEG data ($\text{EEG}_{3\text{aM}}$ and $\text{EEG}_{3\text{bM}}$) acquired in moving sessions of Experiment 3, a and b, (Fig. 7.4B-C).



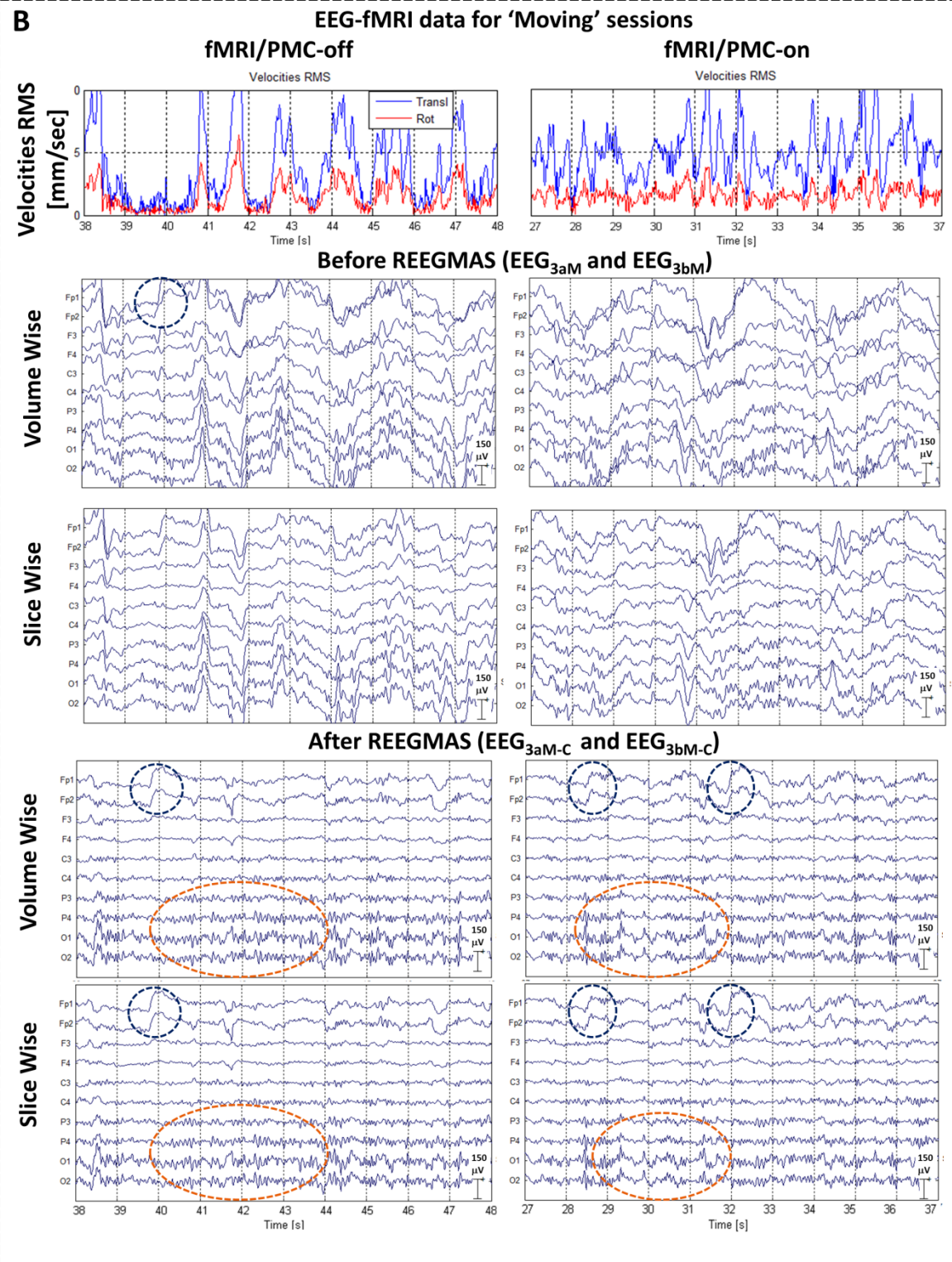
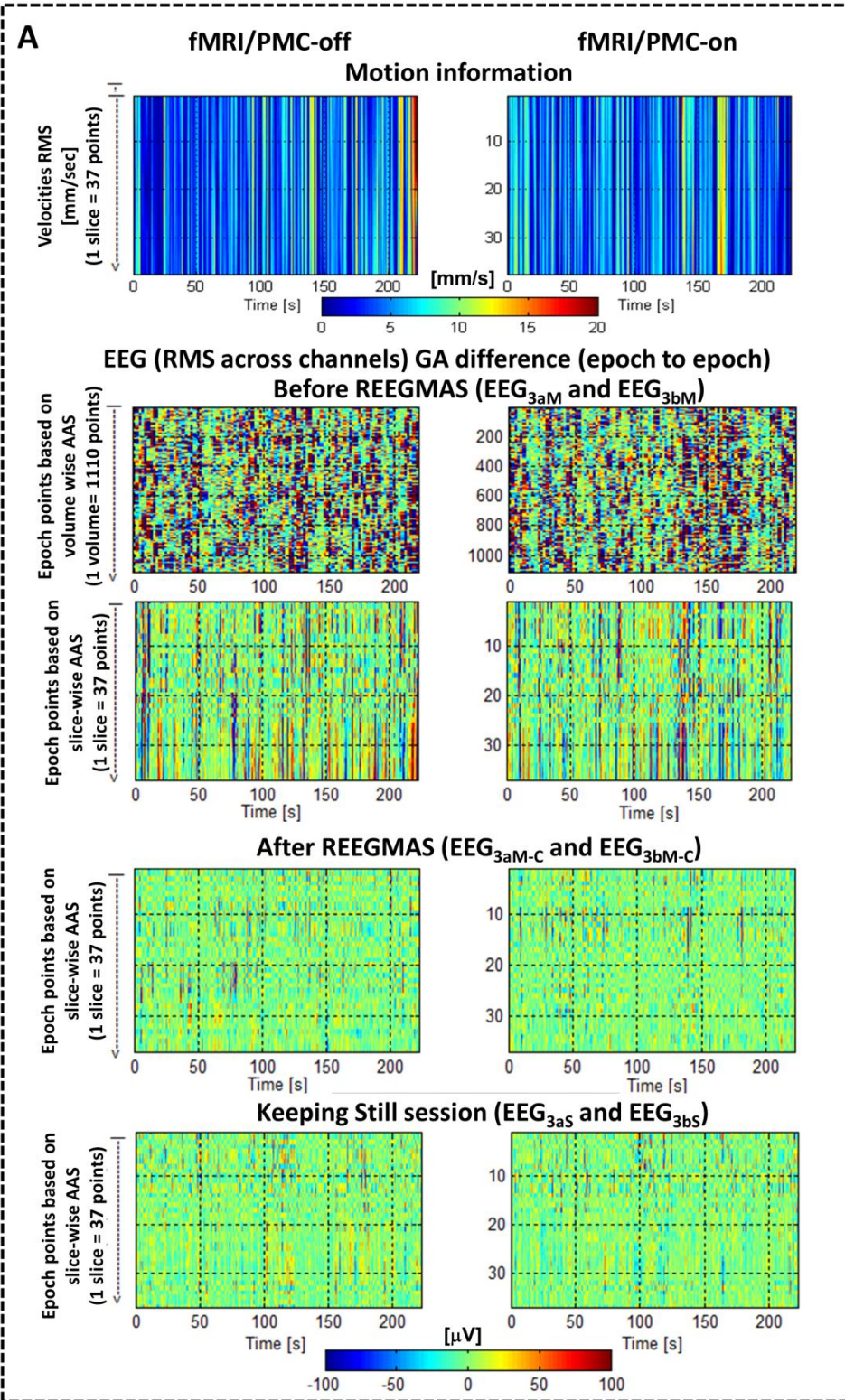


Fig. 7. 6: EEG-fMRI data after AAS_{GA} based on volume or slice-wise templates and AAS_{BCG} correction before (top) and after (bottom) REEGMAS. All figures

show a 10s epoch of the first eyes closed period, for Subect#1. The fMRI/PMC-off acquisition is presented on the left hand side and fMRI/PMC-on the right hand side. A) Data acquired in keeping still sessions. Top panel illustrates the RMS of translational (transl) (blue) and rotational (rot) (red) velocities, middle panels illustrate the EEG data after volume-wise AAS_{GA} correction and the bottom panels the EEG data after slice-wise AAS_{GA} correction. B) Top panel illustrate the RMS of translational (blue) and rotational (red) velocities. Middle panels illustrate the EEG data after volume-wise or slice-wise AAS_{GA} correction but without motion-artefact correction (Before REEGMAS). Bottom panels illustrate the EEG data after volume-wise or slice-wise AAS_{GA} correction and motion-artefact correction (After REEGMAS). The blue regions identify the eye-blink artefacts and the orange highlight the alpha-rhythm detection.

7.4.2.2 Impact of PMC on Gradient Artefact template stability and resultant EEG data

For the fMRI/PMC-off (Fig. 7.7B, top row) and fMRI/PMC-on (Fig. 7.7B, bottom row) scans, the RMS variance across the 3000 artefact epochs was higher for the EEG data acquired during moving sessions (EEG_{3aM} and EEG_{3bM}) than the EEG data acquired during still sessions (EEG_{3aS} and EEG_{3bS}). When the REEGMAS was applied (EEG_{3aM-C} and EEG_{3bM-C}) the variance was strongly attenuated for both acquisitions; fMRI/PMC-off (Fig. 7.7B, top row) and fMRI/PMC-on (Fig. 7.7B, bottom row).



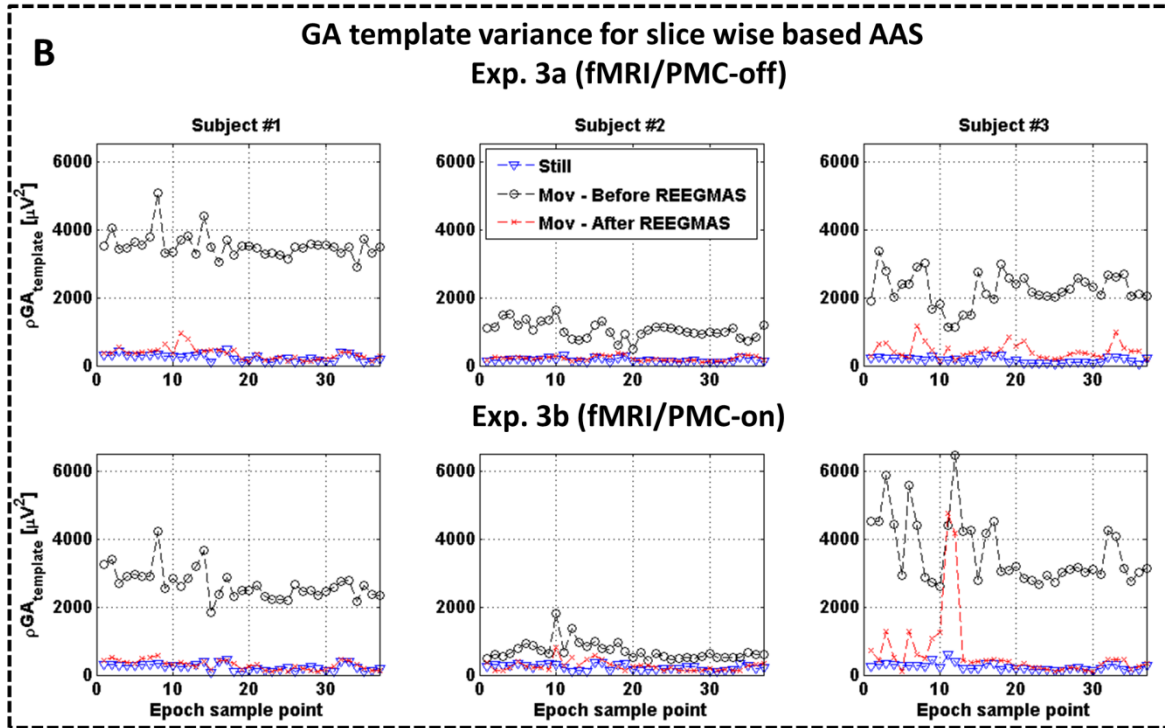


Fig. 7. 7: Improving GA template stability with REEGMAS with and without PMC for fMRI. (A) The y-axis of each panel refers to the sample points within an epoch used for the AAS_{GA} (slice wise=37 and volume wise=1110), the x-axis is the acquisition time in seconds. Top panel illustrates the translational velocities rms in mm/s for moving sessions. All the other panels illustrate GA template the epoch-epoch variability in the EEG (RMS across channels) for different conditions: Before REEGMAS- Moving session displayed based on volume-wise AAS (second panel); Moving session displayed based on slice-wise AAS (third panel); After REEGMAS – Moving session displayed based on slice-wise AAS (fourth panel). The bottom panel illustrates the EEG (RMS across channels) GA difference (epoch to epoch) in the Keeping still sessions without any correction applied for comparison to the correction steps. (B) Summary of slice-wise EEG GA stability for each subject #1-3 (column 1-3) during head motion. Variances ($\rho GA_{template}$, μV^2) across all 3000 artefact epochs are shown during fMRI/PMC-off acquisitions (top row) and fMRI/PMC-on (bottom row). Motion dramatically increases the GA variance in each subject (black ‘o’) compared to the still session (blue ‘▼’); REEGMAS correction (red ‘*’) dramatically reduces the GA variance approaching to levels seen in the keeping still session for most subjects / GA template sample points.

For all subjects and scan conditions (fMRI/PMC-off and fMRI/PMC-on), there was a significant reduction ($p<0.05$ corrected for multiple comparisons) in $\rho GA_{template}$ due to REEGMAS motion correction (Table 7.1). The GA template (slice-wise)

variance reduction after applying REEGMAS varied between 62.6% (Subject #2, fMRI/PMC-on scan) and 81.89% (Subject #3, fMRI/PMC-on scan). The variance of motion-corrected EEG (EEG_{3aM-C} and EEG_{3bM-C}) and still EEG data (EEG_{3aS} and EEG_{3bS}) was not statistically different in all the subjects for fMRI/PMC-on acquisitions and for subjects #1 and #2 for fMRI/PMC-off acquisitions, in subject 3 there was a significant difference.

Table 7. 1. GA template (based on slice-wise AAS) variance through fMRI acquisitions.

	fMRI/PMC-off (EEG _{3a})		fMRI/PMC-on (EEG _{3b})	
	Mean Variance (μV^2)	Difference	Difference	Mean Variance (μV^2)
Subject #1				
Uncorrected	3531.00	* *] *	—	* * [2669.90
Corrected	346.97]	—	294.837
Still	243.29	—	—	232.27
Subject #2				
Uncorrected	1048.97	* *] *	—	* * [697.18
Corrected	209.27]	—	260.85
Still	164.21	—	—	226.66
Subject #3				
Uncorrected	2243.87	* *] *	* —	* * [3596.73
Corrected	432.69	*]	—	651.13
Still	165.18	—	* —	243.41

The mean variance obtained for the uncorrected (EEG_{3aM}, and EEG_{3bM}) and corrected EEG during moving (EEG_{3aM-C} and EEG_{3bM-C}) and also for the keeping still session for both fMRI/PMC-off and fMRI/PMC-on scans. The brackets indicates which comparisons were statistically significant different ($p(\text{bonferroni})<0.05$), where the '*' indicates the higher value.

7.5 Discussion

In summary, we have proposed a method for reducing motion-related artefacts in EEG data acquired inside the MR-scanner. This method is based on recording subject's head position using a MPT system and using this information to model and suppress the motion-induced voltages in the EEG data. Our main finding is that the proposed method is able to considerably reduce motion-induced voltages both during small and large amplitude movements in the absence (Fig. 7.2 and Supplementary Material 2 S2.1-S2.2) and presence of fMRI data acquisition (Fig. 7.6). The motion-induced voltage correction was shown to increase the visual quality of the EEG data and the alpha-rhythm power topography (Fig. 7.5). This was confirmed by quantitative analysis in the frequency domain where the MRMSE (Fig. 7.4) showed a consistent improvement in EEG data quality in 3 subjects when they were moving. The PSD analyses (Fig. 7.3 and Supplementary Material 2 Fig. S2.3-S2.6) showed that the motion correction is beneficial in frequencies between approximately 0.5-8Hz (Fig. 7.3). In this study, motion information at frequencies above 11Hz were filtered based on the assumption that the camera provides more accurate tracking at lower frequencies and that head motion is predominantly in this range. While the motion task was predominantly low frequency, higher frequency events were also corrected such as those relating to cardiac pulsation-related artefacts. Previous studies (Bonmassar et al., 2002; Masterton et al., 2007; Moosmann et al., 2009; Levan et al., 2013) have shown the potential for correcting motion-induced voltages induced by small movements (in the order of 1mm) by linearly modelling motion-induced voltages based on head motion detection. Here we demonstrated for the first time the potential correction of motion-induced voltages in the order of 10mm, 6 degrees and velocities up to 54mm/s. Previous studies (Bonmassar et al., 2002; Masterton et al., 2007, Chowdhury et al., 2014) presented approaches that may be able to capture non-linear effects (e.g. scalp pulsation) that can contribute to pulsation-related artefact in EEG data. However, the dominant contribution is due to rigid body rotation (Yan et al., 2009) which REEGMAS corrects and the non-linear terms (velocities squared) in the REEGMAS model also explained significant variance.

EEG in the MRI scanner is degraded by large amplitude voltages induced by magnetic field gradients. These can be effectively corrected when they are temporally stable using template subtraction methods (Allen et al., 1999). The GA template stability can be degraded by subject motion, scanner instabilities (Goldman et al., 2000) or magnetic field gradient instabilities. However on most modern MRI systems the latter contribution is small. Subject motion affects the GA template used for the AAS_{GA} method in two ways. Firstly, motion-induced voltages are added to those induced by the switching gradients, therefore modifying the GA template. The voltage induced by motion is of comparable magnitude to GA voltages (480 μ V was recorded in this study for a motion with velocity of 20 mm/s and a rotation of 6° around the x-axis at electrode T8, subject #1 while the GA voltage in this case was 50 to 9000 μ V). Secondly, if the subject is in a different spatial location the magnetic field gradient experienced within the EEG circuit is different and correspondingly so is the voltage induced. From previous theoretical work (Yan et al., 2009) the expected alteration in GA is spatially varying but will be 75 μ V for 1mm translation on z-axis and 370 μ V for a 5mm translation at electrode T8, assuming azimuthal angle of 6° between the head and B0 (z-axis). Our experimental data that showed a maximum volume-volume GA template difference in voltage of 382 μ V for a head translation on x-axis of 2.44 mm (Exp. 3a, Fig. 7.6B, middle panel, left hand side). For a slice-wise template both head displacement and correspondingly maximum slice-slice GA template voltage change were reduced to 120 μ V and 0.89mm respectively. For these experiments GA template epoch differences are due to the summation of motion induced voltages and GA artefact differences as explained above. After applying REEGMAS, where motion induced voltages are mainly removed the residual variability is predominantly due to GA changes associated with shifts in spatial position. In this case the maximum volume-volume GA difference for the same conditions (Exp. 3a) was 107.7 μ V and slice-slice GA of 1.06 μ V, broadly comparable to the expected values (Yan et al., 2009). Therefore the error in the GA template found experimentally due to GA variability related to changes in head position are modest provided a slice-wise template is used.

For fMRI with the PMC ‘on’, the magnetic field gradients are updated based on head motion. In this case when the subject moves, the axes of the magnetic field

gradients are maintained in the same plane relative to the EEG circuit. In some special cases the circuit should experience *the same* magnetic field gradients from epoch to epoch as long as the EEG circuit and head move in perfect harmony. In this scenario the PMC updates to the acquisition should contribute to increasing the GA stability. However, translations along each axis due to subject motion will cause a different magnetic field gradient to be experienced from epoch to epoch in either case of the fMRI/PMC being On or Off. Overall this suggests there should not be a significant penalty in GA variability from PMC gradient updates and even be an advantage. We therefore conducted simulations based on Yan et al, 2009 (see supplementary material 2 - simulation for details). The simulations showed that the variance $\rho GA_{template}$ is slightly increased for some of the 37 points of a slice-wise epoch acquisition for fMRI/PMC-on during motion sessions. However, the mean variance considering the whole GA template epoch is not significantly increased for fMRI/PMC-on acquisitions when compared to fMRI/PMC-off acquisitions. This confirmed our experimental findings (Fig. 7.7B and Table 7.1) that despite possible confounding differences in voluntary movement between sessions suggested PMC-on and off sessions had similar GA stability.

In practice not all of the EEG equipment will move with the head i.e. there will be increased GA instability from the cables connecting the amplifier to the cap electrodes. This necessitates the use of an alternative approach for minimising GA variance during movement; we have demonstrated that a slice based GA template approach is an effective solution requiring only equally temporally spaced slice acquisition during the volume acquisition period. Our data does confirm that there was not a significant penalty in EEG quality for using PMC with the large potential benefits of increased fMRI image stability. This is crucial because it suggests that PMC can be used for EEG-fMRI data acquisition to improve fMRI and also EEG data quality during motion. Moreover, the amplitudes of the motion-related EEG artefacts reduced by our approach are on the same order (~10mm and 6°) as the range of motion-related artefacts reported to be corrected by the PMC camera-system when applied to fMRI acquisitions (Todd et al., 2015). Therefore, our results represent the first successful implementation

of motion-related artefact correction for both EEG (offline correction) and fMRI (prospective) by using the same MPT system to monitor subject motion.

For motion correction methods a key requirement is that data quality is not reduced in the most compliant subjects. In our group when the subjects were keeping still, our method did not change the alpha-rhythm wave shape (orange region, Fig. 7.2a) or modify the eye-blink artefact (blue region, Fig. 7.2a). However, the greatest data quality benefit was obtained during large amplitude motion, where the motion-related artefact correction improved the representation of the alpha-rhythm signal (orange region, Fig. 7.2b), and preserved or recovered the eye-blanks (blue regions, Fig. 7.2b). This improvement is clearly illustrated by the topographic distribution of the alpha-rhythm, which after applying motion correction (Fig. 7.5c), is comparable to that expected (Fig. 7.5a). More advanced analysis such as source localisation of in-scanner EEG (Grova et al., 2008; Vulliemoz et al, 2009; Maziero et al., 2015) could be severely affected by these motion induced changes in topography. At the same time, the motion parameters (red and green tracers, Fig. 7.2b) provide a useful aid for visual analysis of EEG data that is frequently used for studies of epilepsy (Salek-Haddadi et al., 2006, Gotman, et al., 2006; Thornton et al., 2010), where the motion parameters displayed alongside the EEG can be used to determine the likely origin of EEG changes and thereby facilitate interpretation. The ability to scan and obtain EEG of sufficient quality during *ictal* events, which are clinically important but typically suffer from motion (Chaudhary et al, 2012b), should improve the yield and quality of these studies e.g. by allowing the ictal phases to be recorded with sufficient reliability while supressing motion related variance in the fMRI time series.

EEG acquired in the scanner suffers from a characteristic cardiac-related artefact (often termed the BCG artefact). The cardiac-related artefact was attenuated by our approach while subjects were keeping still. A recent study (Levan et al., 2013), used similar methodology to ours (camera-tracker system) but applied it exclusively to correct the cardiac-related artefact. In our results, we verified that the motion-correction attenuated the cardiac-related artefact during ‘keeping still’ sessions (red regions, Fig. 7.2a and Supplementary Material 2 Figures S2.1-S2.2). Our method cannot correct for non-rigid components of the BCG artifact, however realistic modeling of the artifact

suggests that bulk head motion is its dominant cause (Yan et al., 2010). We have additionally shown how the system can be used during fMRI motion correction both in terms of effective motion-related voltage suppression and the maintenance of GA temporal stability. In contrast to our approach, Le Van et al (2013) attached the marker on subject's forehead. The forehead is a region susceptible to involuntary movements such as eye blinks, which would be recorded as head motion, increasing tracking noise. We developed a marker fixation device based on a dental retainer thereby limiting the marker movement to movement of the skull. This may explain why in our study we were able to correct for a wide range of motion amplitudes and frequencies.

Marker fixation has been extensively discussed in the literature (for more details see Maclaren et al., 2013) due to the importance of accurate tracking information for PMC to be beneficial to MRI, and the teeth have been suggested as the best place to attach the marker to. Previous motion tracking studies (Masterton et al., 2007) involved the use of additional circuitry, such as loops and wires in close proximity to the subject. In our acquisitions the camera is spatially distant and electrically isolated from the subject (being mounted on the top of the bore) and is therefore unlikely to pose an increased safety risk (i.e. of localised subject heating (Lemieux 1997)).

In our data following motion correction, residual artefacts were visible in the corrected EEG data (e.g. black arrows, Fig. 7.2), during very high amplitude movements. This residual artefact could be due to nonlinear effects when the cap and head do not move together, for example. The residual artefacts appear to occur across channels and so additional spatial (or cross channel) constraint on the motion related artefact removal may further improve the motion artefact correction. There are also limitations to the tracking especially for faster and larger amplitude motion (Maclaren et al., 2013) which might be reduced by using multiple markers and outlier detection and removal in the tracked data. It must be emphasised that these remarks relate to extreme motion, which might be considered by some sufficient grounds to discard entire datasets. It is possible that these residual artefacts are due to GA instability although motion related voltages were in general the source of greater magnitude voltage changes in our data. In the context of the study of difficult-to-scan subjects (due to disease or mental age or other factors making it difficult for them to control their movement), our

method offers the possibility of offering a more robust scanning protocol, thereby optimising the use of patient and scanner time.

The ability to record motion-insensitive EEG-fMRI data should enable the improved study of epilepsy patients during seizures and more generally populations both healthy and with pathology where combined recordings of EEG-fMRI can provide important information about brain function, especially considering that motion differences between populations (Satterthwaite et al., 2012) can lead to bias. Additionally, studies related to different neuroscience areas, such as speech production and motor tasks should also benefit from our approach.

7.6 Conclusions

Motion-related EEG artefacts in simultaneous EEG-fMRI data were corrected using a Moiré Phase tracking system and linear regression called REEGMAS. This was shown to considerably reduce motion-induced voltages both during small and large amplitude movements. Gradient artefact stability was comparable with or without prospective motion correction. The method was verified visually and quantitatively by comparison of EEG data during movement and when subjects were still inside the MRI with reference to data obtained outside the scanner. The motion correction allowed the recovery of physiological information, such as the alpha-rhythm and the eye-blink artefact while suppressing cardiac and bulk head motion induced voltages. REEGMAS improves the quality of EEG data acquired simultaneously with fMRI for both fMRI/PMC-on and fMRI/PMC-off acquisitions. This is an important step forward because it allows simultaneous EEG-fMRI to be obtained in situations where both modalities data are affected by motion, which would allow a wider and more robust application of EEG-fMRI and can allow the study of challenging but important subjects, such as children and epilepsy patients during *ictal* events.

CHAPTER 8 –GENERAL CONCLUSIONS AND FUTURE PERSPECTIVES

In this thesis we focused in improving EEG-fMRI data acquisition and analysis for providing more accurate information about patients with epilepsy. We have verified that the classic EEG-fMRI fails in mapping the epilepsy-related BOLD activities in many patients, mainly those whom few IEDs were detected during the simultaneous EEG-fMRI acquisition. Besides that the classic approach cannot be applied if IEDs are not detected during the simultaneous acquisition. In order to provide useful maps for these patients neglected by the classic EEG-fMRI, we have applied data-driven method such as ICA and 2dTCA and have shown their capability of providing useful information while studying those patients. Due to ICA dimensionality problem, we have proposed an fMRI-independent approach for selecting ICs related to epilepsy based on its spatial correlation with ESI maps. From this approach, we have concluded that an IC-classifier based on canonical hemodynamic response fails in classifying many ICs related to epilepsy, mainly due to its assumptions that higher frequency BOLD signals (0.1-0.25Hz) are related to acquisition artefacts. Therefore, we believe the scientific community might benefit if a new classifier based also on ESI information, is proposed. The application of 2dTCA to fMRI data have shown that the method is more sensitive in mapping epilepsy-related BOLD activities when positive and negative histograms are considered as temporal predictors for the General Linear Model. We have concluded that a conservative t-map threshold provides more accurate results for the 2dTCA, while a less stringent threshold should be used for the EEG-fMRI method. Concordantly to the ICA study, we have verified an increased sensitivity for mapping those patients neglected by the classic EEG-fMRI, which provides valuable information about their epilepsy's activities. Finally, we have proposed a methodology (REEGMAS) that takes advantage of the PMC, based on a camera-tracker system, applied to fMRI motion correction for also improving EEG data quality in simultaneous EEG-fMRI data acquisition. We have verified that REEGMAS is capable of correcting EEG motion-induced artefacts resulting from motion as large as 10mm and 6° and as fast as 55mm/s, and also small and fast motion-related artefacts such as the BCG. Besides that we have verified that the PMC on fMRI data is not a penalty for the EEG data acquired

simultaneously, which is an important finding in order to support the use of PMC on EEG-fMRI data.

In general, we conclude that our findings highlight the importance of exploring different fMRI-analysis approaches, specifically for patients presenting few or none IEDs during simultaneous EEG-fMRI acquisitions. Our results also suggest the importance of faster fMRI acquisition sequences, because higher frequency BOLD components might play important role for studying epilepsy. Therefore, the PMC might be a valuable tool for developing such sequences, because it can provide motion less sensitive fMRI data and also the motion parameters for improving the EEG simultaneously acquired.

REFERENCES

- Abbott DF, Masterton RAJ, Archer JS, Fleming SW, Warren AEL, Jackson GD. Constructing Carbon Fiber Motion-Detection Loops for Simultaneous EEG-fMRI. *Frontiers in Neurology*. 2014; 5: 260.
- Allen PJ, Polizzi G, Krakow K, Fish DR, Lemieux L. Identification of EEG events in the MR scanner: the problem of pulse artifact and a method for its subtraction. *NeuroImage*. 1998; 8(3): 229-239.
- Allen PJ, Josephs O, Turner R. A method for removing imaging artifact from continuous EEG recorded during functional MRI. *NeuroImage*. 2000; 12: 230–239.
- Aziz H, Guvenar A, Akhtar SV, Hassan KZ. Comparative epidemiology of epilepsy in Pakistan and Turkey: population-based studies using identical protocols. *Epilepsia* 1997; 38:716-22.
- Bagshaw AP, Aghakhani Y. EEG-fMRI of focal epileptic spikes: analysis with multiple haemodynamic functions and comparison with gadolinium-enhanced MR angiograms. *Hum. Brain Mapp.* 2004; 22(3): 179–192.
- Bell GS, Gaitatzis A, Bell CL, Johnson AL, Sander JW. Suicide in people with epilepsy: how great is the risk? *Epilepsia*. 2009; 50(8): 1933–42.
- Bénar C, Aghakhani Y, Wang Y, Izenberg A, Al-Asmi A, Dubeau F, Gotman J. Quality of EEG in simultaneous EEG-fMRI for epilepsy. *Clinical Neurophysiology*. 2003; 114: 569–580.
- Bénar CG, Grova C, Kobayashi E, Bagshaw AP, Aghakhani Y, Dubeau F, Gotman J. EEG-fMRI of epileptic spikes: concordance with EEG source localization and intracranial EEG. *Neuroimage*. 2006; 30: 1161–1170.
- Bonmassar G, Purdon PL, Jaaskelainen IP, Chiappa K, Solo V, Brown EN, Belliveau JW. Motion and ballistocardiogram artifact removal for interleaved recording of EEG and EPs during MRI. *NeuroImage*. 2002; 16: 1127–1141.
- Boor R, Jacobs J, Hinzmann A, Bauermann T, Scherg M, Boor S, Vucurevic G, Pfleiderer C, Kutschke G, Stoeter P. Combined spike-related functional MRI and

multiple source analysis in the non-invasive spike localization of benign rolandic epilepsy. *Clinical Neurophysiology*. 2007; 118: 901–909.

Calhoun V, Adali T, Hansen L, Larsen J, Pekar J. Ica of functional mri data: an overview. 4th International Symposium on Independent Component Analysis and Blind Signal Separation; April, 2003; Nara, Japan.

Centeno M, Tierney TM, Perani S, Shamshiri EA, StPier K, Wilkinson C, et al. Optimising EEG-fMRI for Localisation of Focal Epilepsy in Children. *PLoS ONE*. 2016; 11(2): e0149048. doi:10.1371/journal.pone.0149048.

Centeno M, Carmichael DW. Network connectivity in epilepsy: resting state fMRI and EEG-fMRI contributions. *Frontiers in Neurology*. 2014; 5: 93.

Chaudhary UJ, Carmichael DW, Rodionov R, Thornton RC, Bartlett P, Vulliemoz S, et al.. Mapping preictal and ictal haemodynamic networks using video-electroencephalography and functional imaging. *Brain*. 2012a; 135(Pt 12): 3645–3663.

Chaudhary UJ, Rodionov R, Carmichael DW, Thornton RC, Duncan JS, Lemieux L. Improving the sensitivity of EEG-fMRI studies of epileptic activity by modelling eye blinks, swallowing and other video-EEG detected physiological confounds. *Neuroimage*, 2012b; 61: 1383–1393.

Chowdhury MEH, Mullinger KJ, Glover P, Bowtell R. Reference layer artefact subtraction (RLAS): A novel method of minimizing EEG artefacts during simultaneous fMRI. *Neuroimage*. 2014; 84: 307-319.

Christoph MM, Murray MM, Lantz G, Gonzalez S, Spinelli L, Peralta RG. EEG source imaging. *Clinical Neurophysiology*. 2004; 115: 2195–2222.

Damoiseaux JS, Rombouts SAR, Barkhof F, Scheltens P, Stam CJ, Smith SM, Beckmann CF. Consistent resting-state networks across healthy subjects. *Proc Natl Acad Sci USA*. 2006; 103(37): 13848–13853.

De Luca M, Beckmann CF, De Stefano N, Matthews PM, Smith SM. fMRI resting state networks define distinct modes of long-distance interactions in the human brain. *NeuroImage*. 2006; 29: 1359–1367.

- De Martino F, Gentile F, Esposito F, Balsi M, Di Salle F, Goebel R, Formisano E. Classification of fMRI independent components using IC-fingerprints and support vector machine classifiers. *NeuroImage*. 2007; 34 (1): 177–194.
- Diehl B, Salek-Haddadi A, Fish DR, Lemieux L. Mapping of spikes, slow waves, and motor tasks in a patient with malformation of cortical development using simultaneous EEG and fMRI. *Magn. Reson. Imaging*. 2003; 21(10): 1167–1173.
- Eviatar H, Saunders JK, Hoult DI. Motion compensation by gradient adjustment. In Proceedings of the 5th Annual Meeting of ISMRM; May, 1997; Vancouver, Canada, p. 1898.
- Eviatar H, Schattka B, Sharp JC, Rendell J, Alexander ME. Real time head motion correction for functional MRI. In Proceedings of the 7th Annual Meeting of the ISMRM; May 1999, Philadelphia, Pennsylvania, USA, p. 269.
- Fisher R, van Emde Boas W, Blume W, Elger C, Genton P, Lee P, et al. Epileptic seizures and epilepsy: definitions proposed by ILAE and IBE. *Epilepsia*. 2005; 46(4): 470–2.
- Fisher RS. Epilepsy from the patient's perspective: Review of results of a community-based survey. *Epilepsy Behav*. 2000; 1: S9–S14.
- Fox MD, Snyder AZ, Vincent JL, Corbetta M, Van Essen DC, Raichle ME. The human brain is intrinsically organized into dynamic, anticorrelated functional networks. *Proc. Natl. Acad. Sci. USA*. 2005; 102 (27): 9673–9678.
- Friston KJ, Williams S, Howard R, Frackowiak RS, Turner R. Movement-related effects in fMRI time-series. *Magnetic Resonance in Medicine*. 1996; 35(3): 346-355.
- Gallucci Neto J and Marchetti RL. Epidemiologic aspects and relevance of mental disorders associated with epilepsy. *Rev Bras Psiquiatr*. 2005; 27(4): 323-8.
- Glover GH. Deconvolution of impulse response in eventrelated BOLD fMRI. *NeuroImage*. 1999; 9: 416–429.

Goldman RI, Stern JM, Engel JJr, Cohen MS. Acquiring simultaneous EEG and functional MRI. *Clinical Neurophysiology*. 2000; 111 (11): 1974–1980.

Gotman J, Kobayashi E, Bagshaw AP, Bénar CG, Dubeau F. Combining EEG and fMRI: a multimodal tool for epilepsy research. *Journal of Magnetic Resonance Imaging*. 2006; 23(6): 906-920.

Greicius MD, Krasnow B, Reiss AL, Menon V. Functional connectivity in the resting brain: a network analysis of the default mode hypothesis. *Proc. Natl. Acad. Sci. USA*. 2003; 100(1): 253–258.

Gross AR. A brief history of epilepsy and its therapy in the western hemisphere. *Epilepsy research*. 1992; 12: 65-74.

Grouiller F, Thornton RC, Groening K, Spinelli L, Duncan JS, Schaller K, et al. With or without spikes: localization of focal epileptic activity by simultaneous electroencephalography and functional magnetic resonance imaging. *Brain*. 2011; doi:10.1093/brain/awr156.

Grova C, Daunizeau J, Kobayashi E, Bagshaw AP, Lina JM, Dubeau F, Gotman J. Concordance between distributed EEG source localization and simultaneous EEG-fMRI studies of epileptic spikes. *NeuroImage*. 2008; 39: 755–774.

Guerrini R . Epilepsy in children . *Lancet*. 2006; 367: 499–524.

Haacke EM, Brown RW, Thompson MR, Venkatesan R. *Magnetic resonance imaging: physical principles and sequence design*. New York: Wiley; 1999.

Hajnal JV, Myers R, Oatridge A, Schwieso JE, Young IR, Bydder GM. Artifacts due to stimulus correlated motion in functional imaging of the brain. *Magn Reson Med*. 1994; 31: 283–291.

Hamandi K, Powell HWR, Laufs H, Symms MR, Barker GJ, Parker GJM, Lemieux L, Duncan JS. Combined EEG-fMRI and tractography to visualize propagation of epileptic activity. *J Neurol Neurosurg Psychiatry*. 2008; 79: 594–597.

Hamandi K, Salek-Haddadi A, Fish DR, Lemieux L. EEG/functional MRI in epilepsy: the Queen Square experience. *J. Clin. Neurophysiol.* 2004; 21(4): 241–248.

Handwerker DA, Ollinger JM, D'Esposito M. Variation of BOLD hemodynamic responses across subjects and brain regions and their effects on statistical analyses. *NeuroImage*. 2004; 21: 1639–1651.

Harris EC, Barraclough B. Suicide as an outcome for mental disorders. A meta-analysis. *Br J Psychiatry*. 1997; 170: 205–28.

Helmholtz H. Ueber einige Gesetze der Vertheilung elektrischer Ströme in körperlichen Leitern mit Anwendung auf die thierisch-elektrischen Versuche, Ann Physik und Chemie. 1853; 9: 211-233.

Herodes M, Oun A, Haldre S, Kaasik AE. Epilepsy in Estonia: A quality-of-life study . *Epilepsia*. 2001; 42: 1061–73.

Hippocrates(?) The Sacred Disease. In: G.E.R. Lloyd (Ed.), Hippocratic Writings, Penguin Books, Harmondsworth, 1978, pp. 237 251.

Hunyadi B, Tousseyn S, Mijović B, Dupont P, Van Huffel S, Van Paesschen W, De Vos M. ICA Extracts Epileptic Sources from fMRI in EEG-Negative Patients: A Retrospective Validation Study. *PLoS ONE*. 2013; 8(11): e78796. doi:10.1371/journal.pone.0078796.

IFSCN - International Federation of Societies for Clinical Neurophysiology. A glossary of terms most commonly used by clinical electroencephalographers. *Electroencephalogr Clin Neurophysiol*. 1974; 37(5): 538-48.

ILAE - International League Against Epilepsy. Guidelines for epidemiologic studies on epilepsy. Commission on Epidemiology and Prognosis. *Epilepsia* 2011; 34: 592–6.

Isnard J, Guénot M, Ostrowsky K, Sindou M, Mauguière F. The role of the insular cortex in temporal lobe epilepsy. *Ann Neurology*. 2000; 48: 614–623.

Jacoby A. Impact of epilepsy on employment status: Findings from a UK study of people with well-controlled epilepsy. *Epilepsy Res*. 1995; 21: 125–32.

Jacoby A, Buck D, Baker G, McNamee P, Graham-Jones S, Chadwick D. Uptake and costs of care for epilepsy: findings from a UK regional study. *Epilepsia*. 1998; 39 (7): 776–86.

Jennum P, Gyllenborg J, Kjellberg J. The social and economic consequences of epilepsy: a controlled study. *Epilepsia*. 2011; 52 (5): 949–56 .

Jochimsen TH, Norris DG, Mildner T, Mller HE. Quantifying the intra- and extravascular contributions to spin-echo fMRI at 3 T. *Magnetic Resonance in Medicine*. 2004; 52: 724–732

Jorge J, Grouiller F, Gruetter R, Van der Zwaag W, Figueiredo P. Towards high-quality simultaneous EEG-fMRI at 7 T: Detection and reduction of EEG artifacts due to head motion. *NeuroImage*. 2015; 120: 143-153.

Kale R. Bringing epilepsy out of the shadows. *BMJ*. 1997; 315: 2-3.

Khatamian YB, Fahoum F, Gotman J. Limits of 2D-TCA in detecting BOLD responses to epileptic activity. *Epilepsy Research*. 2011; 94: 177-188.

Kobayashi E, Bagshaw AP, Grova C, Dubeau F, Gotman J. Negative BOLD responses to epileptic spikes. *Hum Brain Mapp*. 2006; 27: 488–497.

Laufs H, Daunizeau J, Carmichael DW, Kleinschmidt A. Recent advances in recording electrophysiological data simultaneously with magnetic resonance imaging. *NeuroImage*. 2008; 40(2): 515-28.

Laufs H, Kleinschmidt A, Beyerle A, Eger E, Salek-Haddadi A, Preibisch C, Krakow K. EEG-correlated fMRI of human alpha activity. *NeuroImage*. 2003; 19(4): 1463-1476.

Lemieux L, Allen PJ, Franconi F, Symms MR, Fish DR. Recording of EEG during fMRI experiments: patient safety. *Magn. Reson. Med.* 19997; 38: 943–952.

Lemieux L, Salek-Haddadi A, Josephs O, Allen P, Toms N, Scott C, Krakow K, Turner R, Fish DR. Event-related fMRI with simultaneous and continuous EEG: description of the method and initial case report. *NeuroImage*. 2001; 14: 780–787.

Lemieux L, Salek-Haddadi A, Lund TE, Laufs H, Carmichael D. Modelling large motion events in fMRI studies of patients with epilepsy. *Magn. Reson. Imaging.* 2007; 25(6): 894–901.

LeVan P, Gotman J. Independent Component Analysis As a Model-Free Approach for the Detection of BOLD Changes Related to Epileptic Spikes: A Simulation Study. *Human Brain Mapping.* 2009; 30: 2021–2031.

LeVan P, Tyvaert L, Moeller F, Gotman J. Independent component analysis reveals dynamic ictal BOLD responses in EEG-fMRI data from focal epilepsy patients. *NeuroImage.* 2010; 49: 366–378.

LeVan P, Maclarens J, Herbst M, Sosheim R, Zaitsev M, Hennig J. Ballistocardiographic artifact removal from simultaneous EEG–fMRI using an optical motion-tracking system. *NeuroImage.* 2013; 75: 1–11.

LeVan P, Tyvaert L, Gotman J. Modulation by EEG features of BOLD responses to interictal epileptiform discharges. *Neuroimage.* 2010; 50: 15–26.

Logothetis NK, Pauls J, Augath M, Trinath T, Oeltermann A. Neurophysiological investigation of the basis of the fMRI signal. *Nature.* 2001; 412: 150–157.

Lopes R, Lina JM, Fahoum F, Gotman J. Detection of epileptic activity in fMRI without recording the EEG. *NeuroImage.* 2012; 60: 1867–1879.

Maclarens J, Herbst M, Speck O, Zaitsev M. Prospective motion correction in brain imaging: a review. *Magn Reson Med.* 2013; 69: 621–636.

Mandelkow H, Halder P, Boesiger P, Brandeis D. Synchronization facilitates removal of MRI artefacts from concurrent EEG recordings and increases usable bandwidth. *NeuroImage.* 2006; 32: 1120–1126.

Mansfield P. Multiplanar image formation using NMR spin echoes. *J Phys C Solid State Phys.* 1977; 10:L55–L58.

Marinas A, Elices E, Gil-Nagel A, Salas-Puig J, Sanchez JC, Carreno M, et al. Socio-occupational and employment profile of patients with epilepsy. *Epilepsy Behav.* 2011; 21(3):223–7.

Masterton RA, Abbott DF, Fleming SW, Jackson GD. Measurement and reduction of motion and ballistocardiogram artefacts from simultaneous EEG and fMRI recordings. *NeuroImage.* 2007; 37: 202–211.

Maziero D, Castellanos AJ, Salmon CEG, Velasco TR. Comparison between Different ESI Methods on Refractory Epilepsy Patients Shows a High Sensitivity for Bayesian Model Averaging. *Journal of Biomedical Science and Engineering.* 2014; 7: 662-674.

Maziero D, Sturzbecher M, Velasco TR, Rondoni C, Castellanos AL, Carmichael DW, Salmon CEG. A comparison of independent component analysis (ICA) of fMRI and electrical source imaging (ESI) in focal epilepsy reveals misclassification using a classifier. *Brain Topography.* 2015; 28(6): 813-831.

Maziero D, Velasco TR, Hunt N, Payne E, Lemieux L, Salmon CEG, Carmichael DW. Towards motion insensitive EEG-fMRI: Correcting motion-induced voltages and gradient artefact instability in EEG using an fMRI prospective motion correction (PMC) system. *NeuroImage.* 2016; [doi:10.1016/j.neuroimage.2016.05.003](https://doi.org/10.1016/j.neuroimage.2016.05.003).

McEvoy AW, Spinelli L, Michel CM, Duncan JS, Lemieux L. The spatio-temporal mapping of epileptic networks: Combination of EEG–fMRI and EEG source imaging. *NeuroImage.* 2009; 46(3-13): 834–843.

McKeown M, Makeig S, Brown G, Jung T, Kindermann S, Bell A, Sejnowski T. Analysis of fMRI data by blind separation into independent spatial components. *Hum Brain Mapping.* 1998; 6: 160–188.

Menz M, Neumann J, Muller K, Zysset S. Variability of the BOLD response over time: An examination of within-session differences. *Neuroimage.* 2006; 32: 1185–1194.

Michel CM, Murray MM, Lantz G, Gonzalez S, Spinelli L, Peralta RG. EEG source imaging. *Clin Neurophysiol.* 2004a; 115:2195–2222

Michel CM, Lantz G, Spinelli L, Menendez GPR, Landis T, Seeck M. 128-Channel EEG Source Imaging in Epilepsy: Clinical Yield and Localization Precision. *Journal of Clinical Neurophysiology*. 2014b; 21: 71-83.

Moeller F, LeVan P, Gotman J. Independent Component Analysis (ICA) of Generalized Spike Wave Discharges in fMRI: Comparison with General Linear Model-Based EEG-fMRI. *Human Brain Mapping*. 2011; 32: 209–217.

Moosmann M, Schonfelder VH, Specht K, Scheeringa R, Nordby H, Hugdahl K. Realignment parameter-informed artefact correction for simultaneous EEG–fMRI recordings. *NeuroImage*. 2009; 45(4): 1144–1150.

Morgan VL, Abou-Khalil B, Gore JC. Development of 2dTCA for the Detection of Irregular, Transient BOLD Activity. *Human Brain Mapping*. 2008; 29: 57-69.

Morgan VL, Gore JC. Detection of irregular, transient fMRI activity in normal controls using 2dTCA: comparison to event-related analysis using known timing. *Human Brain Mapping*. 2009; 30(10): 3393-3405.

Morgan VL, Gore JC, Abou-Khalil B. Functional epileptic network in left mesial temporal lobe epilepsy detected using resting fMRI. *Epilepsy Research*. 2010; 88: 168-178.

Moritz CH, Carew JD, McMillan AB, Meyerand ME. Independent component analysis applied to self-paced functional MR imaging paradigms. *NeuroImage*. 2005; 25: 181–192.

Mulert C, Jäger L, Schmitt R, Bussfeld P, Pogarell O, Möller HJ, et al. Integration of fMRI and simultaneous EEG: towards a comprehensive understanding of localization and time-course of brain activity in target detection. *NeuroImage*. 2004; 22: 83–94.

Mulert C, Lemieux L. EEG-fMRI: physiological basis, technique, and applications. Heidelberg: Springer; 2010. 539 p.

Niazy RK, Beckmann CF, Iannetti GD, Brady JM, Smith SM. Removal of FMRI environment artifacts from EEG data using optimal basis sets. *NeuroImage*. 2005; 28: 720-737.

Noronha ALA, Borges MA, Marques LHN, Zanetta DMT, Fernandes PT, de Boer H, Espíndola J, Miranda CT, Prilipko L, Bell GS, Sander JW, and Li LM. Prevalence and Pattern of Epilepsy Treatment in Different Socioeconomic Classes in Brazil. *Epilepsia*. 2007; 48(5): 880–885.

O'Donnell RD, Berkhout J, Adey WR. Contamination of scalp EEG spectrum during contraction of crano-facial muscles. *Electroencephalography and Clinical Neurophysiology*. 1974; 37: 145-151.

Ogawa S, Lee TM, Kay AR, Tank DW. Brain magnetic resonance imaging with contrast dependent on blood oxygenation. *Proc. Natl. Acad. Sci. USA*. 1990; 87: 9868-9872.

Parkes LM, Schwarzbach JV, Bouts AA, Deckers RHR, Pullens P, et al. Quantifying the spatial resolution of the gradient echo and spin echo BOLD response at 3 Tesla. *Magn Reson Med*. 2005; 54: 1465–1472

Pauling L, Coryell CD. The magnetic properties and structure of hemoglobin, oxyhemoglobin and carbonmonoxyhemoglobin. *Proc. Natl. Acad. Sci USA*. 1936; 22(4): 210-216.

Pellerin L, Pellegrini G, Bittar PG, Charnay Y, Bouras C, Martin JL, Stella N, Magistretti PJ. Evidence supporting the existence of an activity-dependent astrocyte-neuron lactate shuttle. *Dev Neuroscience*. 1998; 20: 291-299.

Pfurtscheller G, Stancak A, Neuper C. Post-movement beta synchronization. A correlate of an idling motor area? *Electroencephalography and Clinical Neurophysiology*. 1996; 98: 281-293.

Pittau F, Dubeau F, Gotman J. Contribution of EEG/fMRI to the definition of the epileptic focus. *Neurology*. 2012; 78: 1479–1487.

Power JD, Mitra A, Laumann TO, Snyder AZ, Schlaggar BL, Petersen SE. Methods to detect, characterize, and remove motion artifact in resting state fMRI. *NeuroImage*. 2014; 84: 320–341.

Ratsepp M, Oun A, Haldre S, Kaasik AE. Felt stigma and impact of epilepsy on employment status among Estonian people: exploratory study. *Seizure*. 2000; 9: 394–401,

Reynolds EH. The ILAE/IBE/WHO Global Campaign against Epilepsy: Bringing Epilepsy “Out of the Shadows”. *Epilepsy & Behavior*. 2000; 1: S3-S8.

Rodionov R, De Martino F, Laufs H, Carmichael DW, Formisano E, Walker M, Duncan J, Lemieux L. Independent component analysis of interictal fMRI in focal epilepsy: Comparison with general linear model-based EEG correlated fMRI. *NeuroImage*. 2007; 38: 488–500.

Rondinoni C, Amaro JE, Cendes F, Santos AC, Salmon CEG. Effect of scanner acoustic background noise on strict resting-state fMRI. *Brazilian journal of medical and biological research*. 2013; 46: 359-367.

Rosenow F, Luders H. Presurgical evaluation of epilepsy. *Brain*. 2001; 124: 1683-1700.

Salek-Haddadi A, Friston KJ, Lemieux L, Fish DR. Studying spontaneous EEG activity with fMRI. *Brain Res. Rev.* 2003; 43: 110–133.

Salek-Haddadi A, Diehl B, Hamandi K, Merschhemke M, Liston A, Friston K, Duncan JS, Fish DR, Lemieux L. Hemodynamic correlates of epileptiform discharges: an EEG-fMRI study of 63 patients with focal epilepsy. *Brain*. 2006; 1088(1): 148–166.

Satterthwaite TD, Wolf DH, Loughead J, et al. Impact of in-scanner head motion on multiple measures of functional connectivity: relevance for studies of neurodevelopment in youth. *NeuroImage*. 2012; 60(1): 623–632.

Schmithorst VJ, Brown RD. Empirical validation of the triple-code model of numerical processing for complex math operations using functional MRI and group Independent 150 Part 3. Multimodal Data Integration Component Analysis of the mental addition and subtraction of fractions. *NeuroImage*. 2004; 22:1414–1420.

Seeck M, Lazeyras F, Michel CM, Blanke O, Gericke CA, Ives J, Delavelle J, Golay X, Haenggeli CA, de Tribolet N, Landis T. Non-invasive epileptic focus localization using

EEG-triggered functional MRI and electromagnetic tomography. *Electroencephalogr Clin Neurophysiol.* 1998; 106: 508–512.

Shorvon SD, Farmer PJ. Epilepsy in developing countries: a review of epidemiological, sociocultural, and treatment aspects. *Epilepsia.* 1988; 29 (Suppl. 1): 36–54.

Shorvon SD, Andermann F, Guerrini R. (eds) *The Causes of Epilepsy. Common and Uncommon Causes in Adults and Children.* Cambridge: Cambridge University Press, 2011.

Tana MG, Bianchi AM, Sclocco R, Franchin T, Cerutti S, Leal A. Parcel-Based Connectivity Analysis of fMRI Data for the Study of Epileptic Seizure Propagation. *Brain Topogr.* 2012. DOI 10.1007/s10548-012-0225-2.

Tao JX, Baldwin M. Cortical substrates of scalp EEG epileptiform discharges. *J. Clin. Neurophysiol.* 2007; 24(2): 96–100.

Thorbecke R, Rating D. Was denkt man über Epilepsie? *Epilepsie Blätter.* 1996; 9: 3.

Thornton R, Laufs H, Rodionov R, Cannadathu S, Carmichael DW, Vulliemoz S, et al. EEG correlated functional MRI and postoperative outcome in focal epilepsy. *J Neurol Neurosurg Psychiatry.* 2010; 81:922-927.

Thornton R, Vulliemoz S, Rodionov R, Carmichael DW, Chaudhary UJ, Diehl B, et al. Epileptic networks in focal cortical dysplasia revealed using electroencephalography-functional magnetic resonance imaging. *Ann Neurol.* 2011; 70: 822-37.

Thurman DJ, Hesdorffer DC, and French JA. Sudden unexpected death in epilepsy: Assessing the public health burden *Epilepsia.* 2014; 55(10): 1479–1485.

Tierney TM, Croft LJ, Centeno M, Shamshiri EA, Perani S, Baldeweg T, Clark CA, Carmichael DW. FIACH: A biophysical model for automatic retrospective noise control in fMRI. *Neuroimage.* 2015; doi: 10.1016/j.neuroimage.2015.09.034.

Tikhonov AN, Arsenin VY. *Solutions of Ill-Posed Problems.* W.H. Winston, Washington, DC. 1977.

Todd N, Josephs O, Callaghan MF, Lutti A, Weiskopf N. Prospective motion correction of 3D echo-planar imaging data for functional MRI using optical tracking. *NeuroImage*. 2015; 113: 1–12.

Trujillo-Barreto NJ, Aubert-Vázquez E, Valdés-Sosa PA. Bayesian model averaging in EEG/MEG imaging. *NeuroImage*. 2004; 21: 1300–1319.

Velasco TR, Sakamoto AC, Alexandre V, Walz R, Dalmagro CL, Bianchin MM, et al. Foramen Ovale Electrodes Can Identify a Focal Seizure Onset When Surface EEG Fails in Mesial Temporal Lobe Epilepsy. *Epilepsia*. 2006; 47: 1300–1307.

Velasco TR, Wichert-Ana L, Mathern GW, Araujo D, Walz R, Bianchin MM, et al. Utility of ictal SPECT in mesial temporal lobe epilepsy with hippocampal atrophy: a randomized trial. *Neurosurgery*. 2011; 68(2): 431-436.

Vulliemoz S, Thornton R, Rodionov R, Carmichael DW, Guye M, Lhatoo S. Hemodynamic correlates of epileptiform discharges: an EEG-fMRI study of 63 patients with focal epilepsy. *Brain Res*. 2006; 1088 (1): 148–166.

Vulliemoz, S., Thornton, R., Rodionov, R., Carmichael, D.W., Guye, M., Lhatoo, S.. The spatio-temporal mapping of epileptic networks: combination of EEG-fMRI and EEG source imaging. *NeuroImage*. 2009; 46(3): 834–843.

WHO - World Health Organization - Epilepsy [cited 2016 May 26]. Available from: <http://www.who.int/mediacentre/factsheets/fs999/en>

Worsley KJ, Liao CH, Aston J, Petre V, Duncan GH, Morales F, Evans AC. A general statistical analysis for fMRI data. *NeuroImage*, 2002; 15: 1–15.

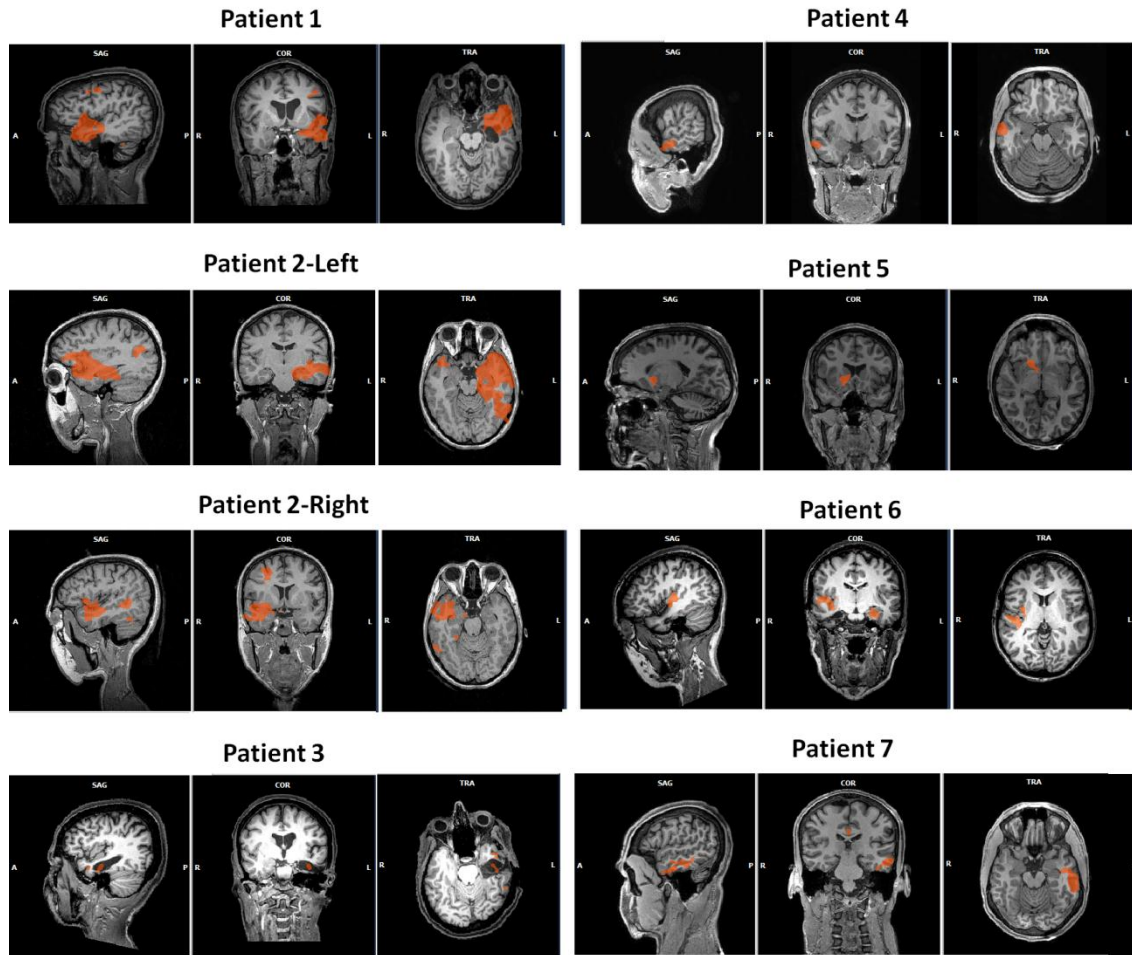
Worsley KJ, Poline JB, Friston KJ, Evans AC. Characterizing the response of PET and fMRI data using multivariate linear models. *NeuroImage*. 2002; 6: 305–319.

Yan WX, Mullinger KJ, Geirsdottir GB, Bowtell R. Physical Modelling of pulse artefact sources in simultaneous EEG/fMRI. *Human Brain Mapping*. 2010; 31(4): 604–620.

Yan WX, Mullinger KJ, Brookes MJ, Bowtell RW.. Understanding gradient artefacts in simultaneous EEG/fMRI. *Neuroimage*. 2009; 46(2): 459–471.

Supplementary Material 1

EEG-fMRI concordant results



Supplementary material Figure S1.1: Classical GLM EEG-fMRI resultant maps.
The spatial maps were obtained with $t > 2.0$, $p < 0.05$ and are overlaid onto 3DT1 images of native space. The areas presented represent only positive BOLD responses.

Evaluation among the different methods:

For comparing the results obtained by each method we adapted the system applied by Grouiller and others (Grouiller el al., 2011) to attributing 0, 1 or 2 points based on the region mapped by each method and its relation to the surgery cavity/indication and surgery outcome. It is important to explain that all the results were first considered as related to the electrical information, which considered the lobar level as a concordance. Here, as a complementary result we re-classified the concordance of each map by a more restrictive comparison. We considered the Epileptic-related area (in Engel I patients) as the resection area and its immediate proximity, which here was assumed to be 15mm from resection margins and within the same sublobar cortical region (Grouiller el al., 2011). We attributed 2 points when the maximum z-score (considering $z\text{-score}>4$) was inside this region, 1 point when there was a non-maximum z-score ($z\text{-score}>4$) ROI inside this region and 0 when no significant region was found inside this region. Extra information (0*) is also given for components related to structures described as epilepsy network-related, e.g. Insula and Thalamus.

Table S1.1, Evaluation among the different methods

	EEG-fMRI Concordance	ESI-IC concordance		IC-finger concordance	
		IC	Points	IC	Points
Patient	Points	IC	Points	IC	Points
1	2	93	2	83	0
		62	2		
2-L	2	51	2	51	2
		58	2		
		67	1	58	2
2-R	0*	N/A	N/A	49	0*
				63	0*
3	2	61	1	46	1
4	2	76	1	64	2
		90	0*		
		102	1	90	0*
		43	0*	114	1
5	2	22	1	22	1
				42	1
6	2	67	1	70	0
				81	2
7	2	91	0*	55	1
		80	1	80	1

		86	2	86	2
8	0	78	0*	66	2
		56	2		
9	0	147	2	95	1
10	0	65	2	51	1
				111	1
				65	2
11	0	48	2	28	0
		83	1	83	1
12	N/A	70	2	70	2
		163	2		
13	N/A	80	2	--	--
		71	0*		
Total/Max	14/24		32/50		26/48

The Supplementary table S1.1 presents the performance of each approach applied in this paper. Applying the criteria explained above we found that the EEG-fMRI approach received 14 points on 24 possible (max of 2 points for each map and the method provided 12 maps). The ESI-IC received 32 points on 50 possible (max of 2 points for each map, the method provided 25 maps). The IC-fingerprint received 26 points in 48 possible (24 maps were provided by this approach). In the manuscript we described the comparison related to the number of patients with epilepsy related maps found by each method. The classical GLM analysis of EEG-fMRI mapped epileptic related BOLD activities in 7/13 patients, the ICA IC-fingerprint provided epileptic-related BOLD activities in 12/13 patients and at least one epileptic-related IC was provided for all the patients by the ESI-IC spatial correlation.

Supplementary Material 2

Table S2.1: Contribution of each parameter to the regression (F-score)

	<i>Subject #1</i>		<i>Subject #2</i>		<i>Subject #3</i>	
	F	pValue	F	pValue	F	pValue
<i>vx</i>	0.008122	0.928192	57.84282	2.96E-14	814.2091	3.13E-177
<i>vy</i>	164.5041	1.42E-37	19.503	1.01E-05	1186.7	3.84E-256
<i>vz</i>	7734.428	0	880.1602	1.64E-189	704.0389	9.69E-154
<i>vrx</i>	1525.861	0	970.6956	2.31E-208	66.39056	3.81E-16
<i>vry</i>	5184.36	0	2611.853	0	21939.22	0
<i>vrz</i>	7110.622	0	3753.607	0	6580.186	0
<i>vxsqr</i>	394.3445	2.76E-87	51.0478	9.31E-13	14.31115	0.000155
<i>vysqr</i>	38.46293	5.64E-10	52.76149	3.90E-13	185.8609	3.19E-42
<i>vzsqr</i>	234.9732	7.22E-53	46.30196	1.04E-11	135.5941	2.76E-31
<i>vrxsqr</i>	43.34559	4.65E-11	39.3227	3.66E-10	10.42539	0.001244
<i>vrysqr</i>	106.7317	5.53E-25	108.77	2.10E-25	21.62743	3.32E-06
<i>vrzsqr</i>	304.2554	7.43E-68	86.31743	1.68E-20	0.649324	0.42036
<i>x</i>	98.5471	3.40E-23	42.66312	6.65E-11	65.93634	4.79E-16
<i>y</i>	951.4529	3.19E-206	53.65207	2.48E-13	1027.699	1.49E-222
<i>z</i>	233.3158	1.65E-52	18.35102	1.85E-05	132.1619	1.55E-30
<i>rx</i>	1251.402	1.78E-269	574.2687	3.18E-125	851.3894	3.84E-185
<i>ry</i>	230.9709	5.32E-52	103.2039	3.44E-24	2.597667	0.107029
<i>rz</i>	20.74349	5.27E-06	37.08924	1.15E-09	133.934	6.36E-31

F-score and *pvalue* resultant of the F-score test applied to determine the importance of each parameter to the motion regression (6 velocities, 6 velocities square, 3 translations and 3 rotations, over the axis x, y and z).

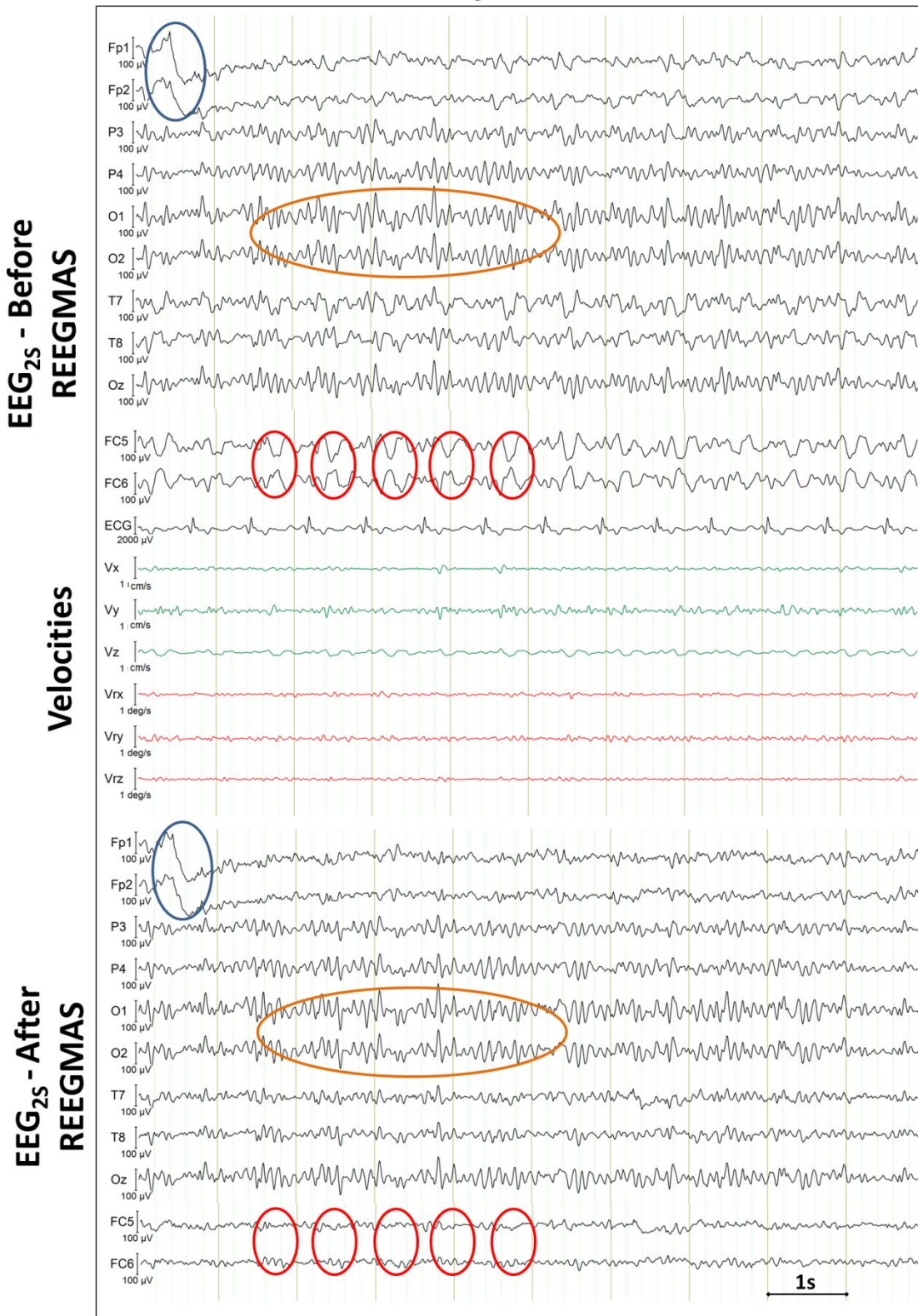
Table S2.2a: RMSE (dB) quantification - Keeping Still						
Subject1						
	no fMRI		PMC off		PMC on	
	MRMSE	std	MRMSE	std	MRMSE	std
Before REEGMAS	16.32	0.60	16.35	0.57	16.30	0.45
After REEGMAS	16.33	0.55	16.41	0.54	16.31	0.42
Before vs After (<i>p</i>)	0.61		0.69		0.43	
Subject2						
Before REEGMAS	16.60	2.25	14.68	2.21	14.52	1.66
After REEGMAS	15.99	1.46	14.59	2.21	14.40	1.74
Before vs After (<i>p</i>)	0.22		0.87		0.75	
Subject3						
Before REEGMAS	9.48	1.29	10.13	1.24	9.46	0.76
After REEGMAS	9.57	1.29	10.39	1.30	9.57	1.00
Before vs After (<i>p</i>)	0.39		0.45		0.76	

Table S2.2b: RMSE (dB) quantification - Moving						
Subject1						
	no fMRI		PMC off		PMC on	
	MRMSE	std	MRMSE	std	MRMSE	std
Before REEGMAS	25.83	6.32	22.18	6.05	20.39	4.43
After REEGMAS	16.96	0.78	16.56	0.38	16.46	0.42
Before vs After (<i>p</i>)	7.33E-06		0.001		4.46*10⁻⁰⁴	
Subject2						
Before REEGMAS	26.41	2.37	20.00	2.40	17.19	1.85
After REEGMAS	16.55	0.82	16.06	1.48	15.57	1.93
Before vs After (<i>p</i>)	1.46*10⁻⁰⁷		3.21*10⁻⁰⁶		1.17*10⁻⁰⁴	
Subject3						
Before REEGMAS	29.09	2.41	21.87	7.96	21.96	8.64
After REEGMAS	16.07	0.90	13.91	2.75	13.94	3.33
Before vs After (<i>p</i>)	7.91*10⁻¹⁵		1.73*10⁻⁰⁵		2.32*10⁻⁰⁵	

The Mean Root Mean Square Error (MRMSE) and its respectively standard deviation are presented for each EEG data acquired during Still (S2a) and Moving (S2b) sessions. The values are shown for uncorrected (Before REEGMAS) and corrected (After REEGMAS) data acquired in the absence of fMRI and during PMC off and on acquisitions for each subject. Before vs After indicates whether the corrected (After REEGMAS) data has a significantly smaller (<) or not (=) MRMSE in comparison to the uncorrected data (Before REEGMAS), the (p) shows the significance for the comparison (t-test).

A

Subject#1 - Still



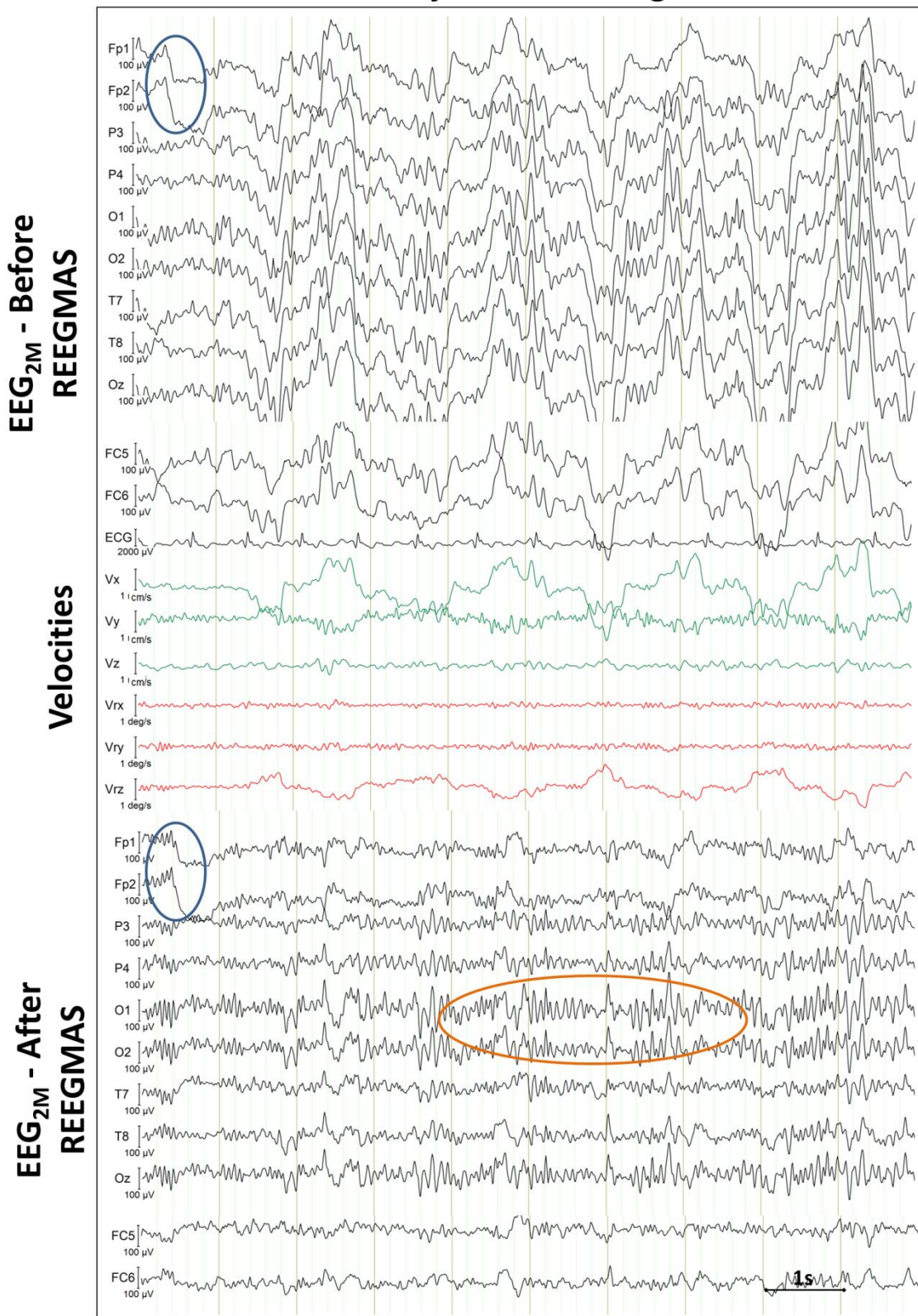
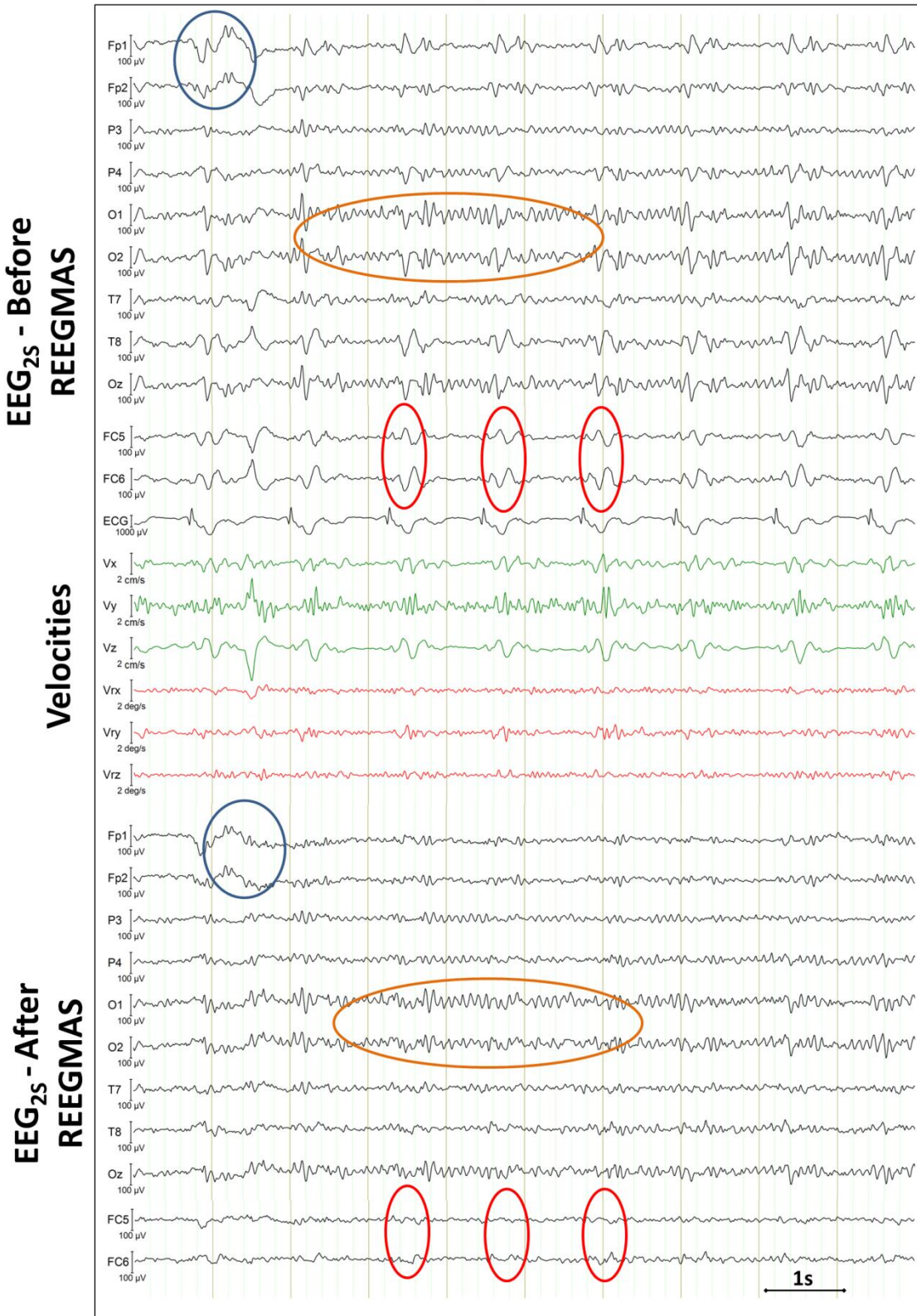
B**Subject#1 - Moving**

Figure S2.1: Representative EEG data from subject #1 obtained in Experiment 2 (inside the MRI scanner, no fMRI acquisition). A ten second epoch following the first eyes closed period is shown for the subject keeping still (A) and subject moving (B) sessions. In both A and B the EEG is displayed before (EEG_{2S} and EEG_{2M}) (top) and after (EEG_{2S-C} and EEG_{2M-C}) (bottom) REEGMAS correction. The middle section shows the translational (green cm/s) and rotational (red degrees/s) velocities measured by the MPT motion tracking system. The blue ellipses highlight the eye-blink artefacts, red ellipses highlight the cardiac pulsation-related artefacts and the orange highlight the alpha-rhythm detection. The black arrows point to residuals remaining after motion correction. The EEG data presented in A-B were not pulse-related artefact corrected by AAS.

A**Subject#3 - Still**

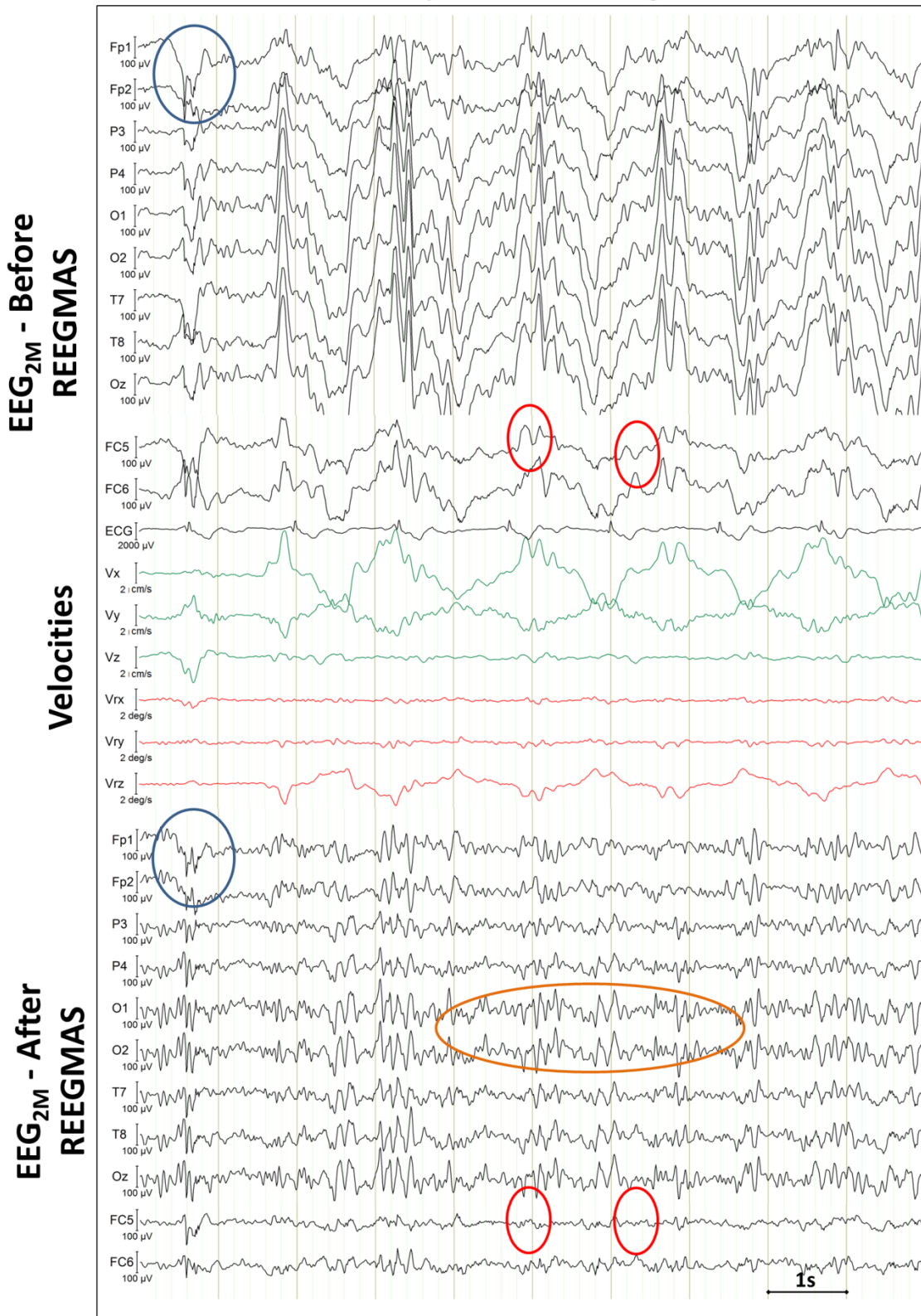
B**Subject#3 - Moving**

Figure S2.2: Representative EEG data from subject #2 obtained in Experiment 2 (inside the MRI scanner, no fMRI acquisition). A ten second epoch following the first eyes closed period is shown for the subject keeping still (A) and subject moving (B) sessions. In both A and B the EEG is displayed before (EEG_{2S} and EEG_{2M}) (top) and after (EEG_{2S-C} and EEG_{2M-C}) (bottom) REEGMAS correction. The middle section shows the translational (green cm/s) and rotational (red degrees/s) velocities measured by the MPT motion tracking system. The blue ellipses highlight the eye-blink artefacts, red ellipses highlight the cardiac pulsation-related artefacts and the orange highlight the alpha-rhythm detection. The black arrows point to residuals remaining after motion correction. The EEG data presented in A-B were not pulse-related artefact corrected by AAS.

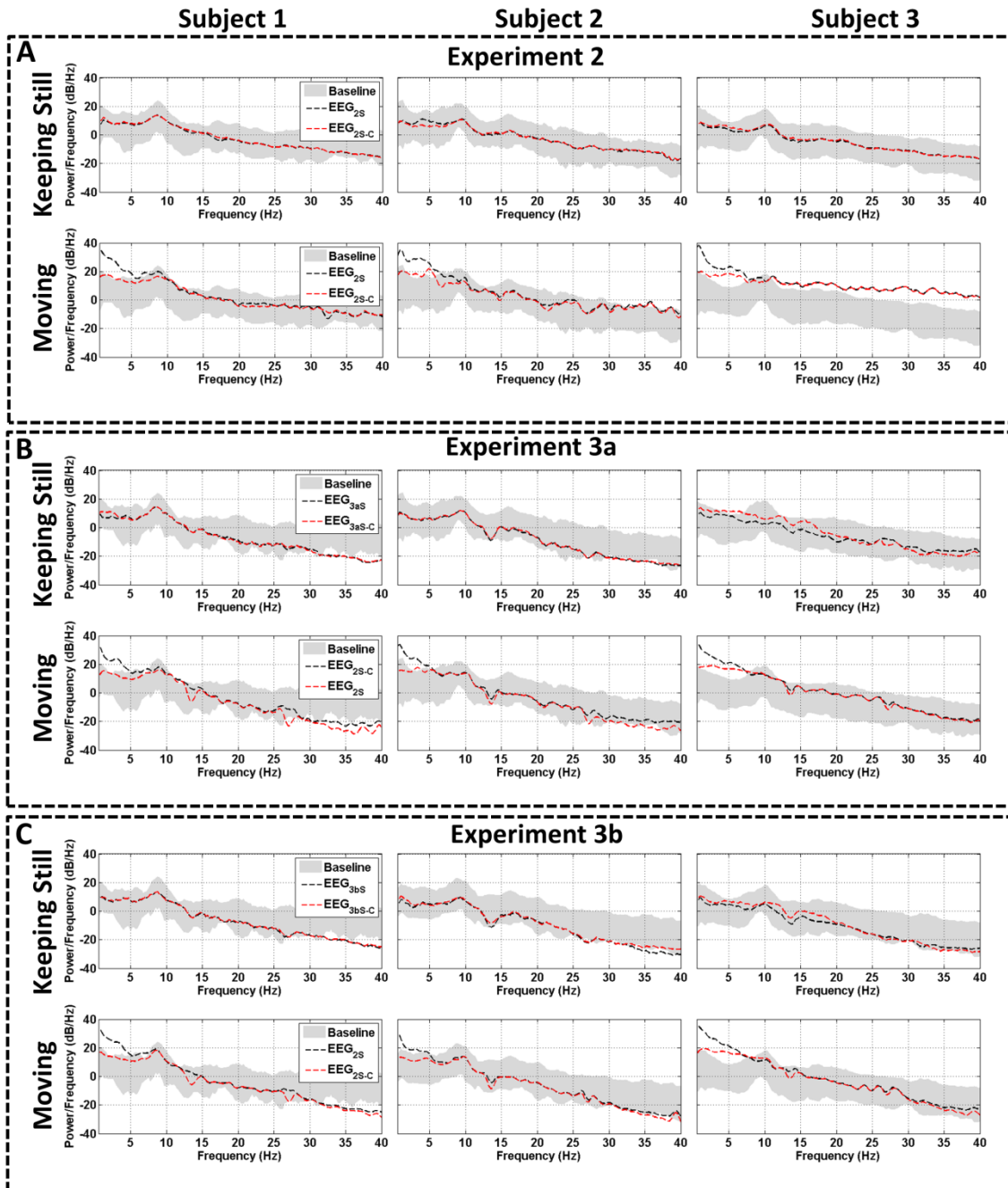


Figure S2.3. The mean power spectral density (PSD) at electrode T8 for each subject with eyes closed during keeping still (top row of each figure) and moving (bottom row in each figure) sessions. The mean PSD for each subject is presented for Experiment 2 (in-scanner, no fMRI) (A), Experiment 3a (PMC off) (B) and 3b (PMC on) (C). The shaded grey area represents two standard deviations from the mean baseline (Exp. 1) spectra obtained outside the MRI scanner. The black dashed line refers to the mean power spectra of the EEG acquired in-scanner

(Experiments 2 and 3) but not corrected by REEGMAS and the red dashed line to the same data corrected by REEGMAS.

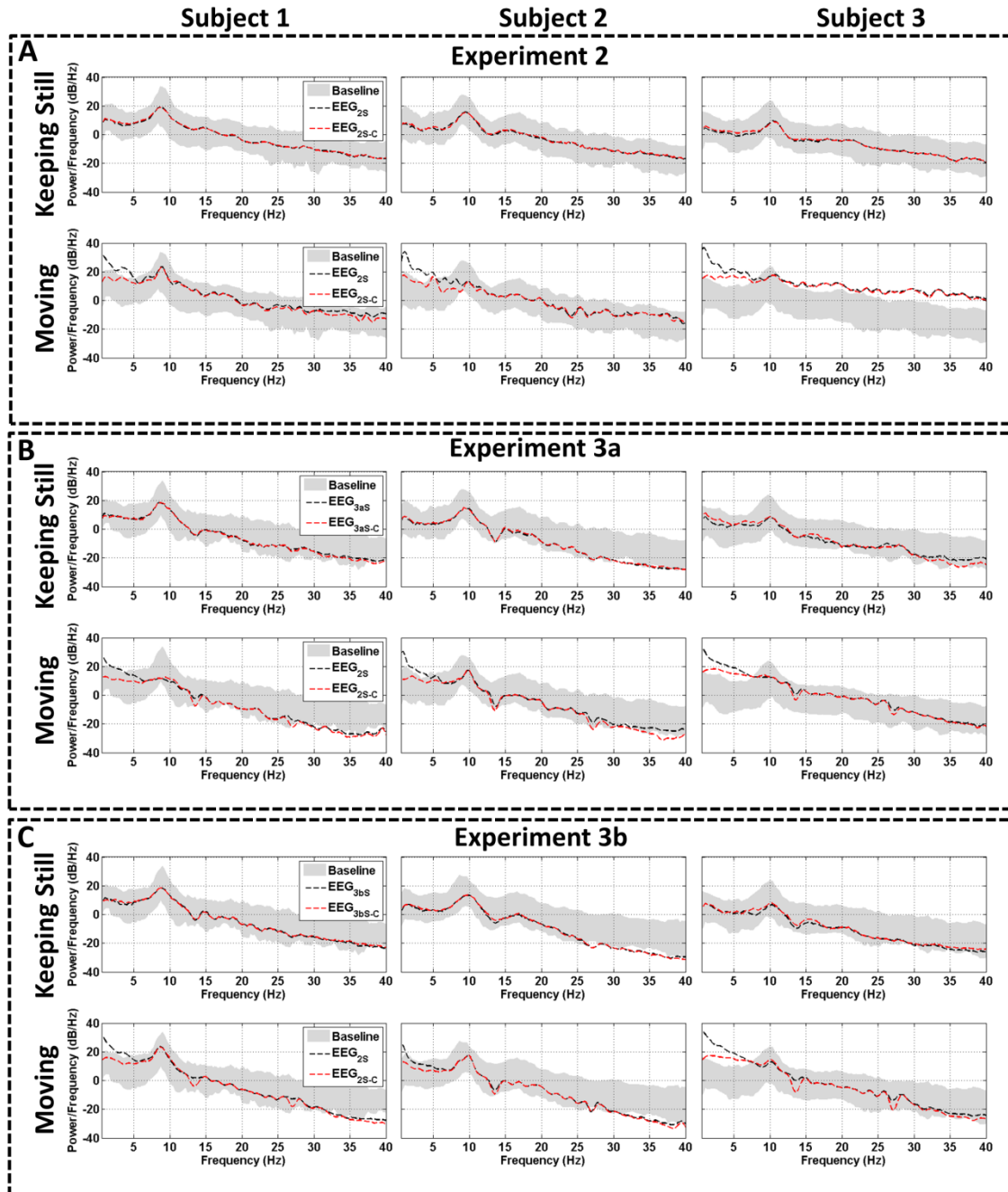


Figure S2.4. The mean power spectral density (PSD) at electrode P4 for each subject with eyes closed during keeping still (top row of each figure) and moving (bottom row in each figure) sessions. The mean PSD for each subject is presented

for Experiment 2 (in-scanner, no fMRI) (A), Experiment 3a (PMC off) (B) and 3b (PMC on) (C). The shaded grey area represents two standard deviations from the mean baseline (Exp. 1) spectra obtained outside the MRI scanner. The black dashed line refers to the mean power spectra of the EEG acquired in-scanner (Experiments 2 and 3) but not corrected by REEGMAS and the red dashed line to the same data corrected by REEGMAS.

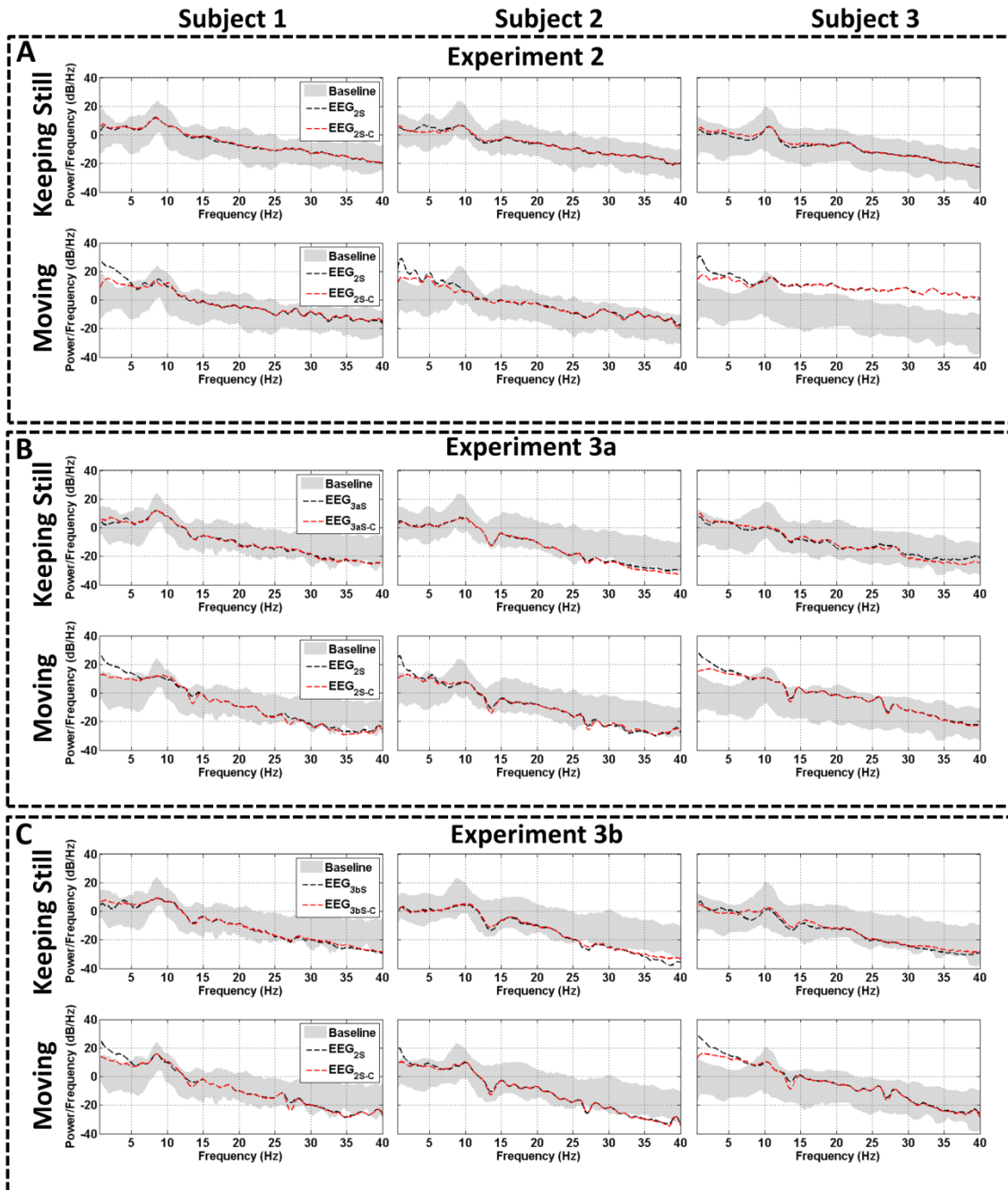


Figure S2.5. The mean power spectral density (PSD) at electrode C4 for each subject with eyes closed during keeping still (top row of each figure) and moving (bottom row in each figure) sessions. The mean PSD for each subject is presented for Experiment 2 (in-scanner, no fMRI) (A), Experiment 3a (PMC off) (B) and 3b (PMC on) (C). The shaded grey area represents two standard deviations from the mean baseline (Exp. 1) spectra obtained outside the MRI scanner. The black dashed line refers to the mean power spectra of the EEG acquired in-scanner

(Experiments 2 and 3) but not corrected by REEGMAS and the red dashed line to the same data corrected by REEGMAS.

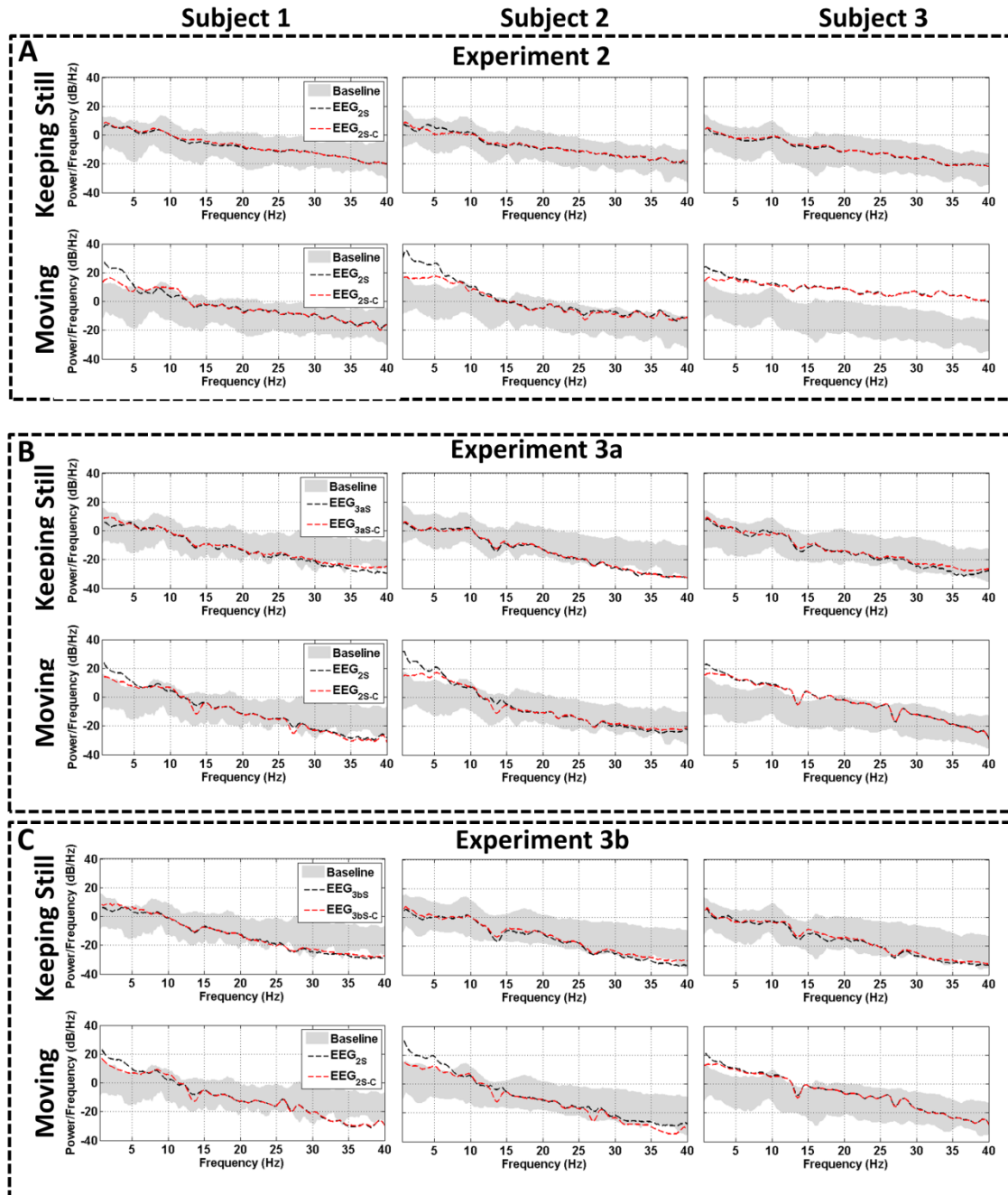


Figure S2.6. The mean power spectral density (PSD) at electrode F4 for each subject with eyes closed during keeping still (top row of each figure) and moving (bottom row in each figure) sessions. The mean PSD for each subject is presented for Experiment 2 (in-scanner, no fMRI) (A), Experiment 3a (PMC off) (B) and 3b

(PMC on) (C). The shaded grey area represents two standard deviations from the mean baseline (Exp. 1) spectra obtained outside the MRI scanner. The black dashed line refers to the mean power spectra of the EEG acquired in-scanner (Experiments 2 and 3) but not corrected by REEGMAS and the red dashed line to the same data corrected by REEGMAS.

Supplementary Material 2 - Simulation

In this supplementary section we simulate the impact of spatial position changes on the gradient artefact (the voltages induced by the magnetic field gradient switching only) with and without updates to the spatial gradients produced by the PMC system. This is based on the assumptions in Yan et al 2009, and does not account for noise in the PMC system.

Gradient pulses designing

In order to estimate the voltages induced on scalp-placed electrodes we have calculated the voltage induced by the switching gradients on a spherical shell, simulating the head. The first step was to simulate the gradient pulses diagram for a standard gradient echo-echo planar image sequence (Fig. S2.7).

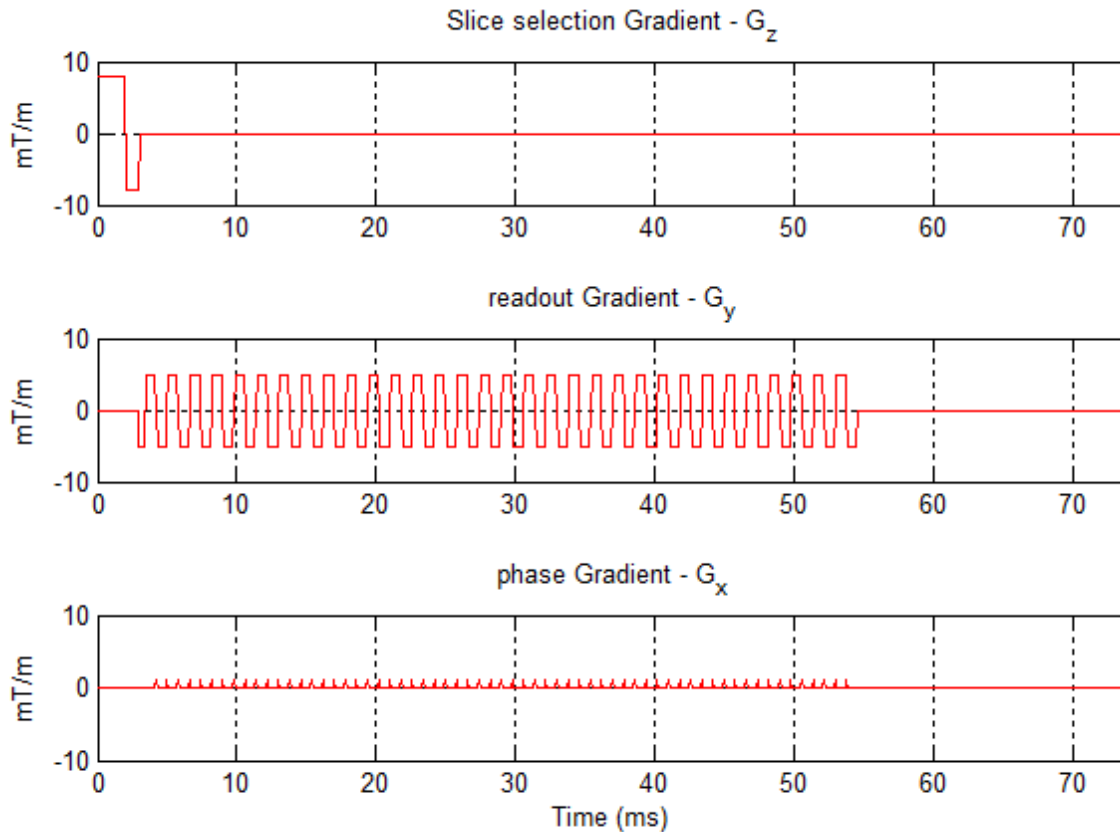


Figure S2.7 Gradients scheme for the situation where the head is at the magnet center

We have assumed TE=30ms, TR_{slice}=74ms, 64x64 k-space lines. In order to simulated the gradients applied for acquiring axial slices of the brain, the slice selection gradient (G_z), readout gradient (G_y) and phase encoding gradient (G_x) were chosen to be placed on z, y and x axis. The gradients were simulated at a sampling rate of 10kHz, with G_z = 8mT/m, G_y=5mT/m and G_x=1mT/m (Fig. S2.7).

fMRI-Prospective Motion Correction (PMC)

PMC-off

The PMC-off acquisitions does not update the gradients based on the subject's head position. Therefore all 3000 slices were acquired with the same gradient pulses while the spatial position was varied based on our experimentally measured head position changes.

PMC-on

The PMC-on acquisitions are updated based on the subject's head position at the beginning of each slice (every 74ms) (Fig. S2. 7). In our simulations we have based the rotations α (about x-axis), β (about z-axis) and γ (about y-axis), and the translations x_0 (left-right), y_0 (posterior-anterior) and z_0 (feet-head) on the motion information recorded by the camera while acquiring the fMRI/PMC-off of each subject. However the gradient updates only use the information related to the rotations about x, y and z, and use a linear combination of the scanner x,y,z gradients to scan in the patients spatial reference frame and the updated gradients can be written as the following equations:

G_z – Slice Selection Gradient:

No β rotation affects the PMC system during the slice selection gradient

$$[G'_z]^t = [G_z]^t R_x R_y \quad (1)$$

$$\begin{bmatrix} G'_{xx} \\ G'_{yy} \\ G'_{zz} \end{bmatrix} = \begin{bmatrix} 0 \\ 0 \\ sin \end{bmatrix}^t \begin{bmatrix} 1 & 0 & 0 \\ 0 & cos \alpha & -sin \alpha \\ sin & cos \alpha & cos \alpha \end{bmatrix} \begin{bmatrix} cos \gamma & 0 & sin \gamma \\ 0 & 1 & 0 \\ -sin \gamma & 0 & cos \gamma \end{bmatrix} \quad (2)$$

G_y – Readout Gradient:

No γ rotation affects the PMC system during the readout gradient

$$[G'_y]^t = [G_y]^t R_x R_z \quad (3)$$

$$\begin{bmatrix} G'_{xx} \\ G'_{yy} \\ G'_{zz} \end{bmatrix} = \begin{bmatrix} 0 \\ G_{yy} \\ 0 \end{bmatrix}^t \begin{bmatrix} 1 & 0 & 0 \\ 0 & \cos \alpha & -\sin \alpha \\ \sin \alpha & \cos \alpha & \cos \alpha \end{bmatrix} \begin{bmatrix} \cos \beta & -\sin \beta & 0 \\ \sin \beta & \cos \beta & 0 \\ 0 & 0 & 1 \end{bmatrix} \quad (4)$$

Gx – Phase encoding Gradient:

No α rotation affects the PMC system during the phase encoding gradient

$$[G'_x]^t = [G_x]^t R_y R_z \quad (5)$$

$$\begin{bmatrix} G'_{xx} \\ G'_{yy} \\ G'_{zz} \end{bmatrix} = \begin{bmatrix} G_{xx} \\ 0 \\ 0 \end{bmatrix}^t \begin{bmatrix} \cos \gamma & 0 & \sin \gamma \\ 0 & 1 & 0 \\ -\sin \gamma & 0 & \cos \gamma \end{bmatrix} \begin{bmatrix} \cos \beta & -\sin \beta & 0 \\ \sin \beta & \cos \beta & 0 \\ 0 & 0 & 1 \end{bmatrix} \quad (6)$$

An example of the gradients for a rotation of 5 degrees about the x-axis is below in figure S2. 8.

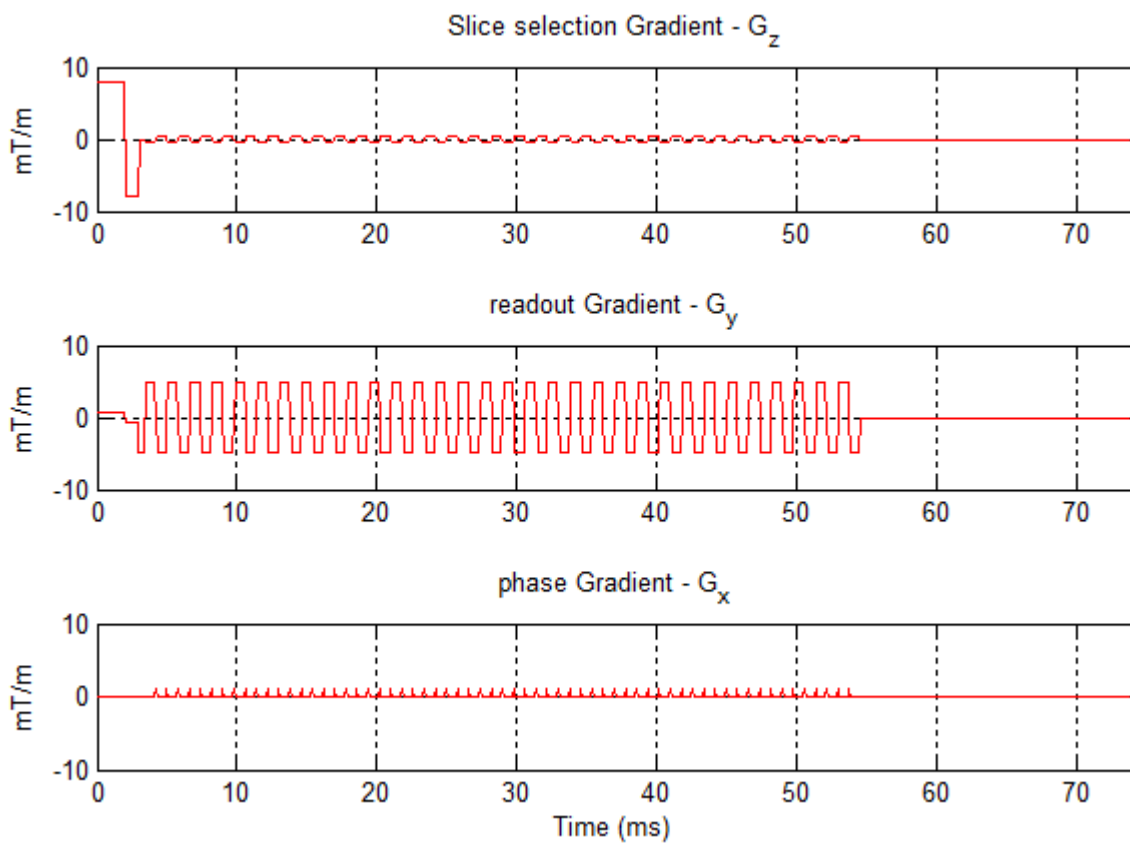


Figure S2.8. Gradients scheme for the situation where the head is rotated 5° about the x-axis.

Voltages induced by the switching gradients

The GA voltages depend on the spatial position of the head. These voltages can be approximated using an analytical solution (equations 7-9 below) based on the electrodes being distributed on a sphere as described in Yan et al., 2009. We and they ignore y-rotations which, in human subjects, commonly have smaller amplitudes than those around the x and z axis. The voltages were derived for the switching gradients in each scanner axis longitudinal (Gz) and transverse (Gy and Gx). The total induced voltage is then the sum of the contributions from each of the gradient directions, $V=V_x+V_y+V_z$ where :

$$V_x(\varphi, \theta) = \frac{1}{6} \dot{G}_x r^2 (2r[(1 - \cos \theta) \sin \alpha \cos 2(\beta + \varphi) - \sin(\beta + \varphi) \cos \alpha \sin \theta] + 3\theta[x_0 \cos(\beta + \varphi) \sin \alpha - z_0 \sin(\beta + \varphi)]) \quad (7)$$

$$V_y(\varphi, \theta) = \frac{1}{6} \dot{G}_y r^2 (2r[(\cos \theta - 1) \sin \alpha \cos 2(\beta + \varphi) - \sin(\beta + \varphi) \cos \alpha \sin \theta] + 3\theta[-x_0 \sin(\beta + \varphi) \sin \alpha - z_0 \cos(\beta + \varphi)]) \quad (8)$$

$$V_z(\varphi, \theta) = \frac{1}{4} \dot{G}_z r^2 (2r \cos(\beta + \varphi) \sin \alpha [(1 - \cos \theta) \sin \alpha \sin(\beta + \varphi) + \cos \alpha \sin \theta] + \theta[\cos(\beta + \varphi) \sin \alpha (2z_0 - y_0 \cot \alpha) + x_0 \sin(\beta + \varphi)]) \quad (9)$$

Where \dot{G} is the switching gradient ratio in mT/m/s⁻¹, r is the head radius, φ and θ are the spherical coordinates defining the location on the sphere where the voltage will be calculated. The coordinates x_0 , y_0 , z_0 are related to the head position on x, y and z axis and the α and β are the rotations about the x and z axis.

Differences in gradient artefact template

The equations above illustrate that if the head is at different positions in two successive epochs (volume-wise or slice-wise) of the GA template, the artefact may differ between them in each point of the sphere, or each electrode. Therefore they also provide the knowledge that the GA template may lose temporal stability, resulting in poorer GA correction when there are large motion into the epochs used for building each part of the template.

The differences in GA template of simulated EEG-data were measured as described in session 2.10, number 3. We were able to estimate the EEG-Root Mean Square for each

of the 37 epoch sample points acquired during the 3000 slices, considering the whole sphere for each time point.

Simulated Results

As expected, the GA-RMS of both fMRI/PMC-off and fMRI/PMC-on are affected by motion (Fig. S2.9), and their values are higher for larger head displacements (in relation to the center of the magnet). For the three subjects (Fig.S2.9, third column) we have verified that the difference between the GA-template RMS of fMRI/PMC-off and fMRI/PMC-on can be positive or negative, which demonstrates that the Gradient Artefact is not always increased by using PMC on fMRI.

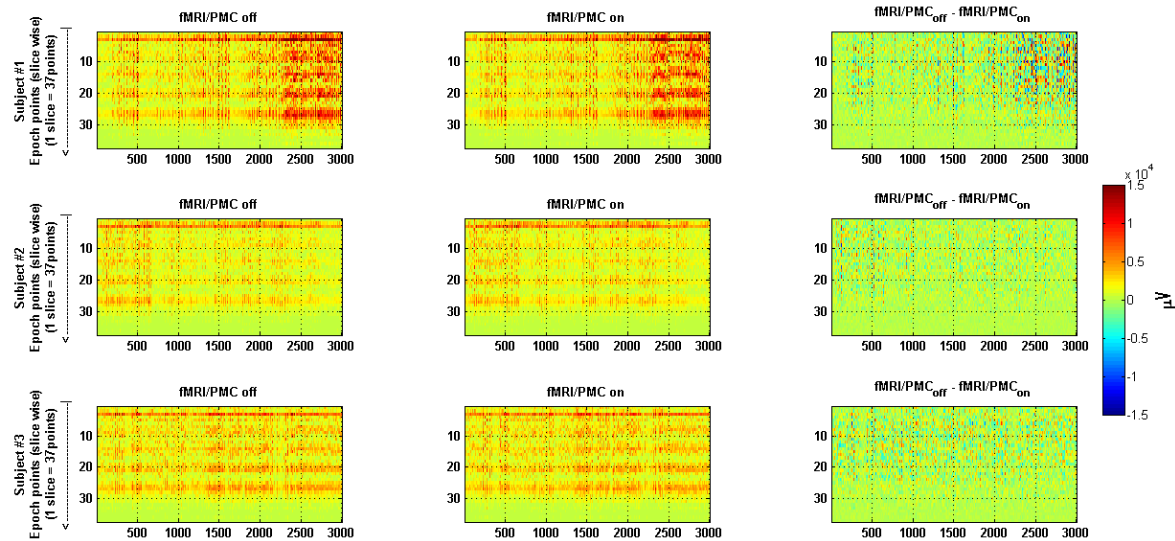


Figure S2.9: GA – RMS across EEG channels of each sample point through the whole 3000 slices acquisition. (First column) fMRI/PMC-off, (second column) fMRI/PMC-on; (Fig. S2.9 third column) differences between fMRI/PMC-off and fMRI/PMC-on GA, for subjects 1 (first line), 2 (second line) and 3 (third line).

The ρ_{GA} measurement (Manuscript Eq. 7.8) was applied in the simulated data presented in Fig. S2.9 in order to estimate the temporal instability of each epoch sample point of the simulated data GA. We have verified that for both simulated conditions (fMRI/PMC-off and fMRI/PMC-on) the variance is similar (Fig. S2.10) for most of the GA epoch sample points.

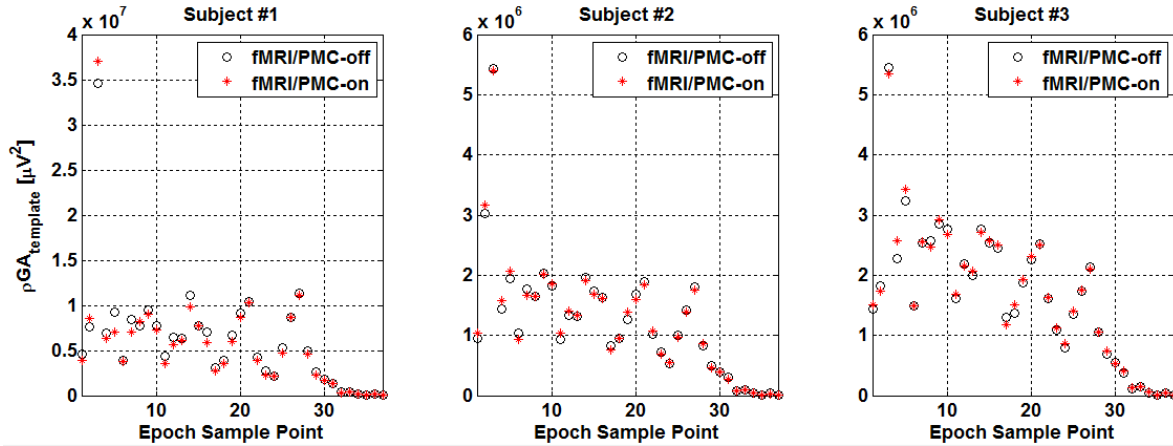


Figure S2.10 – The $\rho GA_{template}$ (Variance) for each epoch sample point (37) for fMRI/PMC-off (black ‘o’) and fMRI/PMC-on (red ‘*’) simulated data. The simulated data is presented for subjects #1, #2 and #3 are presented from the left to the right hand side of the figure.

Finally we have evaluated whether the mean GA variance for fMRI/PMC-off simulated data was different than that for the fMRI/PMC-on simulated data by performing a t-test (procedure similar to that applied for the experimental data acquired in Experiments 2a and 2b, reported on the manuscript). There was no statistical significant differences resulting from those t-tests

Appendix - Ethics Committee Approval



HOSPITAL DAS CLÍNICAS DA FACULDADE DE MEDICINA
DE RIBEIRÃO PRETO DA UNIVERSIDADE DE SÃO PAULO



Ribeirão Preto, 20 de março de 2013

Projeto de pesquisa: "LOCALIZAÇÃO E ESTUDO DE FONTES
EPILEPTOGÊNICAS EM PACIENTES DE EPILEPSIA FOCAL EM FASE PRÉ-
OPERATÓRIA"

Pesquisadores responsáveis: Danilo Maziero (orientando) e Carlos Ernesto Garrido
Salmon (orientador)

Instituição Proponente: Faculdade de Filosofia, Ciências e Letras de Ribeirão Preto –
USP

"O CEP do HC e da FMRP-USP concorda com o parecer ético emitido pelo CEP da
Instituição Proponente, que cumpre as Resoluções Éticas Brasileiras, em especial a
Resolução CNS 196/96. Diante disso, o HCFMRP-USP, como instituição co-
participante do referido projeto de pesquisa, está ciente de suas co-responsabilidades e
de seu compromisso no resguardo da segurança e bem-estar dos sujeitos desta pesquisa,
dispondo de infra-estrutura necessária para a garantia de tal segurança e bem-estar.

Ciente e de acordo:

Drª Marcia Guimarães Villanova
Coordenadora do Comitê de Ética
em Pesquisa - HCFMRP-USP

Prof. Dr. José Alexandre de Souza Crippa
Coordenador Técnico Científico da Unidade
de Pesquisa Clínica – HCFMRP-USP

Campus Universitário – Monte Alegre
14048-900 Ribeirão Preto SP

Comitê de Ética em Pesquisa do HCRP e FMRP-USP
FWA-00002733; IRB-00002186 e
Registro Plataforma Brasil/CONEP nº 5440
(016) 3602-2228
cep@hcsp.usp.br

www.hcrp.usp.br



Universidade de São Paulo
Faculdade de Filosofia, Ciências e Letras de Ribeirão Preto
Comitê de Ética em Pesquisa

Campus de Ribeirão Preto

Of.CEtP/FFCLRP-USP/011-jsl

Ribeirão Preto, 04 de março de 2013

Prezado Pesquisador,

Comunicamos a V. Sa. que o projeto de pesquisa intitulado "**"LOCALIZAÇÃO E ESTUDO DE FONTES EPILEPTOGÊNICAS EM PACIENTES DE EPILEPSIA FOCAL EM FASE PRÉ-OPERATÓRIO"**" foi reanalisado pelo Comitê de Ética em Pesquisa da FFCLRP-USP, em sua 117ª Reunião Ordinária, realizada em 28.02.2013, e enquadrado na categoria: **APROVADO (CAAE - 08219712.7.0000.5407)**.

Solicitamos que eventuais modificações ou emendas ao projeto de pesquisa sejam apresentadas ao CEP, de forma sucinta, identificando a parte do projeto a ser modificada e suas justificativas, e que, ao término do estudo, um relatório final seja entregue, via Plataforma Brasil.

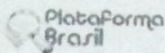
Atenciosamente,

Prof.^a Dr.^a ANDRÉIA SCHMIDT
Coordenadora

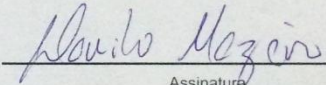
Ao Senhor
Danilo Maziero
Programa de Pós-Graduação em Física Aplicada à Medicina e Biologia da FFCLRP
USP

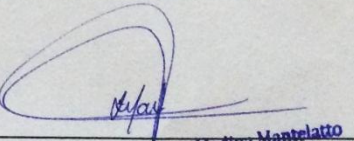
C/C:
Prof. Dr. Carlos Ernesto Garrido Salmon
Departamento de Física da FFCLRP USP

CEP - Comitê de Ética em Pesquisa da FFCLRP
Fone: (16) 3602-4811
Fax: (16) 3633-2660 (direto) ou 3633-5015
Avenida Bandeirantes, 3900 - bloco 3 - sala 16 - 14040-901 - Ribeirão Preto - SP - Brasil
Homepage: <http://www.ffclrp.usp.br> - e-mail: coetp@ffclrp.usp.br



MINISTÉRIO DA SAÚDE - Conselho Nacional de Saúde - Comissão Nacional de Ética em Pesquisa – CONEP
FOLHA DE ROSTO PARA PESQUISA ENVOLVENDO SERES HUMANOS

1. Projeto de Pesquisa: Localização e estudo de fontes epileptogênicas em pacientes de epilepsia focal em fase pré-operatória		2. Número de Sujeitos de Pesquisa: 50	
3. Área Temática:			
4. Área do Conhecimento: Grande Área 1. Ciências Exatas e da Terra , Grande Área 4. Ciências da Saúde			
PESQUISADOR RESPONSÁVEL			
5. Nome: Danilo Maziero			
6. CPF: 367.659.978-06	7. Endereço (Rua, n.º): EXPEDICIONARIO VICENTE GOMES OTERO 65 ADELINO SIMONI RIBEIRAO PRETO SAO PAULO 14071440		
8. Nacionalidade: BRASILEIRA	9. Telefone: (16) 8817-2362	10. Outro Telefone:	11. Email: danibeen@hotmail.com
12. Cargo:			
Termo de Compromisso: Declaro que conheço e cumprirei os requisitos da Resolução CNS 196/96 e suas complementares. Comprometo-me a utilizar os materiais e dados coletados exclusivamente para os fins previstos no protocolo e a publicar os resultados sejam eles favoráveis ou não. Aceito as responsabilidades pela condução científica do projeto acima. Tenho ciência que essa folha será anexada ao projeto devidamente assinada por todos os responsáveis e fará parte integrante da documentação do mesmo.			
Data: <u>06</u> / <u>11</u> / <u>2012</u>		 Assinatura	

INSTITUIÇÃO PROPONENTE			
13. Nome: Faculdade de Filosofia, Ciências e Letras de Ribeirão Preto- USP	14. CNPJ: 63.025.530/0081-99	15. Unidade/Órgão: FFCLRP USP	
16. Telefone: (16) 3602-3653	17. Outro Telefone: (16) 3633-2660		
Termo de Compromisso (do responsável pela instituição): Declaro que conheço e cumprirei os requisitos da Resolução CNS 196/96 e suas Complementares e como esta instituição tem condições para o desenvolvimento deste projeto, autorizo sua execução.			
Responsável: <u>Fernando Luis Medina Mantelatto</u>	CPF: <u>067.722.148-70</u>	 <u>Prof. Dr. Fernando Luis Medina Mantelatto</u> Diretor	
Cargo/Função: <u>Diretor da FFCLRP USP</u>	Data: <u>08</u> / <u>11</u> / <u>2012</u>		
PATROCINADOR PRINCIPAL			
Não se aplica.			